Dichotomy of Radio-Loud and Radio-Quiet Quasars in the Four Dimensional Eigenvector One (4DE1) Parameter Space

A **Dissertation/Thesis** Submitted to the
Office of Postgraduate Program of
Space Science and Geospatial Institute
Entoto Observatory and Research Center
Department of **Astronomy and Astrophysics**
in affiliation with Addis Ababa University

By

Shimeles Terefe Mengistue

In Partial Fulfillment of the Requirements for
the **Degree of Doctor of Philosophy in Astronomy and Astrophysics**

Dichotomy of Radio-Loud and Radio-Quiet Quasars in the Four Dimensional Eigenvector One (4DE1) Parameter Space

By

Shimeles Terefe Mengistue

Dr. Ascensión Del Olmo Orozco

Main Supervisor

Dr. Paola Marziani

Co-Supervisor

Dr. Mirjana Pović

Co-Supervisor

December, 2024

We, the undersigned committee, hereby approve that we have read and recommended to the office of the graduate program for acceptance, of a dissertation entitled "**Dichotomy of Radio-Loud and Radio-Quiet Quasars in the Four Dimensional Eigenvector One (4DE1) Parameter Space**" by **Shimeles Terefe Mengistue** in partial fulfillment of the requirements for the Degree of **Doctor of Philosophy** in Astronomy and Astrophysics.

Approved by	Signature
Dr. Gemechu Muleta	
Chair Person	
Prof. Luka Popović	
External Examiner	
Dr. Solomon Belay	
Internal Examiner	
Dr. Ascensión Del Olmo Orozco	
Main Supervisor	
Dr. Paola Marziani	
Co-Supervisor	
Dr. Mirjana Pović	
Co-Supervisor	
Mr. Abdisa Yilma	
Director General	

Date Approved: **December 3, 2024**

Author's Declaration

I hereby declare that this study is original and has not been submitted for any other degree award to any other University. It is a true copy of the thesis, including any required final revisions, as accepted by my examiners. Permission is herewith granted to Entoto Observatory and Research Center, Space Science and Geospatial Institute, affiliated with Addis Ababa University to circulate and to have copied for non-commercial purposes, at its discretion, the above title upon the request of individuals or institutions.

_____

Author's Signature

_____

Date

Table of Contents

Abstract

Quasars, the most distant and luminous subset of active galactic nuclei (AGN), are historically classified into radio-loud (RL) and radio-quiet (RQ). There has been a long-standing debate about the possibility of a real physical dichotomy between them. Another foundational pillar of AGN is the presence of an accretion disk (AD). A geometrically thin AD around a supermassive black hole (SMBH) might contribute to broad-line emission in type-1 AGN.

This thesis presents two main studies of new and extremely powerful jetted quasars. First, we analyzed the optical and near-UV spectra of 11 of the 12 quasars observed with the Cassegrain TWIN spectrograph on the 3.5 m telescope at the Calar Alto Observatory (CAHA) in Spain, covering a redshift range of $0.35 \lesssim z \lesssim 1$. We aimed to quantify broad emission line differences between RL and RQ quasars and to check the effect of powerful radio ejection on the low ionization lines (LILs) by supplementing the 11 sources with large samples from previous work. Emission lines were analyzed using two complementary approaches: a multicomponent non-linear fitting using the IRAF task `specfit` and the full broad profile analysis. By restricting the RQ population within specific regions of the main sequence (MS) occupied by RL sources, similarities are observed between RL and RQ quasars. However, an unbiased comparison based on matched parameters such as SMBH mass ($M_{\rm BH}$) and Eddington ratio ($\lambda_{\rm E} = L_{\rm bol}/L_{\rm Edd}$) reveals intriguing distinctions. Notably, the most powerful RL quasars exhibit strong redward asymmetries in the Hβ emission lines. Relativistic jets in these powerful RL quasars, do not seem to affect LILs strongly.

In the second study, we focused on the remaining quasar, 3C 47, which exhibits a distinctive double-peaked profile. We employed a relativistic Keplerian accretion disk model, a Bayesian approach, and multicomponent non-linear fitting to explain the unique profile. Additionally, we modeled the prototypical high ionization lines by considering contributions from the accretion disk, outflows, and emissions from the innermost part of the narrow line region. The results provided compelling direct observational evidence supporting the presence of an AD as the source of the broad emission lines observed in quasar 3C 47. A model involving a double broad-line region associated with a binary black hole

is less appealing than the AD model for explaining the characteristics observed specifically in the quasar 3C 47.

Keywords: Galaxies: active – active galactic nuclei – quasars: general – quasars: emission lines – line: profiles – quasars: supermassive black holes – radio-loud and radio-quiet quasars – double-peaked.

Acknowledgements

I am highly indebted to the pioneers who established the Entoto Observatory and Research Center (EORC). This is because I got this great opportunity to carry out my research in Extragalactic Astronomy while pursuing my PhD study, where EORC has availed important facilities including a working compound, internet access, and support personnel to conduct my research. My gratitude also extends to the current Space Science and Geospatial Institute (SSGI) in which EORC is structurally located, for the continual and uninterrupted support for my study. SSGI has provided me with financial support for my visit to Granada, Spain, to conduct part of my research. I would also like to thank the Astronomy and Astrophysics Research and Development Department of SSGI-EORC for managing all the support during my study.

Next to this, I would like to extend heartfelt thanks to my Ph.D. thesis supervisors; Dr. Ascensión Del Olmo Orozco, Dr. Paola Marziani, and Dr. Mirjana Pović, for all the encouragement, kind help and support, continual devotion of their time, and leading me in the correct path of my research that ultimately resulted with this Ph.D. dissertation. Apart from their supervisory role, I would like to thank them again for their commitment to searching for financial support for durations abroad, especially for my 8-month stay at IAA, Spain. In addition, I would like to thank Dr. Jaime Perea (and his wife Dr. Ascensión Del Olmo Orozco) for their warm welcome at IAA, Spain, and their support in every aspect during my stay.

Thirdly, I have to give great thanks to Jimma University (JU) which sponsored my study throughout the study period. I am also very grateful to IAA-CSIC, Spain, for their financial support and for providing me with working space during my two visits.

My heartfelt thanks and appreciation go to my family, especially to my strong and lovely wife Hiwot Tegegne for her great patience, continual encouragement, and for taking care of our sons (Fidoriya Shimeles and Nahom Shimeles) with maximum level of comfort, my mother Abebech Kassa, my sisters Ayehu Terefe and Denkenesh Terefe, my father and brother Tekalign Terefe and his family for their endless love, care, support, prayer, taking care of my sons and en-

couragement throughout my study. I would also like to thank my mother-in-law Birhane Meles and Abebech Mehari, and my sister-in-law, Selamawit Derso (Alganesh) for continually taking responsibility for supporting and taking care of my wife and adorable sons. All of them were doing their best to help me focus on my study. Nothing would have been possible without them.

Finally, my thanks should be extended to all my collaborators at IAA, whose names appeared in publications that came out of this thesis. At this point I have to finally extend my thanks to my friends: Tilahun Getachew (PhD candidate, SSGI-EORC), Dr. Melese Getnet (Postdoctoral Scholar at Lawrence Berkeley National Laboratory) and all the staff members of the SSGI-EORC for their unlimited support and friendly encouragements. Their support was crucial for my progress at different stages during this study.

Sincerely,
Shimeles Terefe Mengistue
Space Science and Geospatial Institute (SSGI)
Enoto Observatory and Research Center (EORC)
Astronomy and Astrophysics Department
Addis Ababa, Ethiopia

Acronyms

Acronym	What it stands for
4DE1	Four Dimensional Eigenvector One
AD	Accretion Disk
AFOSC	Asiago Faint Objects Spectrograph and Camera
AGN	Active Galactic Nuclei
AI	Asymmetry index
BC	Broad Component
BH	Black hole
BLR	Broad-Line Region
CAHA	Hispanic Astronomical Center in Andalusia
CCD	Charge-Coupled Device
CD	Core Dominated
ESO	European Southern Observatory
EW	Equivalent width
FIR	Far infra-red
FIRST	Faint Images of the Radio Sky at Twenty centimeters
FOS	Faint Object Spectrograph
FR	Fanaroff-Riley
FWHM	Full Width Half Maximum
HST	Hubble Space Telescope
IPAC	Infrared Processing and Analysis Center
IR	Infra-red
IRAF	Image Reduction and Analysis Facility
KI	Kurtosis Index

LD	Lobe Dominated
LIL	Low Ionization Line
MCMC	Monte Carlo Markov Chain
MIR	Mid infra-red
MS	Main sequence
NASA	National Aeronautics and Space Administration
NC	Narrow Component
NED	NASA/IPAC Extragalactic Database
NIR	Near infra-red
NLR	Narrow-line Region
NRAO	National Radio Astronomy Observatory
NVSS	NRAO Very Large Array Sky Survey
QSF$_{IT}$	Quasar Spectral Fitting package
QSO	Quasi-Stellar Object
RD	Radio Detected
RI	Radio-Intermediate
RL	Radio-loud
RM	Reverberation Mapping
RQ	Radio-quiet
SBC	Semi-Broad Component
SDSS	Sloan Digital Sky Survey
SED	Spectral Energy Distribution
SL	Scaling Law
SMBH	Super Massive Black Hole
S/N	Signal-to-Noise
ST	Spectral Type
VBC	Very Broad Component
VBLR	Very Broad Line Region
VLA	Very Large Array
VLBA/I	Very Long Base Line Array/Interferometry
ΛCDM	Λ Cold Dark Matter

Symbols

α	Alpha, to represent right ascension
$\mathbf{\AA}$	Angstrom, unit of wavelength
M_B	Absolute Magnitude
m	Apparent Magnitude
V	Apparent Johnson Magnitude
β	Beta
χ^2	Chi squared
δ	Delta
Δ	Delta
ε	Epsilon
η	Eta
γ	Gamma
Γ	Gamma
H_o	Hubble Constant
κ	Kappa
λ	Lambda
$L_y\alpha$	Lyman Alpha
Z	Metallicity
μ	Mu
ν	Nu
ω	Omega
Ω	Omega
Ω_Λ	Omega Lambda
Ω_o	Omega Matter
π	Pi
ϕ	Phi
$\prod$	Product Operator
z	Redshift
ρ	Rho
σ	Sigma
θ	Theta
τ	Tau
ξ	Xi

Astronomical constants

Constant Name (symbol) = Constant Value (with units)

Astronomical unit (AU) = 1.496×10^{11} m
Angstrom (Å) = 1×10^{-10} m
Light year (ly) = 9.463×10^{15} m
Atomic mass unit (amu) = 1.661×10^{-27} Kg
Boltzmann's constant (k) = $1.381 \times 10^{-16} ergs\, K^{-1}$
Boltzmann's constant (k) = $8.617 \times 10^{-5} eV\, K^{-1}$
Gravitational radius (r_g) = $1.482 \times 10^{23} M_{\odot}$ m
Gravitational constant (G) = 6.674×10^{-11} $\mathrm{Nm^2 kg^{-2}}$
Jansky (Jy) = $1 \times 10^{-23} ergs\, cm^2\, s^{-1}\, Hz^{-1}$
Parsec (pc) = 3.086×10^{16} m
Solar luminosity ($L_{\odot}$) = $3.828 \times 10^{33} ergs\, s^{-1}$
Solar mass ($M_{\odot}$) = 1.989×10^{30} kg
Solar radius ($R_{\odot}$) = 6.96×10^{8} m
Stefan-Boltzmann constant (σ_B) = 5.67×10^{-5} ergs $\mathrm{cm^{-2}}\, s^{-1}\, \mathrm{K^{-4}}$
Year (yr) = 3.156×10^{7} s
Speed of light (c) = 2.9979×10^{8} m $\mathrm{s^{-1}}$

List of Figures

List of Tables

Publications, Proceedings, and Presentations

Peer-reviewed publications

The studies conducted in the framework of this Ph.D. thesis have made possible the following scientific contributions.

- **Mengistue S. T., Marziani P., Del Olmo A., Povic M., Perea J., and Deconto Machado A., 2023, "*Quasar 3C 47: Extreme Population B Jetted Source With Double-peaked Profiles*", Astronomy and Astrophysics (A&A), Volume 685, id.A116, 15 pp.**
  DOI: 10.1051/0004-6361/202348800
  (https://ui.adsabs.harvard.edu/abs/2024A%26A...685A.116T/abstract)

- **Mengistue S. T., Del Olmo A., Marziani P., Povic M., Martínez-Carballo M. A., Perea J., and Márquez I., 2023, "*Optical and near-UV spectroscopic properties of extremely jetted quasars in the main sequence context*", MNRAS, 525, 447**
  DOI:10.1093/mnras/stad2467
  (https://ui.adsabs.harvard.edu/abs/2023MNRAS.525.4474M/abstract)

Proceeding papers

- Pursimo, T., Ighina, L., Ihanec, N., Mandarakas, N., Skillen, K., and **Terefe, S.**, "*Quest to find changing look-quasars*", 2019, contributions of the Astronomical Observatory Skalnaté Pleso, 49, 539
  (https://ui.adsabs.harvard.edu/abs/2019CoSka..49..539P/abstract)

- **Terefe**, S. del Olmo, A., Marziani, P., and Pović, M., "*Dichotomy of radio-loud and radio-quiet quasars in four-dimensional eigenvector one (4DE1) parameter space*", 2020, IAU 356 symposium proceedings, IAUS, 356, 351
  (https://ui.adsabs.harvard.edu/abs/2021IAUS..356..351T/abstract)

- Bilata-Woldeyes, B., Povic, M., Beyoro-Amado, Z., Getachew-Woreta, T., and **Terefe, S.**, "Multiwavelength *morphological study of active galaxies*",

2021, IAUS, 356, 295
(https://ui.adsabs.harvard.edu/abs/2021IAUS..356..295B/abstract).

International and national presentations related to this PhD work

- August 6 - 15, 2024, poster presentation (virtual), IAU General Assembly 2024, Cape Town, South Africa.
- July 15 - 19, 2024, two poster presentations (virtual), the 16^{th} scientific meeting of the Spanish Astronomical Society, Granada, Spain.
- July 7 - 12, 2024, talk (in-person), conference 'AGN Populations Across Continents and Cosmic Time', University of Durham, UK.
- July 1 – 5, 2024, a talk (presented by P.Marziani) at the European Astronomical Society (EAS) annual meeting, held in Padova, Italy.
- March 13 - 17, 2023, talk (virtual), the 3^{rd} Annual Conference of the African Astronomical Society (AfAS-2023), University of the Witwatersrand, Johannesburg.
- January 30 - February 1, 2023, poster presentation (virtual), the 6^{th} national AGN meeting in Granada, Spain.
- September 14 - 16, 2022, talk (in-person), Panchromatic view of the life-cycle of AGN, ESA/ESAC, Madrid, Spain.
- October 7 - 11, 2019, poster (in-person), International Astronomical Union (IAU) 356 symposium "Nuclear Activity in Galaxies Across Cosmic Time", Addis Ababa, Ethiopia: Participation, LOC.
- October 2018, talk (in-person), public seminar "Towards Dichotomy of Radio Loud and Radio quiet quasars in 4DE1 Parameter Space", ESSTI, Addis Ababa, Ethiopia.

Chapter 1

Introduction

1.1 General overview

The night sky has always served as a source of wonder and mystery to people. However, it has only been in the past few decades that people truly began to see the universe in all its glory by studying the entire electromagnetic spectrum (EMS). By examining the universe across the whole spectrum, one can better understand the physics behind celestial sources, since each part of the EMS brings valuable and unique information.

The emission from most galaxies is dominated by the hundreds of billions of stars they contain. However, a small fraction of galaxies have been observed to have excess emission across all EMS, compared to that which would be expected from stars, gas and dust alone (e.g., see D'Onofrio et al., 2012, and references therein). These galaxies host active galactic nuclei (AGN) and are called active galaxies. The additional energy release in active galaxies originates from the 'active' nucleus (e.g., Shields, 1999; Di Matteo et al., 2005; Osterbrock and Ferland, 2006), a compact and massive region at the center of a galaxy (e.g., Peterson, 1997; Netzer, 2013). These highly compact regions are thought to be powered by the accretion of matter onto a supermassive black hole (SMBH) that is capable of producing strong radiation across all EMS, and especially in radio, infrared, and X-rays (e.g., Seyfert, 1943; Schmidt, 1963; Peterson, 1997; Osterbrock and Ferland, 2006; Netzer, 2013).

Over the years, AGN have been observed to show different characteristics from each other in almost all wavelength ranges. They have been defined based on radio morphology and optical spectroscopic characteristics (e.g., Urry and Padovani, 1995, and references therein). Different attempts were made to unify all these classes, but the issue is still open.

There has been significant progress in defining and contextualising the characteristics of quasars, some of the brightest AGN, sixty years after their discovery (e.g., Schmidt, 1963; Mushotzky, 2004; D'Onofrio et al., 2012). Quasars are some of the most luminous sources in the universe, with strong variability in luminosity even within days, and show spectra with different emission line profiles, intensity ratios, and ionization levels (e.g., Sandage, 1965; Osterbrock and Mathews, 1986; Marziani et al., 2015). After the discovery of quasars, there is now a consensus on their nature, although much of the empirical understanding has yet to be developed (e.g., D'Onofrio et al., 2012). One of the most fundamental differences among quasars involves the existence of radio-loud (RL) and radio-quiet (RQ) sources, which show the presence and absence of the radio jet, respectively (see Sect. 2.4.1) (e.g., Boroson and Green, 1992b; Sulentic et al., 2000a; Kellermann et al., 2016). There are still important questions that need clarification, such as: do all sources go through an RL phase?, and do RL quasars represent in some way a physically distinct class from the RQ? (Becker et al., 1995). A much-debated problem in AGN studies involves the possibility of a real physical dichotomy between RL and RQ quasars (e.g., Zamfir et al., 2008; Best and Heckman, 2012; Padovani et al., 2017). Initially, it was suggested that an RL vs. RQ dichotomy does not exist (e.g., Antonucci, 1993). Different studies over the last decade reported contradictory results regarding the question of a bimodal distribution of quasars in terms of radio loudness (e.g., Cirasuolo et al., 2003a), where the Sloan Digital Sky Survey (SDSS) based studies defend the existence of quasar bimodality using radio/optical/UV ratios (e.g., Ivezić et al., 2002; White et al., 2007).

A further complication is introduced by the fact that a certain fraction of RQ sources share common properties with RL quasars (e.g., see Zamfir et al., 2008). It has been suggested that about 30% - 40% of RQ quasars are spectroscopically similar to RL quasars and, with the improvement of radio interferometry techniques, it was possible to observe that both types of quasars are capable of producing radio jets (e.g., Sulentic et al., 2000a; Ulvestad et al., 2005; Chiaberge and Marconi, 2011). These radio jets, and in particular from RL sources, extend to much larger scales with high radio power (e.g., Rawlings and Saunders, 1991; Ulvestad et al., 2005). Furthermore, the generation and properties of AGN jets, the amount of energy produced and their enormous size remain unexplained and open questions. In addition, the radio loudness will depend on the redshift, and will increase when the redshift is larger (e.g., Urry and Padovani, 1995; Arshakian et al., 2010; Caccianiga et al., 2024; Keller et al., 2024). However, although the last thirty years have seen an enormous increase in the availability of spectroscopic data on quasars thanks to the development of new instruments on large telescopes and with the arrival of new surveys (e.g., Aihara et al., 2011), the spectra of quasars with a low signal-to-noise ratio

(S/N) may lead to the impression that all quasars are spectroscopically similar (e.g., Marziani and Sulentic, 2012b).

Although a clear boundary between RL and RQ quasars is still elusive, the contradictory results on the dichotomy are affected by the lack of observational data and different biases such as:

- the lack of a unified or standardized definition of an RL and an RQ quasars (e.g., Zamfir et al., 2008; Padovani et al., 2017),
- the dependence on the internal extinction of Kellermann factor, R_K, defined as the radio flux density at 6 cm normalized to B-band flux density (e.g., Kellermann et al., 1989),
- the use of radio and optical flux-limited samples, which leads to unavoidable selection biases (e.g., Ho, 2008), and/or
- the fact that the fraction of RL sources is a strong function of redshift and optical luminosity (e.g., Jiang et al., 2007).

Previous studies have shown that it is possible to systematize quasar spectral diversity in a parameter space called four-dimensional eigenvector 1 (4DE1; see Sect. 2.5.1) (e.g., Marziani et al., 2014). As suggested by Zamfir et al. (2008), the importance of studying the RL phenomenon within the 4DE1 context is at least two-fold: (i) it compares RL and RQ sources in a parameter space defined by properties with no obvious dependence of the radio emission, and (ii) it allows constraining the probability of radio loudness for quasars depending on their optical/UV spectroscopic properties. The RL/RQ separation in 4DE1 is not complete (e.g., Zamfir et al., 2008). About 60% of RQ quasars (Population A) (see Sect. 2.5.3) show properties rarely seen in RL sources, while about 40% of RQ sources are spectroscopically similar to RLs (Population B) (see Sect. 2.5.3).

The majority of AGN spectra have single-peaked emission lines. However, there is an evidence about a disk structure that can be obtained from observations of very broad, double-peaked emission lines and through the identification of asymmetries and substructures in the line profiles (e.g., Popović, 2002; Popović et al., 2002; Kollatschny, 2003; Shapovalova et al., 2004). AGN with double-peaked emission lines are an interesting class of objects, though, only a small fraction of AGN show double-peaked profiles in their spectra (e.g., Eracleous and Halpern, 2003; Strateva et al., 2003; Eracleous et al., 2009; Fu et al., 2023). Miley and Miller (1979) found that powerful radio galaxies and RL quasars with extended radio morphology have the broadest and most complex

Balmer line profiles and are preferred hosts of double-peaked emitters. A variety of mechanisms have been proposed to explain the origin of double-peaked emission-line profiles and their unique kinematic signature, including relativistic motions in an accretion disk (AD) (e.g., Chen and Halpern, 1989, 1990), two separate BLRs as a signature of binary black holes (e.g., Gaskell, 1983), a bi-conical outflow (e.g., Zheng et al., 1990) or highly anisotropic distribution of emission-line gas (e.g., Wanders et al., 1995; Goad and Wanders, 1996) (see Sect. 2.7.1.1). Theoretically, the standard AD model assumes the disk to be geometrically thin and optically thick (Shakura and Sunyaev, 1973). Careful consideration of the basic physical arguments and recent observational results, suggests that the most likely origin of double-peaked emission lines is the AD, and that these double-peaked profiles provide dynamical clues about the structure of the AD (e.g., Ho et al., 2000; Strateva et al., 2003; Eracleous and Halpern, 2003; Barrows et al., 2011; Zhang, 2011; Liu et al., 2017; Ricci and Steiner, 2019; Zhang et al., 2019b).

Many open questions are still present after 50+ years of study of quasars, and scientists are still struggling to have consistent answers regarding the questions behind the RL - RQ dichotomy and the AD origin for double-peaked emitters. In this thesis, we studied the properties of RL and RQ quasars by using the 4DE1 parameter space, a possible dichotomy between them, and the reason behind a low fraction of observed RL quasars, to understand better the properties of radio jets and to evaluate the extent to which the AD is a source of double-peaked profile in the broad Balmer lines and high ionization UV lines. This was achieved by using spectra of extremely jetted quasars obtained at the observatory of Calar Alto in Spain (see Sect. 3.1.1). To evaluate the extent to which the AD is a source of the broad Balmer lines and high ionization UV lines in RL AGN, we focused on a strong RL quasar 3C 47. This new observation of 3C 47 yielded a spectrum with a high S/N ratio and high resolution, and displayed broad and strong blue and red peaks that are typical indicators of double-peaked emission in the Balmer (Hβ and Hα) and near-UV MgIIλ2800 line. We also analyzed the UV spectra using the Hubble Space Telescope (HST) Faint Object Spectrograph (FOS or HST-FOS) [1] archive for the high-ionization lines (HILs) like CIVλ1549.

1.2 Motivation and statement of the problem

We are motivated to focus our research on the dichotomy of RL and RQ quasars in the 4DE1 parameter space, as it is an area that still has many open questions to be worked on, as mentioned above. Although the standard model

[1] HST-FOS-https://archive.stsci.edu/missions-and-data/hst

is generally accepted, many open questions exist related to understanding the diversity observed in the properties of quasars (mainly spectroscopically) and the physical differences between them, as described in Sect. 2.4.1. One of the ways to understand better the RQ-RL dichotomy is through the analysis of optical/UV spectra. In the optical domain of the 4DE1 shown in Sect. 2.5.2, RL quasars are not distributed like most RQ, which may indicate different properties between the two types. However, the fact that the RQs are distributed in both populations A and B (see Sect. 2.5.3), makes the interpretation not so simple and leads to the following question: does this indicate that RL quasars are a distinct population with different broad line region (BLR) structure and kinematics? A better understanding of the RQ - RL dichotomy with the help of high S/N spectroscopic data will be crucial to our better understanding of quasars physics and model. One of the main objectives of this thesis is the analysis of the differences between RL and RQ quasars by using the spectra obtained with the TWIN spectrograph at the 3.5m telescope of the Calar Alto Observatory (Almeria, Spain) in the redshift range of $0.35 \lesssim z \lesssim 1$. In addition, the presence of an AD in AGN has limited and indirect observational evidence. Therefore, empirical evidence that asserts AD as a possible source of strong and broad double-peaked profiles will be analysed in this thesis.

Our motivation study of extremely jetted quasars to improve our understanding of the following fundamental research questions:

- What are the radio emission properties and the relation between radio and optical parameters in our sample of quasars?
- Do the RQ and RL quasars have different physical properties such as SMBH mass ($M_{\rm BH}$), accretion rate, and Eddington ratio ($\lambda_{\rm E} = L_{\rm bol}/L_{\rm Edd}$)[2]?
- Is there any evidence for a physical dichotomy between RL and RQ quasars?
- How is the correspondence between RL quasars and quasars of Population B in the 4DE1 scheme?
- Is FeII emission consistent in RL and RQ data?
- Is there any separation between the orientation effect and the physics of the emitting region?
- What are the kinematics and physical properties of the broad emitting region, as well as the effect of the outflows/winds and jets on the surrounding medium at scales $<$ 1pc?

[2]The $\lambda_{\rm E}$ is defined as $L_{\rm bol}/L_{\rm Edd}$, with $L_{\rm Bol}$ the bolometric luminosity and $L_{\rm Edd}$= $1.26\times 10^{38}(\rm M_{BH}/M_{\odot})$ erg $\rm s^{-1}$.

- Is the AD a source of the broad Balmer lines and high ionization UV lines in double-peaked emitters?, and
- Can the profile of the high ionization lines (HILs) be modelled with the contribution of the AD alone?

1.3 Objectives

1.3.1 General objective

The main objective of this PhD thesis is to study the properties of RL and RQ quasars to reveal a possible dichotomy between them and the reasons behind the observed low RL prevalence by using the 4DE1 parameter space, to better understand the properties of radio jets of RL quasars, and to assert whether the AD can be a source of double-peaked profiles in emission lines.

1.3.2 Specific objectives

The specific objectives of this PhD thesis are:

1. To analyze the broad emission lines, in particular, Hβ, FeII, MgII, the UV lines (CIVλ1549) and the 1900 blend when available, and to study the parameters such as FWHM of the full emission line profiles, and the relation between radio and optical parameters of RL quasars.
2. To study the spectroscopic differences of RL and RQ quasars of population B and their comparison with population A quasars, which are mostly RQ in the 4DE1 scheme.
3. To estimate, for the selected sample, the $M_{\rm BH}$ using both the Hβ and MgIIλ2800 lines and the $\lambda_{\rm E}$ using mainly the Hβ.
4. To apply a model based on a relativistic AD to explain the observed double-peaked profiles of the low-ionization emission lines (LILs) such as Hβ, MgII, and Hα, and HILs such as CIVλ1549 and CIII]λ1909.
5. To study the geometry and kinematics of the AD and the presence of winds/outflows and jets, as well as their effect on the surrounding medium at scales < 1 pc, and to separate the orientation effect from the physics of the emitting region.

1.4 Scope of the study

The scope of our study is limited to the low redshift in the range of $0.35 < z < 1$ and observations of 12 extremely jetted quasars. Additional complementary and comparison samples at law redshift with optical and near-UV measurements are available as archival data, as detailed in Sect. 3.4, and are also used. By analyzing the sources through the multicomponent non-linear fitting techniques and the resulting full broad profile measurements, quantification of broad emission line differences between RQ and RL sources as well as study of the emission from the AD can be possible after exploiting the complete samples with spectral coverage in Hβ, MgIIλ2800, Hα, and CIVλ1549.

1.5 Limitation of the study

We have found that the total number of sources considered in this study is significant for reaching the conclusions of the proposed objectives, however, access to a larger sample in the future would be useful to reinforce our conclusions. Due to time constraints and the diverse nature of the derived properties, analysis of X-ray data obtained by XMM, and UV data from HST for all the sources is not included. We only focused and limited our study on the radio, optical, and near-UV properties for the 11 sources and radio, optical, near-UV, and UV analysis for 1 source with an identified double-peaked emission line structures that are not common. In addition, due to the small number of sources with high S/N spectra, additional studies accounting for the separation between the orientation effect and the physics of the emitting region by applying all methods suggested in previous studies (e.g., Sulentic et al., 2003; Decarli et al., 2011), as well as the kinematics and physical properties of the broad line emitting region and the effect of the outflows/winds on the surrounding medium, are not fully taken into account.

1.6 Significance of the study

Understanding the nature of quasars is crucial for unravelling their complex nature. As mentioned above, a key distinction among quasars is the presence or absence of powerful relativistic radio jets. One of the quasar's populations, the extremely jetted quasars (RLs) (see Sect. 2.4.1) are a rare and fascinating class of AGN and are characterized by highly collimated and powerful jets (e.g., Jiménez Andrade, 2015). In addition, based on the standard model of AGN (see Sect. 2.2.2), an important component of AGN is the AD, and new observational evidence for its presence is also vital. This thesis, titled *"Di-*

chotomy of Radio Loud and Radio Quiet Quasars in Four Dimensional Eigenvector 1 Parameter Space (4DE1)", studies the difference between the two classes and the contribution of the AD to the double-peaked line emission through the use of high S/N spectra to permit a detailed analysis.

Some of the potentially significant contributions we expect to achieve with this thesis are:

- Our study helps to quantify the broad emission line difference between RL and RQ quasars by implementing the 4DE1 parameter space that provides spectroscopic contextualization for all broad-line-emitting AGN classes. It also provides evidence to assert the potential dichotomy between them, which will solve the debated problems associated with bi-modality.
- The results strengthen and provide additional evidence to refine the classification of quasars by providing a more robust method, leading to a better understanding of quasar populations and of the difference between an observational set of accretion parameters such as $M_{\rm BH}$ and $\lambda_{\rm E}$, and the centroid velocity shift and asymmetry measurements as a profile parameter. These results improve our understanding of the physical processes taking place around the SMBH.
- The results provide crucial insight into the processes governing jet activity, including the effect of radio intensity on the structure and kinematics of the emitting regions of broad low-ionisation lines. These findings can help us understand the formation and collimation of jets.
- Our study includes the analysis of 3C 47, a rare example of a quasar with double-peaked profile emission lines, as most AGN spectra have a single peak. This raises the question of to what extent the AD is a source of the observed broad and double-peaked profiles, in particular in the Balmer lines (Hβ, Hα) and the near-UV lines (Mg IIλ2800). The results of these detailed analyses are crucial for understanding the geometry and kinematics of the AD, the presence of winds/outflows, and jet activity.

Finally, our findings may contribute to the development of more refined quasar classification methods, provide additional information for model development, and offer a broader view of the nature of AGN activity and galaxy evolution.

1.7 Structure of the thesis

This thesis consists of eight chapters. Chapter 1 provides the general introduction, including the thesis's basic concepts and terminologies, motivation, ob-

jectives, scope, limitations and significance. Chapter 2 describes the literature review, while data and used telescopes and instruments are given in Chapter 3. Chapter 4 describes the methodology applied. The remaining three chapters present the analysis, results and discussion. Chapter 5 discusses the optical and near-ultraviolet properties of low-redshift quasars, while Chapter 6 discusses the extreme population B source, 3C 47, with a double-peaked profile in emission lines. Chapter 7 presents the preliminary work carried out regarding the data reduction of the larger sample of quasars to be used in the near future. Finally, Chapter 8 presents the overall summary and conclusions of this PhD work.

Throughout this thesis, we adopt a flat ΛCDM cosmology with $\Omega_\Lambda = 0.7$, $\Omega_0 = 0.3$, and $H_0 = 70\,\mathrm{km\,s^{-1}Mpc^{-1}}$. All magnitudes are given in the AB system unless otherwise stated.

Chapter 2

Literature review

This chapter delves into the existing body of knowledge surrounding the dichotomy of radio-loud (RL) and radio-quiet (RQ) quasars in the four-dimensional eigenvector one (4DE1) parameter space. We will explore theoretical backgrounds and identify key themes, methodologies, and findings from previous research works. This literature analysis will not only highlight some inconsistencies and gaps in knowledge but will also situate our research within established bodies of work. After addressing the gaps and unanswered questions, our study aims to contribute a piece of new knowledge in the field. This chapter is organized into eight major sections.

2.1 Normal and active galaxies

Galaxies are the fundamental building blocks of the universe with vast collections of stars, gas, dust, and dark matter bound together by gravity (e.g., Binney et al., 2000; Elmegreen and Elmegreen, 2005). They come in a variety of shapes and sizes from dwarfs containing a few hundred million to the largest objects with a hundred trillion stars. A deep image of a rich field of galaxies captured by the James Webb Space Telescope (JWST) is shown in Fig. 2.1. Galaxies can be broadly categorized into two main types: normal and active galaxies (e.g., Conselice, 2006; Jones et al., 2015; Morell et al., 2020). The key difference between normal and active galaxies lies in the activity of their central regions (nuclear activity) and the availability of gas and dust near the SMBH, as it plays a crucial role in the evolution of galaxies (e.g., Binney et al., 2000; Carroll and Ostlie, 2017).

Normal galaxies have relatively quiet centers as they lack a powerful central energy source due to insufficient matter, usually gas and dust, for the SMBH

to accrete.

Figure 2.1: Infrared image from NASA's James Webb Space Telescope (JWST) taken for the JWST Advanced Deep Extragalactic Survey program. It shows a portion of an area of the sky. More than 45,000 galaxies are visible here. [Image credit: NASA][1]

Active galaxies host active galactic nuclei (AGN), a compact region at the center that has a much higher than normal luminosity over at least some portion and possibly in all ranges of the electromagnetic spectrum (EMS, Fig. 2.2), with characteristics indicating that the excess luminosity is not produced by stars (e.g., Peterson, 1997; Kauffmann et al., 2003). The additional energy release in active galaxies originates from the nucleus (e.g., Di Matteo et al., 2005). These highly compact regions are thought to be powered by matter accretion onto a supermassive black hole (SMBH) which is capable of producing emission across the majority of the EMS (e.g., Peterson, 1997).

2.1.1 Comparison between normal and active galaxies

A detailed comparison can be made between normal and active galaxies based on their spectral energy distribution and emission lines, as well as supermassive black hole mass ($M_{\rm BH}$), jet activity and star formation rate (e.g., Heckman and Best, 2014; Schutter and Shamir, 2015; Vaddi et al., 2016; Lacerda et al., 2020;

[1] https://webbtelescope.org

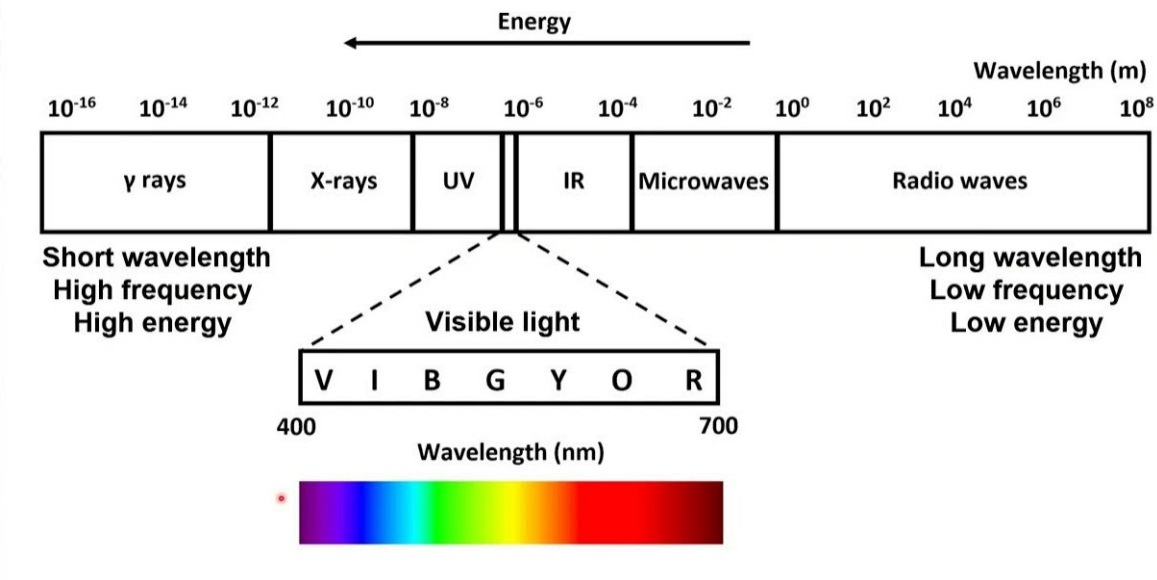

Figure 2.2: A depiction of the electromagnetic spectrum, from high-energy gamma rays to very low–energy radio waves.

Cavanagh et al., 2021; Mountrichas et al., 2022). Below, I will provide an overview of each of these criteria for their classification.

1. **Emission lines and spectral energy distribution (SED)** Normal galaxies primarily emit radiation in the visible and near-infrared wavelengths, corresponding to the light emitted by their stars and stellar absorption lines dominate their spectra. In some cases, additional, fainter contributions in the form of emission lines come from the heating and cooling of the gas component (Fig. 2.3 top).

   Active galaxies emit radiation across a wide range of the EMS, in radio, infrared, ultraviolet, X-rays, and gamma rays (e.g., Netzer, 1990; Padovani, 2017a). These diverse and broad wavelength bands reveal the presence of hot gas, energetic particles, and powerful jets. Their spectra can show strong emission lines that can be broader and more intense than in normal galaxies (e.g., Lakićević et al., 2018, Fig. 2.3 middle and bottom).

2. **Luminosity** Normal and active galaxies can differ in terms of their luminosity, in which, active galaxies can be almost 10,000 times or brighter than normal galaxies and span a broad range of luminosity, from the brightest quasars ($\approx 10^{47} - 10^{48}$ ergs s^{-1}) to the less luminous Seyfert galaxies ($\approx 10^{44} - 10^{45}$ ergs s^{-1}) (e.g., Shen et al., 2011). Moreover, compared with the size of the galaxy, the origin of activity is extremely com-

[2] www.spacetelescope.org

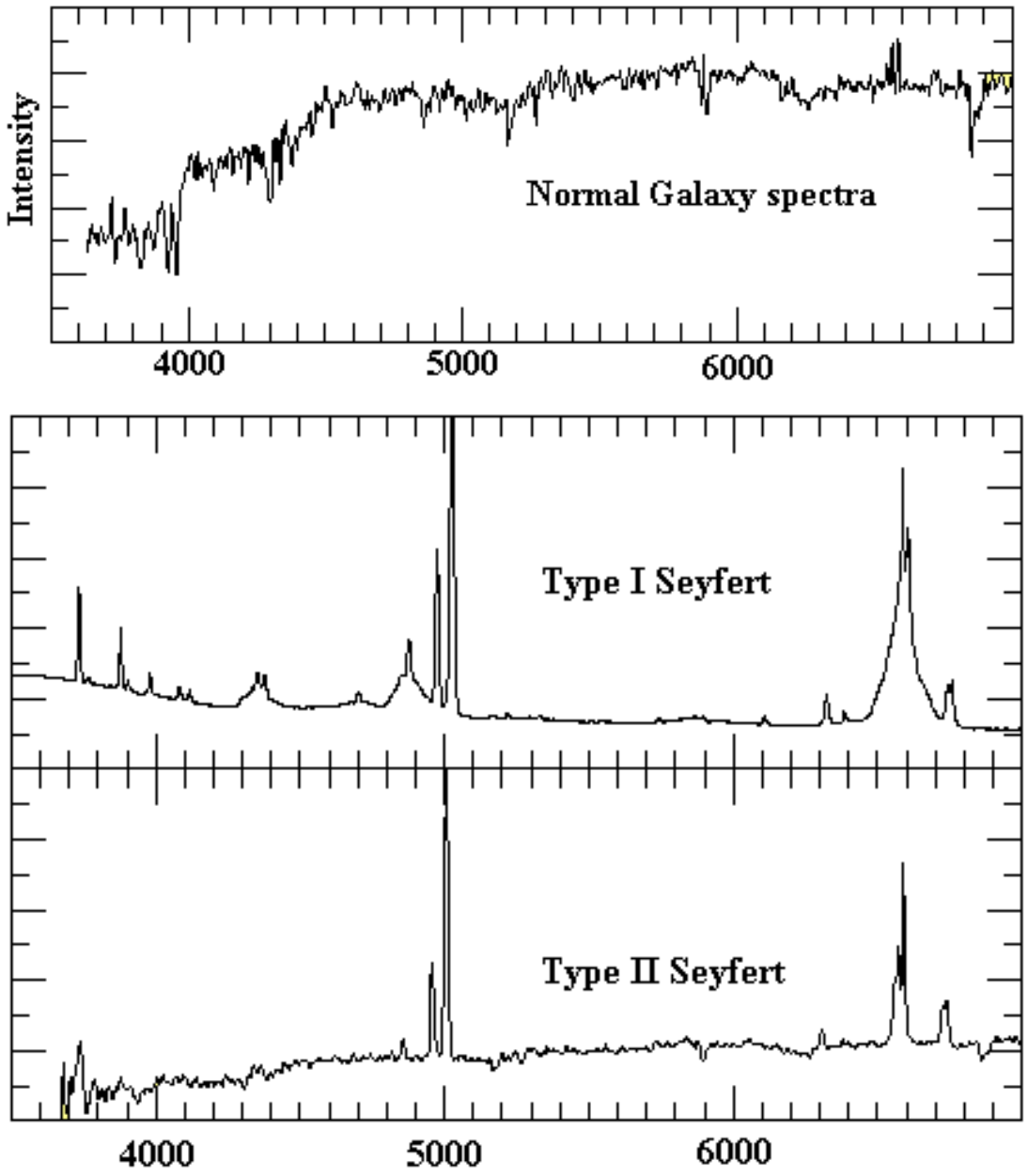

Figure 2.3: Typical spectra of normal and active (Seyfert) galaxies. Top: spectra of a normal galaxy (NGC 3368), the stellar component dominates its spectrum. Middle: spectra of Seyfert 1 galaxy (NGC 4151) with observed broad and narrow lines in the spectra. Bottom: spectra of Seyfert 2 galaxy (NGC 4941) with only observed narrow lines. [Image credit][2]

pact, as indicated by the variation of the observed fluxes in short period of time on daily and even hourly time scales (e.g., Ulrich et al., 1997). Such peculiar properties of AGN are explained in detail in Sect. 2.2.1.

3. **Supermassive black hole:** Both normal and active galaxies can harbor SMBHs at their centers, but their activity levels and $M_{\rm BH}$ can differ significantly. In normal galaxies, either the $M_{\rm BH}$ is low (so that the nucleus

would not be detected as active because of its low luminosity) or the M_{BH} is in the same range of the one of active nuclei but the level of activity is very low. The M_{BH} ranges from billions of solar masses in huge galaxies with huge stellar masses, to a few thousand solar masses in smaller galaxies, as there is a tight correlation between the stellar mass of a galaxy and the mass of its central SMBH (e.g., Lu et al., 2003; Kormendy and Ho, 2013; Simmons et al., 2017). Normal galaxies accrete matter at a very low rate, if at all, and emit only minimal radiation, compatible with the possible presence of inactive supermassive black holes (SMBHs) at their centers. (e.g., Heckman and Best, 2014).

4. **Jet activity** By definition, normal galaxies do not produce the powerful relativistic radio jets that are often observed in active galaxies. However, some normal galaxies exhibit weak, low surface brightness radio emissions (Condon, 1992) suggesting synchrotron emission from supernova remnants (e.g., Weiler et al., 1986; Chevalier, 1998) at low frequency, while at relatively high frequencies free-free emission from HII regions is expected to dominate (Johnson, 2004). Both processes are ultimately associated with massive star formation and evolution (Condon, 1992). In this case, radio emission is diffuse and lacks the collimated jet-like morphology. The radio emission from RQ AGN can be more collimated compared to star-forming galaxies (e.g., Ulvestad et al., 2005). In both the cases of normal galaxies and RQ AGN, radio emission is considerably weaker as compared to RL AGN. RL AGN possess powerful jets, i.e., ejected plasma at relativistic speeds, that can travel into larger spatial scales (e.g., Gabuzda, 2015; Foschini, 2018; Hada, 2019; Lister et al., 2021; Foschini, 2022).

5. **Star formation:** Star formation in normal galaxies occurs within their disks or throughout their irregular structures. In galaxies like spirals and irregulars, star formation is primarily driven by gravity, where cold molecular gas clouds within the galactic disk collapse under their weight. These galaxies exhibit a moderate rate of star formation, in which creation of a new star may be sustained over a long period. Regions of star formation in normal galaxies are marked by bright blue stars, hot gas clouds emitting infrared radiation, and nebulae with glowing star-birth regions. Elliptical and S0 galaxies, along with the bulges of early-type spirals (Sa, Sb), contribute minimally to the recent star formation rate in the Universe. In contrast, the majority of star formation is dominated by the disks of later-type spirals, such as Sbc, Sc, and Sd galaxies (González Delgado et al., 2016).

   In active galaxies, the AGN influence can trigger enhanced star formation, leading to bursts of new stars within the galaxy. As these galaxies host a SMBH that accretes vast amounts of gas and dust, the accreting

SMBH releases tremendous amounts of energy in the form of jets, winds and radiation, impacting the surrounding gas and triggering star formation(see e.g., Silk, 2013; Cresci et al., 2015; Perna et al., 2020; Hermosa Muñoz et al., 2024). This star formation in active galaxies can be several times more intense than in normal galaxies but is often confined to shorter bursts. Due to feedback, the SMBH energy can trigger star birth, but it can also disrupt and suppress star formation in the long run, creating complex patterns of young and old stars (e.g., Di Matteo et al., 2005; Harrison et al., 2018; Kim et al., 2022; Loubser et al., 2024).

The study of normal and active galaxies is a fascinating and rapidly evolving field. By understanding the differences between these two types of galaxies, we can gain valuable insights into the formation and evolution of galaxies. Despite our growing understanding of normal and active galaxies, a lot more unsolved problems remain. Some of the open questions include: what determines whether a galaxy becomes normal or active? What is the effect of AGN on their host galaxy, and vice versa? What is the origin of the accreting material? what is the triggering mechanism that converts a normal galaxy into an active one? How long is the duration of the active phase? How do SMBHs and galaxies co-evolve over time? What role do active galaxies play in the overall structure and evolution of the universe? and What is the effect of the relativistic jet on the surrounding medium? These are just some of the interesting questions that continue to drive research in this field of astronomy. A careful selection of active galaxies and quasars with a high enough S/N ratio, and studying their properties could lead to a better understanding and will tackle some of the open questions as detailed in this thesis.

2.2 Active galaxies and active galactic nuclei (AGN)

2.2.1 Properties of AGN

- The first property that distinguishes AGN distinctly is their emission across the complete EMS, with bolometric luminosity typically exceeding 10^{44} ergs s^{-1}(e.g., Padovani, 1997; Netzer, 2013). The emission spans from radio waves to X-rays and even gamma rays. Their luminosity often reaches the range of 10^{47} to 10^{48} ergs s^{-1}. This luminous output far surpasses the energy emission observed from ordinary/normal galaxies. This fundamental disparity in luminosity elucidates the exceptional nature of AGN, where their brightness across the EMS serves as a marker of the profound and energetic processes occurring within their central regions.

[3] https://science.nasa.gov

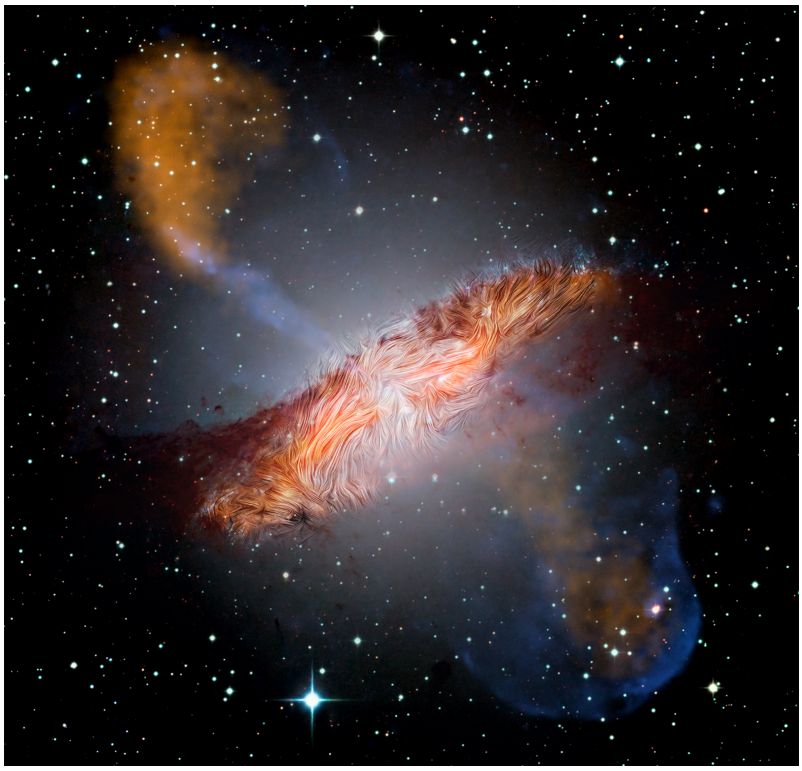

Figure 2.4: Color composite image of Centaurus A, the closest radio galaxy to Earth obtained with three instruments, optical: European Southern Observatory (ESO) Wide Field Imager; Submillimeter: Max Planck Institute For Radio Astronomy/ESO/Atacama Pathfinder Experiment (APEX); X-Ray and Infrared: NASA/Chandra.[Image credit][3]

.

- The second notable property lies in the pronounced variability of their emission observed across all frequencies (for the visual, see e.g., Li et al., 2018), manifesting changes over time scales that range from years to mere hours. This rapid variability in luminosity implies that the region from which the radiation is emitted is immensely compact (e.g., Soldi et al., 2014; Rashed et al., 2015; Kozłowski, 2021). Mathematically, if we denote R as the linear dimension of this region and Δt_{var} as a characteristic timescale for variability, a straightforward deduction based on the speed of light c necessitates that R is approximately on the scale of $c \times \Delta t_{var}$ for the observed variability to be apparent. Considering the measured Δt_{var} in AGN, the value will be smaller than 0.1 parsec for low-z sources (Peterson, 1993, 1997, 1998), which indicates that the emission region resides well within the confines of the galactic nucleus. This substantiates the nomenclature AGN by affirming that the emission source remains significantly confined within the nucleus, endorsing the compact nature of these highly dynamic and swiftly changing phenomena (e.g., Ulrich et al., 1997; Witzel et al., 2021).

- Thirdly, the SEDs of AGN, differ significantly from that of normal galaxies, particularly in their predominantly non-thermal origin, which spans the entire EMS (e.g., Osterbrock and Ferland, 2006; Lefa, 2012; Fedorova et al., 2022). Across the various wavelength bands, it is often possible to effectively represent a power-law, with the flux density expressed as $f(\nu) \propto \nu^{-\alpha}$ (measured in ergs s^{-1} cm^{-2} Hz^{-1}), where α stands as the spectral index characterizing the shape of the spectrum (e.g., Korista et al., 1997; Dietrich et al., 2002). At higher energies, an alternate parameterization of the AGN spectrum is given by $N(E) \propto E^{-\Gamma}$), where E signifies the energy, $N(E)$ represents the number of photons emitted per second per square centimeter per keV, and Γ is termed the photon index, and is obviously $\Gamma = \alpha + 1$.

  Different mechanisms and regions of the AGN contribute to various sources of radiation: synchrotron radiation from highly energetic particles is assumed to be the dominant source of emission in radio bands as powerful jets, and collimated beams of charged particles (Porth et al., 2011; Pe'er, 2015). Dust heated by the central engine, where thick tori of dust that encircles the SMBH and the AD causes it to re-emit at infrared wavelengths, is assumed to be the main cause of IR emission (Pier and Krolik, 1992b,a; Jaffe et al., 2004; Fritz et al., 2006; Nenkova et al., 2008a,b; Schnülle, 2017). Optical emission in AGN arises from two main regions, from the AD, which produces a continuum of optical emission through intense frictional heating, and from the broad line region (BLR) in which gas clouds orbiting close to the SMBH are bathed in intense radiation from the disk and the central SMBH cause them to emit characteristic bright emission lines in the optical spectrum (e.g., Stern and Laor, 2012; Padovani, 2017b). The UV continuum emission in AGN originates from the AD, with possible contribution from the jet synchrotron emission in RL AGN, as well from the BLR in the NUV due to the Balmer continuum (Malkan and Sargent, 1982; Kovačević et al., 2014; Kovačević-Dojčinović et al., 2017; Müller and Romero, 2020; Panagiotou et al., 2022). X-ray emission from AGN originates from the scattering of optical/UV photons from the innermost regions of the AD by hot electrons in a corona, where inverse Compton processes generate high-energy photons (e.g., Ballo et al., 2012; Jiang, 2020; Król et al., 2023). Finally, at the highest energies, AGN also emits gamma rays, thought to be generated by processes like Compton scattering of lower-energy photons by relativistic electrons in the jets or by pair production near the SMBH (e.g., Nandra et al., 1998; George and Fabian, 1991; Nandra and Pounds, 1994; Araudo et al., 2010; Sahakyan et al., 2017).

- Fourthly, accompanying the multi-frequency continuum, the optical spec-

trum of an AGN typically exhibits strong emission lines. This includes both permitted, semi-forbidden and forbidden narrow emission lines, and only permitted broad emission lines have been identified so far (e.g., Vanden Berk et al., 2001; Mullaney and Ward, 2008; Netzer, 2013). The widths of these emission lines provide valuable insights into the velocity characteristics of the emitting material. By interpreting these line widths in the context of Doppler broadening, it has been observed that narrow lines exhibit velocity dispersion around $\sigma \approx 300$ to 400 km s^{-1}, whereas broad lines display order of magnitude higher dispersion, approximately $\sigma \approx 3000$ to 4000 km s^{-1}(e.g., Sulentic et al., 2000b; Osterbrock and Ferland, 2006; Marziani et al., 2010; Netzer, 2013).

- In addition, a minority of AGN ($\approx 10\%$, Baloković et al. 2012) exhibit strong radio emissions, exhibiting remarkable jets and extended lobes. These distinctive radio structures can extend to distances approximately ranging from $\approx$ 100 Kpc up to $\approx$ 1 Mpc from the AGN core, far surpassing the optical boundaries of the host galaxy. Nevertheless, it is important to note that most AGN are RQ and appear to exhibit minimal radioactivity (see Sect.2.4.1).

2.2.2 Standard model of AGN

As explained in the previous sections, AGN are some of the most energetic and mysterious objects in the universe, and the entire emission cannot be due to a single component alone. Understanding how the AGN functions requires a powerful framework, and that's where the standard model of AGN comes into play to explain the diverse observations. The standard model of AGN, in general, implies the existence of a central SMBH surrounded by an AD, a BLR, the dust toroid that obscures the SMBH, a narrow line region (NLR), and the presence of winds, outflows, and, in some cases, material ejected at relativistic speed, which appears in the form of jets in radio frequencies (e.g., Marziani et al., 2018, references therein). Generally, an AGN comprises the following components, and each of them occupies a specific place in the standard model of an AGN. They will described in detail below.

- **A central supermassive black hole:** It is a region of space-time exhibiting such strong gravitational effects that nothing, including particles and electromagnetic radiation, can escape from it (e.g., Wald, 1984, 1997; Montgomery et al., 2009). It is widely accepted within the scientific community that all massive galaxies harbor SMBHs at their center (e.g., Ho and Kormendy, 2000). In addition, there is also observational evidence for the presence of such a massive SMBH at the center of the host galaxy, e.g.,

in Messier 87 (M87), a giant elliptical galaxy and the home of several trillion stars, a SMBH, stellar clusters and the first ever to be directly imaged (Event Horizon Telescope Collaboration et al., 2019) (see Fig. 2.5). The growth of these SMBHs is considered instrumental in shaping the structure and evolution of galaxies (e.g., Marconi et al., 2004; Ferrarese and Ford, 2005). These SMBHs are rotating, and they accrete the surrounding material towards their center (e.g., Wang et al., 2006; Nemmen et al., 2006; Du et al., 2018). The parameters that define the AGN phenomena are then the black hole mass $M_{\rm BH}$, the mass accretion rate $\dot{M_{BH}}$ and the spin. Commonly, the range of the $M_{\rm BH}$ spans from $10^6 M_\odot$ to $10^{10} M_\odot$ (e.g., Urry, 2004; Marziani and Sulentic, 2012b; Shen, 2013; Pan et al., 2015). In a broader sense, AGN with higher luminosity tends to harbor more massive SMBHs (e.g., Peterson et al., 2004; Ferrarese and Ford, 2005). Quasars are known to host the most massive SMBHs, with masses ranging within $10^7 M_\odot < M_{BH} < 10^{10} M_\odot$ (e.g., Hopkins and Hernquist, 2009; Kormendy and Ho, 2013; Lupi et al., 2021), and are capable of releasing gravitational energy through matter accretion onto them.

Figure 2.5: An image of the SMBH at the center of the galaxy M87 using the Event Horizon Telescope [Image credit: Event Horizon Telescope Collaboration, (Event Horizon Telescope Collaboration et al., 2019)]

.

- **Jets**. The accretion process in AGN activity releases tremendous energy, some of which is channeled into powerful collimated jets emanating from the vicinity of the SMBH. These powerful relativistic jets, are ionized,

narrow streams of high-energy particles from the AD that spiral along magnetic field lines and that are propelled away from the central SMBH (e.g., Blandford et al., 2019; Boccardi et al., 2021; Foschini et al., 2024). Jets are believed to be perpendicular to the plane of the AD and can extend from the SMBH to a large distance, in some cases exceeding the size of the host galaxy and significantly impact their surrounding environment (e.g., Blandford et al., 2019; Boccardi et al., 2021; Fischer et al., 2023). They have strong radio and X-ray emission may be due to synchrotron radiation (e.g., Landt et al., 2008; Worrall, 2009; Rawes et al., 2015). With the improvement of radio interferometry techniques, it was possible to notice that both RL and RQ quasars are capable of producing radio jets, although RQ jets are far less powerful and at least in some cases sub-relativistic (e.g., Ulvestad et al., 2005; Padovani, 2016; Hartley et al., 2019; Sbarrato et al., 2021). The radio power of RQ quasars can be even 2 - 3 orders of magnitude lower than that of their RL counterparts for the same optical power (e.g., Ganci et al., 2019).

- **Accretion disk (AD):** An AD is a structure formed by the accumulation of matter, typically gas and dust, spiraling around a central gravitational source, such as a SMBH. It is known from dynamical arguments that matter orbiting a central massive object (specifically material surrounding the central SMBH), will spread into a flattened disk structure, because of loss of angular momentum, and form a flattened, swirling geometrically thin disk (e.g., Shakura and Sunyaev, 1973; Eracleous, 1998; West and Krawczynski, 2023; Czerny et al., 2023a). It is the viscosity within this disk to generate immense heat, raising temperatures to millions of degrees Celsius, and is thought to provide the necessary mechanism to transfer outward the angular momentum of the gas in the form of radiation in all ranges of the EMS (e.g., Kimura et al., 2017; Lasota, 2023). The gas spirals towards the center, losing some of its gravitational energy. Part of the lost energy is converted into radiation with high efficiency and part is converted to kinetic energy of gas that can be blown away from the disk, or otherwise can heat the gas to high temperatures (e.g., Balbus and Hawley, 1998). The AD is the primary source of UV photons, while a corona of hot material forms above the disk, contributing to the production of high-energy X-rays (e.g., Armitage, 2004; Done et al., 2012; Panda et al., 2019a). A more detailed explanation AD models is presented in Sect. 2.6.

- **Broad-line region (BLR):** The BLR is often represented a high-velocity cloud system with large electron density surrounding the AD, located close to the SMBH (10 - 100 light days from reverberation mapping studies). The BLR is responsible for the production of UV/optical broad lines in quasar spectra (e.g., Peterson et al., 2004; Laor, 2004). The electron den-

sity of this region is typically 10^{10} - $10^{11} cm^{-3}$ (e.g., Ferland et al., 1992; Grier et al., 2014). Since, the BLR electron densities are sufficiently high, nearly all forbidden lines are collisionally suppressed. It is traditionally believed that the BLR consists of fast-rotating gas clouds in a disk-like structure rather than a spherical one (e.g., Urry, 2004). This arrangement intercepts a portion of the radiation emitted from the disk that ionizes the surrounding gas (e.g., Goad et al., 2012). Consequently, the ionized gas recombines and emits radiation at distinct frequencies, manifesting as broad emission lines (e.g., Osterbrock and Ferland, 2006; Netzer, 2013). The lines are broadened because of both the turbulent and bulk motion of gas, while thermal broadening is reputed to be negligible at the temperatures typical of photoionized gas. These broad emission lines in an AGN spectrum provide valuable clues about the conditions near the SMBH. Furthermore, the geometry of the BLR significantly influences the estimation of the $M_{\rm BH}$(e.g., Rakshit, 2020; Cackett et al., 2021; Villafaña et al., 2023).

- **Narrow line region (NLR):** This region is located at a larger distance from the SMBH ($\approx$ 100 pc) near/outside the torus, and is composed of small gas clouds with low electron densities in the range of 10^2 - 10^4 $\rm cm^{-3}$ (Netzer, 2013). A bi-conical structure has been revelead in several instance(e.g., Xu and Komossa, 2011; Ludwig et al., 2012; Meena et al., 2023). The NLR can have a clumpy and inhomogeneous or clumpy configuration, leading to variations in electron density across different regions. The density might systematically decrease with distance from the central SMBH (e.g., Bennert et al., 2006; Kakkad et al., 2018). This region is responsible for the production of narrow optical emission lines that, as the BLR, absorb part of the AGN radiation and re-emit it in the form of lines; however, these emission lines have relatively small line widths, indicating lower velocities compared to the broader emission lines from the BLR. Since, the electron density is low enough in this region, forbidden, semi-forbidden and permitted lines can be produced (e.g., Vaona et al., 2012; Dojčinović et al., 2023).

- **Obscuring torus:** Obscuring torus refers to a thick, doughnut-shaped ring structure composed of dust and gas that surrounds the central region. This torus plays a crucial role in the phenomenon of obscuration, where it blocks and absorbs some of the emitted light and radiation from the central engine of the AGN (e.g., Elitzur and Shlosman, 2006; Mason, 2015; Bannikova and Sergeyev, 2017). High-resolution infrared observations, particularly with instruments like ALMA and JWST, have revealed a typical size of a few parsecs for a dusty region to be located at 1 - 10 pc from the AD disk, forming a toroidal structure (i.e., torus). The dusty torus

intercepts part of the disk and coronal radiation and re-emits it in the IR band (e.g., Davies et al., 2015; Baloković et al., 2021; García-Bernete et al., 2024). This dusty structure, commonly referred to as the torus, is composed of various absorbing components, including cold molecular gas and dust grains of varying sizes. It obscures the inner regions of the AGN and is responsible for the distinction between type-1 and type-2 AGN (e.g., Elitzur, 2008; Tristram, 2012; Hönig, 2019). In type-1 AGN, the broad-line region (BLR) is visible because the line of sight avoids the dense dust in the torus, while in type-2 AGN, the line of sight passes through the dust, obscuring the BLR and restricting the view to the narrow-line region (NLR) (e.g., Ramos Almeida et al., 2011; Zou et al., 2019).

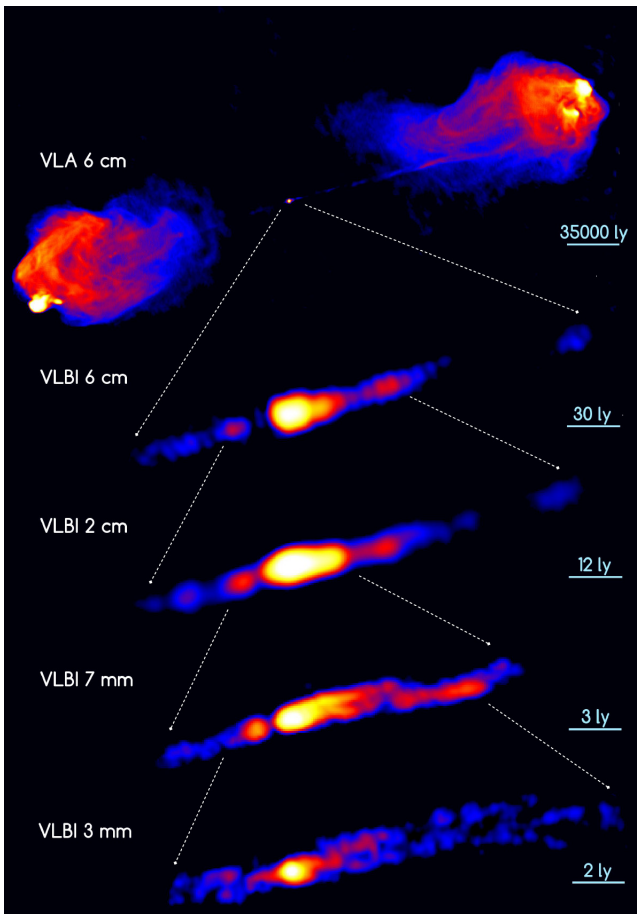

Figure 2.6: The radio galaxy Cygnus A on scales from hundreds of kilo-parsecs imaged with the VLA to the sub-parsec probed with mm-VLBI after stacking several epochs [Image credit: Boccardi et al. (2017)]

.

2.2.2.1 Observational evidence for the standard model of AGN

The standard model isn't only a theoretical model but is supported by various observational evidence using powerful telescopes. Observational evidence sup-

porting the standard model of AGN includes the detection of both broad and narrow emission lines in AGN spectra, which point to different regions of the central engine. Additional evidence comes from the presence of a dusty torus, whose orientation-dependent effects help explain the classification into type-1 and type-2 AGN (e.g., Urry and Padovani, 1995; Suh et al., 2019). The observation of radio jets and outflows, as well as the measurement of SMBH masses at the centers of AGN (Peterson and Wandel, 1999; Marziani and Sulentic, 2012b; Shen, 2013; Jun et al., 2017), further reinforces the standard model.

2.2.2.2 Drawbacks and challenges

While the standard model provides a robust framework for understanding and classifying AGN, recent research continues to refine and expand our understanding and also shows some of the key drawbacks and challenges of the standard model of AGN. It struggles to fully explain the wide variety of AGN properties observed, including line ratio, complex spectral features, and variability patterns (e.g., Bianchi et al., 2012; Villarroel and Korn, 2014; Czerny et al., 2023b). The model doesn't capture the full complexity of AGN structure, as recent observations show the dusty torus may be more complex than a simple doughnut shape, and its role in obscuration may vary (e.g., Bianchi et al., 2012; Yousef and Davis, 2020). The standard model also treats the AGN as a static object even if AGN are likely to evolve over time as the accretion rate onto the SMBH may change. The structure of the dusty torus, and the properties of the jets may also change on timescales of years to millions of years and understanding these evolutionary processes is crucial (e.g., Fanidakis et al., 2012). The standard model doesn't fully address the relation between AGN and their host galaxies, as AGN activity can have profound effects on the evolution of galaxies, and the precise mechanisms of this feedback are still being explored (e.g., Harrison et al., 2018; Silk et al., 2024). The analysis of the vertical structure of the standard model AD in AGN also has potential inconsistencies with observational constraints and changes in the BLR structure and kinematics over time (e.g., Komossa et al., 2024). In addition, the detailed physics of AD and the jet including the precise mechanism for the energy transfer, jet formation, and the role of the magnetic field is not fully understood, even if landmark models were already proposed in the late 1970s (e.g., Blandford and Znajek, 1977; Blandford and Königl, 1979; Falanga et al., 2015; Blandford et al., 2019). Though the above issues present challenges, the standard model of AGN has been highly successful in explaining the diverse phenomena observed in these intriguing objects. Ongoing research continues to refine the model, integrating new observations and theoretical advancements.

2.3 Types, classification, and unification of AGN

2.3.1 Types of AGN

AGN manifest in a wide array of types, each exhibiting distinct characteristics shaped by the interplay of various factors. The observed diversity in AGN is thought to result from a combination of factors such as $M_{\rm BH}$, spin, viewing angle, and accretion rate. Higher black hole mass and faster spin are generally associated with increased luminosity and jet production, influencing both the appearance and power of the AGN. The distribution of gas and dust helps define the shape of the obscuring torus, which in turn affects the visibility of the central region. Consequently, the viewing angle can significantly impact the observed properties, underscoring the importance of orientation in understanding AGN diversity (e.g., Berton et al., 2017; Suh et al., 2019; Spinoglio et al., 2021). Researchers are still working to understand exactly how these factors influence the properties of AGN and the most fundamental types are classified based on their radio emission and the optical spectra (e.g., Mickaelian, 2015; Tadhunter, 2016; Spinoglio et al., 2021). A scheme summarizing our present understanding is shown in Fig. 2.7.

- **Radio-loud (RL) vs. radio-quiet (RQ) AGN:** This classification is based on the presence or absence of the radio jet. RL AGN has strong radio emissions, often visible as extended structures in radio images, thought to be due to powerful jets of particles ejected from the SMBH at relativistic speed. These jets can be seen as extended structures on either side of the galaxy (e.g., Bridle et al., 1994). Blazars and radio galaxies will be discussed in detail in the coming sections.

  On the other hand, the RQ AGN have much weaker non-relativistic radio emission, and their luminosity is dominated by other forms of radiation, such as ultraviolet and X-rays. These AGN are much more common than RL, making up about 90% of all known AGN (e.g., Padovani, 2011). This class of AGN includes low-ionization nuclear emission-line regions (LINERs), Seyfert galaxies, and RQ quasars. More detail about RL and RQ quasars is given in Sect. 2.4.1.

- **Type-1 vs. Type-2 AGN:** This classification is mainly based on emission lines and the presence of broad components in the optical spectra (e.g., Khachikian and Weedman, 1974; Antonucci, 1993; Bornancini and García Lambas, 2018; Zou et al., 2019; López-Navas et al., 2023). Type-1 AGN have both, broad emission lines in their optical spectra that indicate the presence of rapidly moving gas swirling around the SMBH and narrow emission lines suggesting slower moving gas located farther from the

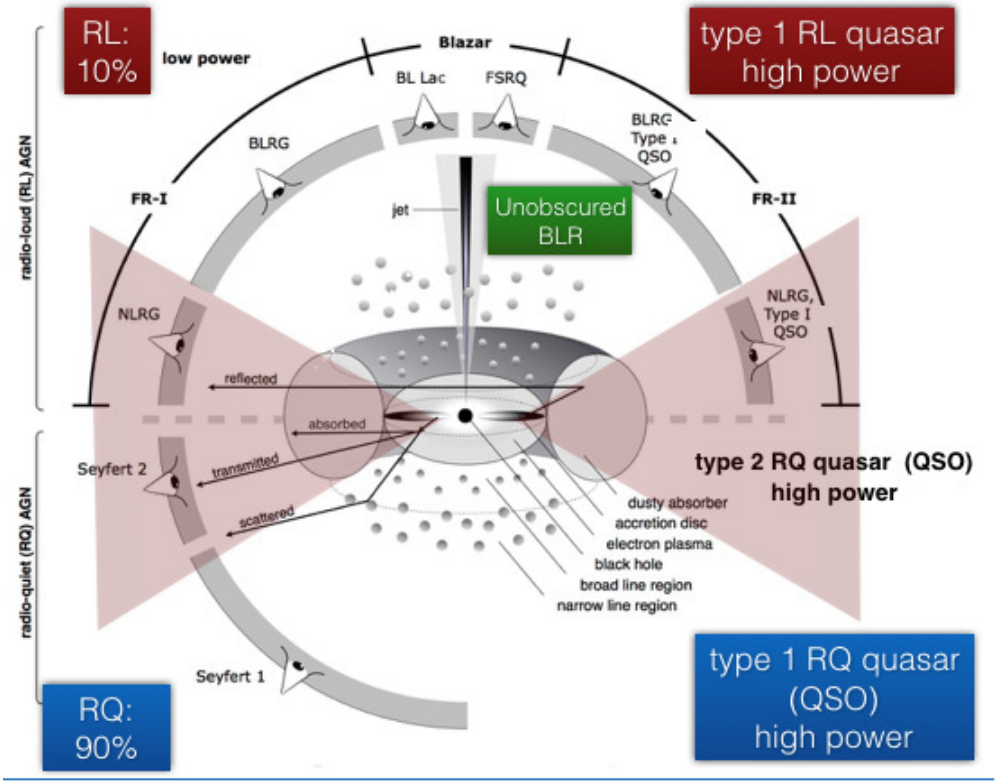

Figure 2.7: An artistic depiction showing the standard and unification AGN model, graphic by Marie-Luise Menzel, from Beckmann and Shrader (2012), annotated by Paola Marziani.

SMBH. In addition, the unobstructed view of the central region allows for direct observation of the hot and dense gas, offering insights into the inner working of the AGN. In contrast, the spectra of type-2 AGN display narrow emission lines, indicating slowly moving gas located farther from the SMBH. The absence of these broad lines suggests that the central region of the AGN is obscured from our view, possibly by a thick torus of dust and gas covering the central region to obscure our direct view.

2.3.2 Unification model of AGN

The two terms, classification and unification, are not mutually exclusive. Classification helps us to organize and understand AGN observations, while unification provides a powerful conceptual framework for interpreting their differences (e.g., Tadhunter, 2008; Netzer, 2015; Spinoglio et al., 2021). Over the years of observation, diverse types of AGN have been identified and classified into distinct categories. They can be broadly classified into different types based on their observed properties, such as the presence and strength of jets, the emission of

broad or narrow emission lines, and the relative brightness of their radio emission compared to their optical emission. In this section, we'll discuss the most important classes outlining their defining characteristics, before delving into potential unification scenarios for these AGN variants. In doing so, an AGN can fall into multiple categories due to its diverse set of defining features (e.g., Antonucci, 1993; Tadhunter, 2008).

A detailed scheme for classifying Active Galactic Nuclei (AGN) based on their observed radio and optical properties, which has historical significance and still provides a foundational understanding of AGN diversity, is as follows:

- **Seyfert galaxies:** Seyfert galaxies are galaxies that are usually spiral galaxies that host a bright $(10^{11} - 5 \times 10^{12})L_{\odot}$, star-like active nucleus (e.g., Chen and Hwang, 2018). They are defined based on emission line features at UV and optical bands. Because of their relatively low luminosity, Seyfert galaxies are currently found at a low redshift ($z \leq 0.5$) and have visible host galaxies (e.g., Zhang et al., 2008; Jha et al., 2020; Grafton-Waters, 2020). There are two subclasses of Seyfert galaxies, depending on the widths of permitted emission lines (e.g., Malkan et al., 2017; Foschini, 2020): Seyfert 1 galaxies contain both broad (FWHM 1000 - 2000 km s^{-1}) and narrow emission lines (FWHM 300 - 1000 km s^{-1}) and the two sets of lines are emitted in different regions, the BLR and the NLR, respectively. The second, Seyfert 2 galaxies only contain sets of narrow emission lines and are characteristic of a low electron density ($n_e \approx 10^3 - 10^6 cm^{-3}$) ionized gas. It contains permitted and forbidden strong emission narrow lines with (FWHM 300 - 1000 km s^{-1}) and no broad permitted lines (e.g., Bornancini and García Lambas, 2018; Suh et al., 2019; Mountrichas et al., 2021). There exist intermediate classifications that assign fractional type values based on the relative strength of broader and narrower components (Seyfert 1.2, 1.5, 1.8, 1.9; see e.g., Chen, 2021). For instance, Osterbrock and Ferland (2006); Ehler et al. (2018); Peruzzi et al. (2021) discuss intermediate types.

  The Type-1 and Type-2 classifications can be generalized including quasars too (e.g., Ramos Almeida et al., 2011; Villarroel and Korn, 2014) for higher luminosity, as well as Low-Ionization Nuclear Emission Regions (LINERs), discussed later in this section, on the low-luminosity side. Although the distinction between type-1 and type-2 AGN is still widely used in AGN classification, recent observations, especially in far infrared (FIR), suggest that the type-1 and type-2 differences may, in some instances, arise from the real physics behind AGN and not only the orientation effect (Netzer, 2015, references therein).

- **Radio galaxies:** These are galaxies that have strong radio sources and are

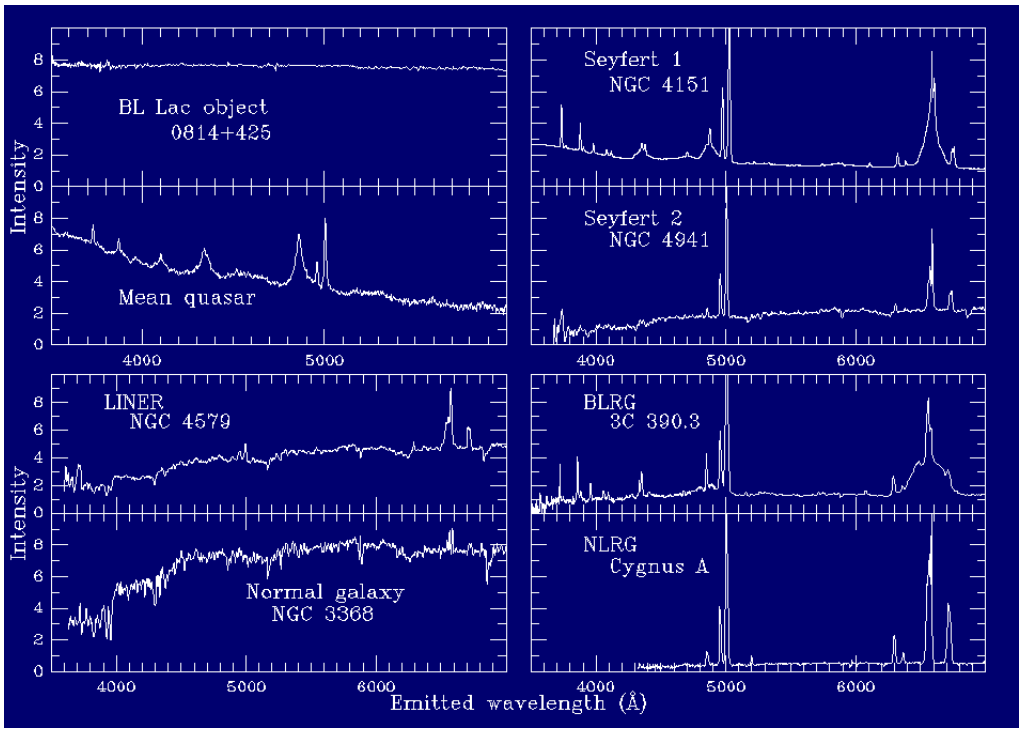

Figure 2.8: Example of the optical spectrum of different classes of galaxies and AGN.

typically associated with giant elliptical galaxies. They have strong radio emissions compared with emissions in other wavebands. They are characterized by relativistic jets extending beyond the galaxy itself and by GHz radio power emissions higher than 10^{22} W Hz^{-1} (e.g., Machalski et al., 2008, 2011; van Velzen et al., 2012). Similar to Seyfert galaxies, radio galaxies can also be divided into broad-line radio galaxies (BLRG) and narrow-line radio galaxies (NLRG).

In the 1970s, Fanaroff and Riley (Fanaroff and Riley, 1974) introduced a simple distinction between two morphological types (e.g., Sadeghi et al., 2021; Hossain et al., 2023). This classification separates the extended radio sources based on where the brighter part of their radio emission is located. The subclassification of the radio galaxies according to their radio morphology can also be based on the measurement of the ratio R of the distance between the two brightest spots and the overall extent of the radio emission (Fanaroff and Riley, 1974): Fanaroff-Riley (FR I, (Edge-darkened) with $R < 0.5$, has bright jets rising from the nucleus, becoming fainter as they expand farther away from the core, and ending up in plumes or diffuse low surface brightness lobes (left plot of Fig. 2.9. Fanaroff-Riley (FR II, Edge-brighter) with $R > 0.5$, have typically faint (or invisible) jets that end in bright hot spots, representing the interaction between the jet and the interstellar medium, and diffuse lobes are visible

around the jet (Edge-brighter). It is important to note that the distinction between FR I and FR II can be somewhat ambiguous (e.g., Kawakatu et al., 2009; Mingo et al., 2019).

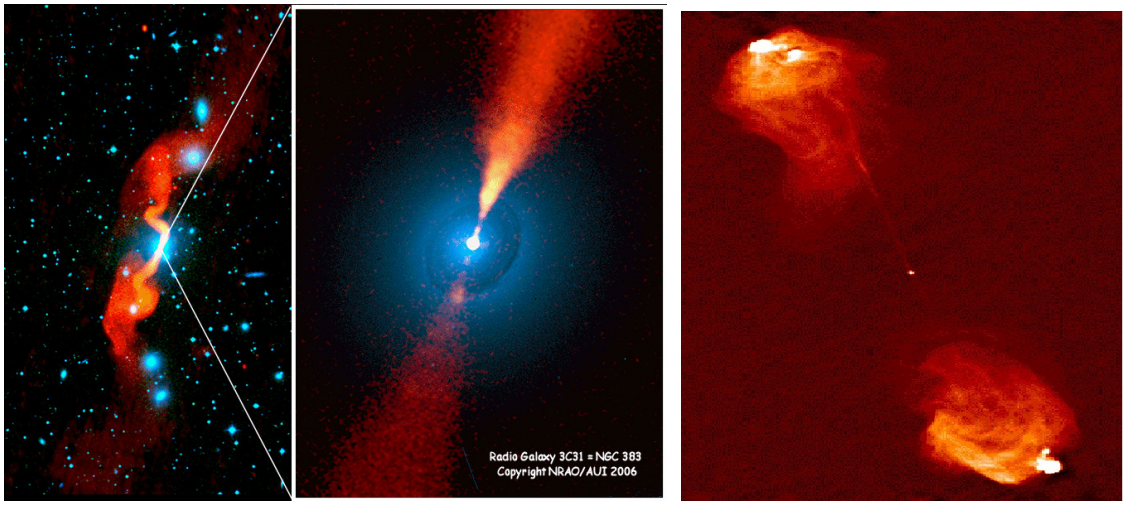

Figure 2.9: An example of Fanaroff-Riley sources. Left: VLA radio image of 3C 31 superposed on the Palomar sky survey optical image shown in blue, and resolution of the inner jet. Right: radio map at 1.4 GHz of FR II galaxy, Cygnus A. [Image credit: (Martel et al., 1999; Laing et al., 2008) (left) and NRAO (right)][4]

.

- **Quasars:** They are the most distant and more luminous subset of the overall population of AGN, often with $L_{bol} \geq 10^{46}$ ergs s^{-1} (e.g., Onken et al., 2022). In most UV and optical sky images, quasars are point-like sources. Spectroscopically, they exhibit similar features as Seyfert 1 galaxies, with prominent $L_{y\alpha}$ emission lines and/or other broad emission lines, but with little contribution from host galaxies. As we mentioned in the introduction, quasars have been classified as RL and RQ by using radio and optical measurements as well. As quasars are the main theme of the thesis, additional and detailed description is given in Sect. 2.4.

- **Blazars:** They encompass certain AGN, BL Lacertae object (BL Lacs), and flat-spectrum radio quasars (FSRQ) exhibiting highly atypical spectra and distinctive features, such as featureless spectra, a strong variability over a short timescale (e.g., within hours), and notable, fluctuating polarization (e.g., Landt et al., 2004; Rani et al., 2011). It's important to note the substantial disparity in the optical spectra between BL Lacs and FSRQ. While FSRQ exhibits prominent broad emission lines, BL Lacs, unlike FSRQ, show either weak lines or lack prominent emission lines

[4] https://public.nrao.edu/

entirely in their optical spectra. Despite this optical dissimilarity, they are grouped within the Blazar classification due to their shared distinctive continuum properties, such as strong variability and polarization properties (e.g., Ghisellini et al., 2011; Mondal and Mukhopadhyay, 2019). Additional entities like Optically Violently Variable Quasars (OVV), Highly Polarized Quasars (HPQ), and Core Dominated Quasars (CDQ) initially had distinct empirical definitions. They have since been recognized as variations of the same object type and are presently categorized within the FSRQ class.

- **Low-Ionization Nuclear Emission Regions (LINERs)):** They are weak AGN with Bolometric luminosity less than 10^{44} ergs s^{-1} and Seyferts are, on average, 10 times more luminous than LINERs (e.g., Singh et al., 2014; Hernández-García et al., 2016). Although the spectra of LINERs resemble those of Seyfert 2 galaxies and H II regions, the two classes can be distinguished by considering the intensity ratios of two pairs of lines (e.g., Heckman, 1980; Dessauges-Zavadsky et al., 2000; Feltre et al., 2023).

  In this thesis, we mainly focus on extremely jetted quasars, and in Sect. 2.4, additional detailed points about quasars, as well as RL and RQ classification are presented.

The most basic unification of AGN is the unification in luminosity, which historically served as a distinguishing characteristic across the AGN classes. AGN are unified by the basic process producing their radiative output, namely accretion onto a central supermassive black hole. So, low-luminosity AGN, such as Seyfert galaxies and LINERs, typically found in local or nearby galaxies, as well as quasars and blazars, that radiate over a very broad range of powers, are all different manifestations of the same physical phenomenon.

The unified scheme is a model that interprets the different observational properties of the various classes of AGN based on apparent differences that arise because of their different orientation to the observer (Antonucci, 1993; Urry and Padovani, 1995). It provides a powerful framework for interpreting their differences (e.g., Netzer, 2015). The unification based on orientation again follows from the fact that all AGN sub-classes share a common mechanism of energy production, the accretion of matter onto a SMBH in their center. However, this unification model proposes that types 1 and 2 of AGN might not be fundamentally different, but rather represent different viewing angles of the same underlying phenomenon relative to an obscuring torus (e.g., Netzer, 2015; Berton et al., 2017).

The unification model of AGN depends primarily on three key factors: the orientation, that affects the emission lines properties, and the radio classes (e.g.,

Jackson and Browne, 2013; Netzer, 2015).

- **Orientation on optical properties:** Our view of the central engine of an AGN and its surrounding AD, is heavily influenced by whether we are looking straight into its central SMBH or if the obscuring torus blocks our view. Face-on view (type-1 AGN) is when there is a clear view through the torus hole and can see the bright AD and BLR, leading to a Seyfert 1 or quasar with broad emission lines. Edge-on view (type-2 AGN) is when the obscuring torus blocks our line of sight, and we are only able to see the weaker, indirectly scattered light and narrower emission lines from the more distant gas clouds. This leads to a Seyfert 2 or narrow line radio galaxy, with only narrow emission lines (e.g., Antonucci and Miller, 1985; Berton et al., 2017).

- **Emission lines:** The width of emission lines in the AGN spectra provides crucial clues about orientation. BLRs, which are dense, rapidly rotating gases close to the central SMBH, can produce broad emission lines. This region is only visible if our view isn't blocked by the obscuring torus. As a result of an unobscured view, strong broad lines point to a type-1 AGN, where we see directly into the central SMBH. Whereas, absent broad lines and strong narrow lines suggest a type-2 AGN, where the torus obscures the central engine. The NLRs are the more extended gas clouds farther out, producing these narrower lines visible from all angles.

- **Orientation on radio properties:** Another fascinating aspect of AGN is their radio emission. Some AGN emit powerful radio jets, while others do not. The orientation of these jets can also affect their observed properties. When the jet is pointed towards the observer, we see a core-dominated radio morphology. Optically, we may classify the sources as a Blazar. When the jet is pointed away, we start resolving the radio lobe that may be brighter than the core (lobe-dominated sources). Optically, the source may appear as a type-1 (if the line-of-sight is not far from the radio axis) or type-2 (if the line-of-sight is at an angle $\theta \gtrsim 45-60$ degree from the radio axis. However, other factors, besides orientation, might also influence radio loudness. The efficiency of jet production, the properties of the surrounding interstellar medium, the spin and the presence of large-scale magnetic fields can all play a role (e.g., Blandford and Znajek, 1977; Podigachoski et al., 2015, 2016).

The unification model is successful in explaining the diverse appearances of AGN. This elegant torus model beautifully explains the type-1/type-2 dichotomy, supported by observations of dust and gas distribution (e.g., Urry and Padovani,

1995). However, like any good scientific theory, it has limitations and unanswered questions.

The first open question can be due to a clumpy torus, in which the obscuring torus assumed to have a doughnut shape might not be a smooth ring but a collection of gas clouds. This can lead to variations in the strength and visibility of both broad and narrow lines depending not only on the specific viewing angle but also on cloud configuration (e.g., Bianchi et al., 2012; Netzer, 2015). The second open question is related to winds from the disk that could create a dynamic obscuring region, in place of a stationary torus. The wind dynamics could affect the emission lines, potentially causing them to vary over time (e.g., Hopkins et al., 2012; Williamson et al., 2019). The third point among the limitations and unanswered questions can be host galaxy properties which, like gas distribution, can also influence how much light is emitted and obscured, in turn influencing the observed emission line strengths (e.g., Hopkins et al., 2005). Also in this unification approach, there are some challenges, including the efforts to explain why some AGN are powerful radio emitters while others are not. Additional factors beyond the viewing angle, like black hole spin or host galaxy properties, need to be taken into consideration. Apart from the limitations, the unification model is supported by several lines of evidence. However, it is still an active area of research, and the exact details of the unification scheme are still debated.

2.4 Quasars

The story of quasars begins in the late 1950s with the radio source 3C 273, initially mistaken for a nearby star due to its star-like appearance on photographic plates, but its strong radio emission revealed its true nature and astronomers soon discovered more of these "quasi-stellar radio sources," eventually shortening the name to the now-familiar "quasar" (e.g., Schmidt, 1963; Mushotzky, 2004). When recognized in 1963 for the first time, they appeared as faint at optical wavelengths, and point-like objects with unusual optical emission spectra quite unlike those of stars (e.g., Kellermann, 2013, 2014, see Fig. 2.10).

Understanding quasars requires a multiwavelength approach, employing telescopes across the electromagnetic spectrum. Optical and UV data allow the study of the hot ADs and winds ejected from the SMBH vicinity. Radio telescopes trace the jets and their interaction with the surrounding medium and probe the vast, swirling clouds of gas surrounding the quasar to provide insights into the feeding mechanisms and the influence of quasar activity on their host galaxies. X-ray and gamma-ray telescopes delve into the extreme environments near the

SMBH itself to study the innermost regions. The optical and UV emission lines can be very broad (FWHM $\geq$ 10000 km s^{-1}) and prominent equivalent width (W $\approx$ 100Å) in the rest frame.

Quasars are numerous and, except for the short-lived powerful explosions responsible for supernovae and gamma-ray bursts, they are the most luminous objects in the universe with $L \geq 10^{48}$ ergs s^{-1} (e.g., Bloom et al., 2009). The luminosity of some quasars changes rapidly in the optical range and even more rapidly in the X-ray range (e.g., Giustini et al., 2011; Shen et al., 2019). Quasars do show self-similar broad line spectra with varying luminosity, BH mass, and redshift, and they are anisotropic sources most easily seen at radio frequencies where relativistic beaming is observed (e.g., Urry and Padovani, 1995; Marziani and Sulentic, 2012b). When a quasar jet interacts with the gas surrounding the galaxy, radio waves are emitted and radio lobes can be observed (e.g., Cavagnolo et al., 2010).

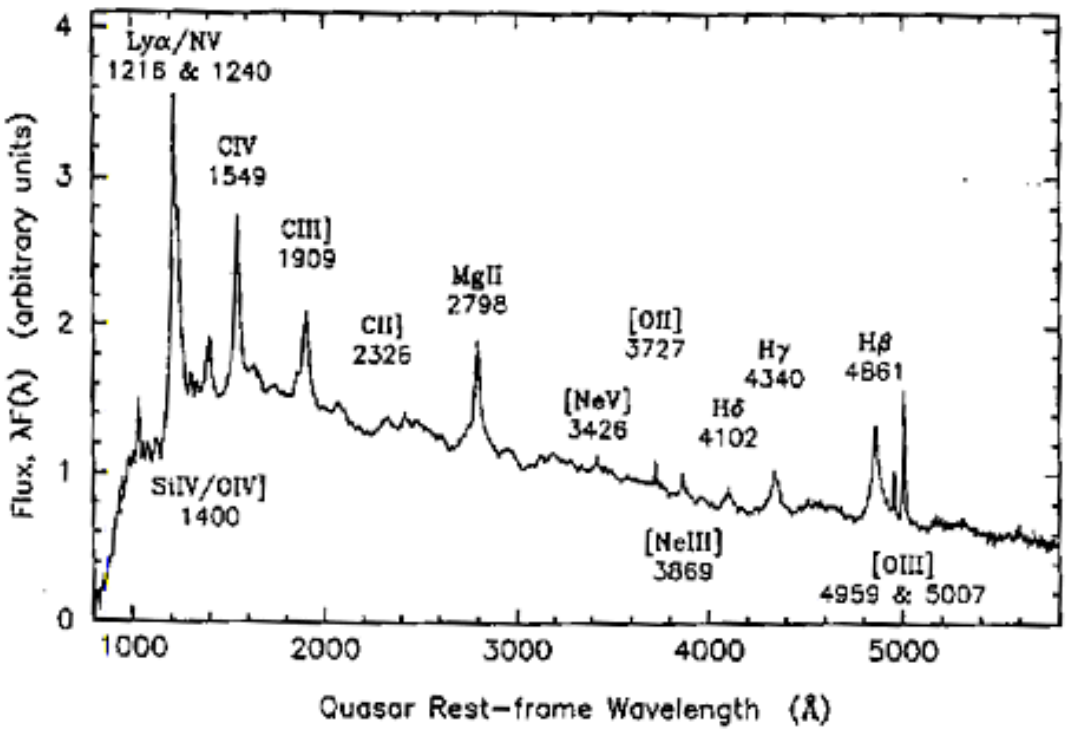

Figure 2.10: Composite spectrum of a quasar to show familiar lines signatures [Image credit: Francis et al. (1991)]

.

Studying quasars allows us to understand the processes of galaxy formation and evolution, the early growth of SMBHs, and the role they play in shaping the universe (e.g., Sulentic et al., 2014; Czerny, 2017; Smith and Bromm, 2019). They can be helpful:

- In unveiling the early universe, when galaxies were young and SMBHs were growing from seeds. They are a time capsule, since they are some of the most distant objects known, existing billions of light-years away and offer windows into the early universe (e.g., Wolf et al., 2020a; Yang et al., 2021).

- In the study of galaxy formation and evolution, as their powerful jets can trigger star formation in the host galaxy while simultaneously preventing further star formation by expelling gas and dust. In turn, this delicate interplay shapes the morphology and growth of galaxies (e.g., Cattaneo, 2001; Koudmani et al., 2023).

- In cosmology and dark matter study, as quasars at different cosmic epochs help to understand the evolution of the universe (e.g., Czerny, 2017; Marziani et al., 2019b; Dultzin et al., 2020). Their immense luminosity makes them ideal probes of the large-scale structure, and allows us to study the distribution of dark matter that makes up most of the universe's mass by bending and distorting the light from even more distant objects behind them by the phenomenon known as gravitational lensing.

- In probing large-scale structures. By studying their distribution and clustering, it is possible to understand the formation and evolution of cosmic filaments and voids, revealing the intricate web that binds the universe together (e.g., Song et al., 2016; Tanimura, 2017).

- In the field of black hole physics, quasars can be used as a unique laboratory to study the extreme physics around SMBHs due to their immense gravitational pull and the high temperatures near the SMBH event horizon. By observing their behavior, it is possible to test theories of gravity and accretion. Also, they can be used in the study of SMBH growth and feeding by observing how matter falls into the SMBH and forms the AD (e.g., McLure and Dunlop, 2004; Gasparini, 2022).

The study of quasars extends beyond the realm of astrophysics and influences other fields. For instance, in general relativity, the extreme conditions around quasars provide a natural laboratory for testing the predictions of Einstein's theory of general relativity in a strong gravitational field (e.g., Zakir, 2000; Schmidt and Wambsganss, 2010). Also in the field of nuclear Physics, they help in understanding the processes occurring in the AD around the SMBH to shed light on star formation under extreme conditions (Siemiginowska, 1998; Collin and Zahn, 1999; Wang et al., 2023). In addition, in the development of technology, the sophisticated instruments and techniques used to study quasars drive advancements in fields like optics, detectors, and data analysis.

With the advent of powerful new telescopes and instruments, such as the James Webb Space Telescope (JWST), the Atacama Large Millimeter Array (ALMA), and the Square Kilometer Array (SKA), astronomers are poised to make groundbreaking discoveries about quasars. These advancements will enable us to study these celestial objects in greater detail than before, providing deeper insights into their formation, evolution, and impact on the universe. JWST's infrared sensitivity will enable to study of the dusty environments surrounding quasars and probe deeper into the early universe to search for the first quasars (e.g., Gardner et al., 2023; Menzel et al., 2023). ALMA's ability to observe millimeter and submillimeter wavelengths will reveal the cold gas reservoirs that fuel quasar activity (e.g., Carpenter et al., 2020). SKA's unprecedented radio sensitivity will allow the detection of ever fainter quasars and radio sources down to $1\mu Jy$ and map the large-scale distribution of quasars throughout the universe (e.g., Garrido et al., 2023). Despite significant advancements in the understanding, many questions about quasars remain unanswered: how SMBHs accrete matter so efficiently, what triggers the transition between a quasar's active and inactive phases, and the role of quasars in the overall evolution of the universe are some of them. Future research with innovative instruments like SKA and the Vera C. Rubin Observatory (VRO) promises to revolutionize the understanding of quasars. By mapping vast areas of the sky at unprecedented sensitivity and resolution, these telescopes will unveil fainter, more distant quasars, providing a comprehensive picture of their population and their impact on the universe (e.g., D'Onofrio and Marziani, 2018; Garrido et al., 2023).

2.4.1 Radio-quiet and radio-loud quasars

Although quasars were originally discovered in radio, only about 8 - 10 % of them in the local universe have substantial radio emissions (e.g., Begelman et al., 1984). When their radio emission is considered, quasars are typically classified into RQ and RL quasars (e.g., Begelman et al., 1984; Padovani, 2016). Indeed, for the same optical power, the radio powers of RQ quasars are a few orders of magnitude smaller than those of their RL counterparts. A source whose ratio of specific optical fluxes in the radio and in the optical is larger than 10 is customarily considered RL (Kellermann et al., 1989), even if a clear consensus on a boundary between them has been difficult to achieve and several radio- loudness criteria have been used in the literature (Hao et al., 2014; Ganci et al., 2019). A more detailed explanation about the estimation of such radio loudness parameters by using the radio and optical measurements as well as the boundaries for the classification is given in Sect. 3.4.1.2.

These labels, which are more than fifty years old, are obsolete, misleading, and wrong (e.g., Padovani et al., 2017). It was later understood that RQ quasars

were only radio faint, but the name stuck. Padovani et al. (2017) argues that AGN should be classified based on a fundamentally physical rather than just an observational difference, namely the presence (or lack) of strong relativistic jets, and that we should use the term "jetted" and "non-jetted" AGN instead. It is now known that RQ AGN are the norm, not the exception, as they make up the large majority ($\geq$ 90%) of the AGN class (e.g., Padovani et al., 2017). RL quasars behave exactly like RQ quasars, with the addition of emission in the form of a jet. The dichotomy between RL and RQ quasars remains one of the central mysteries in AGN research. Both types are powered by SMBHs accreting massive amounts of gas, yet exhibit different radio output, hinting at underlying physical differences. Understanding the dichotomy between these two populations is crucial for our understanding of black hole accretion, jet formation, and galaxy evolution (e.g., Zamfir et al., 2008; Garofalo et al., 2014).

As also argued in Padovani et al. (2017), despite what the odd labels might suggest, the differences between the two classes are not restricted to the radio band, they are not simply taxonomic either, as the two classes represent intrinsically different objects, with most RL AGN emitting a large fraction of their energy non-thermally over the whole EMS, while the multi-wavelength emission of RQ AGN is dominated by thermal emission, directly or indirectly related to the AD. In the hard X-ray to γ-ray band, many RL sources emit up to GeV energies, while nearby RQ bright Seyfert galaxies have a sharp cut-off at energies 1MeV, i.e., no RQ AGN has ever been detected in γ-rays except NGC 1068 and NGC 4945, two Seyfert 2 galaxies in which the γ-ray emission is thought to be related to their starburst component (e.g., Malizia et al., 2014; Lohfink et al., 2017). This could mean that RQ AGN are not RQ, they might be γ-ray quiet.

Although a signature of the presence of an AGN is the detection of a relativistic jet, the morphology of a radio source associated with quasars can vary. In the 1970s, Fanaroff and Riley (1974) introduced a simple distinction between the two morphological types, FR I and II. This classification separates the extended radio sources based on where the brighter part of their radio emission is located, as explained above in the case of radio galaxies in Sect. 2.3.2.

The identification of RL and RQ quasars can also be made based on a parameter space called the 4DE1 parameter space Sulentic et al. (e.g., 2008): RL sources show a restricted space occupation relative to the RQ majority. RL quasars are predominantly Population B (see Sect.2.5.3) which are characterized by: (1) broad Balmer line profiles, full width at half maximum (FWHM) of broad $H\beta$ > 4000 km s^{-1}, (2) weak Fe II optical emission ratio $R_{\rm FeII}$= I(FeII4570Å)/I(Hβ), (3) absence of a C IVλ1549 blueshift, and (4) absence of a soft-X-ray excess (see Sect. 2.5.1 for the detail).

2.4.1.1 Fundamental physical differences

The dichotomy between RL and RQ quasars remains one of the central mysteries in AGN research. Although both are fueled by SMBHs accreting gas and dust, their distinct radio output hints at underlying physical-process disparities. While traditionally, a radio-to-optical luminosity ratio (R) (discussed in Sect. 2.4.1) exceeds 10 distinguished RLs, recent studies reveal a smoother distribution with potential overlap at lower R values (e.g., Kellermann et al., 2016). Distinguishing intrinsic differences from extrinsic factors like viewing angle and dust obscuration remains a challenge, requiring advanced modeling and multi-wavelength observations (e.g., Kalfountzou et al., 2014; Zhu et al., 2021; Shaban et al., 2022). The following are some of the potential factors that drive this intrinsic dichotomy:

- **Spin state:** Recent studies suggest that the spin of a SMBH plays a critical role as an intrinsic factor. RLs are often associated with rapidly spinning SMBHs, potentially leading to more efficient extraction of rotational energy for jet formation through mechanisms like the Blandford-Znajek process. This theoretical mechanism explains how rotating SMBHs can extract energy and launch powerful jets of matter and radiation. Though direct spin measurements remain challenging, RQs might harbor slower-spinning SMBHs, hindering strong jet production (e.g., Schulze et al., 2017).
- **AD properties:** The differences in black hole spin could influence the geometry and stability of the AD. Thin, geometrically thick disks, prevalent in RLs, enhance magnetohydrodynamic jet launching. RQs might possess more standard, optically thick disks with less efficient jet production (e.g., Chakraborty and Bhattacharjee, 2021).
- **Magnetic field structure:** The structure and strength of magnetic fields surrounding the SMBH critically influence jet channeling and collimation towards the outward. Stronger, ordered magnetic fields are often associated with RLs, potentially enabling efficient jet formation. RQs might have weaker or more chaotic magnetic fields, hindering jet production (e.g., Li and Cao, 2019; Chamani et al., 2021).
- **Corona:** Hot coronae surrounding the SMBH in RLs are thought to provide plasma and energy for jet formation. Recent observations suggest RQs might have weaker coronae, which limits their jet production capacity (e.g., Wehrle et al., 2009; Timlin et al., 2021; Liu et al., 2021; Zhu et al., 2021; Liu and Qiao, 2022).
- **Environment:** Gas density and surrounding galactic structure might influence jet collimation and propagation. Denser environments in RL host

galaxies might contribute to denser, more collimated jets compared to RQs residing in sparser environments (e.g., Shatalov et al., 2019; Couto and Storchi-Bergmann, 2023).

- **Mergers:** Galaxy mergers are known to trigger star formation and inject turbulence into the surrounding gas, impacting the AD and potentially influencing jet production. Additionally, mergers can generate large-scale magnetic fields that play a role in jet collimation and propagation. While both RLs and RQs can be found in merging systems, a higher prevalence of mergers in RLs might contribute to their stronger radio luminosity (e.g., Chiaberge and Marconi, 2011; Gao et al., 2020; Silva et al., 2021).

In addition, there are discrepancies in terms of luminosity functions and the host galaxy types. There are also intrinsic differences like the nature of the AD, the host galaxy's magnetic field, or the SMBHs, which might play a crucial role in shaping the jet formation and the radio loudness, independent of the orientation considered in the unification model (e.g., Kellermann et al., 2016; Chakraborty and Bhattacharjee, 2021). The properties of the AD, such as its density, temperature, and turbulence, significantly influence jet formation and the radio loudness in which thicker, hotter, and more turbulent disks can create powerful jets (e.g., Bhatta et al., 2018; Dihingia and Vaidya, 2022). The strength of the magnetic field within the disk also plays a vital role in channeling the jets along its path (e.g., de Gouveia Dal Pino et al., 2010). The story of RL and RQ quasars doesn't unfold in isolation, their host galaxies and the surrounding environment play a crucial role in shaping their behavior.

Distinguishing intrinsic differences between RL and RQ quasars from extrinsic factors remains a challenge. High-resolution multi-wavelength observations to identify fainter and distant RQ quasar jet morphology and magnetic field structure coupled with advanced theoretical jet formation models incorporating black hole spin, AD dynamics, and magnetic field configurations, are crucial for understanding their dichotomy. Future research also needs to explore the interplay between these factors and their evolution over time to gain a deep understanding of the diverse radio luminosity landscape of quasars. In conclusion, quasars are one of the powerful tools for unlocking the secrets of the universe and their study continues to push the boundaries of our knowledge, shaping our understanding of the universe. While significant progress has been made in understanding the potential underlying physical and environmental differences, many questions remain. The RL - RQ dichotomy continues to be a captivating puzzle, with each discovery unveiling new layers of complexity. The interplay between black hole spin, AD dynamics, magnetic field configurations, and environmental factors plays a crucial role in shaping the diverse radio output of quasars. Con-

tinued research, technological advancements, and theoretical refinement provide a piece of crucial information to unlock the mystery of radio emission.

2.4.2 Quasar surveys

2.4.2.1 Optical and NIR

Quasar surveys are large-scale astronomical projects designed to identify and catalog quasars. There have been many multiwavelength surveys targeting finding and observing quasars since they were discovered in the 1960s, aiming to understand their properties, distribution, evolution, and the role they play in the universe. There are two main types of quasar surveys: photometric surveys, which use broad-band filters to identify quasars based on their characteristic colors, and spectroscopic surveys, which use spectroscopy to confirm the presence of quasars by identifying the specific emission lines in their spectra. The most famous quasar surveys are the Sloan Digital Sky Survey (SDSS) (York et al., 2000), the 2dF Quasar Redshift Survey (2QZ) (Croom et al., 2004), Global Astrometric Interferometer for Astrophysics (GAIA) (Lindegren and Perryman, 1996), Wide-field Infrared Survey Explorer (WISE) (Wright et al., 2010), and the Pan-STARRS surveys (Chambers et al., 2016).

- **PHL survey:** The acronym "PHL" stands for Palomar-Haro-Luyten. The PHL Survey, which cataloged a large number of blue stellar objects, contained several objects that later turned out to be quasars. These were initially classified as blue stars due to their appearance in the optical, but follow-up spectroscopic observations showed that they had the unusual properties associated with quasars. The survey remains a significant resource listing some of the bluest quasars observed to date.

- **Sloan Digital Sky Survey (SDSS):** The SDSS uses a dedicated 2.5-meter telescope located at Apache Point Observatory, New Mexico, to obtain images in five bands (ugriz) over approximately 10,000 deg^2 of high Galactic latitude sky. The survey also obtained spectra from $\approx$ 3800 Å to $\approx$ 9200Å at a spectral resolution of $\approx$ 2000. Between 2000 and 2008 (the Sloan Legacy Survey), the SDSS imaged over 11,600 deg^2 of the sky and obtained spectra of galaxies and quasars from 9,380 deg^2 of that imaging (e.g., Schneider et al., 2002; Wu and Shen, 2022). SDSS has different surveys and data releases in which each quasar survey is done for different science goals, the SDSS DR7 consists of 105,783 spectroscopically confirmed quasars. The aim is to study the quasar luminosity function, and clustering properties (e.g., Hennawi et al., 2006; Shen et al., 2007).

2.4.2.2 Radio

In addition to the above large surveys, there are other quasar surveys in the radio domain of the EMS. Below are summarized the nine important quasar surveys in the radio related to this thesis.

- **3C radio survey :** In the context of quasars, the term "3C survey" refers to the Third Cambridge (3C) Catalog of Radio Sources. The 3C survey was a pioneering effort in radio astronomy that identified and cataloged hundreds of radio sources, many of which turned out to be quasars. It is a catalog of extragalactic radio sources compiled from observations made at the Mullard Radio Astronomy Observatory near Cambridge, England, in the 1950s and 1960s (e.g., MacDonald et al., 1968; Elsmore and Mackay, 1969). It was one of the earliest comprehensive catalogs of extragalactic radio sources and played a crucial role in the study of radio astronomy. This catalog of radio sources is a compilation of radio sources detected originally at 159 MHz. Subsequently, a revised version of the 3C at 178 MHz, was formally named 3CR. This catalog was further revised and 25% of the entries are optically identified as quasars, and they are, of course, strong radio sources (e.g., Smith et al., 1976; Veron, 1977).

- **PKS Survey:** The term "PKS survey" likely refers to a compilation of astronomical objects detected using the Parkes Radio Telescope, a prominent radio telescope located in New South Wales, Australia. It is one of the well-known and historically significant radio telescopes globally, operated by the Commonwealth Scientific and Industrial Research Organization (CSIRO). Originally compiled in the 1960s and continuously updated through subsequent observations and surveys, the catalog includes various types of astronomical objects emitted in radio, such as pulsars, galaxies, and quasars (e.g., Ekers, 1969).

- **B2 Survey:** It is a catalog of compact radio sources compiled from very long baseline interferometry (VLBI) observations conducted at the University of Bologna in Italy. "B2" indicates that it's the second version or iteration of a catalog produced by the Bologna group. The B2 survey focused on compact radio sources, including quasars and other types of AGN to provide information about their positions, radio flux densities, and other observational characteristics (e.g., Grueff et al., 1980).

- **S1 to S5 survey:** The S series of catalogs refers to lists of radio sources with well-definited flux limits, $\lesssim 1$ Jy (e.g., Jauncey, 1977; Pauliny-Toth et al., 1978). It was one of the early surveys designed to identify and classify strong radio sources in the sky.

- **NVSS survey:** The NRAO VLA Sky Survey (NVSS)[5] completed in the late 1980s and early 1990s is a comprehensive survey of the sky at a 20 cm wavelength that utilizes the National Radio Astronomy Observatory's (NRAO) Very Large Array (VLA) located in New Mexico, USA. Due to technical and observational constraints, approximately 82% of the sky was mapped in the NVSS. It is one of the most extensive surveys of the sky carried out in the radio frequency range by aiming to cover the entire sky visible from the VLA with a high angular resolution of about 45 arcseconds. It offers data on various extragalactic radio sources including radio galaxies and quasars. While its resolution (around 45 arcseconds) is lower compared to later surveys, NVSS remains a crucial resource for studying large-scale structures and the evolution of these radio sources. This resolution allowed the detection and detailed mapping of numerous radio sources across the sky. The NVSS produced a catalog of detected radio sources, with their positions, integrated, and peak flux densities. In this thesis, we used this catalog to get information about flux densities and radio maps (e.g., Condon et al., 1998).

- **FIRST survey:** The Faint Images of the Radio Sky at Twenty Centimeters (FIRST)[6] is a large-scale radio survey, another significant radio survey conducted using the Very Large Array (VLA) telescope in its B-configuration operated by the National Radio Astronomy Observatory (NRAO) in New Mexico, USA. The survey was designed to map a significant portion of the sky at a frequency of 1.4GHz (20 centimeters) and a resolution of around 5 arcseconds to identify and catalog faint radio sources that NVSS missed. It was designed to produce the radio equivalent of the optical Palomar observatory sky survey over 9,900 deg^2 of the North Galactic Gap, corresponding to the sky regions covered by SDSS. This survey, with flux density sensitivity of $\approx$ 1 mJy, is much deeper than the C bridge radio surveys. The survey was sensitive enough to detect faint radio emissions from various sources, including galaxies, quasars, AGN, and other celestial objects emitting radio waves at the surveyed frequency. This catalog contains detailed information about the identified radio sources, their positions, flux densities, and other relevant parameters. Complementary to NVSS: While NVSS covered a larger portion of the sky at a lower resolution, FIRST concentrated on smaller areas with higher resolution, providing complementary datasets for radio astronomers (e.g., Becker et al., 1995).

- **VLBI Observations:** VLBI stands for Very-Long-Baseline Interferometry, a technique used in radio astronomy to observe celestial objects with ex-

[5]NVSS-https://www.cv.nrao.edu/nvss/NVSSPoint.shtml
[6]FIRST-http://sundog.stsci.edu/cgi-bin/searchfirst

tremely high angular resolution. It involves multiple radio telescopes separated by large distances, sometimes spanning continents or even across the globe, working together as a single large telescope and synchronized to observe the same region of the sky simultaneously. VLBI observation allow astronomers to achieve extremely high resolution often down to fractions of a milliarcsecond (mas) images of e.g., quasars, revealing fine details that are not possible to observe with individual telescopes (e.g., Schilizzi, 1986; Van Langevelde et al., 2018).

2.5 Spectroscopic properties of quasars and optical classification

2.5.1 Four dimensional eigenvector 1 (4DE1) parameter space

Quasar properties can be described using various parameters, such as luminosity, $M_{\rm BH}$, $\lambda_{\rm E}$[7], accretion rate, emission line strengths, and more such as radio loudness, variability, host galaxy properties, dust extinction, chemical composition (e.g., Wilhite et al., 2008; Mazzucchelli et al., 2017; Marziani et al., 2019b; Rakshit et al., 2020). Researchers often explore multidimensional spaces defined by these parameters that allow them to analyze and categorize type-1 AGN based on their characteristics and study correlations between different properties. Traditionally, quasar diversity was analyzed using individual emission line measurements or principal component analysis (PCA) on a few selected spectral features by focusing on key aspects of the quasar's activity and the physical conditions within the AD and surrounding regions (e.g., Boroson and Green, 1992b). However, these methods don't capture the full complexity and diversity of the spectra.

The search for a parameter space that might provide spectroscopic unification for all classes of broad line emitting AGN motivated the 4DE1 concept, a relatively new approach in quasar research aimed at analyzing the diversity of quasar spectra systematically (e.g., Sulentic et al., 2000a; Marziani et al., 2010). The eigenvectors in the parameter space represent principal components that capture the most significant variations in the spectra, and each eigenvector corresponds to a particular pattern of spectral features that provide valuable information about the physical properties of quasars. The Eigenvector 1 (E1) was originally defined from a PCA of 87 PG quasars involving an anti-correlation between optical FeII intensity, half-maximum profile width of Hβ and peak intensity of [OIII]$\lambda\lambda$4959,5007 (e.g., Boroson and Green, 1992a). Different works

[7]The $\lambda_{\rm E}$ is defined as $L_{\rm bol}/L_{\rm Edd}$, with $L_{\rm Bol}$ the bolometric luminosity and $L_{\rm Edd}$= $1.26\times 10^{38}(\rm M_{BH}/M_{\odot})$ erg s^{-1}.

have shown that it is possible to systematize quasar spectral diversity in the 4DE1 parameter space by establishing a connection between a physical and an observational set of parameters involving optical, UV, and X-ray measures designed to serve as a 4D equivalent of the 2D H-R diagram (e.g., Sulentic et al., 2001) and E1 expanded to 4DE1 with the addition of X-ray photon index and CIVλ1549 profile shift measures (e.g., Sulentic et al., 2011; Fraix-Burnet et al., 2017; Marziani et al., 2018).

The 4DE1 parameter space provides a potentially fundamental discrimination between major AGN classes (e.g., Sulentic, 2007). Overall, the 4DE1 parameter space is a promising tool for understanding the diversity of type-1 AGN spectra systematically and comprehensively. Its potential lies in unraveling the complex processes underlying quasar formation, evolution, and their interaction with the surrounding environment (e.g., Sulentic et al., 2014; Sulentic and Marziani, 2015). The 4DE1 method addresses the full complexity of quasar spectra, mainly by:

- **Utilizing an easy to measure set of spectral features:** Instead of focusing on a handful of lines, 4DE1 parameter space leverages hundreds to thousands of data points across a broad wavelength range, encompassing the rich information within the spectra (e.g., Sulentic and Marziani, 2015; Marziani et al., 2018).
- **Employing advanced dimensionality reduction techniques:** 4DE1 parameter space goes beyond simple PCA by utilizing sophisticated algorithms like sparse PCA and non-negative matrix factorization (NMF). These techniques extract a smaller set of "eigenvectors" that explain the majority of the spectral variations more effectively (e.g., Jolliffe and Cadima, 2016).
- **Focusing on the dominant mode of variability:** The first eigenvector, embodies the most significant pattern of spectral variation across the quasar population, providing a concise representation of the most crucial information.

The principal parameters of the 4DE1 parameter space are:

1. **FWHM of broad Hβ:** It is the diagnostic line and related to the velocity field of the low-ionization emitting region. This line, together with the FWHM of MgIIλ2800, is thought to be a measure of assumed virialized motions in the AD and is thus crucial for estimating the mass of the SMBH (e.g., Marziani et al., 2013a).

2. **Ratio of the Intensity/equivalent widths of the 4570Å (which is the summation over $\lambda\lambda$4484 - 4686Å) optical FeII blend and the broad Hβ lines ($R_{\rm FeII,opt}$= I(FeII4570)/I(Hβ)):** It is sensitive to the ionization state, the electron density, and the column density of the BLR (e.g., Panda et al., 2019c). The correlation between the FeII and Hβ flux variations is of higher significance, as discussed in Shapovalova et al. (e.g., 2012).

3. **Centroid shift at half maximum of the high-ionization lines (HILs), such as CIVλ1549:** It is a strong diagnostic of winds/outflows component (e.g., Marziani et al., 1996; Richards et al., 2011).

4. **Soft X-ray photon index** (Γ_{soft}):, a diagnostic of the thermal emission from the AD and this index depends on the accretion state (e.g., Bensch et al., 2015; Jin et al., 2017; Panda et al., 2019a).

The above four key parameters exploit the fundamental trends and source differences that exist along the selected plane. The main advantage of this parameter space formulation is its weak or absent dependence on source luminosity (e.g., Zamfir et al., 2008).

2.5.2 4DE1 Optical plane: the quasar main sequence

Figure 2.11 shows source occupation in the optical plane of the 4DE1 parameter space, involving FWHM($H\beta$) and $R_{\rm FeII}$ measures, for a spectroscopic sample of 470 SDSS quasars (e.g., Zamfir et al., 2008, 2010). It can be seen as a clear sequence of sources extending from the narrowest FWHM($H\beta$) and strongest $R_{\rm FeII}$ at the lower right end of the sequence to sources with broadest FWHM($H\beta$) and weakest $R_{\rm FeII}$ at the upper left. It also organizes observables with the largest intrinsic dispersion, including the most statistically significant line profile differences. Analyzing the spectra of different types of quasars will give empirical results, will help to find a spectroscopic unification for quasars and a diagram like the H-R diagram in stars with a main sequence for quasar population, and will also help to look at active galaxies in a slightly different way than the one commonly used (e.g., Richards et al., 2011). This plane helps us to analyze, and identify correlations between different optical characteristics, study the underlying physical mechanisms driving the observed optical emissions, and visualize the relationships between key spectral features of type-1 AGN by revealing patterns that provide insights into their behavior (e.g., Sulentic and Marziani, 2015; Panda et al., 2017).
The FWHM of Hβ full profile (FP) (H$\beta_{\rm FP}$) and $R_{\rm FeII}$ define a type-1 AGN main sequence (MS) (e.g., Sulentic et al., 2000a; Marziani et al., 2001; Shen and Ho, 2014; Panda et al., 2018). The quasar MS is a diagonal band on

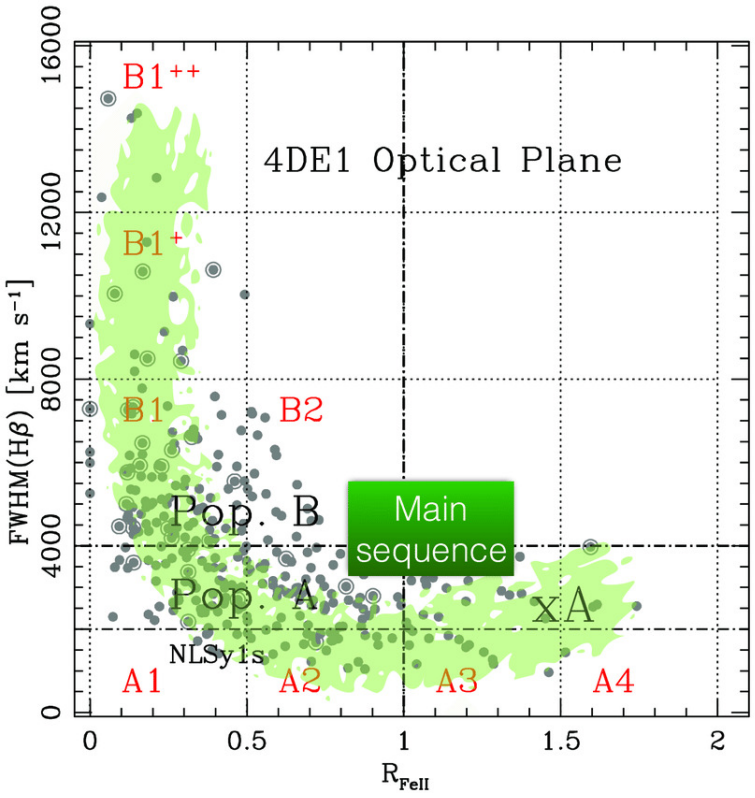

Figure 2.11: 4DE1 Optical plane for quasars main sequence. Different spectral classes are labeled as A1,A2,A3, A4 and B1, B2, $B1^{+}$, and $B1^{++}$ with a thin dotted separation lines. The thick horizontal dot-dashed line separates populations A and B at FWHM = 4000 km s^{-1} and the vertical one marks the limit for extreme Population A (xA) sources with $R_{\rm FeII} \geq 1$. The green shaded area indicates the distribution of a quasar sample from Zamfir et al. (2010), and traces the quasar MS [Image taken from Marziani et al. (2018)]

.

the optical plane as the H-R diagram does for stars (e.g., Greenstein, 1978). It allows contextualization of the observed empirical spectroscopic properties of type-1 AGN and their connection with the physical conditions of the BLR (see e.g., Marziani et al., 2018; Panda et al., 2019c). Its existence suggests a fundamental relation between BLR kinematics in which, a broader Hβ line implies higher gas velocities and turbulence in the BLR and a stronger FeII emission might be associated with specific abundances and ionization states of gas (e.g., Marziani et al., 2009). The MS position might be linked to the properties of the AD, influencing BLR conditions. Moreover, the MS helps to define a sequence of spectral types (ST) or a grid of bins on the optical plane that shows different spectral line profile properties (e.g., Sulentic et al., 2002): bins A1 to A4 are defined in terms of increasing $R_{\rm FeII,opt}$ with bin size $\Delta R_{\rm FeII,opt}$ = 0.5 (from A1 with $R_{\rm FeII} < 0.5$ to A4 with $1.5 < R_{\rm FeII,opt} \leq 2$, while bins B1, $B1^{+}$ and $B1^{++}$ are defined in terms of increasing FWHM

with ΔFWHM= 4000km s^{-1}, from B1 with 4000 < FWHM $\leq$ 8000 km s^{-1} to B1^{++} with FWHM > 12000 km s^{-1}(see Fig. 2.11). The binning of this MS has reduced interpretative confusion and assisted the interpretation of several observational aspects that appear puzzling if, for example, sets of spectra are indiscriminately averaged together. Spectra can be averaged, but only in a well-defined context like 4DE1 optical plane MS, in which a set of spectra in the same bin can be averaged or considered as sources that share similar properties (e.g., Sulentic et al., 2012).

2.5.3 Population A and Population B quasars

Exploration of the 4DE1 parameter space also gave rise to the concept of two populations of quasars, Population A (hereafter Pop. A) and Population B (hereafter Pop. B), that present important spectroscopic differences in the Hβ FWHM (e.g., Zamfir et al., 2008; Sulentic et al., 2011; Marziani et al., 2018). The separation line between Pop. A and Pop. B was taken to be FWHM of Hβ = 4000 km s^{-1} that was originally proposed based on a rather abrupt discontinuity in the shape of this Balmer line Hβ profiles around 4000 km s^{-1} (e.g. Sulentic et al., 2002; Collin, 2007; Sulentic et al., 2011).

The main drivers for the Pop. A and Pop. B distinction can be related to the accretion rate onto the central SMBH and the geometry of the AD. Pop. A, are fast-accreting objects with a relatively small $M_{\rm BH}$, with higher $\lambda_{\rm E}$ and accretes matter closer to the SMBH theoretical limit that leads to denser and thicker disks with narrower emission lines (e.g., Marziani et al., 2009). Whereas, Pop. B, are the ones with high M$_{\rm BH}$ and low $\lambda_{\rm E}$ with lower accretion rates, has thinner disks and broader lines. At low $z(\lesssim 1)$, the most powerful RL sources belong to Pop. B (e.g., Sikora et al., 2007; Zamfir et al., 2008).

The two populations can be described as follows (e.g., Sulentic et al., 2007b):

- Population A, characterized by narrower broad emission lines whose sources generally have FWHM(Hβ) < 4000 km s^{-1}, showing Lorentzian profiles in the broad emission lines, tend to have R_{FeII} > 0.5. They show significant blue shifts in HILs, have soft X-ray excess, and are primarily populated with RQ quasars (e.g., Sikora et al., 2007; Zamfir et al., 2008).
- Population B, distinguished by broader broad emission lines with a very wide range of FWHM (Hβ), values higher than 4000 km s^{-1}, whose broad line profiles show Gaussian components (broad and an additional very broad redshifted component) and with $R_{\rm FeII}$ < 0.5. In general, at low-z they do not show important blue shifts in HILs and no X-rays ex-

cess and are populated with both RL and RQ quasars (e.g., Zamfir et al., 2008, 2010).

Research on Pop. A and Pop. B quasars are actively progressing, thanks to the advancement in observational techniques in which high-resolution spectroscopy reveals detailed emission line profiles with high S/N ratio, providing more detailed insights into quasar properties (e.g., Sulentic et al., 2011). In addition, improved simulations are also helping to understand the interplay between accretion rate, disk geometry, black hole spin, and other factors in shaping observed differences. The Pop. A and Pop. B classification isn't absolute, and some quasars show intermediate properties, blurring the lines between the two groups (e.g., Zamfir et al., 2008). Additionally, factors beyond accretion rate and disk geometry like black hole spin or jet formation mechanisms might influence the classification into the two populations (e.g., van Velzen and Falcke, 2013; Schulze et al., 2017). For instance, higher black hole spin could contribute to thicker disks and narrower emission lines, aligning with the Pop. A characteristic (e.g., Schulze et al., 2017). Differences in jet launching mechanisms might also be associated with Pop. A and Pop. B quasars, potentially influencing their radio loudness and emission line profiles (e.g., van Velzen and Falcke, 2013; Saikia, 2022).

Refining the Pop. A and Pop. B classification by identifying additional spectral or physical parameters that can more precisely distinguish between the two populations, understanding the underlining physics by unveiling the precise interplay between accretion rate, disk geometry, black hole spin, and other factors in shaping the observed differences is crucial. Understanding the evolutionary connections by exploring how quasars transition between Pop. A and Pop. B over cosmic time and how these transitions might relate to their host galaxies and environments are the key areas of ongoing investigations (e.g., Fraix-Burnet et al., 2017).

In conclusion, the 4DE1 parameter space has emerged as a powerful tool for systematically analyzing the complexities of quasar spectra, quasar classification, environmental studies, and model development. The optical plane also remains a powerful tool in quasar research by offering a lot of the complex interplay of gas dynamics, accretion physics, and quasar evolution.

2.5.4 UV-plane

In a close analogy to the optical plane, it is also possible to analyze the UV plane by using MgII, and $\mathrm{FeII_{UV}}$ line parameters. This is possible mainly because both Hβ and MgII lines belong to LILs and are supposed to be emitted

from a similar region (e.g., Collin-Souffrin et al., 1988; Kovačević-Dojčinović and Popović, 2015; Sun et al., 2015; Kovačević-Dojčinović et al., 2017; Popović et al., 2019). The UV plane is also formed by using $MgII_{FP}$ FWHM and the strength of the $FeII_{UV}$, $R_{FeII,UV}$, which is defined as the ratio of the intensity of $FeII_{UV}$ at 3000Å (which is the summation over $\lambda\lambda$2200 - 3010Å) emission to the intensity of $MgII_{FP}$, $R_{FeII,UV}$= I($FeII_{UV}$)/I($MgII_{FP}$) (e.g., Śniegowska et al., 2020). As compared to the optical plane, the UV plane shows a larger range in $R_{FeII,UV}$. This is mainly because the range of the integrated flux in $FeII_{UV}$ is broader as compared to the optical, $FeII_{opt}$.

2.6 Accretion disk and accretion disk models

As mentioned before, the energy responsible for the immense luminosity of an AGN is derived from the accretion of matter onto a SMBH. This accretion can occur in two ways, 1) in a chaotic way, in which accretion can be described assuming a spherical symmetry or 2) in a more structured manner with the formation of an AD, in this case accretion occurs only on the equatorial plane (with respect to the BH rotation axis), matter is heated to high temperatures ($T \approx 10^4 - 10^5 K$), part of it accretes the SMBH while a small fraction is converted into radiation (e.g., Abramowicz and Fragile, 2013; Falanga et al., 2015). The AD, which plays a crucial role in understanding the physics of AGN as the radiation emitted by the AD can shape the surrounding environment and the relative emission (e.g., Abramowicz and Fragile, 2013; Jha et al., 2023). ADs are thought to be thin and geometrically flat structures surrounding the BH, with a thickness of approximately one-tenth of their radius, and its inner and outer radii depend on the M_{BH} and the rate of infalling material (e.g., Jiang et al., 2019; Liu and Qiao, 2022). They are composed of mostly hydrogen and helium, with trace amounts of heavier elements like oxygen and carbon. The inner regions of the disk are hotter and denser than the outer regions, with temperatures reaching up to billions of degrees near the SMBH. Densities can reach up to 10^{18} particles per cubic centimeter (e.g., Abramowicz and Fragile, 2013). Inward flow is hindered by friction, requiring a mechanism to transport angular momentum outwards and allow material to spiral toward the SMBH. As the material spirals inward, its gravitational potential energy is converted into thermal energy, heating the disk to millions of degrees and releasing tremendous amounts of radiation. The opacity, the intense radiation and magnetic fields within the AD are responsible for the wide range of phenomena observed in AGN, including powerful jets of particles ejected at nearly the speed of light, broad emission lines from highly ionized gas, and strong X-ray and gamma-ray emission (e.g., Azadi, 2017; Saikia, 2022).

Many models have been developed, including relativistic effects to infer the main properties of the AD and the central SMBH (Abramowicz and Fragile, 2013, and references therin). The main theoretical models of ADs, ordered by increasing accretion rate, are:

1. **Advection-Dominated Accretion Flows (ADAFs):** Unlike the more common standard thin disk model, ADAFs can operate at low accretion rates. This means less material is falling into the SMBH, giving it less opportunity to release gravitational energy via friction and radiation (e.g., Narayan and Yi, 1994; Mineshige, 1996; Yi, 1999; Narayan et al., 2010). As most of the gravitational energy advected inwards with the matter and less energy is radiated away, ADAFs are much hotter and thicker than standard thin disks. ADAFs are thought to be important in explaining the behavior of low-luminosity AGN (e.g., Narayan and Yi, 1994; Narayan and McClintock, 2008; Nemmen et al., 2014; Falocco et al., 2020).

2. **Shakura-Sunyaev Model (Standard thin Disk model):** Developed by Shakura and Sunyaev in the 1970s, is the most widely used mode and assumes the disk is in local thermal equilibrium (LTE), meaning the temperature is uniform throughout any given annulus and any heat generated by friction is efficiently radiated away (e.g., Shakura and Sunyaev, 1973; Novikov and Thorne, 1973). Viscosity, generated by turbulence, transports angular momentum outwards, allowing matter to spiral inwards and release gravitational energy as heat. The disk radiates this heat efficiently, leading to a geometrically thin disk with a temperature that decreases with increasing distance from the central object. The Shakura-Sunyaev model is successful in explaining many observed features of ADs, such as their overall luminosity and spectral emission (e.g., Lu et al., 2004). However, it has limitations, particularly in situations where the disk is not efficient at radiating away heat (e.g., McClintock et al., 2006; Czerny, 2019).

3. **Slim Disks:** In cases where the accretion rate is high, the disk may not be able to radiate away heat efficiently, the disk becomes optically thin, and LTE breaks down (e.g., Abramowicz et al., 1988; Gu and Lu, 2007; Sądowski et al., 2011). This leads to a hotter, thicker disk known as a slim disk, with most of the energy advected (carried inwards) with the accreting matter (e.g., Abramowicz and Fragile, 2013; Czerny, 2019). Due to the radial advection of mass and energy, the temperature gradient is shallower than in the optically thick, geometrically thin model of Shakura and Sunyaev (1973). Slim disks are thought to be responsible for the X-ray emission from some SMBHs, at high accretion rates (e.g., Abramowicz, 2005; Miller, 2007; Straub et al., 2011).

4. **Polish Doughnut Model (Thick Disk model):** This model applies to non-LTE disks where vertical motions and radiative transfer are important. The disk is geometrically thick even at high accretion rates and has a complex temperature structure, with hot and cool regions coexisting (e.g., Qian et al., 2009; Pugliese et al., 2013). This can occur if the turbulence is highly efficient at transporting angular momentum outwards, preventing the disk from settling into a thin configuration. Polish doughnuts are thought to be relevant for highly super-Eddington accretion states, as found in some quasars and X-ray binaries (e.g., Pugliese et al., 2013; Wielgus et al., 2016).

These are the main theoretical constructs used to study ADs. The choice of which model to use depends on the accretion rate (typically normalized by the Eddington accretion rate) of the source being studied.

Despite significant progress in understanding ADs, many aspects remain a mystery. These include the exact mechanisms for transporting angular momentum outwards, the role of magnetic fields in disk dynamics and emission processes, the connection between the disk and other AGN components such as jets and coronæ, the impact of the environment on the disk's structure and evolution and the origin of the highly collimated jets observed in some AGN.

2.7 Double-peaked profiles in quasars spectra

AGN with double-peaked emission lines are an interesting class of objects, though, only a small fraction of them show double-peaked profiles in their spectra (e.g., Eracleous and Halpern, 2003; Strateva et al., 2003; Eracleous et al., 2009; Fu et al., 2023). According to Wang et al. (2005), these double-peaked lines are among the broadest optical emission lines with FWHM in some cases exceeding 15000 km s^{-1}.

Powerful radio galaxies and RL quasars with extended radio morphology have the broadest and most complex Balmer line profiles, and they are assumed to be preferred hosts of double-peaked emitters (e.g., Steiner, 1981; Antonucci, 1984). Following the classification scheme of Sulentic et al. (2002), they are more frequently found in extreme Pop. B, and, more precisely, in spectral type $B1^{++}$ (see Sect. 2.5.1). They are evolved sources with spectacular extended NLR, and a high prevalence of powerful radio jets (e.g., Marziani et al., 2013b; Ganci et al., 2019). In physical terms, sources belonging to this ST are seen at a relatively high inclination and/or have a large $M_{\rm BH}$, and very low $\lambda_{\rm E}$ (~ 0.01) (e.g., Panda et al., 2019c). Observationally, several authors proposed the double-peaked Balmer line found in the optical spectra of broad-line

radio galaxies such as 3C 390.3 (e.g., Perez et al., 1988), PKS 0235+023 (e.g., Dunlop et al., 1989), 3C 332 (e.g., Halpern, 1990), OX 169 (e.g., Stockton and Farnham, 1991), IRAS 0236.6-3101 (e.g., Colina et al., 1991), NGC 1097 (e.g., Storchi-Bergmann et al., 1993), Pictor A (e.g., Sulentic et al., 1995), M81 (e.g., Bower et al., 1996), NGC 1097 (e.g., Storchi-Bergmann et al., 2003), J153636.22+044127.0 (e.g., Chornock et al., 2010). In addition, there are some more double-peaked emitters in the work of Gezari et al. (2007); Lewis et al. (2010). The double-peaked emission is also shown in Seyfert galaxies like Akn 120 (e.g., Alloin et al., 1988), IC 4329A (e.g., Marziani et al., 1992), Arp 102B (e.g., Chen and Halpern, 1989; Halpern and Eracleous, 1999) and LINERs, NGC 4450 (e.g., Ho et al., 2000). Elitzur et al. (2004) also gave a theoretical explanation of the double-peak emission from Seyfert galaxies.

2.7.1 Models for a double-peaked profile

The origin and appearance of the observed double-peaked profile in the spectra of AGN is predicted by different models, and the proposed alternative scenarios explain with varying degrees of success. To ascertain and investigate a suitable model that provides a good description of the observed profiles and their unique kinematic signature, mainly there are four alternative scenarios suggested: A Keplerian AD model (e.g., Chen and Halpern, 1989, 1990), two separate broad-line regions as a signature of binary SMBHs (e.g., Gaskell, 1983), originate in a biconical outflow (Zheng et al., 1990) or produced by a highly anisotropic distribution of emission-line gas (e.g., Wanders et al., 1995; Goad and Wanders, 1996). Below, we will give a detailed explanation of each model.

2.7.1.1 Accretion disk as the origin of double-peaked profile

The theory that rotating ADs are responsible for the observed broad emission-line profiles in quasars is frequently put forth. However, the presence of ADs in AGN had limited and indirect observational support until binary star systems a white dwarf and a normal star companion (cataclysmic variable stars) give rise to the direct kinematic evidence. This is mainly due to the well-studied properties of such variables, which originate from the ADs (e.g., Horne, 1998; Vrielmann, 2001; Harlaftis, 2001). With this analog, there are lines of evidence about double-peaked structure that can be obtained from observations of very broad, double-peaked emission lines and identification of asymmetries and substructure in the line profiles (e.g., Popović et al., 2002; Kollatschny, 2003; Shapovalova et al., 2004). A careful consideration of the basic physical arguments tends to confirm the most likely origin of double-peaked emission lines is AD. On the converse, these double-peaked profiles provide dynamical evidence about the structure of the AD (e.g., Strateva et al., 2003; Zhang, 2011; Liu

et al., 2017). Several other observational tests combined with physical considerations also favored the AD origin over other possibilities, which can be used as the most direct dynamical evidence for the presence of ADs (e.g., Zhang, 2013; Wada et al., 2021).

ADs provide an efficient mechanism for dissipating the angular momentum of the accreting matter via viscous stresses (e.g., Shakura and Sunyaev, 1973; Dai et al., 2021). Emission from the surface of a photoionized, relativistic, Keplerian AD produces profiles of double-peaked lines with three distinctive features: the splitting of the line profile into a double-peaked structure due to rotation, the blue peak being stronger than the red peak because of relativistic beaming, and an asymmetry towards the red due to a net gravitational redshift of the entire line. Later on, Eracleous and Halpern (1994), Eracleous (1998), and Ho et al. (2000) defined a set of characteristics that distinguish them from the majority of AGN and also confirmed that in the disk profiles, there is typically a peak on the red side and a peak on the blue side of the central emission line, though in some cases the peaks are very broad and shallow. However, such a strong and broad profile will raise the question of the energy budget in the context of emission from a certain region, especially the power dissipated by viscous stresses in the line-emitting portion of the disk.

To overcome difficulties associated with the energy budget of the AD, the most commonly proposed solution for double-peaked emission from the AD that incorporates the above properties is the assumption of an elevated structure around the inner disk (e.g., Chen and Halpern, 1989; Eracleous and Halpern, 2003; Ricci and Steiner, 2019). According to the model of Chen and Halpern (e.g., 1989), the emission is assumed to be driven by illumination of the outer part of the disk at a radius ξ_2 from an elevated, thick, and vertically extended inner part of the AD at a radius ξ_1 (see Fig. 2.12) which is capable of powering the line emission. This proposed vertical and elevated structure is assumed to be an ion-supported torus, and it photoionizes the geometrically thin outer disk to produce the observed profiles. This ion torus emits more energy than the standard, geometrically thin, optically thick AD and solves the energy budget problem of the disk.

To fit the double-peaked line profiles observed in the spectra of a quasar, Chen and Halpern (1989, equation 7) can be applied. This relation indicates the integral expression for the line profile (line flux, written here as equation 2.1) of an optically thick disk that can be applied for a model fitting. According to the model of Chen and Halpern (1989) and Eq. 2.1, there are five crucial and freely varying parameters; the two line emitting portions ξ_1 and ξ_2, the inclination angle (θ), broadening parameter (σ) and the line emissivity index (q). The line-emitting portion of the disk is assumed to be circular with disk

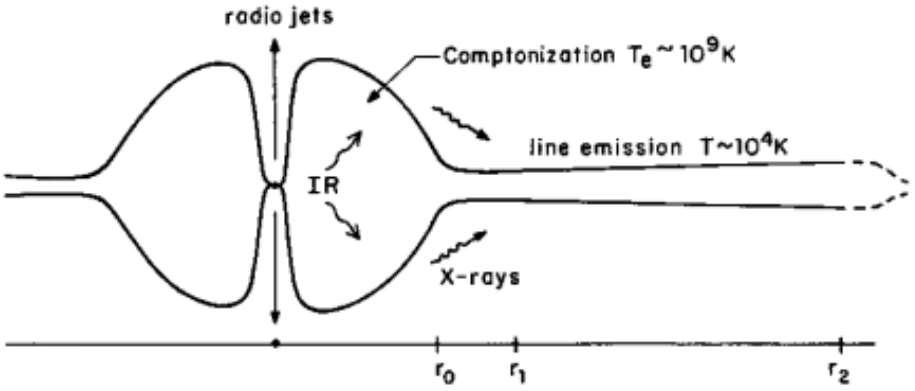

Figure 2.12: Accretion disk structure to explain how the disk's geometry contributes to the observed emission lines according to Chen and Halpern (1989).

radius ξ in units of the gravitational radius $r_g = GM_{BH}/c^2$ where $M_{\rm BH}$ is the mass of the black hole and is located between an inner and outer radii ξ_1 and ξ_2, respectively. This model also assumes the line originates from the surface whose axis is inclined by an angle θ relative to the line of sight, between the two radii. Electron scattering or turbulent motion is assumed to be the cause of line broadening and is represented by a Gaussian profile of velocity dispersion σ expressed in km s^{-1} in the rest frame of the emitter. An axisymmetric emissivity that varies continuously without boundaries is represented with emissivity (Q) as a function of the radius of the disk and a dimensionless power-law index q as $Q = \xi^{-q}$.

$$F_x = \frac{2\varepsilon_0 M^2 cosi}{4\pi d^2} \frac{\nu_0}{(2\pi)^{1/2}\sigma} \int_{\xi_1}^{\xi_2} \int_{-\pi/2}^{\pi/2} d\xi d\varphi' exp\left[-\frac{(1+X-D)^2 \nu_0^2}{2\sigma^2 D^2}\right] D^3 \xi^{1-q} g(D) \tag{2.1}$$

Where

$$g(d) = 1 + \xi^{-1}\left\{\frac{2D^2}{D^2 cos^2 i + \xi[D-(1-3/\xi)^{1/2}]^2} - 1\right\} \tag{2.2}$$

From the theoretical predictions and study on double-peaked profile sources, a conclusion was made based on the fact that the disks emit predominantly LILs such as Balmer lines, MgIIλ2800 and FeII. They are much more convenient for the study of double-peaked profiles because of photoionization and electron scattering in geometrically thin ADs (e.g., Chen and Halpern, 1989; Strateva et al., 2006; Eracleous et al., 2009). Nonetheless, open questions concerning the disk emission in this class of rare AGN remain. UV spectroscopy of double-peaked emitters with the HST did not provide unambiguous evidence for an AD origin (e.g., Eracleous et al., 2004; Zhang, 2011). HILs (e.g., $L_{y\alpha}$ and

CIVλ1549) may not be produced there at all and frequently lack double-peaked profiles since UV lines may find it difficult to escape from the dense AD, and they will be suppressed there (e.g., Eracleous et al., 2004, 2009).

2.7.1.2 Binary black hole model

Even though AD emission is the best-developed model for the origin of double-peaked emission lines in radio-loud AGN, it is not the only way of explaining the observed profile. The second proposed scenario as an explanation for the observed double-peaked profile in the Balmer lines is attributed to emission from a twin BLR associated with a supermassive binary black hole. This scenario was proposed for AGN by Gaskell (1983); Peterson et al. (1987) to explain the displaced broad Balmer line peaks of objects such as 3C 227 (e.g., Prieto and Zhao, 1997) for which it may still provide the most viable interpretation. The SMBH binary can form as a result of the merging of two galaxies, each with its nuclear black hole, and the resulting line profiles will have double peaks or single but displaced peaks if only one of the two black holes has an associated BLR (Begelman and Meier, 1982). In the specific case of the double-peaked lines of OX 169, Stockton and Farnham (1991) concluded that a binary black hole resulting from a recent merger is the most plausible interpretation. Under this assumption, each of the black holes has an associated broad-line region and the orbital motion of the binary system will produce Doppler shifts in the emission lines that result in the observed double-peaked profile (e.g., Peterson et al., 1987; Chornock et al., 2010). In addition, the spectroscopic properties of the double-peaked emitters should not differ from the wide group of AGN and the two peaks of a double-peaked line need to drift in opposite directions due to the orbital motion of the binary.

The binary black hole scenario can be tested by looking at the variations in the locations of the two displaced peaks, or the absence of this variation to constrain the mass of the hypothesized supermassive binary. The lower limit on the total mass of the binary $M = M_1 + M_2$ can be estimated from the observed spectra using Kepler's third law. We utilized the equations from Eracleous et al. (1997, their equation 3) to estimate the lower limits on M that correspond to the minimal period and projected orbital velocities:

$$M > 4.7 \times 10^8 (1+q)^3 \left(\frac{P}{100\,\mathrm{yr}}\right) \left(\frac{v_1 \sin i}{5000\,\mathrm{km\,s^{-1}}}\right)^3 M_\odot, \tag{2.3}$$

where $q = M_1/M_2 \geq 1$ is the ratio between the two black hole masses, M_1 with orbital velocity v_1, M_2 with orbital velocity v_2 and P is the orbital period. The v_1 corresponds to the radial velocity of the blue peak and v_1 with the red peak.

The expected orbital periods for such a system can range from decades to centuries, and the signature of orbital motion can be detected in spectra spanning one or two decades. Halpern and Filippenko (1988) and Halpern and Filippenko (1992) searched for radial velocity variations in the displaced peaks of Arp 102B and 3C 332, using spectra spanning a decade, but did not find any variation. A more extensive study of Arp 102B, 3C 390.3, and 3C 332 also did not find any evidence for the orbital motion and this is also in contradiction with a suggestive variability trend found by Gaskell (1996) in 3C 390.3 which lasted only until 1988 (e.g., Burenkov et al., 2001; Sergeev et al., 2002). The lack of evidence for orbital motion yielded lower limits on the binary masses of $10^{10} - 10^{11} M_{\odot}$. This conflicts with several other observations and theories, leading to the rejection of this scenario as a general explanation for double-peaked emission lines (see Eracleous et al., 1997, for more discussion).

2.7.1.3 Bipolar or biconical outflows

The third scenario proposed for the explanation is emission from the oppositely directed sides of a bipolar or biconical outflow. In the process of accreting matter by the SMBH activity, powerful gas and dust jets can be launched perpendicular to the AD, forming a bipolar outflow with a conical shape and extending outwards. The double-peaked lines originate in pairs of these oppositely directed cones of outflowing gas that are accelerated by the passage of the relativistic radio jets through the line emitting region and interaction with the gas immediately around the central engine (e.g., Norman and Miley, 1984; Zheng et al., 1990; Sulentic et al., 1995). With the combined effect of these Doppler shifts from the approaching and receding gas clouds, a double-peaked profile will be observed and the separation between the two peaks mainly depends on the velocity of the outflowing gas. Evidence of line broadening after a flare-like event has been found, and it can be interpreted as an unresolved bipolar outflow (e.g., León-Tavares et al., 2013; Chavushyan et al., 2020).

This model was applied to the double-peaked Hβ lines of 3C 390.3 and Pictor A (e.g., Zheng et al., 1991; Sulentic et al., 1995). The conclusions of these studies and the fact that most double-peaked emitters are associated with double-lobed radio sources argue against bipolar outflows. Further, due to the dramatic difference between the observed Hβ profiles of Arp 102B (Halpern et al., 1996), the reverberation mapping of 3C 390.3, and the need for the outflow to be viewed nearly at right angles, bipolar outflow models for double-peaked emission lines are unlikely. Since the model is strongly dependent on outflows, and the physical understanding of the formation and collimation of outflows is still developing a purely kinematic approach, depending on the parametric description of the geometry, structure, and velocity field of the outflow-

ing gas, the determination of the model parameters will be in question.

2.7.1.4 Anisotropic source of ionizing radiation

The fourth scenario is emission from a spherically symmetric BLR illuminated by an anisotropic source of ionizing radiation. It was discussed in its general form by (e.g., Korista et al., 1995; Goad and Wanders, 1996). An isotropic source emits radiation equally in all directions; the gas throughout the BLR would be ionized to a similar degree, regardless of location. The broad-line region is assumed to consist of numerous clouds in randomly inclined Keplerian orbits occupying a thick, spherical shell. In the specific picture discussed by Goad and Wanders (1996), the isotropic emission was described by two conical beams that could be superposed on anisotropic background illumination. The BLR is assumed to incorporate clouds that are randomly inclined with Keplerian orbits, and these randomly inclined clouds are then photoionized by a continuum central source, seemingly an AD that emits anisotropically. According to this model, double-peaked emission lines can be produced for a range of orientations of the ionizing beam relative to the line of sight. The resulting emission line profiles appear double-peaked for specific combinations of opening angle and orientation of the observer. By the geometry it invokes, this scenario requires observation of either double-peaked Balmer lines or a weak non-stellar continuum in an object. In addition, this model doesn't give a clue as to why double-peaked profiles are associated with radio-loud AGN.

Leaning on previous works that have been done on sources that show a double-peaked profile, the alternative scenarios mentioned above are much less appealing than disk models. This is due to the lack of either direct observational support, unable to explain all the unusual properties, or the physical foundation is in question as explained in the works of (e.g., Eracleous and Halpern, 2003; Eracleous et al., 2009).

Chapter 3

Instrumentation and data sources

In this chapter, we briefly describe the data used in the thesis. Since most of our work is based on observations made using the Calar Alto 3.5-meter telescope, we first briefly describe the basics of the Calar Alto observatory, its 3.5-meter telescope, and the instruments used. Then, we describe the new spectroscopic data obtained from it and other data from astronomical archives, which together were used to achieve the objectives of this thesis. This chapter is organized into four major sections.

3.1 Observations, data, and data acquisition

3.1.1 The Calar Alto observatory

Studying and understanding the enigmatic nature of AGN or quasars requires a meticulous combination of cutting-edge instrumentation in data acquisition across the EMS, data processing, and rigorous analysis. We proposed observations with a high-resolution instrument with broad wavelength coverage to achieve our scientific objectives. The exceptional resolving power will enable us to analyze the faint emission lines embedded within the quasar spectra, extracting crucial details and characterizing their physical properties and environments. The wide wavelength coverage will help encompass both the optical and near-UV regimes with a single instrument, to capture main emission lines that harbor valuable information about quasars. To study the nature of extremely powerful RL quasars, based on our scientific objectives (see Sect. 1.3), this work uses the 3.5-meter telescope at Calar Alto Observatory (CAHA) in conjunction with its multiple state-of-the-art spectrographs.

[1] https://www.iaa.csic.es/meetings/public-surveys

Figure 3.1: View of the Calar Alto observatory with the five telescopes [Image credit: CAHA][1]

The Calar Alto observatory, which boasts exceptional observing conditions and attracts astronomers from all over the world, is named the "German-Spanish Astronomical Centre" (in Spanish, Centro Astronómico Hispano-Alemán (CAHA) also known as the Centro Astronómico Hispano en Andalucía (CAHA) is an astronomical observatory located in Almería province in Spain on Calar Alto, a 2,168-meter-high mountain in the Sierra de Los Filabres range, the largest mountain range in Almería Province, Andalusia, Spain. It is the largest astronomical observatory in continental Europe and was founded in 1973 following an agreement between the German and Spanish governments (e.g., Gredel, 2001). The Calar Alto observatory has two main properties: a well-characterized and excellent astronomical site for observations (including spectroscopy) with an appropriate location in continental Europe, and outstanding logistics for communication. Its location provides clear skies and low light pollution. Beyond its location and clear skies, specific properties like seeing, wind speed and other environmental factors further contribute to its suitability as an ideal site for diverse astronomical observations and research. CAHA is a home for large and versatile telescopes, with different apertures and optical systems, as can be seen in Figure 3.1: the largest 3.5-meter telescope, multipurpose 2.2-meter telescope, 1.5-meter telescope, 1.23-meter telescope, and the 0.9-meter telescope (e.g., Barrado et al., 2011). In addition, CAHA is equipped with a wide range of state-

of-the-art astronomical instruments, including spectrographs, different CCD cameras for photometric observations, and polarimeters. These instruments allow astronomers to make a detailed and broad range of observations, from objects in the solar system to distant quasars.

Several factors contribute to a prime location for ground-based astronomy, including night sky brightness across optical and near-infrared wavelengths, the frequency of clear nights, atmospheric seeing conditions, transparency, and photometric stability (e.g., Sánchez et al., 2007, 2008; Barrado et al., 2011). The Calar Alto Observatory generally experiences clearer skies in winter, with a typical V-band extinction of around 0.15 magnitude and minimal variation with a wider range of extinction values during the summer, likely due to a rise in dust particles in the atmosphere that causes aerosol extinction. Its exceptional seeing with a median value of 0.9 arcseconds, which contributes to high-resolution observations, is attributed to its high altitude, arid climate, and remote location with minimal light pollution (e.g., Sánchez et al., 2007; Barrado et al., 2011). The low wind speed that CAHA experiences, with average speeds of around 5 m/s, significantly lower than many other astronomical observatories, allows for stable telescope operation and minimizes image blurring caused by atmospheric turbulence. The average annual temperature at CAHA is around $10^{o}C$, with minimal temperature fluctuations throughout the night and this stable temperature range minimizes telescope dome effects and ensures consistent instrument performance (e.g., Sánchez et al., 2007). The humidity levels are generally low (around 50%), contributing to excellent seeing conditions and minimizing potential issues with instrument dew formation. Such stable temperature and humidity minimize the instrumental calibrations needed and ensure consistent data quality. Regarding light pollution, CAHA's remote location significantly reduces artificial light interference, though it is not in an entirely light-pollution-free zone. The combination of these favorable properties allows CAHA to support a wide range of astronomical observations.

3.1.1.1 The Calar Alto 3.5-meter telescope

Occupying a prominent position at the CAHA observatory, the largest telescope has a 3.5-meter aperture, shown in Figure 3.2, resulting in a good light-gathering power. The robust equatorial fork mount provides smooth tracking of celestial objects across the night sky, and the versatile 12.195-meter (primary focus) focal length offers multiple configurations for a wide range of instruments. It is a reflecting telescope of Cassegrain type with a Ritchey-Chrétien design, which is common among large telescopes due to its ability to minimize optical aberrations over a wide field of view. The telescope and its instruments incorporate cutting-edge technology, including active optics that constantly adjust

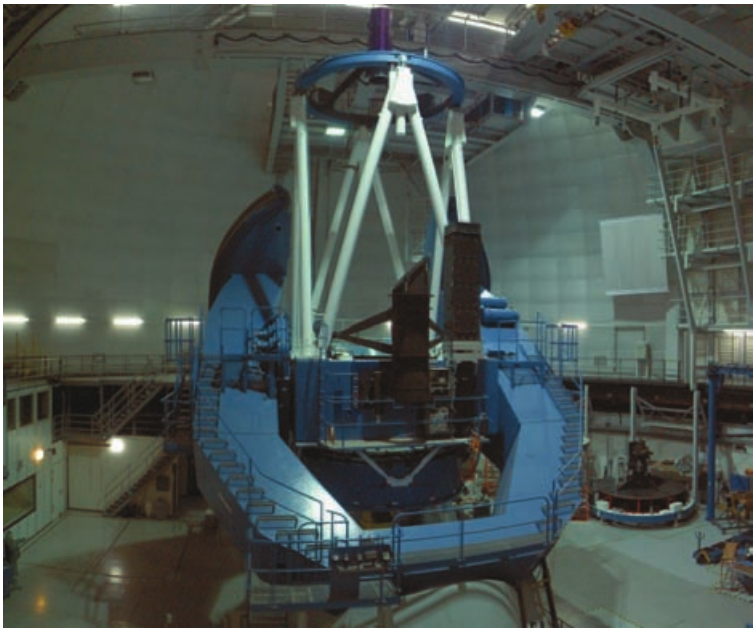

Figure 3.2: The 3.5-meter telescope on Calar Alto and its 43-meter tall dome [Image credit: Max Planck Institute for Astronomy Annual Report]**.**

the telescope's mirror to counteract distortions caused by wind and temperature variations and sensitive electronic light sensors (CCD detectors) (e.g., Hippler et al., 2000). The telescope is used for optical and NIR observations and a wide range of astronomical studies, including exoplanet search, stellar, galactic and extragalactic astronomy, and cosmology. It is equipped with different instruments, spectrographs and CCD cameras, enabling different types of observations (e.g., imaging, spectroscopy, photometry), including the Cassegrain Twin Spectrograph (TWIN) used in this work and described below. The other instruments currently available include[2]: CARMENES (Calar Alto high-Resolution search for M dwarfs with Exoearths with Near-infrared and optical Échelle Spectrographs), Omega2000 imager in the NIR, PMAS (Potsdam MultiAperture Spectrophotometer integral field unit), LAICA (Large Area Imager for Calar Alto), and MOSCA (Multi-Object Spectrograph for Calar Alto).

3.1.1.2 Scientific instrumentation: TWIN spectrograph

A large telescope will become a powerful discovery tool only in combination with an efficient instrument. The Cassegrain Twin Spectrograph (TWIN) is a long-slit spectrograph that has been designed for spectroscopic observations in the wavelength range from 3200Å to 11000Å (e.g., Pfeiffer et al., 1998). It includes two separate spectroscopic channels, the "blue" and "red" arms, behind the common entrance slit aperture, as can be seen in Figure 3.3. The light

[2] http://www.caha.es/observing-mainmenu-148/telescopes-aamp-instruments-mainmenu-155

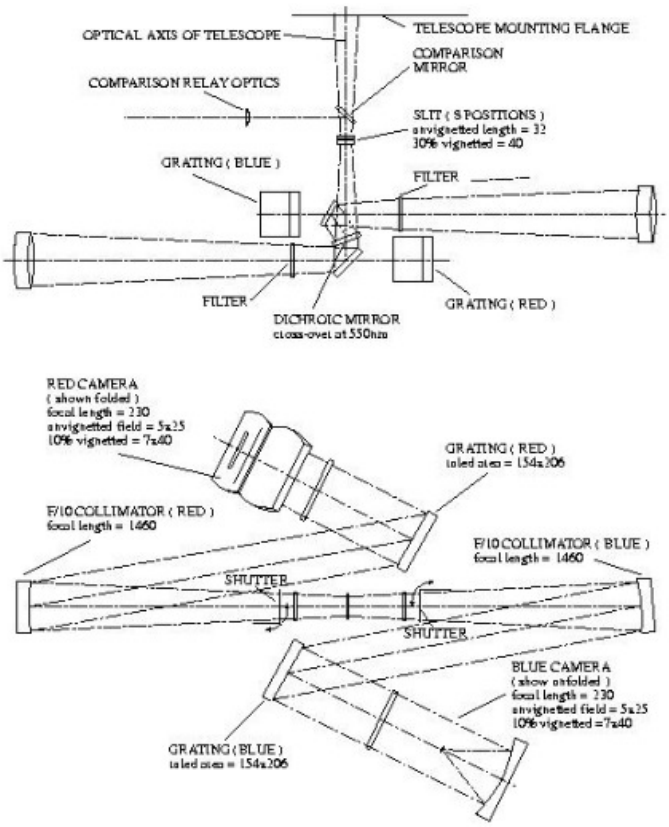

Figure 3.3: Optical diagram of the TWIN [Image credit: Cassegrain TWIN Spectrograph 3.5 m Telescope Calar Alto User´s Manual].

from the slit is divided into two beams using a dichroic mirror, which acts like a beam splitter, strategically dividing the incoming light into two separate paths based on their wavelengths. It is designed to reflect a specific range of wavelengths (typically the UV and optical, or "blue" region) while allowing other wavelengths (usually visible and NIR, or "red" region) to pass through to create two distinct light paths. The first is reflected light (blue path), which contains the shorter "blue" wavelengths and is directed towards a dedicated detector, often paired with a specific grism (a diffraction grating) labeled like "#T13" in this case. The grism disperses this blue light into its constituent colors, allowing the analysis of the object's properties in the UV and optical spectrums. The second is transmitted light (the red path), which contains the longer red wavelengths and passes straight through the dichroic mirror. It is then directed towards a separate detector, potentially paired with a different grism labeled, like "#T11". This grism disperses the red light, enabling analysis of the object's visible and NIR spectra. This configuration using a dichroic mirror allows the TWIN spectrograph to achieve efficiency by splitting the light and analyzing both regions simultaneously, effectively doubling the observing time and obtaining complementary data from both the blue and red, providing a more comprehensive picture of the celestial objects.

The blue arm captures light from the UV and optical regions, in the wavelength range from 3300Å to 5500Å, which makes it ideal for studying objects that emit strongly in the UV, such as hot stars and AGN, as it is well-suited for detecting faint UV emission lines. This translates to several key advantages for studying quasars, as their energetic processes within AGN produce intense UV radiation, which the blue arm can dissect to understand their structure and how they are triggered. In contrast, the red arm handles longer wavelengths, from about 5500 to 10000 Å, suited for studying cooler stars, redshifted objects, and emission lines in the optical red and NIR parts of the spectrum. Together, these arms provide a broad spectral range, enhancing the versatility of the instrument for various astronomical studies.

3.1.2 TWIN spectroscopic observations

Driven by the curiosity to answer whether the RL quasars are fundamentally different from the majority of RQ quasars or not, what are the similarities and differences between them and their broad emission line regions, and the contribution of the AD to the broad emission lines, we observed a sample of RL quasars using the 3.5-meter CAHA telescope and its TWIN spectrograph. This spectrograph was selected for our observations due to its high resolution and wide wavelength coverage, as discussed in Sect. 3.1.1.1. In addition, as the best clues to explain the RQ - RL dichotomy lies in the optical/UV spectra and many of the brightest RL quasars with extensive radio coverage have a few published optical spectra with S/N high enough to permit a detailed study, the data obtained by using this state-of-the-art instrument are fundamental.

Our primary goal was to quantify broad emission line differences between RL and RQ quasars by using the 4DE1 parameter space and its MS, to check the effect of powerful radio ejection on the low-ionization broad emission lines and address whether the AD can account for the double-peaked profiles observed in the Balmer lines (Hβ, Hα), near-UV (MgIIλ2800), and high-ionization UV lines (CIVλ1549, CIII]λ1909). For the development of this thesis, in addition to the new spectroscopic data obtained from Calar Alto, we used additional radio, optical, and UV data from astronomical archives for a better characterization of the sources. Details regarding the observing strategy, data acquisition, exposure times, and data reduction procedures of TWIN data are detailed below. The details of the archival data are provided in Section 3.4. This combined approach allowed us to achieve the objectives mentioned above.

3.1.2.1 Sample selection

This PhD thesis is developed within the 4DE1 formalism (discussed in Sect. 2.5.1), as mentioned above. It focuses on extreme RL type I quasars, as they can be unambiguously identified based on the presence of a broad component in the Balmer emission lines (mainly in Hβ), near-UV (MgIIλ2800), or in HILs like CIVλ1549 in the UV, when available. For this, while selecting the sample, Kellermann factor (R_K) (see Table 3.3), redshift range for concomitant coverage of the optical and near-UV lines, and a high S/N ratio were considered. Spectra of RL quasars in the optical and near-UV brighter than $m_v \approx 19$ (and $z < 1.0$) that can easily be observed from Calar Alto were selected from the 13^{th} edition of Véron-Cetty and Véron (2010) and were screened based on CIVλ1549 observations archived in the Mikulski Archive for Space Telescopes (MAST) from the Hubble Space Telescope (HST)[3]. With this notion, to achieve the objectives of this study, we selected 12 RL quasars, listed in Table 3.1, based on their strong radio emission that satisfies a criterion of extreme radio loudness, with $R_{\rm K}$ exceeding 10^3 (see Table 3.3, Col. 7). Such extremely powerful jetted sources permit a detailed study of the effects of powerful radio ejections on the LILs. The 12 sources are optically bright, with $\log L_{Bol}$ in the range of 44.9 to 46.7 [ergs s^{-1}], and were selected in a redshift range $0.35 \lesssim z \lesssim 1$ (Véron-Cetty and Véron, 2010) that makes possible the coverage of Hβ, MgII, FeII, and their adjacent spectral regions employed for the underlying continuum definition. Such observations provide consistent information, as observed spectra at different times may suffer a significant continuum variability. Our high S/N spectra with spectral range 3500 - 10000Å provide an extended view of the quasar continuum in each spectral region and allow us to make accurate measurements of emission line parameters such as the intensity of optical and UV FeII features. High S/N spectra are crucial in the study of quasars, as low S/N spectra can give the impression that all quasars are spectroscopically similar (Zamfir et al., 2008), in contrast to the study of 4DE1 parameter space that led to the concept of two populations of quasars (see Sect. 2.5.1) that show important spectroscopic differences (e.g., Sulentic et al., 2008).

There are not so many observations of RL quasars with $R_{\rm K} \gtrsim 10^3$, and therefore the uniqueness of this study rests on the selection of extremely powerful jetted sources. In addition, in our sample, all sources are not only with $\log R_{\rm K} \gtrsim 3$, but 7 of them have $\log R_{\rm K} \gtrsim 4$.

3.1.2.2 Near-UV and optical observations

The TWIN spectrograph, used in our observations, is optimized to cover a wavelength range from about 3500Å to 11000Å, dividing the light from the slit

[3]HST-https://archive.stsci.edu/missions-and-data/hst

into two channels (blue and red) by a dichroic mirror, as mentioned above. We selected the beam splitter at 5500Å and gratings T13 and T11, for the blue and the red channels, respectively, to obtain simultaneously the spectra corresponding to the MgII and Hβ regions at the redshift of the objects (see Table 3.1 and 3.2, Col. 4). T13 grating provides a spectral coverage from 3500Å to 5500Å with a reciprocal dispersion of 2.14Å/pixel, meanwhile, T11 grating covers the range from 5500Å to 11000Å with a spectral dispersion of 2.41Å/pixel. The observations were obtained with a slit width of 1.2 arcseconds and oriented at the parallactic angle to minimize the effects of atmospheric differential refraction in the spectra.

To achieve our research objectives, the above-mentioned observational criteria, and observational setups, the target observations were separated into two different phases:

- **Phase I:** Long-slit optical spectroscopic observations were obtained on two observing nights, between October 22 and 23, 2012. This observing run resulted in 13 extreme RL sources with high-quality spectra (with S/N of $\approx$ 50) in the continuum near Hβ and Hα lines, when available. One of the quasars (3C 57) was analysed in (Sulentic et al., 2015) and not considered in this study. The remaining 12 sources were considered for this PhD work, together with archival sources used as a comparison and complementary data (see Sect. 3.4). For each target, we obtained three individual exposures with a total exposure time of 3600 per object for seven sources and 2700 per object for five sources (see Table 3.1). This observation strategy allowed us to mitigate the effects of cosmic rays by combining multiple exposures during the data reduction. Among the 12 extreme jetted RL quasars, the quasar 3C 47 is the one found to possess a double-peaked broad emission line profile, plus three spectacular emission lines corresponding to Hβ and Hα in the red arm, as well as MgII in the blue arm of the spectrograph. Due to its unique nature, it was singled out for the more detailed analysis presented in Chapter 6. The remaining 11 sources have been analysed in Chapter 5.

- **Phase II:** Long-slit optical spectroscopic observations of an additional 25 sources with redshift $z \leq 1$, excellent S/N ratio, and whose spectra covering the region of CIVλ1549 are already available in the HST archive. These additional observations were made to study the effect of orientation since the properties of RL quasars are orientation-dependent. In this phase, we needed a sufficiently large sample of RL sources to facilitate the separation of the effects of orientation. Observations were obtained on the nights of January 7 – 9 and February 5 – 6 with the same arrangements as in **phase** I.

Tables 3.1 and 3.2 summarize the main properties of our observations in 2012 for 12 sources, and in 2014 for 25 sources observed during five different nights. The tables report the quasar identification (Col. 1), the equatorial coordinates at J2000 (Cols, 2 and 3), median redshift estimated for each quasar as explained in Sect. 3.3 (Col. 4), the apparent and absolute magnitudes taken from Véron-Cetty and Véron (2010) (Cols. 5 and 6, respectively) from where we also took the initial redshift for the sample selection. In addition, the tables include the date of observation (Col. 7), total exposure time (Col. 8), air mass (Col. 9), and the estimated S/N ratio for the sources observed in the first phase (Col. 10).

During the observations, standard spectroscopic practices were meticulously followed to ensure the quality of the data. This process included acquiring spectra from calibration stars for flux calibration and using standard arc lamps for wavelength calibration, taking care to do this both before and after each science observation to maintain precision. Bias frames, taken without exposure time, were used to eliminate unwanted noise from the electrostatic charge that accumulates in the sensor. Dome flat frames were also routinely obtained to correct for variations in pixel sensitivity, ensuring that light intensity measurements were consistent across the detector. The science frames were then divided by the flats, after bias subtraction, to ensure the sources light intensity was measured uniformly. The raw data, captured in FITS format, consisted of two-dimensional spectra for each quasar observation, providing a detailed and calibrated dataset for analysis.

Once processed, the one-dimensional spectra for each quasar from **phase I** were further analyzed, their results discussed, and two papers, Mengistue et al. (2023) and Mengistue Terefe et al. (2024) were published in a reputable journal. All the detailed results and related discussions from these two separate works are presented in Chapters 5 and 6. The data from **phase II** observations and preliminary studies are presented in Chapter 7.

3.2 Data reduction

In this thesis, data reduction was carried out in a standard way using IRAF[4] (Tody, 1986). Those sources observed in phase I and used for the two publications as an outcome of this thesis work have been already reduced by the team, following the standard data reduction procedure. This includes bias and overscan correction and flat-field correction with a normalized flat-field obtained from a

[4]**IRAF** is the Image Reduction and Analysis Facility, a general-purpose software system for the reduction and analysis of astronomical data, `iraf.net`

Table 3.1: Summary of the properties of the phase I sample and observations with the Cassegrain TWIN spectrograph in 2012.

Object	Coordinates		z	m^a	M_B^a	Date of observation	Total exp. time (s)	Airmass	S/N
	RA (2000)	Dec (2000)							
(1)	(2)	(3)	(4)	(5)	(6)	(7)	(8)	(9)	(10)
PHL 923	00 59 05.6	+00 06 51	0.7183	17.9	-24.6	22-10-2012	3600	1.26	18
B2 0110+29	01 13 24.2	+29 58 16	0.3625	17.0	-24.2	23-10-2012	2700	1.08	12
3C 37	01 18 18.5	+02 58 06	0.6667	18.8	-23.7	23-10-2012	3600	1.29	20
3C 47[b]	01 36 24.41	+20 57 27	0.4248	18.1	-23.3	22-10-2012	3600	1.07	60
PKS 0230-051	02 33 22.1	-04 55 08	0.7807	17.0	-25.9	23-10-2012	3600	1.47	43
3C 94	03 52 30.6	-07 11 02	0.9648	16.7	-26.4	23-10-2012	2700	1.48	34
PKS 0420-01	04 23 15.8	-01 20 33	0.9136	17.0	-25.9	22-10-2012	3600	1.30	38
3C 179	07 28 10.8	+67 48 47	0.8416	18.4	-24.9	23-10-2012	3600	1.17	19
3C 380	18 29 31.8	+48 44 46	0.6919	16.8	-25.5	23-10-2012	2700	1.12	40
S5 1856+73	18 54 57.4	+73 51 19	0.4604	16.8	-25.0	23-10-2012	3600	1.35	68
PKS 2208-137	22 11 24.1	-13 28 10	0.3912	17.0	-24.4	23-10-2012	2700	1.62	18
PKS 2344+09	23 46 37.0	+09 30 45	0.6724	15.9	-26.3	22-10-2012	3600	1.16	74

Notes: Col. 2 is in units of hours, minutes, and seconds, while Col. 3 is in units of degrees, minutes, and seconds. [(a)] From the catalog of quasars and AGN (Véron-Cetty and Véron, 2010, 13th Ed.). Col. 5 corresponds to the apparent magnitude, while Col. 6 is the absolute magnitude in the B-band. [b] This source shows a double-peaked profile and is considered for a separate analysis as detailed in Chapter 6.

median combination of the flats obtained for each spectral region (blue and red) separately. Wavelength calibration was obtained using the standard lamps (He-Ar and Fe-Ne) exposures and standard IRAF tasks, such as `identify`, `reidentify`, `fitcoor` and `transform`. The `apall` task in IRAF was used for object extraction and background subtraction. Instrumental response and absolute flux calibration were obtained each night through observations carried out with the same instrumental setup of the two spectrophotometric standard stars, G191B2B and BD+28d4211. They were also used to remove telluric bands observed in the red channel. The final calibrated rest-frame spectra for the 12 sources observed in phase I, once the blue (MgII region) and red (Hβ region) spectra were combined for each object, are shown in Figs. 3.4, 3.5, 3.6, and 3.7. The detailed data reduction process performed for those sources observed in phase II is given in Chapter 7.

3.3 Redshift determination

Due to the Universe's expansion, light emitted from celestial objects experiences a redshift, stretching their wavelength and causing their emission lines to appear shifted towards the red end of the spectrum compared to their intrinsic rest-frame values. Empirically, a powerful method for determining the redshift of quasars relies on prominent emission line analysis in their rest-frame spectra. However, achieving accurate measurements depends on lines with a high S/N

Table 3.2: Summary of the properties of the phase II sample and observations with the Cassegrain TWIN spectrograph in 2014.

Object	Coordinates		z	m^a	M_B^a	Date of	Total exp.	Airmass
	RA (2000)	Dec (2000)				observation	time (s)	
(1)	(2)	(3)	(4)	(5)	(6)	(7)	(8)	(9)
First night								
PKS 0214+10	02 17 07.7	+11 04 10.1	0.4080	16.5	-24.9	07-01-2014	3600.0	1.11
3C 95	03 51 28.5	-14 29 08.7	0.6163	16.2	-25.8	07-01-2014	3600.0	1.62
PKS 0405-12	04 07 48.4	-12 11 36.7	0.5726	14.9	-27.1	07-01-2014	2700.0	1.56
B2 0742+31	07 45 41.7	+31 42 56.6	0.4611	15.8	-25.6	07-01-2014	3600.0	1.01
3C 215	09 06 31.9	+16 46 11.9	0.4121	18.3	-22.9	07-01-2014	4500.0	1.07
B2 0923+39	09 27 03.0	+39 02 20.9	0.6953	17.0	-25.4	07-01-2014	3600.0	1.40
PKS 1103-006	11 06 31.8	-00 52 52.5	0.4233	16.5	-25.1	07-01-2014	3600.0	1.28
PG 1201+436	12 04 24.0	+43 30 56.9	0.6626	16.4	-25.9	07-01-2014	3600.0	1.01
Second night								
[HB89]0042+101	00 44 58.7	+10 26 53.7	0.5830	...	...	08-01-2014	4500.0	1.15
3C 110	04 17 16.7	-05 53 45.0	0.7752	15.9	-26.6	08-01-2014	3600.0	1.43
PKS 0420-01	04 23 15.8	-01 20 33.1	0.9160	17.0	-25.9	08-01-2014	3600.0	1.28
3C 207.0	08 40 47.5	+13 12 23.6	0.6808	18.2	-24.0	08-01-2014	4500.0	1.24
3C 254	11 14 38.7	+40 37 20.5	0.7366	17.4	-25.1	08-01-2014	3600.0	1.17
3C 263	11 39 57.0	+65 47 49.4	0.6460	16.3	-25.9	08-01-2014	3000.0	1.20
3C 286	13 31 08.3	+30 30 32.9	0.8499	17.3	-25.7	08-01-2014	4500.0	1.06
Third night								
PKS 0003+15	00 05 59.2	+16 09 49.0	0.45099	16.4	-25.1	09-01-2014	3000.0	1.15
HB890042+101	00 44 58.7	+10 26 53.7	0.58300	...	...	09-01-2014	4500.0	1.26
3C 48	01 37 41.3	+33 09 35.1	0.36900	16.2	-24.6	09-01-2014	3600.0	1.30
PKS 0420-01	04 23 15.8	-01 20 33.1	0.91600	17.0	-25.9	09-01-2014	3600.0	1.30
OJ 601	08 04 25.0	+60 40 08.1	0.68900	18.5	-24.2	09-01-2014	4500.0	1.13
Fourth night								
4C 63.15	11 58 39.9	+62 54 28.0	0.59244	16.8	-25.2	05-02-2014	3600.0	1.22
3C 281	13 07 53.9	+06 42 13.9	0.60200	17.0	-25.1	05-02-2014	4500.0	1.16
SDSS J13053+5116	13 5 22.8	51 16 39 O	0.785	17.4	-25.3	05-02-2014	4500	1.26
Fifth night								
3C 175	07 13 02.4	+11 46 14.7	0.7700	16.6	-25.8	06-02-2014	3000.0	1.20
OJ 601	08 04 25.0	+60 40 08.1	0.6890	18.5	-24.2	06-02-2014	4500.0	1.32

Note: Col. 2 is in units of hours, minutes, and seconds, while Col. 3 is in units of degrees, minutes, and seconds. $^{(a)}$ From the catalog of quasars and AGN (Véron-Cetty and Véron, 2010, 13$^{\text{th}}$ Ed.). Col. 5 corresponds to the apparent magnitude, while Col. 6 is the absolute magnitude in the B-band.

ratio in spectra, as it ensures the precise identification and measurement of the emission line's center, whose shape is like a Gaussian profile. Optical and UV lines do not all show the same profile, and therefore significant differences can be found in quasar redshifts measured on different lines of the same spectra, as emission line shifts relative to laboratory wavelengths are seen for many of the ionic species.

We determined the redshift of the quasars, following Bon et al. (2020), by measuring the rest-frame vacuum wavelengths of individual narrow emission lines, in particular [OII]λ3727Å, Hδ, Hγ, Hβ, and [OIII]$\lambda\lambda$4959,5007ÅÅ that are available in our rest-frame spectra. For that, we used the IRAF task `splot`, taking as reference vacuum wavelengths the ones from (e.g., Vanden Berk et al., 2001). We took the median value of the redshifts obtained from the different emission lines, as each of them may have an internal line shift. By compar-

ing the measured wavelengths of these lines with the known rest-frame vacuum wavelengths, we calculated the redshift (z) of the quasar using the standard equation: $z = (\lambda_{observed} - \lambda_{rest})/\lambda_{rest}$. This method offers a robust and direct determination of redshift. We determined the redshifts with a range in standard deviation, or typical root-mean-square (rms), of $0.0003 - 0.0009$, and only for the source PKS 2344+09 the standard deviation is 0.001. The lines obtained from the spectra by the newly determined redshifts have been moved to their rest-frame and are in agreement with the previously measured values by Véron-Cetty and Véron (2010). The list of the median redshifts determined for phase I sources is shown in Table 3.1 (Col. 5) which are in the range of 0.3625 for B2 0110+29 to 0.9648 for the 3C 94.

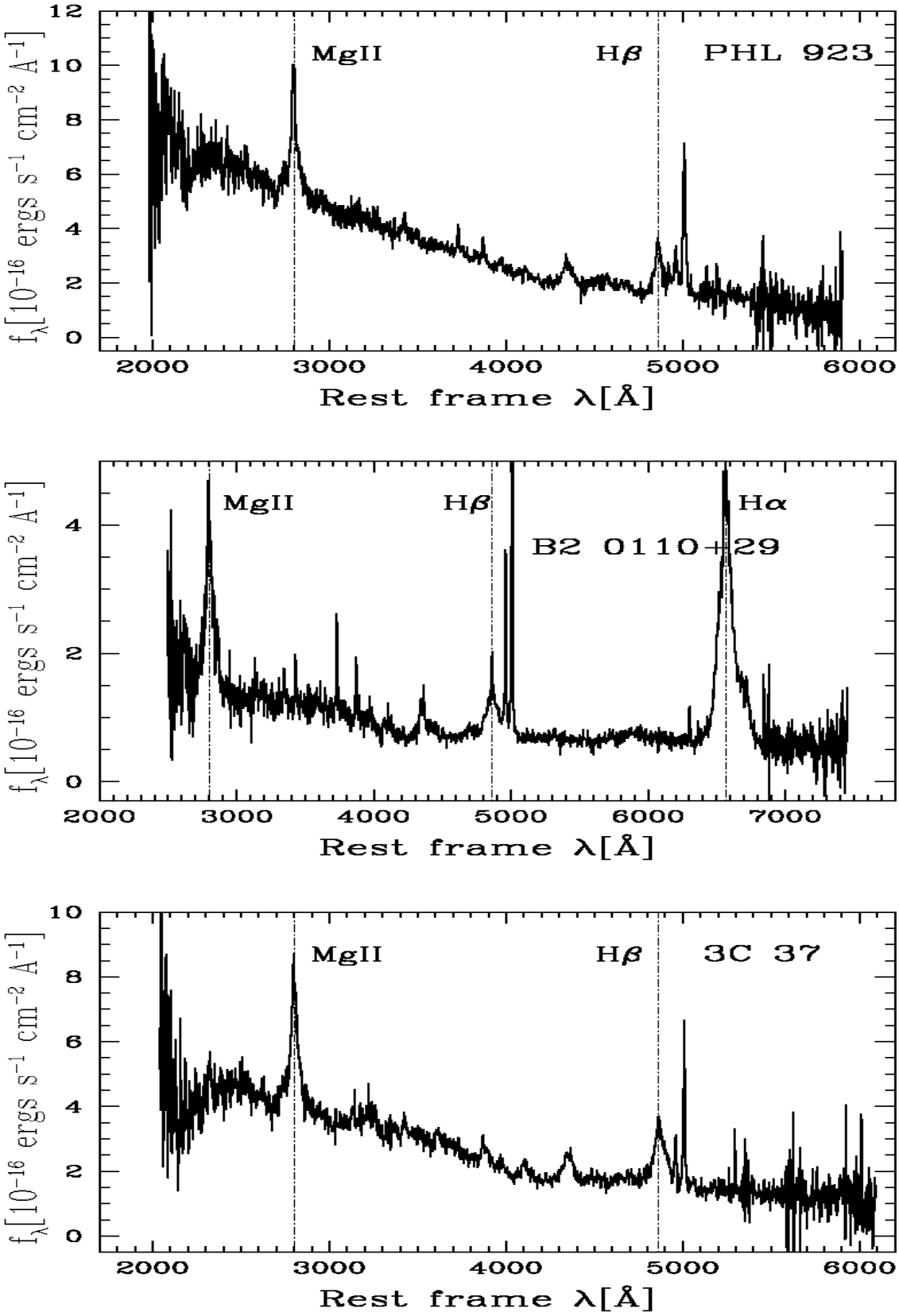

Figure 3.4: Rest-frame spectra of our 12 quasars, with MgII,Hβ, and Hα (in some sources) regions. Abscissas are rest-frame vacuum wavelengths in Å and ordinates are specific flux in units of 10^{-15}ergs s^{-1} cm^{-2} Å^{-1}, except for PHL 923, B2 0110+29, 3C 37, and 3C 179 that are in units of 10^{-16}ergs s^{-1} cm^{-2} Å^{-1}. Dot dashed vertical lines trace the rest-frame wavelength of MgIIλ2800, Hβ, and Hα when available.

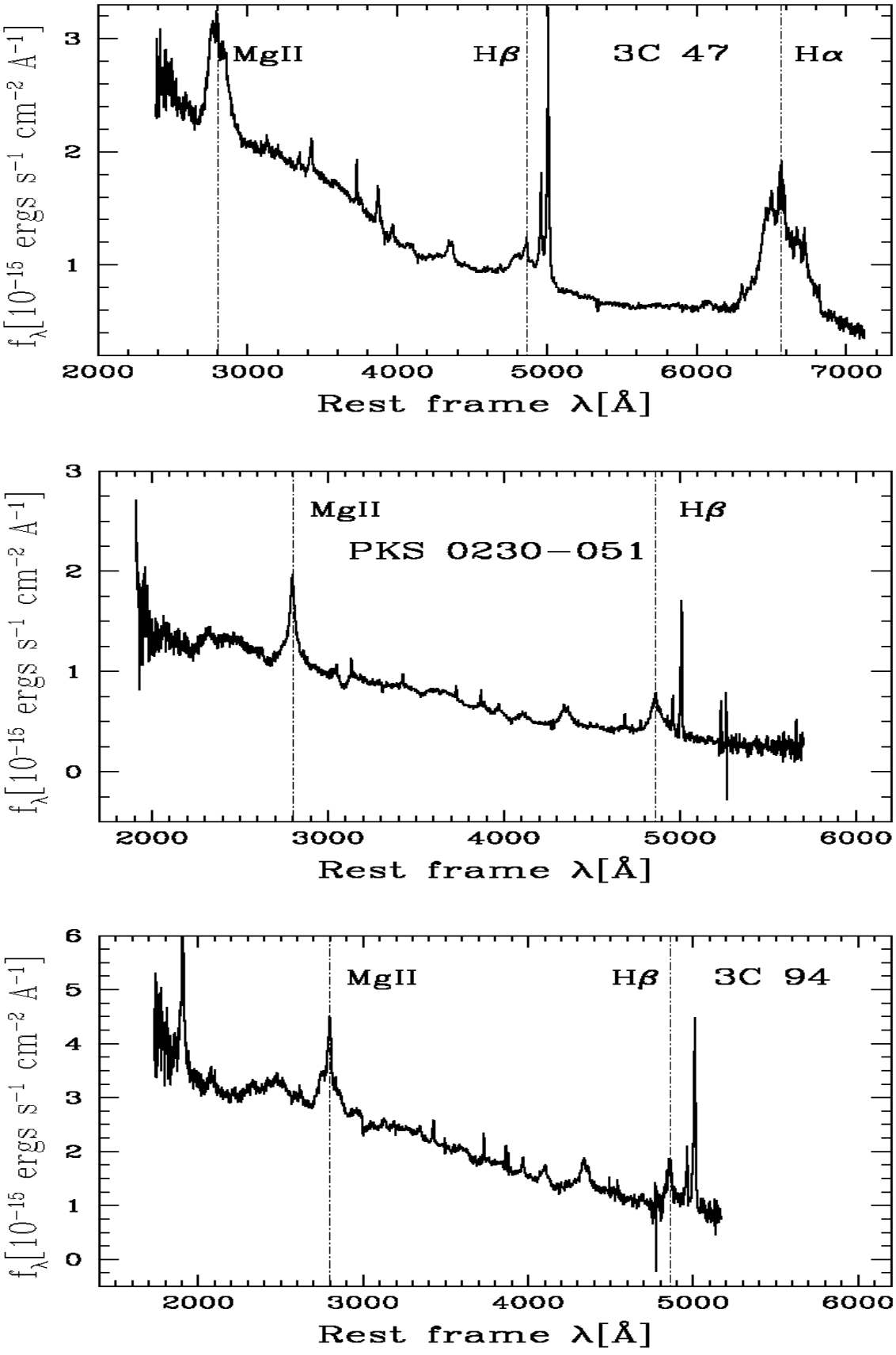

Figure 3.5: Rest-frame spectra (cont.)

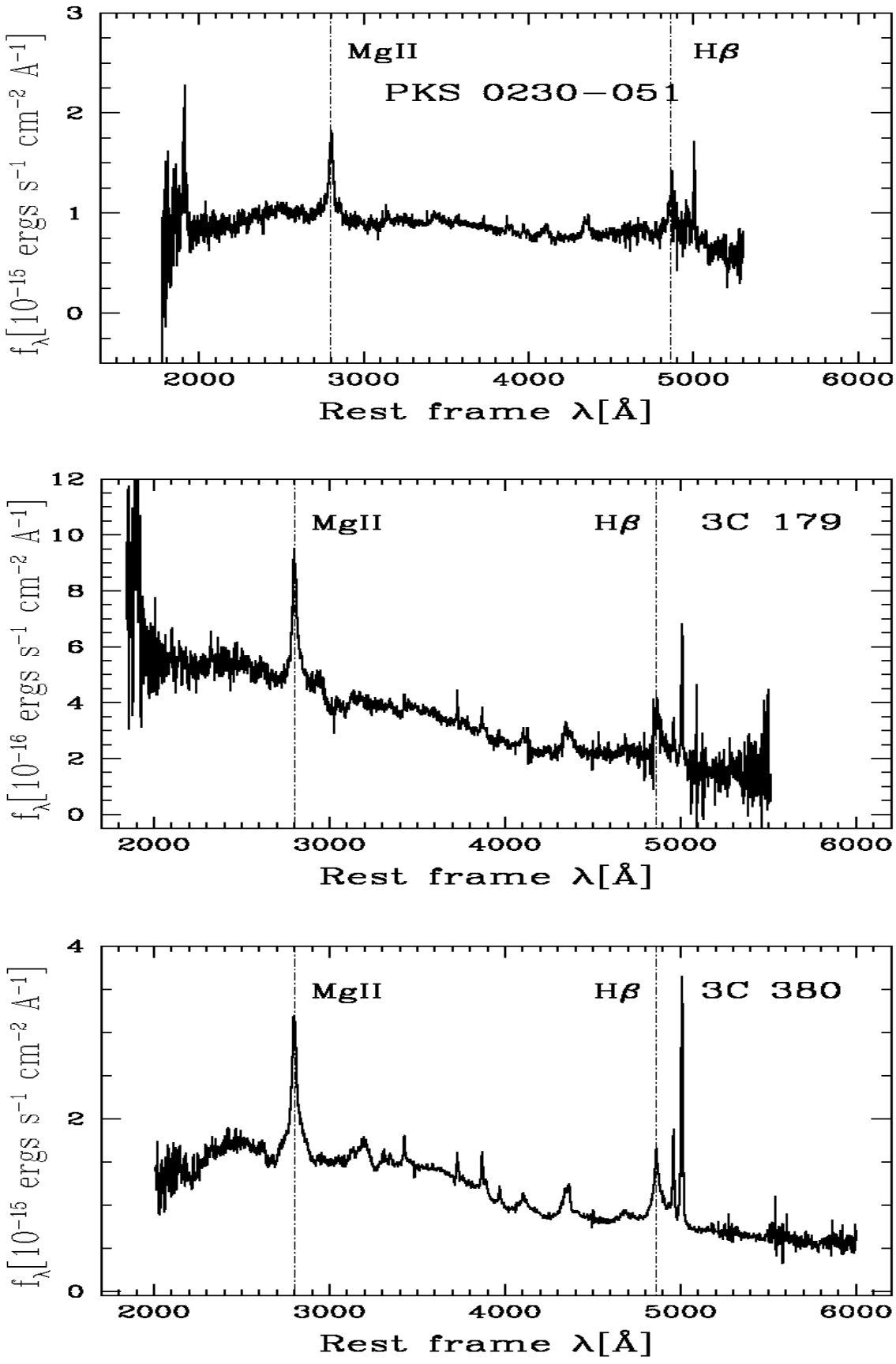

Figure 3.6: Rest-frame spectra (cont.)

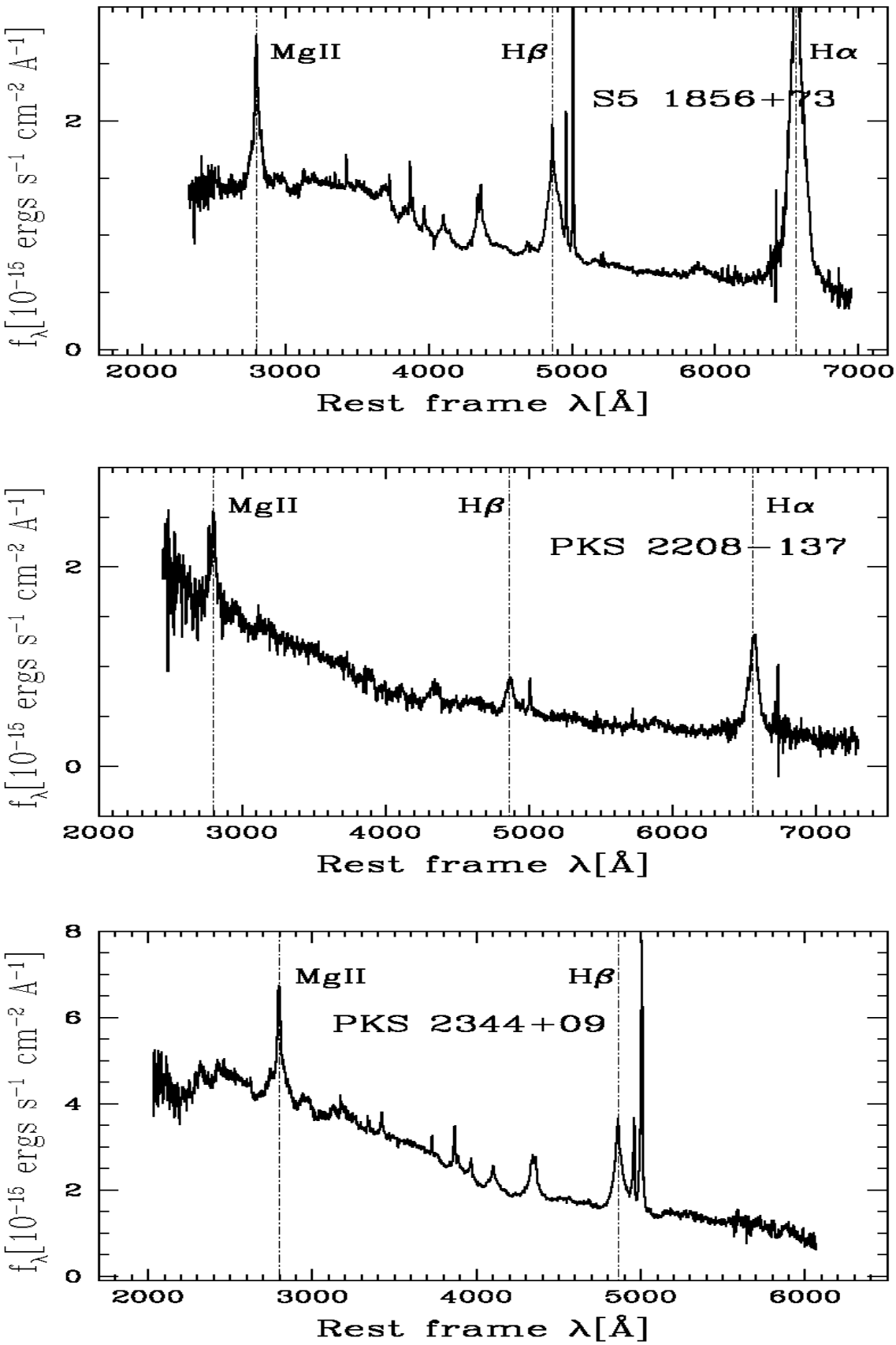

Figure 3.7: Rest-frame spectra (cont.)

3.4 Archival data

Modern astronomical research thrives on the synergy between new cutting-edge observations and the wealth of information stored as archival data. In this work, we didn't rely on the above observations alone, but also on the rich tapestry of archival data, combining our ground-based observations with different multi-wavelength data and space missions. In general, this study utilized a combination of additional archival radio, optical, and UV data. This combined approach provides a more holistic understanding and a detailed study of the dichotomy between RL and RQ quasars, which is one of our main objectives. Additional archival data used in this thesis are described below.

3.4.1 Radio data

Radio sources exhibit a wide range of morphological types, which provide clues to the source class, emission mechanism, and properties of the surrounding medium (e.g., Begelman et al., 1984). In high-angular-resolution surveys, different components may be resolved into distinct parts. In recent years, to resolve different parts of an RL quasar, radio surveys such as the National Radio Astronomy Observatory (NRAO) Very Large Array (VLA) Sky Survey (NVSS)[5] (e.g., Condon et al., 1998) and the Faint Images of the Radio Sky at Twenty Centimeters (FIRST)[6] survey (e.g., Becker et al., 1995), described in Sect 2.4.2 that covered substantial fractions of the sky down to milliJansky (mJy) flux densities, have been extensively used. Both the FIRST and NVSS observed the sky at 20 cm (1.4 GHz), where FIRST has two measures of continuum radio flux density with the peak value and the integrated flux density, whereas NVSS provides only a measurement of integrated radio flux density. In addition, for comparison purposes, the radio flux density at 6 cm (5 GHz) is obtained from VizieR catalog of quasars and AGN (13th Ed.) of Véron-Cetty and Véron (2010) and NORTH6CM - 6cm radio catalog of Becker et al. (1991).

3.4.1.1 Radio morphology classification

A significant improvement to the definition of RL quasars is provided by incorporating the classical radio morphology as a criterion. In the 1970s, Fanaroff and Riley introduced a simple distinction between two morphological types of extended radio sources based on their radio emission (e.g., Fanaroff and Riley, 1974), as discussed in Sect. 2.3.2. The radio emission from RL quasars takes the form of unresolved core, collimated jets, extended lobes, and hot

[5]NVSS-https://www.cv.nrao.edu/nvss/NVSSPoint.shtml
[6]FIRST-http://sundog.stsci.edu/cgi-bin/searchfirst

spots. Morphological classification of radio sources can also be done observationally from multi-frequency observations with the use of new powerful radio instruments like Very Large Baseline Array (VLBA), global Very Long Baseline Interferometer (VLBI), Low-Frequency Array Radio Telescope (LOFAR), and MeerKAT, in addition to large sky area radio continuum surveys such as FIRST/NVSS. Since the resolution of NVSS and FIRST are inadequate to provide a view of the weaker jet, we supplemented them with VLBI maps whenever available to obtain a view of the objects with two different angular scales: one that is related to kpc (or arcsec) scale associated with extended features such as the radio lobes, and one related to pc (or milli-arcsec) sized relativistic jets. We classified our sources, as listed in Table 3.3, according to the following scheme:

- **On the arcsec scale** using FIRST when available, or NVSS. The sources have been classified as core-dominated (C) if the core appears unresolved, as core plus lobe/s (CL) if we have a visible bright core and at least one lobe, and as lobe-dominated (LD) if we see the lobes without core in the spatial scales of VLA or if lobes dominate the radio emission.
- **On the milli-arcsec scale** using VLBI the sources have been classified as core-jet (CJ) if the object presents both a core and a jet.

Finally, to get additional insight into the source's radio morphology, we obtained an overlay between the NVSS/FIRST radio images and the optical Pan-STARRS images, which allowed us to identify more clearly sources with a CJ configuration or with the presence of two radio lobes. The radio images we used for the radio morphology determination from different surveys when available (e.g., VLBA/VLBI, VLA, NVSS, FIRST cutout image) and an overlay of NVSS/FIRST cutout on the optical Pan-STARRS image are shown in Appendix A.

3.4.1.2 Radio and optical measurements for RL and RQ classification

Quasars have also been classified as RL and RQ by using radio and optical measurements, even if a clear consensus on a boundary between them has been difficult to achieve and several radio-loudness criteria have been used in the literature (e.g., Hao et al., 2014; Ganci et al., 2019). In this work, we used two of the most commonly used criteria. The first rough division is made based on the strength of radio emission, usually parameterized by a parameter called radio-loudness (R_K), as the ratio of radio flux density at $5GHz$ to the B-band

optical flux density as originally defined by Kellermann et al. (e.g., 1989):

$$R_K = \frac{f_{5GHz}}{f_B}. \tag{3.1}$$

Recently, this radio loudness can also be estimated by using a modified version of the above parameters, based on the ratio of the rest-frame radio flux density at $1.4GHz$ to the rest-frame optical flux density in the g-band (we represent it as R_{KS}) (e.g., Zamfir et al., 2008; Gürkan et al., 2015; Ganci et al., 2019):

$$R_{KS} = \frac{f_{1.4GHz}}{f_g}. \tag{3.2}$$

Three radio flux density measures were used to provide the radio information depending on the availability of data in their equatorial coordinates, the flux at 1.4 GHz from NVSS and FIRST, and the flux at 5 GHz from Véron-Cetty and Véron (2010)[7] catalogs. In all cases, the k-corrected emitted radio flux density at 1.4 GHz and 5 GHz can be measured from the observed integrated radio flux density by using the spectral index α obtained from Vollmer et al. (2010) and the relation from Ganci et al. (2019, their equation 7):

$$f_{\nu_{o,e}} = f_{\nu,o}[(1+z)^{\alpha-1}], \tag{3.3}$$

where the subscript *"o"* refers to the observer's frame, and the subscript *"e"* refers to quantities in the quasar rest-frame and the convention for the spectral index can be $S \propto \nu^{-\alpha}$. The rest-frame optical fluxes around the effective wavelengths of λ 4770Å for the g band and λ 4450Å for the B band were obtained from our optical spectra after changing the flux in λ into flux in ν.

To estimate the radio loudness parameters, before dividing the k-corrected radio flux density by the optical flux density, we need to make them consistent by taking into account the effect of redshift on the observed spectra considering both the expansion of the universe and the peculiar motion of the source relative to the observer. The optical spectra were corrected for both the expansion of the universe and the Doppler shift while changing the observed spectra into the rest-frame spectra by multiplying it with a total factor of $(1+z)^3$. By assuming the k-corrected radio flux density as a linear term, then to make it consistent with the optical flux density, we need to multiply it by the remaining quadratic term $(1+z)^2$ to get the emitted radio flux density.

The other essential parameter that characterizes radio sources is their radio power (P_ν), which can be measured by using the luminosity distance and the k-corrected

[7] https://vizier.u-strasbg.fr/viz-bin/VizieR-3?-source=VII/258/vv10

Table 3.3: Radio properties of the phase I observed sample.

Object	NVSS Int.flux (mJy)	FIRST Int.flux (mJy)	Flux at 5 GHz[a] (mJy)	$D_L^{(b)}$ (Mpc)	$\alpha^{(c)}$	$logR_K^{(d)}$	$logR_{KS}^{(e)}$	$log(P_\nu)$ (ergs s^{-1} Hz^{-1})	Morph.
(1)	(2)	(3)	(4)	(5)	(6)	(7)	(8)	(9)	(10)
PHL 923	2508	2494	1410	4401	0.42	4.63	4.37	34.63	CL
B2 0110+29	810	–	311	1937	0.54	4.34	3.99	33.50	LD
3C 37	1522	1646	621	4015	0.92	4.49	4.15	34.45	CL
3C 47	3900	–	621	2333	0.9	4.12	4.00	34.50	LD
PKS 0230-051	210	139	160	4871	0.52	3.13	3.03	33.59	CL
3C 94	3061	2798	790	6330	1.04	4.23	3.57	35.18	LD
PKS 0420-01	2726	–	1580	5912	0.23	3.94	3.71	34.71	LD
3C 179	2123	–	1000	5343	0.72	4.63	4.29	34.79	CL
3C 380	13753	–	5000	4200	0.75	4.73	4.34	35.41	CL
S5 1856+73	490	–	610	2563	0.12	3.03	3.22	33.42	C
PKS 2208-137	1330	–	620	2120	0.66	3.71	3.45	33.81	CL
PKS 2344+09	1804	1734	1690	4063	0.19	3.44	3.49	34.37	C

Note: [a]From (Véron-Cetty and Véron, 2010). [b] Luminosity distance in Mpc. [c]From Vollmer et al. (2010). [d]With NVSS k-corrected radio flux density at 5 GHz and optical rest frame flux density in B band. [e]With k-corrected radio flux density at 1.4 GHz and rest frame optical flux density in g band. Units in Col. 9 are ergs s^{-1} Hz^{-1}.

radio flux density at 1.4 GHz by using Ganci et al. (2019, their equation 7) as:

$$logP_{1.4GHz} = 20.08 + 2logD_L + logF_{1.4GHz}, \tag{3.4}$$

where D_L is the luminosity distance determined by using the redshift of each object and reported in Table 3.3, Col. 5.

Table 3.3 shows the main radio properties of our sample observed in phase I. The object identification, the NVSS 1.4 GHz integrated flux, the integrated flux at 1.4 GHz compiled from FIRST (when available), and the flux at 5 GHz (6 cm) are presented in Cols. 1 - 4, respectively. The luminosity distance, radio spectral index (α), measured radio loudness parameters, radio power, and radio morphology are given in Columns 5 - 10, respectively.

With the definition of Kellermann et al. (1989) (Eq. 3.1), conventionally RQ quasars are defined as those with $\log R_K < 1.0$ while RL quasars are those with $\log R_K > 1.0$, and it is estimated that $\approx 10\%$ of AGN are RL in the local universe (e.g., Zamfir et al., 2008; Rafter et al., 2011; Hada, 2019). In addition, previous works showed a well-defined lower limit for R_K in which lobe-dominated (LD) RL sources have a value of $\log R_K > 1.8$ and a radio power $\log P_\nu > 31.6$ [ergs s^{-1} Hz^{-1}] (e.g., Sulentic et al., 2003; Zamfir et al., 2008). As can be seen in Table 3.3, the resulting radio-power for all sources

is extremely high with $\log P_\nu$ between 33.4 and 35.3 $\mathrm{ergs\,s^{-1}\,Hz^{-1}}$ and with $\log R_\mathrm{K} > 3$, meeting by far the requirement to classify them as RL. Based on the modified version of the radio loudness parameter (Eq. 3.2), Ganci et al. (2019) classified as radio detected (RD) sources with $\log R_{KS} < 1.0$, radio intermediate (RI) sources with $1.0 \leq \log R_{KS} < 1.8$, and RL if $\log R_{KS} \geq 1.8$.

3.4.2 Optical and near-UV data

Beyond the wealth of information obtained from radio observations like NVSS and FIRST, incorporating optical and near-UV archival data significantly enhances our work, as it provides a crucial complementary perspective and a detailed comparison between RL and RQ quasars with other samples. As the main comparison in the optical, we used the low redshift samples of Marziani et al. (2003a) and Zamfir et al. (2010) that have information for centroid velocities shift (see Sect. 4.1.1) at different fractional intensities of the peak, FWHM of the full profile, asymmetry indices and the radio loudness parameters.

The sample of Marziani et al. (2003a) originally had 215 sources and provided line measurements for RQ and RL type-1 AGN at $z < 0.8$. Before using it as a main comparison sample, we excluded sources in common with our main sample (2 in total), with Zamfir et al. (2010) (38 sources in total) and other sources that may create doubt in the interpretation of the spectra after a careful examination (6 in total). There are, therefore, 169 remaining objects, of which 94 belong to Pop. B (see Sect. 2.5.3) containing information for the line center ($c(\frac{1}{2})$) and the line base ($c(\frac{1}{4})$) of Hβ. Zamfir et al. (2010) have done spectral fitting of the SDSS (see Sect. 2.4.2) DR5 spectra of $\approx$470 sources at $z < 0.7$ in the Hβ region, of which 209 sources are classified as Pop. B, and contain information about the emission lines profile parameters, such as centroid velocity at the line base ($c(\frac{1}{4})$) and radio loudness parameter.

To examine an alternative scenario as an explanation of the observed double-peaked profile for one of our sources, 3C 47 (see Chapter 6), two additional optical spectra were used, namely an ESO spectrum obtained at the 1.52-meter telescope on October 14, 1996, (Marziani et al., 2003a), and a spectrum obtained at the Copernico telescope equipped with AFOSC on Nov. 27 2006, covering Hβ and MgII regions (Decarli et al., 2008).

The redshift and luminosity ranges, the number of sources (Pop. A and B discussed in Sect. 2.5.3) considered in each sample, and the number of Pop. B RL sources in different radio loudness ranges, in addition to emission lines used and profile measures available in each are summarized in Table 3.4. In our sample, all sources are not only with $\log R_\mathrm{K} \gtrsim 3$, but 7 of them are with $\log R_\mathrm{K} \gtrsim 4$. The histogram in Fig. 3.8 shows the distribution of $\log R_\mathrm{K}$ for Pop.

B RLs of ours and the comparison samples. Only a handful of sources in the main comparison samples have $\log R_{\rm K} \gtrsim 4$ and a few tens have $\log R_{\rm K} \gtrsim 3$. In the optical plane of 4DE1 parameter space (see Sect. 2.5.1), our extreme $\log R_{\rm K} \gtrsim 3$ represent non-negligible addition to RL sub-samples of optically selected quasars that are represented in Pop. B spectral type bins B1, B1+, and B1++ (Zamfir et al., 2008). The extremely jetted quasars enhance the significance of statistical comparisons between the highest radio loudness sources and RQ as well as other RL sub-samples.

In the near-UV region, we used, in particular, MgII region information from the composite spectra of Marziani et al. (2013a) that are generated in a clear and unbiased way by using spectral binning of physically similar quasars for a sample of 680 SDSS-DR7 spectra with $0.4 < z < 0.75$ that are built for different STs (see Sect. 2.5.2) along the MS (see Sect. 2.5.2), i.e., A1 to A4 for Pop. A quasars and in Pop. B for the STs B1, B2, B1^{+}, and B1^{++} besides within the B1 bin for those classified by the authors as RL. The information from this composite spectra has measurements for both UV and optical regions. In addition, a comparison sample in this region is also obtained from the QSFIT catalog (Calderone et al., 2017) with $z < 2$ using the fifth SDSS quasar catalog (Schneider et al., 2007) as a comparison of the placement of our quasars in the UV plane (see Sect. 3.4.3). Furthermore, a comparison sample between Hβ and MgII FWHM is obtained from Wang et al. (2009), in which they considered sources with a redshift of $0.45 < z < 0.75$ from the SDSS DR5 spectroscopic database.

3.4.3 UV data

The public archives at MAST provided access to UV data from HST, a powerful observatory specifically designed for space-based observations beyond the obscuring effects of Earth's atmosphere. Quasars not only emit intense light across a broad range of the EMS but, also drive vast quantities of material/powerful winds outwards, called outflows, that blast material back into the host environment, as mentioned above. While optical observations provide a strong foundation, incorporating UV data can significantly enhance outflow signatures. A search for the HST archive yielded useful spectra for semi-forbidden line CIII]λ1909 and the HIL CIVλ1549 which is a highly ionized form of carbon and a powerful tracer of outflows. This information provides invaluable insights into the energetics driving the outflows, their impact on the surrounding environment, and their potential role in regulating star formation within the quasar's host galaxy as feedback. This can be achieved by analyzing the strength, profile, and velocity shifts of the CIVλ1549 line obtained from the HST data.

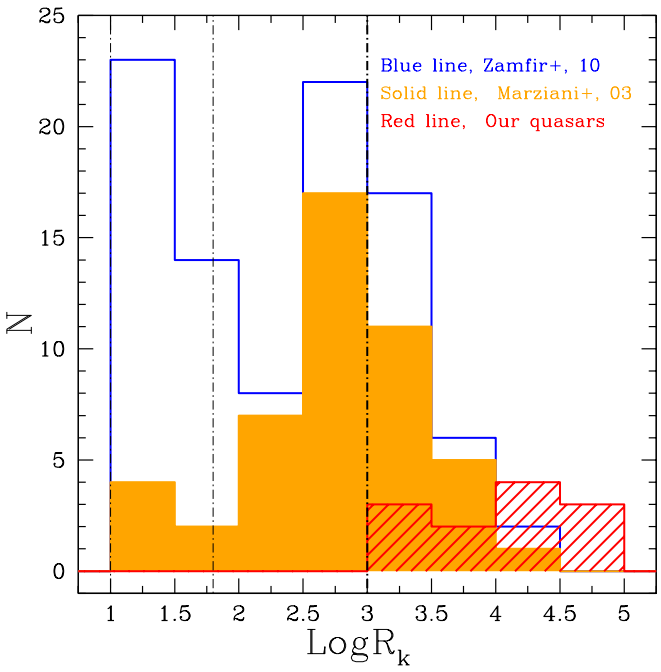

Figure 3.8: Distribution of radio loudness parameter for Pop. B RLs from our sample (red striped area) and the main comparison samples used in this work, Marziani et al. (2003a) (solid orange) and Zamfir et al. (2010) (blue line). The vertical dot-dashed lines at 1 and 1.8 mark the nominal RQ-radio intermediate and radio intermediate-RL boundaries (Ganci et al., 2019). The vertical dot-dashed line at 3 marks the boundary for extreme radio loudness values.

Table 3.4: Summary of the main comparison samples and the sample of this work .

Information	Marziani+03	Zamfir+10	Marziani+13[a]	This work[b]
Redshift range	z < 0.8	z < 0.7	0.4 < z < 0.75	0.35 < z < 1
No. of sources	168	469	8[a]	12
Parameters	c($\frac{1}{2}$), c($\frac{1}{4}$), R_K FWHM,AI	c($\frac{1}{4}$), R_K, AI FWHM,$R_{FeII,opt}$	c($\frac{1}{2}$), c($\frac{1}{4}$) FWHM,AI	c($\frac{1}{2}$), c($\frac{1}{4}$), R_K FWHM, AI $R_{FeII,opt}$,$R_{FeII,UV}$[b]
Lines used	Hβ	Hβ	Hβ and MgII	Hβ and MgII
Log L_{bol} [ergs s^{-1}]	43.7–47.8	43.0–47.0	45.7–46.9	45.15–46.57
No. Pop. B RLs:				
logR_K > 1.8	42	61	–	12
logR_K > 3	17	25	–	12
logR_K > 4	1	2	–	7

Note: [a]This sample provides 8 composite spectra generated using spectral binning of physically similar quasars of 680 SDSS spectra. [b]All the profile parameters measured for our quasars, using the FP and the multi-component fittings are detailed in Sect. 4.1.1. c($\frac{1}{2}$) and c($\frac{1}{4}$) represent the centroid velocity shift at $\frac{1}{2}$ and $\frac{1}{4}$ fractional intensity of the lines, respectively. In the table, AI denotes the asymmetry index.

Specifically focusing on the quasar 3C 47, to analyze the frequently shown blue-shifted profile and its contribution to the observed double-peaked emission line profile in the UV region, we used the spectra from the HST-FOS archive which resulted in a useful rest frame spectra covering HeIIλ1640, the semi-forbidden line CIII]λ1909 and the high ionization UV line CIVλ1549 for this particular source. In the rest-frame spectra, the double-peaked profile is also clearly visible in these regions, and the detailed disc profile analysis, its results, and related discussions are presented in Chapter 6.

Chapter 4

Methods of data analysis

4.1 Profile and physical parameters

Quasars hold a wealth of information about the universe's most energetic phenomena, and to understand such celestial phenomena, a range of emission line profiles and physical parameters are crucial, each offering a unique piece of information about the quasar's nature. In addition, emission lines are prominent features in AGN's UV and optical spectra, as previously discussed (e.g., Osterbrock and Ferland, 2006). Quasar's broad line spectra show a wide range of line profiles, line shifts, and line intensities as profile parameters. To explain this spectroscopic diversity, much emphasis was placed on properties: profile parameters (e.g., Martínez-Aldama et al., 2015; Rakić, 2022; Kovačević-Dojčinović et al., 2022), and physical parameters like SMBH mass (M_{BH}) (e.g., Hernitschek et al., 2016; Marziani et al., 2019a; Bao et al., 2022), luminosity (e.g., Marziani et al., 2009; Popović and Kovačević, 2011; Rakić et al., 2017) and accretion rate (e.g., Mathur et al., 2001; Marziani et al., 2001).

4.1.1 Profile parameters

The profile parameters refer to a range of characteristics used to describe the shape and properties of spectral emission lines emitted by the AGN. These parameters, along with other physical properties, provide valuable information about the physical conditions in the gas surrounding the SMBH. For instance, the gas motions within the BLR can be parameterized by the Full Width at Half Maximum (FWHM), a measure of the width of an emission line at its half peak intensity. A broader FWHM indicates a larger velocity spread in the gas, which could be due to various factors like turbulence, rotation, or outflows, and its value can probe the physical conditions and dynamics of the gas in the

BLR. In addition, some broad emission lines might exhibit asymmetry in their profiles; one side of the line might be steeper or broader than the other, and such a behaviour is expressed by using the line asymmetry measures. The line asymmetries are mainly parameterized by the centroids at different fractional intensities, ($c(i/4)$ for i = 1, 2 and 3) and ($c(9/10)$), asymmetry index (A.I), and kurtosis index (K.I). Such diagnostic measures provide information about the shape of a spectral line profile, capture different aspects of that shape, and can be expressed mathematically according to Zamfir et al. (2010):

$$c(x) = \frac{\upsilon_{r,R}(x) + \upsilon_{r,B}(x)}{2}, \tag{4.1}$$

$$A.I = \frac{\upsilon_{r,R}(\frac{1}{4}) + \upsilon_{r,B}(\frac{1}{4}) - 2\upsilon_{r,peak}}{\upsilon_{r,R}(\frac{1}{4}) - \upsilon_{r,B}(\frac{1}{4})}, \tag{4.2}$$

$$K.I = \frac{\upsilon_{r,R}(\frac{3}{4}) - \upsilon_{r,B}(\frac{3}{4})}{\upsilon_{r,R}(\frac{1}{4}) - \upsilon_{r,B}(\frac{1}{4})}, \tag{4.3}$$

where $\upsilon_{r,R}(x)$ and $\upsilon_{r,B}(x)$ refer to the radial velocity of the red and blue sides of the line at the $\frac{i}{4}$ fractional intensities, respectively, and are calculated relative to the rest-frame of the quasar. The "peak" represents the wavelength at the 9/10 fractional intensity.

The centroid of a spectral line refers to the point where the total flux is divided equally. However, the centroid's position may vary slightly depending on the intensity level. These parameters focus on the position of the centre of the line profile and analyze how the centroid's location varies depending on the fractional intensities considered. The second parameter, A.I quantify the overall asymmetry, which means one side is taller or wider than the other of the line profile, and as in the case of the centroid, it doesn't consider specific locations within the line but provides a single value representing the degree of asymmetry. For the AI, positive/negative values indicate a skewed profile towards the red/blue end, respectively, and it is useful for understanding the overall dominance of inflows/outflows. The third parameter, K.I describes the tailedness, or how sharply the intensity of the line drops off at its edges (wings) in the line profile compared to a normal Gaussian distribution. By analyzing all the above three metrics alongside FWHM, a comprehensive understanding of the line profile and the physical processes within the AGN can be found.

4.1.2 Physical parameters

Some of the key physical parameters that are crucial for quasar studies are the $M_{\rm BH}$, which dictates the gravitational influence, and the Eddington ratio ($\lambda_{\rm E} = L_{\rm bol}/L_{\rm Edd}$ which relies on knowledge of the $M_{\rm BH}$ to compare a quasar's luminosity (L) to its Eddington luminosity. One of the main objectives of this work is to estimate the physical parameters of our selected quasars, $M_{\rm BH}$ and $\lambda_{\rm E}$, since they are crucial to understand the AGN phenomenon, their evolution across cosmic time, and the properties of their host galaxies (e.g., Marconi and Hunt, 2003).

4.1.2.1 Black hole mass

Black holes (BHs) are huge concentrations of matter packed into very tiny spaces, and they are some of the most mysterious cosmic objects, much studied but not fully understood. The SMBH is the largest type of black hole, with its mass being on the order of hundreds of thousands, or millions to billions, of times the mass of the Sun ($M_{\odot}$). To explain quasars spectroscopic diversity, much emphasis was placed on the SMBH properties, in particular, their mass (e.g., Boroson, 2002). In addition, $M_{\rm BH}$ is a fundamental parameter that relates to the evolutionary stages and the accretion processes occurring within quasars, as the power output is directly proportional to $M_{\rm BH}$ (e.g., Lapi et al., 2006; Fraix-Burnet et al., 2017). However, directly observing the $M_{\rm BH}$ is not easy (although not impossible anymore, as shown by the Event Horizon Telescope[1] project and the use of radio interferometry), and therefore, astronomers rely on direct (reverberation mapping), indirect (scaling laws), and spectrophotometry methods to probe their mass, even if the methods have their strengths and limitations, as described here:

- **Reverberation mapping** (RM, Blandford and McKee, 1982): Is a powerful astrophysical technique for studying the BLR and estimating $M_{\rm BH}$ in quasars. This technique capitalizes on the variability of the quasar's central engine. Fluctuations in the quasar's UV continuum light, originating from the AD surrounding the SMBH, illuminate the BLR, causing it to emit light at various wavelengths, including the creation of broad emission lines. These emission-line fluxes vary strongly in response to changes in the continuum of the AD, and the emission lines, which are excited in response to the AD's light, will reverberate or vary in response.

  However, due to the finite speed of light, the response of the BLR observed as variations in the broad emission line intensity, is delayed compared to the original continuum variations. Monitoring the quasar's light

[1] https://eventhorizontelescope.org/

variations over time and measuring the time delay, known as the reverberation lag between the continuum and the broad emission line response, holds crucial information about the size of the BLR. Assuming that this delay is solely due to light travel times, the time delay (τ) between the variability of the continuum and the broad-line emission can be related to the size of the BLR as $R_{BLR} = c\tau$.

Once the BLR size is determined, it can be combined with the measured FWHM of the broad emission line (which reflects the gas velocity) within the framework of the virial theorem to estimate the mass of the central SMBH directly. From Newton's law of gravity, for matter orbiting a SMBH, combined with the broad-line width (δV) which is a proxy of the virial velocity of gas clouds in the BLR, the $M_{\rm BH}$ based on reverberation mapping computed from the virial equation is:

$$M_{BH} = f\frac{R_{BLR}\delta V^2}{G}, \tag{4.4}$$

where R_{BLR} is the size of the BLR as estimated by the mean time delay relative to continuum variations, δV is the width of the variable part of the emission line and can be measured directly using the broadening of spectral line profiles due to the motion of the line emitting gas - the line FWHM, G is the universal gravitational constant, and f is a scale factor/virial coefficient that depends on the structure and geometry of the BLR, such as its orientation, kinematics, or structure (e.g., Onken et al., 2004; Woo et al., 2010; Graham et al., 2011). If we include the orientation, the above formula can be re-written by including the viewing angle (θ) between the line-of-sight and the axis of symmetry of the source, like the AD axis or the radio axis, and the above virial equation becomes:

$$M_{\rm BH} = f(\theta)\frac{R_{\rm BLR}{\rm FWHM}^2}{G}. \tag{4.5}$$

In practice, the Keplerian velocity ($\delta v_{\rm K}$) and isotropic velocity ($\delta v_{\rm iso}$) play a role in understanding the broad emission lines observed in the spectra and can be connected to the measured FWHM of those lines as the FWHM of these broad emission lines is a key measurement used to understand the kinematics of the gas in the AGN. This is mainly because as different parts of the rotating gas move at different speeds depending on their distance from the central SMBH, the emission line will become wider (larger FWHM) as the distance decreases. In addition to the Keplerian rotation, the gas also has isotropic velocity distributions, and random motions in all directions due to factors like turbulence and high temperatures, and this random motion also contributes to the broadening of the

emission lines and brings larger values in the FWHM.

Mathematically, the relation of the measured FWHM to the intrinsic properties of the gas ($\delta v_{\rm K}$) and ($\delta v_{\rm iso}$) is:

$$\frac{FWHM^2}{4} = v_{iso}^2 + v_k^2 sin^2\theta, \tag{4.6}$$

and the true Keplerian velocity can be expressed in terms of the scaling factor and the FWHM as:

$$v_k^2 = f(\theta) FWHM^2. \tag{4.7}$$

Combining Eq. 4.6 and 4.7 with the above considerations, the virial factor $f(\theta)$ that connects the Keplerian velocity ($\delta v_{\rm K}$) and isotropic velocity ($\delta v_{\rm iso}$) to the observed FWHM can be written as (e.g., Decarli et al., 2008; Mejía-Restrepo et al., 2018; Negrete et al., 2018):

$$f(\theta) = \frac{1}{4[k^2 + \sin^2\theta]}, \tag{4.8}$$

where $k = \frac{\delta v_{\rm iso}}{\delta v_{\rm K}}$ and its value can be determined based on the type of disk we are considering: a Keplerian disk (a disk of material that obeys Kepler's laws of motion) or thick-disk (representation that has a thicker vertical scale height). In general, as the mass is measured directly from the motion that its gravitational force induces in the nearby gas at all estimated weighted distances different from object to object, this method is considered a more direct method for determining $M_{\rm BH}$. As an advantage, it provides a more direct and model-independent measurement of $M_{\rm BH}$, by using the fundamental physics, i.e., the relationship between velocity, size, and mass rather than statistical correlations, which allows for the investigation of the BLR's geometry and the dynamics of the gas within it, which gives valuable insights into the immediate environment of the SMBH. However, this technique is not without its challenges. It demands extensive observational campaigns with high-frequency monitoring to capture the rapid variability of quasars, and thus observations are time-consuming, especially for luminous quasars, which require significant telescope time. Additionally, analyzing complex light curves and extracting reliable time delays involves intensive computational processing and is a process with more than one solution (e.g., Peterson et al., 2004).

■ **Scaling laws.** Another method of determining $M_{\rm BH}$ is a scaling law, which provides an indirect method for estimating $M_{\rm BH}$ by correlating it with readily observable properties of the quasar's BLR. Mainly, it utilizes the

FWHM of a strong, broad emission line available in the spectra of the source. The underlying principle is the virial theorem, which relates the gas motions within the BLR to the central mass, in which a broader line reflects the Doppler-broadening of the emission lines because of faster gas motions within the BLR under the influence of the SMBH and its stronger gravitational pull. An empirical relationship between the BLR size and the continuum luminosity (R_{BLR} – L) or (FWHM - L) scaling enables the $M_{\rm BH}$ estimation, which can be easily applied to a large and diverse sample of AGN (e.g., Shen and Liu, 2012; Shen, 2013; Wu and Shen, 2022). Such empirically calibrated formalisms are based on single-epoch spectra (e.g., Vestergaard and Peterson, 2006; Ho and Kim, 2015).

Depending on the redshift, different line estimators (Hβ, MgII, CIVλ1549) are often used with optical/NIR spectroscopy. At low redshift (z $\lesssim$ 0.7), the line of choice for estimation can be Hβ (e.g., Kaspi et al., 2000; Vestergaard and Peterson, 2006; Collin, 2007), at intermediate redshift ($0.4 < z < 1.4$), the line of choice is MgII (e.g., McLure and Jarvis, 2002; McLure et al., 2006), while at high redshift ($1.6 < z < 5.6$) the CIVλ1549Å line can be used (e.g., Vestergaard, 2002; Vestergaard and Peterson, 2006).

In terms of correlations between line widths (FWHM) and continuum/line luminosities, the luminosity can be calculated by using the continuum flux at 5100Å (λL_λ(5100Å)) from Hβ or at 3000Å (λL_λ(3000Å)) for (MgII) and the distance-luminosity relation:

$$L = 4\pi D_L^2 f, \tag{4.9}$$

where f is the continuum flux at a specified wavelength and L is the resulting luminosity at a luminosity distance D_L.

The FWHM can be obtained from the full broad profile (FP) measurements (see Sect. 4.4) of the appropriate emission lines considered for the $M_{\rm BH}$ estimation. Once the two parameters are measured, the empirically determined $M_{\rm BH}$ through scaling relations can be obtained through Hβ (e.g., Vestergaard and Peterson, 2006; Sulentic et al., 2006; Assef et al., 2011; Shen and Liu, 2012) and MgII (e.g., Vestergaard and Osmer, 2009; Shen et al., 2011; Trakhtenbrot and Netzer, 2012; Shen and Liu, 2012) lines, as indicated here.

➤ **Balmer line estimator method.** This established method relies on the FWHM of hydrogen Balmer lines (like Hβ) to estimate the BLR dynamics and infer the $M_{\rm BH}$, i.e., using the Hβ emission line continuum flux at 5100Å (λL_λ(5100Å)), and the FWHM of the FP of the Hβ line. The following scaling relations are the commonly used ones to estimate the $M_{\rm BH}$:

* Using McLure and Jarvis (2002, their equation 8):

$$\frac{M_{BH}}{M_{\odot}} = 4.74 \left[\frac{L_{5100}}{10^{45} ergs\, s^{-1}}\right]^{0.61} \left[\frac{FWHM(H\beta)}{kms^{-1}}\right]^{2}, \quad (4.10)$$

* Using Sulentic et al. (2006, their equation 7):

$$M_{BH}(M_{\odot}) \approx 5.48x10^{6} \left[\frac{\lambda L_{\lambda}(5100)}{10^{44} ergs\, s^{-1}}\right]^{0.67} \left[\frac{FWHM(H\beta)}{1000 kms^{-1}}\right]^{2}, \quad (4.11)$$

* Using the classical formula from Vestergaard and Peterson (2006, their equation 5):

$$LogM_{BH}(M_{\odot}) = Log\left\{\left[\frac{FWHM(H\beta)}{1000 kms^{-1}}\right]^{2} \left[\frac{\lambda L_{\lambda}(5100)}{10^{44} ergs\, s^{-1}}\right]^{0.5}\right\} + (6.91 + 0.02), \quad (4.12)$$

* Using Assef et al. (2011, their equation 4):

$$\frac{M_{BH}}{M_{\odot}} = 6.71x10^{6} * f * \left[\frac{FWHM(H\beta_{bp})}{1000 kms^{-1}}\right] \left[\frac{\lambda L_{\lambda}(5100}{10^{44} ergs\, s^{-1}}\right]^{0.52}, \quad (4.13)$$

with f = 1.17,

* Using Shen and Liu (2012, their equation 3 and the appropriate constants taken from their Table 5):

$$Log\left(\frac{M_{BH}}{M_{\odot}}\right) = a + bLog\left[\frac{L}{10^{44} ergs\, s^{-1}}\right] + cLog\left[\frac{FWHM}{kms^{-1}}\right], \quad (4.14)$$

where the coefficients a, b, and c are determined by using linear regression analysis, and are a = 1.390, b = 0.555, c = 1.873 with L_{5100} and $FWHM_{H\beta}$.

➤ **MgIIλ2800 line estimator method.** This established method relies on the FWHM of MgIIλ2800 to estimate the BLR dynamics and infer the $M_{\rm BH}$, i.e., using the MgIIλ2800 emission line continuum flux at 3000Å or luminosity (λL_{λ}(3000Å)), and the FP of the MgIIλ2800 line. The following scaling relations are the commonly used ones to estimate $M_{\rm BH}$:

* Using McLure and Jarvis (2002, their equation 7):

$$\frac{M_{BH}}{M_{\odot}} = 3.37 \left[\frac{L_{3000}}{10^{45} ergss^{-1}}\right]^{0.47} \left[\frac{FWHM(MgII)}{kms^{-1}}\right]^{2}, \quad (4.15)$$

* Using Vestergaard and Osmer (2009, their equation 1):

$$M_{BH}(M_{\odot}) = 10^{zp(\lambda)} \left[\frac{\lambda L_{\lambda}}{10^{44} ergs s^{-1}}\right]^{0.5} \left[\frac{FWHM(MgII)}{1000 kms^{-1}}\right]^{2}, \quad (4.16)$$

where $zp(\lambda)$ can be amended depending on the line we are going to use, and is 6.72, 6.79, 6.86, and 6.96 for λ1350Å, λ2100Å,λ3000Å, and λ5100Å, respectively.

* Using Trakhtenbrot and Netzer (2012, their equation 12):

$$M_{BH}(M_{\odot}) = 5.6x10^{6} \left[\frac{\lambda L_{\lambda}(3000)}{10^{44} ergs s^{-1}}\right]^{0.67} \left[\frac{FWHM(H\beta BC)}{1000 kms^{-1}}\right]^{2}, \quad (4.17)$$

* Using Shen and Liu (2012, their equation 3 and the appropriate constants taken from their Table 5):

$$Log\left(\frac{M_{BH}}{M_{\odot}}\right) = a + bLog\left[\frac{L}{10^{44} ergs\, s^{-1}}\right] + cLog\left[\frac{FWHM}{kms^{-1}}\right], \quad (4.18)$$

where a = 1.816, b = 0.584, and c = 1.712 for L_{3000} and $FWHM_{MgII}$.

Such scaling relations offer significant advantages, as they are observationally efficient, requiring only a single spectrum of the quasar to measure the FWHM and flux. They allow for the estimation of $M_{\rm BH}$ in numerous quasars, which facilitates statistical studies of quasar populations. However, they also come with inherent limitations. Such relations are derived empirically, and their underlying physical connections may not be perfect, leading to potential inaccuracies. The BLR can exhibit broadening mechanisms beyond virial motions, such as outflow or inflow of gas. These non-virial processes can distort the line profile and lead to inaccurate mass estimates, particularly for lines more susceptible to such effects. Therefore, to be reliable, it is crucial to focus on LILs.

In conclusion, reverberation mapping and scaling laws serve as complementary tools for $M_{\rm BH}$ estimation in quasars. The choice between scaling laws and reverberation mapping depends on the specific scientific goals and the available resources. Scaling laws offer a statistically powerful approach to study large quasar samples, enabling astronomers to investigate population trends and correlations with other quasar properties. In contrast, reverberation mapping provides a more detailed view of the BLR dynamics and a more model-independent mass determination, albeit with greater observational and computational demands.

- **Spectrophotometry.** This plays a role in $M_{\rm BH}$ estimation, but it's not a completely independent method like single-epoch or reverberation mapping. Instead, it acts as a powerful tool to complement these methods. Current interferometers like the Very Large Telescope Interferometer (VLTI) with its GRAVITY instrument achieve incredibly high angular resolution (e.g., Schoeller, 2007). This allows the observer to directly measure the size and structure of the dust continuum around the SMBH in some AGN. Researchers are investigating a connection between the dust continuum size and the size of the BLR measured through reverberation mapping or the single-epoch method (e.g., Gravity Collaboration et al., 2023). By establishing this link, interferometry could potentially offer an alternative way to estimate the BLR radius and kinematics. It could also offer a potentially faster way to determine the BLR size compared to reverberation mapping, which requires extensive monitoring. In addition, it could be applied to a wider range of AGN, even those with lower variability, which might not be suitable for reverberation mapping. The link between dust continuum size and BLR size is a promising area of research, but it's still under development. More data and analysis are needed to establish the connection and accuracy of using dust measurements for $M_{\rm BH}$ estimation.

4.1.2.2 Eddington ratio ($\lambda_{\rm E}$)

The $\lambda_{\rm E}$ is a parameter that expresses the relative balance between gravitational and radiation forces, a major factor influencing both the dynamics and the physical conditions of the line emitting gas (e.g., Marziani et al., 2010; Netzer and Marziani, 2010; Marziani et al., 2018). Having unravelled the $M_{\rm BH}$ using techniques like scaling laws or reverberation mapping, the $\lambda_{\rm E}$ steps into shed light on the rate at which it devours infalling matter. This ratio offers a crucial window into the energetic processes fueling quasars, and it relates the Bolometric luminosity (L_{Bol}), the total amount of energy emitted by a source, to the Eddington luminosity (L_{Edd}), a theoretical upper limit on the luminosity attainable for a stable configuration around a SMBH. The latter represents a critical threshold resulting from the balancing of gravitational and radiation forces.

As the matter falls inwards, its potential energy is converted into various forms of radiation and makes the source extremely luminous. However, there's a limit to how much radiation pressure a SMBH can handle. If the radiation pressure becomes too strong, it can push outward, overcome the gravitational pull of the SMBH, and halt further accretion. In short, $\lambda_{\rm E}$ is a parameter that expresses the relative balance between gravitational and radiation forces (e.g., Netzer and Marziani, 2010), a major factor influencing both the dynamics and the physical

conditions of the line emitting gas (e.g., Marziani et al., 2018).

Mathematically, the $\lambda_{\rm E}$ is expressed as:

$$\lambda_E = \frac{L_{bol}}{L_{Edd}}, \tag{4.19}$$

where L_{bol} is the bolometric luminosity that can be corrected through the Eq. 4.9 and the correction factor (k_{Bol}) from the relation of Netzer (2019, their equation 3 and the appropriate constants taken from their Table 1) for the luminosity in question (L_{5100} or L_{3000}), measured as:

$$k_{Bol} = c \times \left(\frac{L_{observed}}{10^{42} ergs\, s^{-1}} \right)^{d}, \tag{4.20}$$

whereas L_{Edd} can be expressed as:

$$L_{Edd} = 1.3x10^{38} \left[\frac{M_{BH}}{M_{\odot}} \right] ergs\, s^{-1}. \tag{4.21}$$

The $\lambda_{\rm E}$ remains a valuable tool for understanding a quasar's activity. A quasar radiating near its Eddington limit ($\lambda_{\rm E} \approx 1$) is likely experiencing a period of intense accretion, which suggests the availability of fuel supply in the form of gas and dust in the surrounding environment of the SMBH. Conversely, a quasar with a lower $\lambda_{\rm E}$ (e.g., < 1) might indicate a limited fuel source.

$\lambda_{\rm E}$ of 1 indicates that the quasar is radiating at its Eddington limit ($L_{Bol} = L_{Edd}$) which represents a delicate balance between inward gravitational pull and outward radiation pressure. While a $\lambda_{\rm E} > 1$ suggests the quasar might be exceeding this limit, a situation currently thought to be physically unrealistic due to radiation pressure limitations. Several factors can contribute to an apparent $\lambda_{\rm E}$ exceeding unity. The first reason can be related to our understanding of the Eddington luminosity, which might be incomplete, particularly for objects with complex environments. The second reason can be related to the challenges in measuring the source's luminosity, as additional activities, like dust, between the source and the line of sight obscure and lead to an underestimate of the true luminosity. Finally, the BLR, where the broad emission lines used for mass estimation originate, might not be governed by the SMBH gravity alone (not virialized). Rather, the viewing angle close to the face-on can lower the FWHM and the $M_{\rm BH}$ estimate, increasing $\lambda_{\rm E}$.

The condition $\lambda_{\rm E}$ exceeding unity also seems to go against the physics. There are some more alternative explanations, including the beaming effect and vari-

ation in the accretion process. The beaming effect comes into play when the radiation from the quasar is not radiated uniformly in all directions but rather emits a powerful jet or beam of radiation along a specific axis. During the observation, if the line of sight happens to be aligned with this beam, one might observe a much higher luminosity than the actual, which leads to an inflated λ_{E}. In addition, quasars might not constantly accrete at a steady rate; instead, they might undergo a period of intense accretion and then relative quiescence. If the observation is done during a peak accretion episode, the λ_{E} might appear higher than usual.

4.2 Spectral fitting of quasar spectra

Quasars exhibit distinct spectral features in the UV and optical bands, featuring narrow, broad, and very broad emission lines with a continuum that a power-law can approximate. The spectrum is a fingerprint of the physical processes occurring around the SMBH and the lines, in turn, offer a wealth of information. The continuum represents the underlying continuous emission from the quasars AD and the surrounding hot gas. The broad and very broad emission lines arise from the high-velocity BLR close to the SMBH, and the narrow emission lines represent the region of slowly moving gas further out from the quasar's centre.

By comparing the observed spectrum with theoretical models that incorporate those processes, it is possible to achieve the best fit that accurately reproduces the observed features. Spectral fitting is a fundamental technique employed to extract this information by modelling the observed spectra and identifying their constituent components. Commonly, there are two approaches for fitting a spectrum: an empirical and model fitting approach.

4.2.1 `Specfit` as an empirical fitting approach

The empirical fitting approach focuses on finding the best mathematical function to describe the data, without necessarily considering a physical model for the underlying process. The primary goal is to achieve a good fit between the function and the fitted data by minimizing the differences between the two (or residual). The interpretation focuses on the mathematical properties of the fitted function and, unlike the model-fitting approach, it doesn't necessarily provide insights into the physical mechanisms at play. This approach is often simpler to implement and is computationally less expensive. In addition, such an approach offers a variety of mathematical functions to choose from, such as polynomials, Lorentzian, or Gaussian functions, whose choice depends mainly on the shape

of the spectra. However, such an approach cannot incorporate prior knowledge or provide probabilistic insights into the underlying physical process.

One software tool commonly used for spectral fitting is `specfit` (Kriss, 1994). It is a powerful and interactive tool that runs in the **IRAF** environment and is used for fitting one-dimensional spectra with a user-defined mathematical model. It can fit complex physical models, from different instruments, and meets the desirable characteristics for a general-purpose fitting program.

In `specfit`, the model parameters can be adjusted to find the best possible fit between the model and the calibrated data (rest-frame spectra). The model parameters can be varied to find the parameter values that give the most desirable fit statistics, and the values can be called the best-fit parameters. The model spectrum obtained from the best-fit parameters is considered the best-fit model.

The most common fit statistic in use for determining the best-fit model is chi-square (χ^2). It evaluates how well a theoretical model fits an observed spectrum, in other words, it assesses the goodness of fit. The χ^2 method, which is the squares of the differences from the model prediction to the actual data measured, divided by the variance of the data as determined by the standard measurement errors for a total of N_d measurements, is defined as:

$$\chi^2 = \sum_{i}^{N_d} \left[\frac{N_i - f_i}{\sigma_i} \right]^2 . \tag{4.22}$$

The fitting process typically aims to minimize the χ^2 value. This minimization signifies that the differences (N_i - f_i) between the observed data N_i and the modelled data f_i, weighted by the uncertainties (σ_i), are as small as possible. If χ^2 exceeds a critical value, one can conclude that f_i is not an adequate model for N_i.

The goodness of fit is determined by estimating the probability that the value of the χ^2 minimum would occur if the fitting could be repeated numerous times with the same setup, and can be considered as a good fit if χ^2 falls within the 1σ (68.3%) percentile of all the trials. However, we can't repeat the experiment numerous times with the same setup, so we need some way to estimate the value of χ^2 that corresponds to a given percentile level, called the confidence level. For a given value of χ^2, we need to estimate the degrees of freedom (ν) to determine the confidence level, which is the difference between the number of data values and the number of parameters to fit. The reduced chi-squared, denoted by χ^2_r and defined as $\sim \chi^2/\nu$, is a statistical quantity used extensively as it incorporates an additional factor to account for the complexity

of the model being fitted. A χ_r^2 value much greater than one indicates a poor fit, while a χ_r^2 much less than one indicates that the errors in the data have been overestimated.

While using `specfit`, two minimization techniques are available, a simplex algorithm Kim (1997) and the Levenburg-Marquardt algorithm from (e.g., Bevington and Robinson, 2003). The simplex algorithm is a general optimization method used to minimize or maximize a function. It starts with a set of points called the simplex, iteratively evaluates the function at each point, replaces the worst point with a better one, and moves the simplex towards the region with lower function values. This algorithm provides fast initial convergence irrespective of whether the parameters have poor initial guesses or not. However, the algorithm can be slower to converge to the optimal solution, especially for complex fitting problems, and it can get trapped in points that appear to be minima (local minima) but aren't the global minimum (the best fit). Such results may lead to inaccurate results.

The Levenberg-Marquardt algorithm is generally more popular and well-established for spectral fitting due to its efficiency and robustness. It combines the strengths of two other optimization algorithms: Gauss-Newton algorithm, which takes large steps towards the minimum but can be unstable, especially when the initial guess is far from the solution, and the steepest descent, which is more stable but can be slow to converge. The Levenberg-Marquardt algorithm interpolates between these two approaches and keeps the balance between taking large steps and smaller but more stable steps. Levenberg-Marquardt algorithm is more robust and converges to the solution faster, as a result, it is the preferred choice for spectral fitting in most cases.

The detailed procedures for multicomponent non-linear fitting, using the `specfit` routine, are given below for our sources observed in phase I.

4.2.1.1 Multi-component non-linear fitting using `specfit`

Once we got a flux and wavelength-calibrated spectrum by using IRAF (see Sect. 3.2), to get the measurement of relevant parameters of the line components that are blended, we need an empirical model fitting technique that matches and represents the observed spectrum. In addition, the selected model for the fitting needs to be a collection of several components, each representing a specific contribution to the observed optical and UV spectra.

The Space Telescope Science Data Analysis System (STSDAS) fitting package contains several powerful and flexible tasks that perform a wide range of functions supporting the entire data analysis process, including fitting and analyz-

ing spectra. This package is layered on top of the IRAF. The `specfit` task, in the `STSDAS contrib` package, is another powerful interactive facility for non-linear multi-component fitting of a wide variety of emission line, absorption line, and continuum models and was found to fit spectral data spanning a large range in wavelength (e.g., Marziani et al., 2010, 2013a; Martínez-Aldama et al., 2015; Sulentic et al., 2016, 2017; Marziani et al., 2022).

In this work, each spectrum was analyzed independently in the two observed spectral regions, corresponding to the red and blue arms of the spectrograph, respectively. The red arm includes low ionization features such as Hβ, FeIIλ4570Å, and narrow HILs like [OIII]$\lambda\lambda$4959,5007 as its main representatives. The low ionization MgII doublet is located in the redshifted UV region, along with prominent FeII$_{\rm UV}$ emission covered by the blue arm. To get relevant physical parameters for the emission lines observed in our spectra, an empirical model that matches the observed spectrum was applied. The fitting tool we used was the general purpose package, `specfit` (detailed in Sect. 4.2.1) that contains several powerful, flexible, and interactive tasks for fitting a wide variety of several components, each representing a specific contribution to the observed optical and UV spectrum. We used a chi-square χ^2 minimization technique (see Sect. 4.2.1), which is appropriate for nonlinear multicomponent fitting in order to obtain the best-fit parameters. In addition, the `specfit` routine allowed us to simultaneously fit a continuum, a scalable FeII emission, and individual line components to yield measurements for the FWHM, peak wavelengths, and intensities of several components, each representing a specific contribution to the observed optical and UV spectrum.

For non-linear multi-component fitting, we included the following two major components and conditions in the fittings: the first one is a component related to the continuum emission, and the second one is a component related to the discrete prominent emission lines. Below, we will discuss each of them and their contribution to the spectral fitting process.

4.2.1.2 Continuum emission and its fitting

In quasars, the energetic central region powered by a SMBH produces a vast amount of radiation across the electromagnetic spectrum. This continuous emission, spanning a wide range of wavelengths, is called the continuum emission. Quasar spectra also exhibit prominent emission lines superimposed on the continuum. To isolate and analyze these emission lines, we need to separate them from the underlying continuum. This separation is achieved through a process called continuum fitting. The continuum emission can arise from various processes, including a combination of thermal emission from the AD surrounding the SMBH and non-thermal processes like synchrotron radiation in the corona

or inverse Compton scattering within the object (e.g., Nandra et al., 1998; Murphy et al., 2018).

Considering the emission lines from the UV to optical, the above continuum emissions can be summarized into three: (i) a power-law continuum (F_λ^{PL}), (ii) an FeII pseudo-continuum (F_λ^{FeII}), and (iii) a Balmer continuum (F_λ^{BaC}). While fitting the spectra, the general continuum can be considered as a collection of the three components and it is possible to use various mathematical models to represent the model continuum, F_λ, as (e.g., Sameshima et al., 2011):

$$F_\lambda^{cont} = F_\lambda^{PL} + F_\lambda^{FeII} + F_\lambda^{BaC}. \tag{4.23}$$

The three components can be described as follows:

- **Power-law continuum** (F_λ^{PL}) represents a general non-thermal emission process across a wide range of wavelengths. It is often attributed to synchrotron radiation or inverse Compton scattering and the power-law continuum is a general workhouse for capturing the overall trend of non-thermal emission across a broad wavelength range. The power-law continuum relationship that captures how the intensity changes with respect to wavelength for Hβ line can be expressed mathematically as:

$$F_\lambda^{PL} = F_{5100} \left(\frac{\lambda}{5100} \right)^{\alpha}, \tag{4.24}$$

  where the free parameters of the model are a scaling factor F_{5100} and a power-law index α that offer insights into the physical conditions within the AGN. By fitting a power-law continuum and subtracting it from the original spectrum, it is possible to isolate the continuum contribution from other emission and absorption features for further analysis. However, in some cases, a single power-law might not perfectly capture the entire continuum, especially in regions with significant contributions from other processes. For this, fitting ranges that have little emission or are free of emission lines need to be considered as a power-law continuum window of the fitting.

- **Pseudo FeII continuum** (F_λ^{FeII}) refers to a broad emission feature due to features of iron (Fe) ions blended together and appears as a broad bump in the spectrum, typically centred around the rest wavelengths of prominent FeII emission lines (around 4570Å and 5000Å). The exact origin and physical processes behind the pseudo FeII continuum are still under investigation and are assumed to arise from a combination of various processes,

not just iron emission alone. In addition, since FeII has enormous energy levels, neighbouring emission lines contaminate heavily with each other, making it difficult to measure the FeII emission lines. Therefore, accurately modelling this complexity using physical models can be challenging. One approach to measuring the FeII emission lines is to use FeII templates, which are pre-defined spectra that provide an empirical approach to capturing the overall shape and behaviour of the pseudo-continuum based on observations of many AGN (e.g., Vestergaard and Wilkes, 2001; Véron-Cetty et al., 2004; Tsuzuki et al., 2006; Bruhweiler and Verner, 2008; Marziani et al., 2009). Compared to building complex physical models from scratch, templates offer a simpler and more efficient way to fit the pseudo-continuum. So far, several FeII templates are derived from the narrow-line Seyfert galaxies, including the I Zw 1 galaxy (e.g., Zwicky, 1964; Zwicky and Zwicky, 1971).

Véron-Cetty et al. (2004) carefully analyzed the FeII emission lines in I Zw 1 and found that the FeII lines are emitted from both BLR and NLR. Tsuzuki et al. (2006) also analyzed the spectrum of I Zw 1 and derived the optical FeII template, which was however not separated into the BLR and the NLR components. They used a synthetic spectrum calculated with the Cloudy photoionization code to separate the FeII emission from the MgIIλ2800 line and derived semi-empirically the FeII template, which covers around the MgII line. Also, Vestergaard and Wilkes (2001) provided FeII templates in the UV. Fitting the pseudo continuum helps to model the broad emission feature around the rest-frame wavelength of FeII emission lines and helps to separate this broad component from the true FeII emission lines and the underlying continuum.

- **Balmer-continuum (F_{λ}^{BaC}).** The observed features arise specifically from the blending of numerous high-order Balmer emission lines with the proper Balmer bound free continuum. As we move up in the Balmer series, the energy transitions become closer to the ionization threshold due to physical processes within the AGN and start to overlap significantly. This blending creates a smooth rise in emission towards the shorter wavelengths (blueward) of the spectrum, and such smooth, rising emission merges with the true Balmer continuum shortwards of 3646Å and it has a significant contribution to the overall continuum emission, particularly in the UV part of the spectrum. The mathematical relation for approximating such continuum emission with uniform temperature and optically thick cloud assumption is given by Grandi (1982):

$$F_{\lambda}^{BaC} = F_{BaC} B_{\lambda}(T_e) \left[1 - exp \left\{ \tau_{BE} \left(\frac{\lambda}{\lambda_{BE}} \right)^3 \right\} \right], \tag{4.25}$$

where F_{BaC} is a scale factor, $B_\lambda(T_e)$ is the Planck function at the electron temperature T_e, and τ_{BE} is the optical depth at the Balmer edge at λ =3646Å. To determine the strength of the Balmer continuum, it is possible to assume gas clouds of uniform temperature (T_e = 15, 000 K) and τ_{BE} to be 1 (e.g., Kurk et al., 2007).

4.2.1.3 Emission line components and their fitting

Emission lines, sharp spikes of intensity at specific wavelengths that arise from the BLR, NLR, and, in some cases, the AD are particularly valuable and reveal a wealth of information for studying quasars. There are three distinct classes of emission line profiles depending on their width or the region from where they originate, as the location of the emitting region determines the line type. Studying such line profiles is a way of understanding the gas motion in the nucleus, and the width of the emission line reflects the velocity of the gas emitting the line (e.g., Netzer, 1990; Marziani et al., 1996). By analyzing these different categories of emission lines and fitting their profiles, it is possible to probe the structure, dynamics, and physical conditions within the quasar.

These lines can be permitted, forbidden, or semi-forbidden. Permitted lines, also known as allowed lines, are a fundamental type of emission line observed and arise from electron transitions between allowed energy levels in atoms or ions. The principles of quantum mechanics govern such energy levels and the transitions between them, specifically the selection rules, which define the specific conditions under which an electron transition has a high probability of occurring in terms of factors like the change in an atom's angular momentum and spin during the transition (Ewart, 2019, their chapter 7). Permitted transitions have a high probability of happening since they adhere to the selection rules that allow for a more efficient energy transfer between the electron's energy levels.

The forbidden lines arise from electron transitions between energy levels in atoms or ions that are not normally allowed according to the selection rules of quantum mechanics. Such transitions have a very low probability of happening because of the significant change in an atom's properties. They require special conditions to be emitted, like intense emission or highly random collisions between atoms or ions to trigger a forbidden transition. Forbidden lines are commonly labelled with square brackets "[]" with the elemental symbol and its ionization state placed between the square brackets.

The semi-forbidden lines arise from electron transitions that slightly deviate from the selection rules and are not strictly forbidden, even if they have a lower probability of occurring than the allowed transitions. Semi-forbidden lines are often designated with a closing bracket "]" following the element symbol and

its ionization state.

In addition to the above classification, the lines can also be classified taking into account their profiles and in particular their widths. This includes the following:

- **Narrow Emission Lines (NELs), 300 km s^{-1} - 1000 km s^{-1}.** These sharp, narrow lines originate from regions farther away from the centre of the SMBH, and the gas in these regions experiences less extreme conditions, weaker gravitational force, and intense radiation pressure that has a strong impact on the surrounding environment. These conditions lead to slower gas motions and narrow emission lines, and such a profile is modelled as a narrow component (NC) in the fitting process.
- **Broad Emission Lines (BELs), 1000 km s^{-1} - 10000 km s^{-1}.** These prominent lines arise from the BLR consisting of gas clouds orbiting the surrounding SMBH at high velocities as a result of the immense gravitational pull of the SMBH. Due to the high velocities of the gas clouds in the BLR, the motion undergoes Doppler broadening with a smeared-out and broad profile that can reveal information about the gas motions within the BLR (e.g Popovic et al., 2008; Kovačević-Dojčinović and Popović, 2015). Such a profile is modelled as a broad component (BC) in the fitting process.
- **Very Broad Emission Lines (VBELs), 10000 km s^{-1} - 30000 km s^{-1}.** VBELs are a subcategory of BELs with exceptionally broad line widths. Their origin is still under debate, but they are thought to arise from regions very close to the SMBH, experiencing extreme velocities due to the SMBH's intense gravity. Such a profile is modelled as a very broad component (VBC) in the fitting process. The VBC was postulated because of the typical Hβ profile of Pop. B sources, that can be empirically modelled with good confidence by assuming such a very broad component while fitting the spectra in addition to the other components (e.g., Zamfir et al., 2010).

In quasars, the observed emission lines can be categorized not just by their width alone, as above, but also by the ionization state of the atoms or ions responsible for the emission. This distinction leads to the concept of LIL and HILs. The LILs exhibit strong emission lines from lowly ionized elements and have lost only a few electrons compared to their neutral state. The dominant mechanism responsible for the ionization state in the emission line region is the intense radiation field from the quasar's AD and the SMBH at its centre. In contrast, the HILs show strong emission lines from highly ionized elements.

These atoms or ions have lost a significant number of electrons, leaving them in a high ionization state.

4.2.2 Spectral fitting procedures using `specfit`

By carefully defining the model components and using `specfit` effectively, it is possible to extract valuable information about the emission line profiles and continuum shape in our quasar spectrum. The general spectral fitting procedure we followed can be categorized into the following three main steps:

Step one: Preparing the data to be fitted. Before performing the spectral fitting using `specfit`, the spectra were changed to vacuum wavelength using the **IRAF** task `disptrans` and to rest frame using `dopcor`. The spectra also corrected for dispersion using `dispcor`, changed to **IRAF** image (.imh) by using `rfits` to ensure readability and scaled by multiplying it with appropriate scale factor using `sarith`.

Step two: Define the model file. The task `dbcreate` is used in conjunction with `specfit` to prepare the model, a text file with the model definition that allows building complex models by combining various mathematical functions. Database creation using the `specfit` task `dbcreate` mainly involves the database name, the component type to be used (power-law, user-defined, linear, Lorentzian, Gaussian, or absorption), the parameters in the components (like peak intensity, slope, central wavelength, width or velocity dispersion, and an optional fixed parameter string to account for asymmetry), and the value of each parameter, including the initial guess, end value, a step, tolerance, and values, giving a command whether the initial guess is free to vary between the two starting and ending values with "0" signifies free to vary and "-1" to be fixed with the initial guess.

The database file strongly depends on the region we want to fit, the availability of potential emission lines, and additional physical processes in the specified region for fitting. It is possible to edit this file once it has been created by taking measurements from the emission lines in the specified fitting window.

For the user-defined fitting function (userline), the list of synthetic files, their wavelength value, and the corresponding intensity are provided as a template to account for the model values. Also, while creating the database, the order of the components is very important, in which the power-law continuum is the first component, then userline, and then the fitting function used for the emission lines available in the quasar spectra. It is also possible to create a link between the components by following

some atomic physics laws. A sample database used in the fitting process is included in Appendix B.

Step three: Running `specfit`. Once the database is created by filling in the above appropriate components, the next step is to fit it with a simplex algorithm. `specfit` will iteratively adjust the parameters to minimize the difference between the model and the actual spectrum. Once we get this file, which is called the global fitting, we can use this output as an input for the next fitting with the Levenburg-Marquardt algorithm, which can be considered the final best fit of the input values with fewer iterations.

The actual model is the sum of all the components included in the database. The fitting process will result in three output files: the final file resulting from the fitting process, a plot file (*.sm*) for visualization, and "log-file" (*.com*) which gives the overall output of the fitting process, including files for the userline, the list of components used, and the resulting χ^2 value. By using the three output files, it is possible to analyze the output from `specfit`, including the fitted spectrum, the difference between data and the model fit (residuals), and final parameter values for further analysis and physical inference.

In general, by carefully defining the model components and applying `specfit` effectively, it is possible to extract valuable information about the emission line profiles and the continuum for a given quasar spectrum. This, in turn, provides insights into the physical processes within the quasars. Below, I will show the application of the fitting procedures for the optical and near-UV regions of our spectra separately.

4.2.3 Optical region

A clear distinction between Pop. A and Pop. B can be made by using the optical region Balmer line profile shapes and parameters. Pop. B sources often show Balmer line profiles with a redward asymmetry that can be modelled with a narrower, almost unshifted broad Gaussian function and a third very broad and redshifted component. The narrower component is likely associated with a virialized region. The broader one, which might still be virialized and could be associated with the reprocessed emission by the AD, is closer to the central SMBH (Sulentic et al., 2016). The latter feature is seen in Pop. B AGN only (e.g., Bachev et al., 2004; Marziani et al., 2003b). We used a Gaussian profile to fit all the emission line components since all our sources are Pop. B quasars. To get the best fit, we first used a simplex algorithm with an iteration up to 200 and afterwards, a Levenberg-Marquardt algorithm with a lower number of

iterations to ensure convergence to the global minimum χ^2 (Levenberg, 1944). The components included in our fitting of the optical region are:

- A power-law local continuum underlying the Hβ region to consider the thermal AD emission in optical (Shields, 1978). We defined the continuum by using three to four regions that are free of emission lines.
- A scalable FeII template for modelling the FeII_{opt} emission lines and accounting for the FeII_{opt} in optical (which is the integrated flux over 4484Å - 4686Å) that are blended with Hβ, as FeII has a large number of transitions producing overlapping and blended lines (Marziani et al., 2009).
- We assumed that the Balmer line Hβ has three components with Gaussian profiles, as appropriate for Pop. B sources (e.g., Marziani et al., 2010; Buttiglione et al., 2010):
  a) A narrow component (NC) that represents the NLR with low-density and more slowly moving clouds with narrow line width, which infers this region is far from the central SMBH;
  b) A broad component (BC) associated with the BLR with almost unshifted component and corresponds to dense and fast-moving clouds which indicates the proximity to the central SMBH;
  c) A very broad component (VBC) associated with a VBLR with high ionization and large column density that corresponds to broader and redshifted components.
- The [OIII] emission lines, represented by two Gaussian NC set at rest-frame plus two blue-shifted semi-broad components (SBC).
- A HeIIλ4686Å line when there were hints of its presence with a BC and/or VBC component.

The fitting for this region was done in a different wavelength range (see Table 5.1, Col. 3) for each object to account for the complex nature observed in some of the spectra. In the fitting procedure, the number of free parameters was reduced by assuming constraints related to emission lines coming from the same region. All the narrow lines were assumed to have roughly the same width and shift. The two [OIII] lines were assumed to have a flux ratio I([OIII]λ4959Å)/I([OIII]λ5007Å) of 1:3 (Dimitrijević et al., 2007). In all sources except PHL 923, 3C 94, and PKS 2344+09, the HeIIλ4686Å line contributes to the blue wing of Hβ, and we constrained the shift and FWHM of the HeIIλ4686Å VBC to be the same as Hβ VBC (Snedden and Gaskell, 2007).

The power-law that defines the continuum level and the FeII contribution obtained from the `specfit` analysis are plotted in Fig. 4.1 as red and green lines, respectively.

The plot of the other components from the `specfit` fitting for Hβ and [OIII] is presented in the right plots of Fig. 4.2, where the black line represents the rest-frame spectrum and the dashed magenta line shows the model fit. Residuals from the fittings are shown in the bottom panels. In 3C 94, PKS 0420-01, and 3C 179, with the highest redshift in the sample, the Hβ region is close to the edge of the observed spectrum and thus affected by more noise. This resulted in larger uncertainties in the determination of parameters related to the Hβ line profile.

4.2.4 UV region

The doublet MgII is located in a complex spectral region of the UV known as the small blue bump (e.g., Antonucci, 2012; Popović et al., 2019; Gaskell et al., 2022). To determine the parameters of the broad MgII line profiles, we carried out, as in optical, a multi-component fitting of the region of interest including:

- A power-law continuum underlying MgII, to approximate the thermal AD emission in UV region (e.g., Malkan and Oke, 1983).
- An FeII scalable template for accounting the FeII_{UV} (which is the integrated flux over 2200Å – 3090Å) emission lines blended with MgII. This template is based on CLOUDY simulations assuming ionization parameter $\log U = -2.25$, $\log n_{\text{H}} = 12.25$, solar chemical abundances and standard (i.e., Mathews and Ferland, 1987) AGN continuum. For practical purposes, it is analogous to the Bruhweiler and Verner (e.g., 2008) "best" template.
- A UV Balmer continuum, found to be important at $\lambda < 3646$Å (Kovačević et al., 2014; Kovačević-Dojčinović et al., 2017).
- As MgII is a doublet, we fitted the blended line component by using multiple Gaussian:

– Two NCs, accounting for the doublet of MgII at $\lambda 2796.35$Å and $\lambda 2803.53$Å, with an assumed ratio of 1.5:1.

– Two BCs, where the intensity ratio between the blue and red broad component of the doublet is taken to be 1.25, which is representative of the physical conditions observed in the BLR according to CLOUDY simulations (see details in Marziani et al., 2013a).

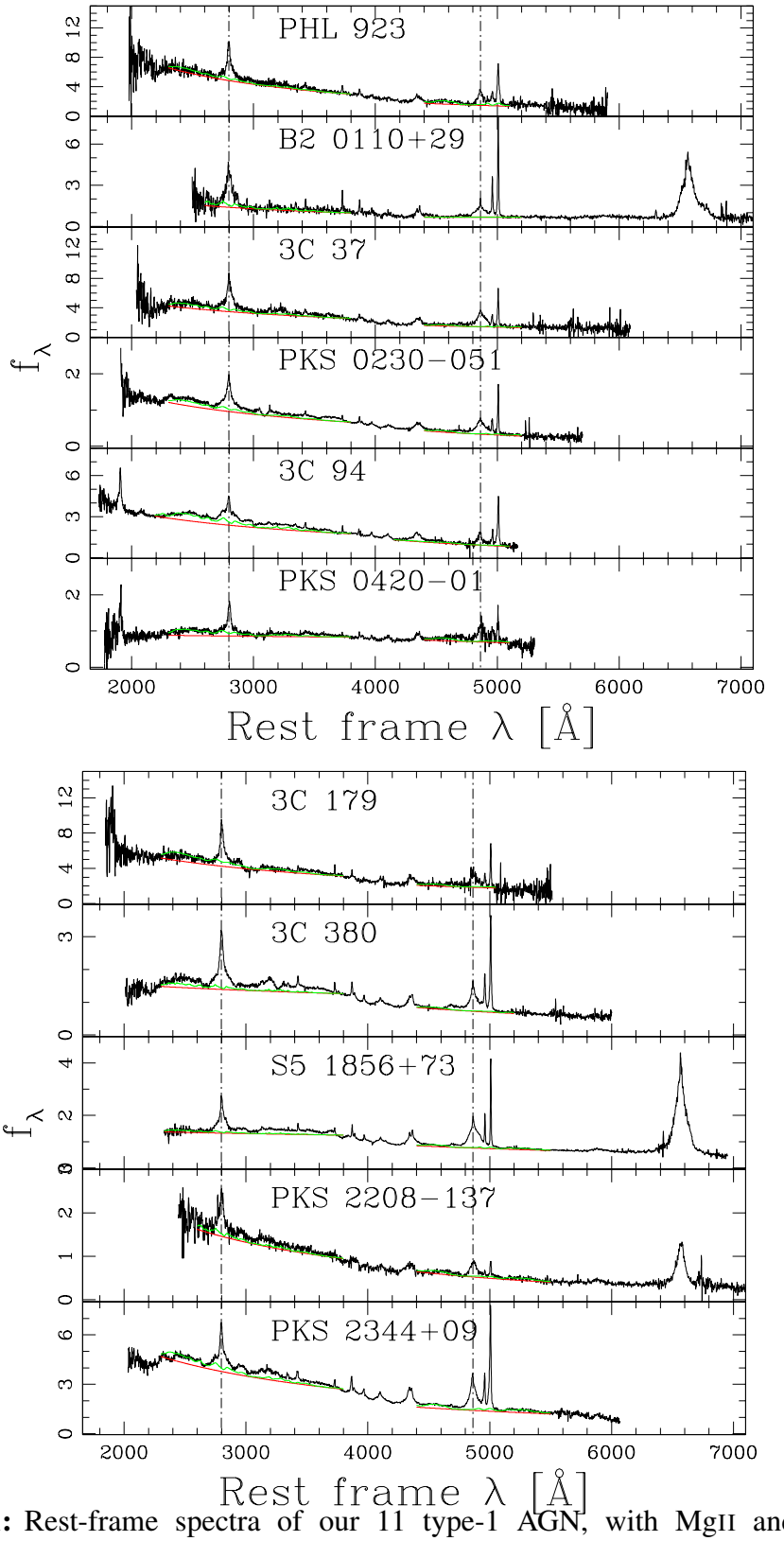

Figure 4.1: Rest-frame spectra of our 11 type-1 AGN, with MgII and Hβ regions after joining the two observed spectra. Abscissas are rest-frame vacuum wavelengths in Å and ordinates are specific flux in units of 10^{-15}ergs s^{-1} cm^{-2} Å^{-1}, except for PHL 923, B2 0110+29, 3C 37, and 3C 179 that are in units of 10^{-16}ergs s^{-1} cm^{-2} Å^{-1}. In each panel, the green line traces FeII emission and the red one represents the power-law continuum. Dot dashed vertical lines trace the rest-frame wavelength of Hβ and MgII.

– One VBC, instead of two, due to the small doublet separation of $\sim$8Å which is much less than the FWHM of the VBC components. This restrains us from separating two VBCs with the spectral resolution we have.

The fitting was done over a wide wavelength range, from 2600Å to 3800Å, to include the narrow LIL [OII]λ3727Å and to obtain measurements for FeII emission in UV, which is not well known for jetted sources (Marziani et al., 2018). We also included a Gaussian profile fitting for OIIIλ3133Å and the two HILs of [NeV] at $\lambda\lambda$3346,3426ÅÅ when the lines are present. For the low redshift quasars, with z < 0.4 (B2 0110+29 and PKS 2208-137), the MgII doublet measures are affected by a higher uncertainty because it is located at the extreme blue edge of the observed spectrum, which could usually imply more noise and a worse determination of the blue continuum level.

The overall fitting result for MgII spectral region for each object is shown in the left plots of Fig. 4.2 (adjacent to the Hβ fitting, in the right panels). Residuals from the fittings are also shown in the bottom panels.

4.3 Empirical and model fitting of the quasar 3C 47

The detailed fitting procedures for one of our sources, 3C 47, which shows a double-peaked profile, are detailed below. For this particular source, we implemented two types of fitting procedures for each of the observed spectra regions, Hβ, MgIIλ2800, Hα, CIVλ1549, and CIII]λ1909: i) a model fitting by using a relativistic Keplerian AD model in combination with Bayesian approach, and ii) an empirical multicomponent nonlinear fitting of the continuum and the emission features by using `specfit`.

4.3.1 Bayesian approximation and accretion disk model

Understanding the underlying physical processes that create the spectral features allows a more accurate interpretation of the data. The model-fitting approach leverages probabilistic models to represent the relationship between the data and the underlying physical phenomenon.

Applying the AD model as an explanation for the observed double-peaked profile using Chen and Halpern (1989) model fitting is traditionally done through optimization techniques, but, it is also possible to incorporate a Bayesian approach. The Bayesian approach is a statistical approach that incorporates prior knowledge or beliefs about the parameters (η) which represents the unknowns we are trying to estimate through prior probability distributions for fitting a

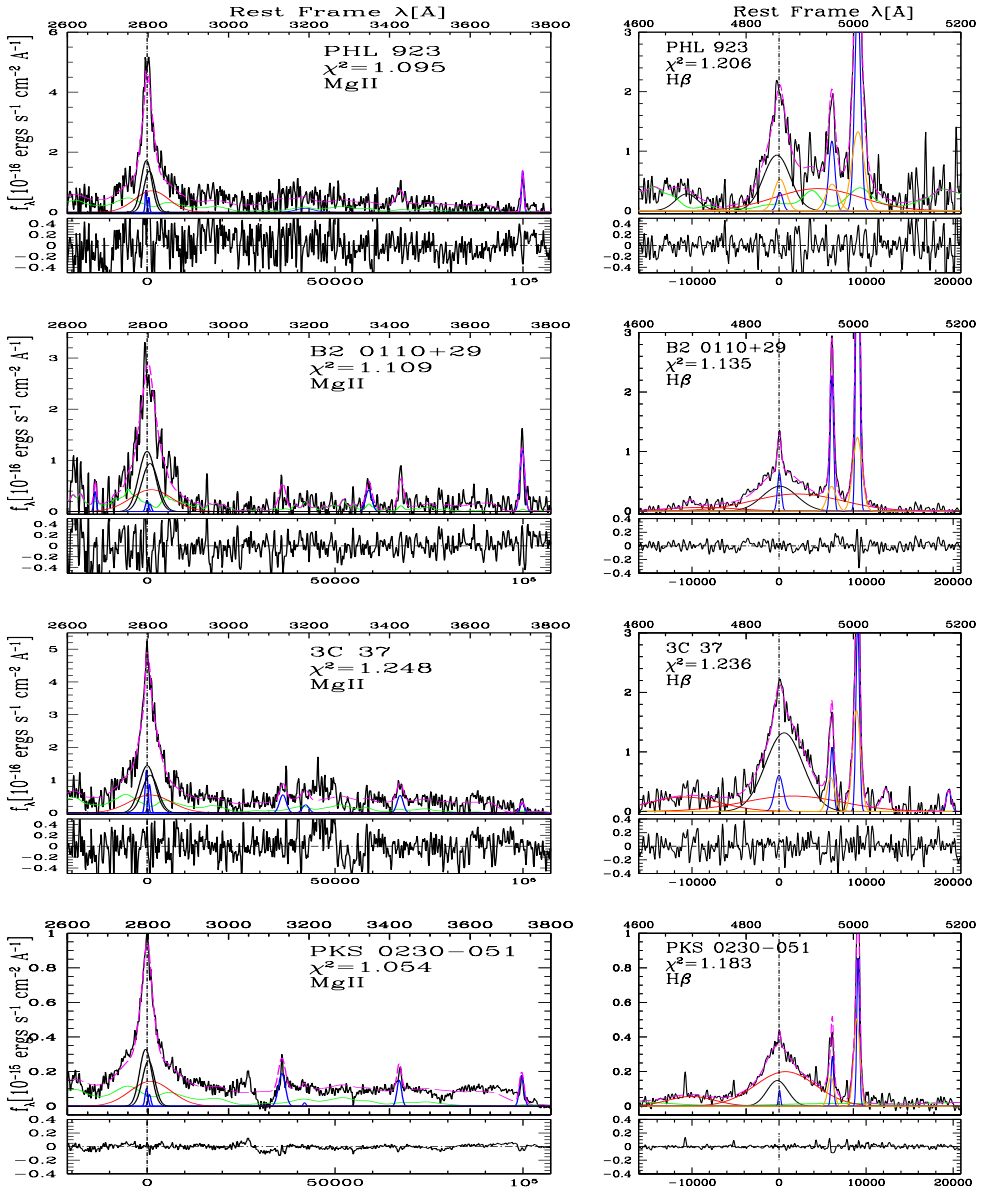

Figure 4.2: Multicomponent fitting results of our quasars `specfit` analysis in the region of MgII and Hβ lines (adjacent left and right panels), represented after subtracting the continuum. In both cases, the upper abscissa is rest-frame wavelength in Å and the lower abscissa is in radial velocity units. The vertical scales correspond to the specific flux in units of 10^{-15} ergs s^{-1} cm^{-2} Å^{-1}, and 10^{-16} ergs s^{-1} cm^{-2} Å^{-1} (PHL 923, B2 0110+29, 3C 37, and 3C 179) in both panels. Black continuous lines correspond to the rest-frame spectrum. The emission line components are FeII (green), VBC (red), BC (black), all the NCs as blue lines, and [OIII] SBC as an orange line. The dashed magenta line shows the model fitting. The dot-dashed vertical lines trace the rest-frame wavelength of MgII and Hβ. The lower panels show the residuals of the fit. The reduced χ^2 values indicated in each panel are estimated in a window of λ around the main lines, Hβ and MgII.

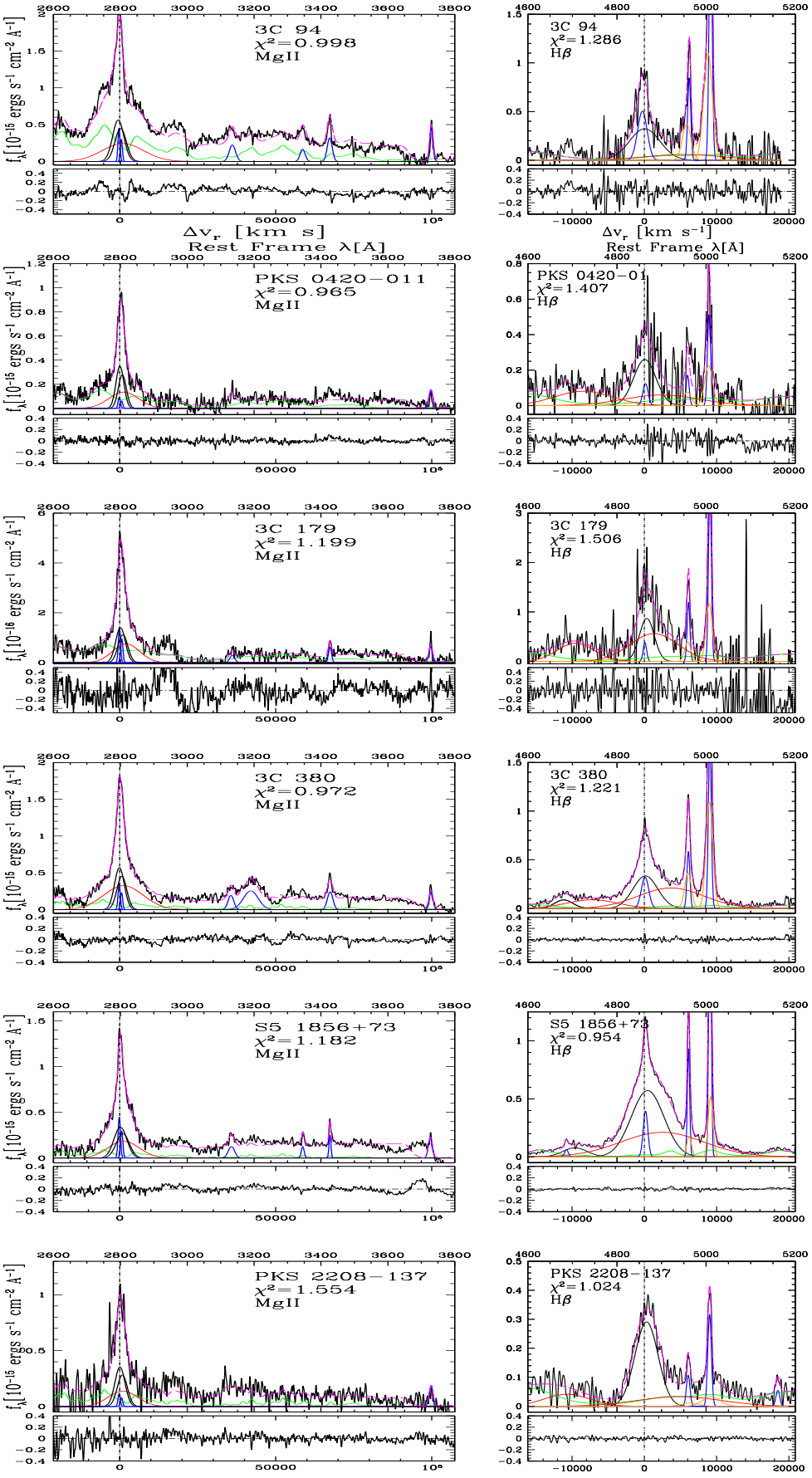

Results of the `specfit` analysis (cont.)

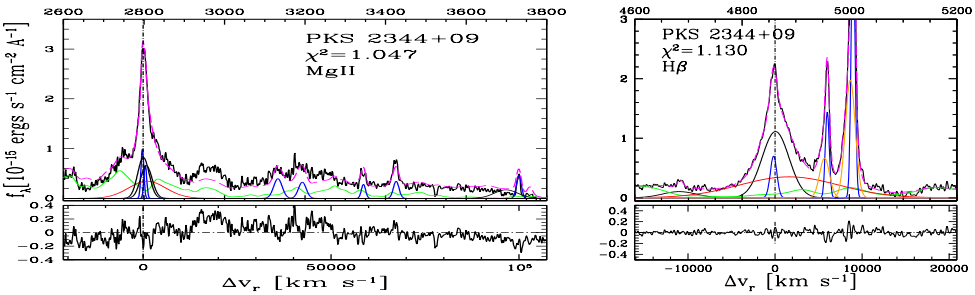

Results of the `specfit` analysis (cont.)

double-peaked emission line profile by using theoretical models. The Bayesian approach mainly involves model selection that determines the mathematical relationships between the variables, model parameterization, model fitting, comparison, and optimization to check for the goodness-of-fit metric using the chi-squared value. The model parameters are then adjusted iteratively to minimize the difference between the model and observed data to achieve the best possible fit.

As a scientific procedure, in the approach first, the probability distribution of the unknowns is determined after considering both prior knowledge and new data that reflects the most likely range of values for the parameters. The prior knowledge is directly involved with the expected ranges or typical values for the unknown parameters based on theoretical models, observations, or available literature, which leads to more accurate and informative results. The prior probability distribution is the knowledge about the expected ranges of the model parameters (η) which represents how probable different values are for each parameter before considering any new data or observations.

Second, the probability of observing the data given a specific set of parameter values is then calculated using statistical functions that are specific to the chosen models. In Bayesian inference, this is termed the likelihood and it represents the probability of observing the specific data given a particular set of parameter values for the model using the prior range of values. It tells how well a certain combination of parameter values in the model fits the actual data and measures the goodness of fit. Instead of being a range of values, the likelihood now becomes a combination of the likelihood function, a function of n parameters that determines the optimal parameter values that best explain the observed profile.

Lastly, the posterior distribution, which combines the prior distribution and the likelihood using Bayes' theorem to get the posterior distribution, is performed. The posterior distribution represents the probability distribution of each model parameter (η) after considering both the observed data and any prior knowledge about those parameters. Baye's theorem provides a framework to combine the

likelihood with the prior distribution to obtain the posterior distribution. This posterior distribution provides a more comprehensive picture of the likely parameter values of the model compared to just the likelihood alone. This distribution incorporates the strengths of both the data and the prior knowledge for understanding the most likely values of the parameters, as well as the uncertainty associated with those estimates. In essence, the posterior distribution is the outcome we are interested in when performing Bayesian inference using a specific model, like the Chen and Halpern (1989).

4.3.1.1 Corner plots

In Bayesian inference, corner plots are powerful tools for interpreting the results of the Bayesian analysis as a graphical tool to visualize the posterior distribution of multiple parameters in the context of fitting a model. It also provides a summary of the parameter space and the relationships between the different components, leading to a more comprehensive understanding of the model fit and the underlying physical phenomena. Furthermore, it provides a concise way to visualize the posterior distributions of multiple parameters in a single plot, making it easier to compare them and identify trends in a compact way to see the marginal distributions and pairwise relationships (see Fig. 4.3):

- **Marginal distributions (diagonals):** Each diagonal panel in the corner plot shows a histogram representing the probability distribution of a single parameter after considering the data and prior information to see the range of likely values for each parameter. The diagonal elements (from top left to bottom right) represent individual posterior probability distributions for each parameter. A wider spread indicates a larger range of probable values for that parameter, and a tighter spread suggests a more constrained value based on the data and prior information. The shape of the distribution also reveals insights about the parameter, for instance, a symmetrical distribution asserts the absence of inherent bias towards a particular value.
- **Pairwise relation (off-diagonal):** The remaining elements (except the diagonal) display scatter plots showing how two specific parameters vary with each other according to their posterior probability distributions. Each scatter plot shows how two specific parameters vary with each other according to their posterior probability distributions, and depicts scatter plots between each pair of parameters. The spread and direction of the points in these plots indicate the strength and direction of the correlation between the parameters.

  A diagonal line represents the parameters are relatively independent and no significant influence on each other's values is seen, a positive slop

indicates an increasing value of one parameter tends to correspond with increasing values of the other, negative correlation indicates the increasing values of one parameter tend to correspond with decreasing values of the other, and no clear trend or a random scatter pattern indicates weak or no correlation between the parameters in the posterior distribution.

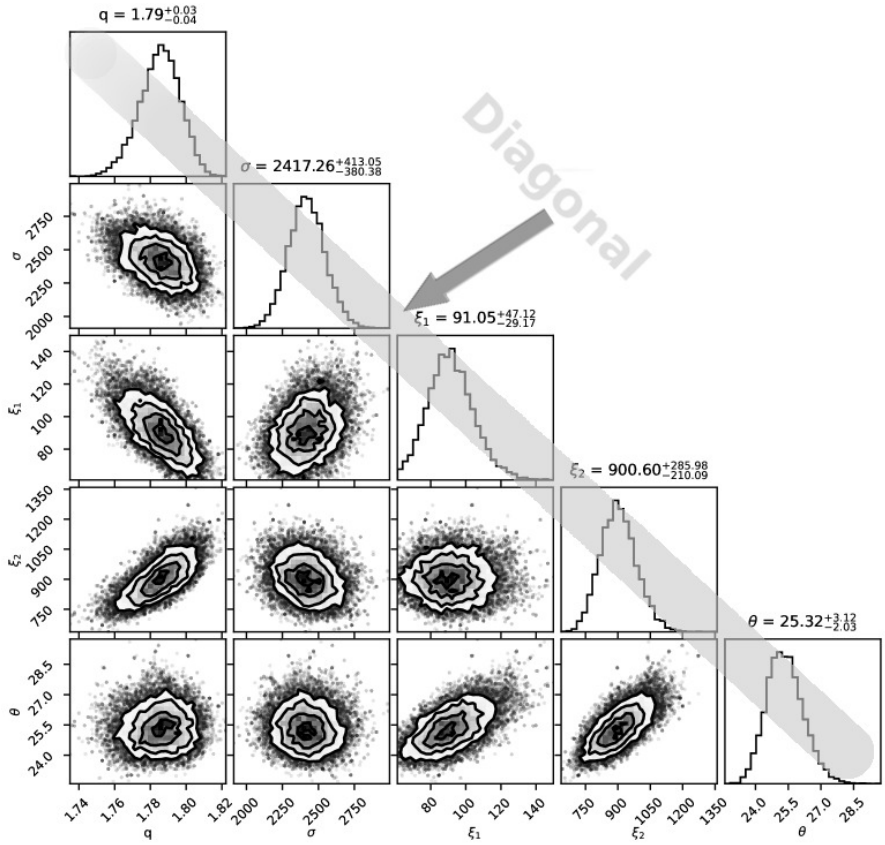

Figure 4.3: Corner plot showing the results of our MCMC parameter estimation for the Keplerian AD model of Chen and Halpern (1989), the histograms on the diagonal represent the probability distribution of a single parameter or the marginalized posterior densities for each parameter. The off-diagonal display scatter plots show how two specific parameters vary with each other according to their posterior probability distributions [Image: the result of Bayesian analysis used in this thesis].

By analyzing both the posterior distributions and their relationships visualized in a corner plot, valuable insight into the applied model, the most likely range of parameter values, their potential interdependence, and the overall confidence in explaining the observed line profile can be obtained.

4.3.1.2 Software programs for performing Bayesian fit

Several software packages and libraries are commonly used for Bayesian analysis and generating corner plots. The most popular software is the `emcee`, (often referred to as the `MCMC Hammer`), developed by Goodman and Weare (2010) is a popular and powerful Python library for performing probability distributions in Bayesian inference using the Monte Carlo Markov Chain (`MCMC`) approach, where we obtained model approximations using the `emcee` for high-dimensional problems (e.g., Foreman-Mackey et al., 2013). It utilizes multiple walkers that efficiently explore the parameter space for a more thorough and efficient exploration of parameter spaces in a complex problem with many parameters. The workflow for using the `emcee` for model fitting involves defining a model, specifying the likelihood function, defining the prior distributions, setting up the emcee, running the `MCMC` for sampling the posterior distribution, and analyzing the results using plots like a corner plot. By utilizing `emcee` effectively, it is possible to get efficient Bayesian inference for complex astrophysical models and obtain reliable estimates of the most likely parameter values and their uncertainties.

For the Bayesian inference, to comprehensively explore the impact of different prior assumptions on the final results, two different prior functions ($p(\eta)$) for each model parameter can be used:

- **Uniform prior.** This prior embodies a scenario where we have minimal prior knowledge about the specific values of the parameters and assigns an equal probability to all possible values within a defined range for each parameter. This essentially allows the data to play a more significant role in shaping the posterior distribution, and with minimal prior influence, the posterior will more closely reflect the observed data patterns. Mathematically, the probability density function (PDF) is constant across that range, and the actual formula for a uniform prior distribution depends on the parameters we are dealing with. For a continuous parameter (η) defined within a range from η_1 (minimum value) to η_2 (maximum value), the PDF of a uniform prior is:

$$p(\eta) = \begin{cases} \frac{1}{\eta_2 - \eta_1}, & \text{if } \eta_1 \leq \eta < \eta_2 \\ 0, & \text{otherwise} \end{cases} \tag{4.26}$$

  This formula essentially states that the probability density ($P(\eta)$) is constant across the range (η_2 - η_1). The total probability integrates to 1 by multiplying this constant probability density with the range (η_2 - η_1).

- **Gaussian distribution priors.** In Bayesian inference, a Gaussian distribu-

tion can be used as a prior probability distribution to represent the initial beliefs or assumptions about the value of a parameter η before incorporating any data. In such a distribution, the probability is highest around a central value (mid-value) and gradually tapers off on either side. The width of the distribution, controlled by the σ reflects how strong is the initial guess, a narrow width indicates a strong belief in a specific value range, while a wider width indicates more uncertainty. The formula for a Gaussian distribution, also known as a normal distribution, is:

$$p(\eta) = \frac{1}{\sigma_\eta \sqrt{2\pi}} e^{-\frac{(\eta-\eta_c)^2}{2\ \sigma_\eta^2}} \tag{4.27}$$

where $p(\eta)$ represents the PDF of the distribution at a specific value of η with η_c and σ_η describing the centre and spread of each probability $p(\eta)$ prior, in which σ represents the standard deviation of the distribution.

By understanding the impact of both uniform and Gaussian priors, it is possible to make informed choices when performing Bayesian inference and effectively utilize prior knowledge to arrive at a more robust and informative posterior distribution. In such a way, the total prior is then the product of each parameter prior distribution $p(\eta)$, and the product is expressed as:

$$\prod_\eta p(\eta), \text{with } \eta \in \{q,\ \sigma/v_o,\ \xi_1,\ \xi_2,\ \theta \tag{4.28}$$

Total prior distribution ($p(\eta)$) represents the overall probability distribution of all the model parameters η before considering any new data or observations. It reflects the beliefs or assumptions about the likely range of values for each parameter. The individual parameter prior distribution ($p(\eta_i)$) refers to the prior probability distribution for a single parameter (η_i) within the model. It specifies how probable different values are for that specific parameter before incorporating any data. The Product of individual Priors is then the total prior distribution as indicated in Eq. 4.28, and it signifies that the prior knowledge about each parameter is independent of the values of other parameters. In simpler terms, the initial belief about one parameter doesn't influence the belief about another.

4.3.2 Spectral analysis for 3C 47

The detailed fitting procedures for one of our sources, 3C 47, which shows a double-peaked profile, are described in this section. For this particular source, we implemented three types of fitting for each of the observed spectral regions, Hβ, MgIIλ2800, Hα and the HILs such as CIVλ1549 and CIII]λ1909:

I) An empirical fitting of the observed spectra by using `specfit` to represent the observed broad profile of each double-peaked line (i.e., for Hβ, MgII and Hα). We assumed two Gaussian BCs of the same FWHM (corresponding to the blue and red components of the double-peaked profile) and an additional VBC to represent the double-peaked profile and the fitting was done by the same procedure discussed above (Sect. 4.2.2). The resulting fitting is then used as an input for the fitting of the profiles using Bayesian techniques (see Sect. 4.3.1) to estimate the χ^2 by using the model output (discussed below) as an expected value and the rest-frame spectra plus the resulting noise from the empirical fitting.

II) A model fitting by using a relativistic Keplerian AD model in combination with the Bayesian approach to get the best model values that can fit the double-peaked line profiles observed in our spectra with minimum uncertainty. Such a model was intended to fit the double-peaked profiles observed in the spectra. The detailed model fitting procedure is given in Sect. 4.3.2.1 below, and

III) A second empirical multicomponent nonlinear fitting of the continuum and the emission features by using `specfit`. In this case, while applying `specfit`, we replaced the double-peaked profiles with the model output flux as a user-defined component and re-run `specfit` by including the non-disk components like NCs. Again, the detailed procedure is given in Sect. 4.3.3 below.

4.3.2.1 Model fitting using Bayesian approach

We applied the model of Chen and Halpern (1989), in which AD emission surrounding a single SMBH is assumed to be the origin of double-peaked broad emission lines observed in our spectra. The model assumes that a uniform axisymmetric disk model produces double-peaked line profiles, with the blue peak stronger than the red peak due to Doppler boosting. In the Chen and Halpern (1989) model, the emission is driven by illumination of the outer part of the disk from an elevated or vertically extended structure. This structure could be an ion-supported torus that photoionizes the geometrically thin outer disk to produce the observed disk line profiles, as detailed in Sect. 2.7.1.1. We used the integral expression for the line profile of an optically thick AD (Eq. 7 of Chen and Halpern (1989), see the equation in Eq. 2.1) to fit the double-peaked profiles observed in our spectra.

The fit of the observed broad-line profiles of 3C 47 to the AD model was carried out by using the Bayesian method (detailed in Sect. 4.3.1) independently for each spectral region MgII, Hβ, and Hα. The input double-peaked lines

Table 4.1: Model parameter input list.

Parameters	Range of values
q	1.3 – 2.5
σ/v_0	$1.5\text{x}10^{-3}$ – $1.1\text{x}10^{-2}$
$\xi_1(r_g)$	40 – 300
$\xi_2(r_g)$	100 – 2000
θ (degrees)	15 – 42

were obtained after removing the power-law continuum, the FeII template, and the narrow components (NCs) obtained by using the empirical fitting results obtained by treating the double-peaked profiles as separate broad components.

A first estimate of the parameters $\{q,\ \sigma/v,\ \xi_1,\ \xi_2,\ \theta\}$ was obtained by evaluating the χ^2 of the fit of the broad profiles to the function defined by Eq. (7) of Chen and Halpern (1989) for several thousand combinations. This was done to obtain the physically possible range of values that are compatible with the observed double-peaked profiles, as well as initial estimates for each parameter. After inspecting the distribution of χ^2 for MgII, Hβ and Hα, we can ensure that for values outside the range of the parameters given in Table 4.1, χ^2 grows monotonically outward. A nonlinear least-squares (as well as a maximum likelihood) fit was obtained by using the midpoints of the ranges as initial values, resulting in parameter solutions that are contained well inside the ranges in all the lines.

In addition, we applied `MCMC` approach, where we obtained model approximations using the `emcee`: The `MCMC` hammer package (Foreman-Mackey et al., 2013), which is based on slight modifications to the Metropolis-Hastings method. For the Bayesian inference, we used two different prior functions ($p(\eta)$): 1) a uniform prior for each AD model parameter with Eq. 4.26 and the range of values listed in Table 4.1 and 2) Gaussian distribution priors with Eq. 4.27 with central values corresponding to the midpoints and σ guaranteeing the full range of parameters to be sampled.

In our case, the two sets of priors provide the same results with negligible differences between them, and they are well within the posterior distributions. Fig. 4.4 shows the corner plot (left panel) and 250 randomly selected posterior solutions (right) for the AD model (green lines) over the broad double-peaked profile (red) of MgII. The corner plot shows the covariances and posteriors of the five parameters for the fit, in which we display at the top of each posterior distribution the median value of each parameter and the errors measured as per-

Table 4.2: Summary of the output parameters from the Bayesian inference model fittings.

	MgII	Hβ	Hα
Parameters (1)	Median (2)	Median (3)	Median (4)
q	$1.64^{+0.01}_{-0.01}$	$1.79^{+0.03}_{-0.03}$	$1.62^{+0.01}_{-0.01}$
σ^a	1747^{+163}_{-139}	2445^{+404}_{-368}	2223^{+120}_{-120}
$\xi_1(r_g)$	131^{+24}_{-22}	105^{+43}_{-36}	103^{+13}_{-13}
$\xi_2(r_g)$	1632^{+236}_{-204}	1013^{+340}_{-242}	1472^{+148}_{-130}
θ(degrees)	$32.6^{+2.4}_{-2.0}$	$26.7^{+3.1}_{-2.5}$	$30.1^{+1.3}_{-1.2}$

Note: $^a\sigma$ is in units of km s^{-1}. The uncertainties in each parameter correspond to the confidence interval corresponding to 0.13% and 99.87% of the distribution of obtained values shown in the corner plots (Figs. 4.4 and 4.5).

centiles at the 0.135% and 99.865% levels (which correspond to 3σ errors in a normal distribution). In Fig. 4.5 we show the corner plots for Hβ (left) and Hα (right). Table 4.2 contains the final measurements of the five model parameters for MgII (Col. 2), Hβ (Col. 3) and Hα (Col. 4) and the corresponding uncertainties.

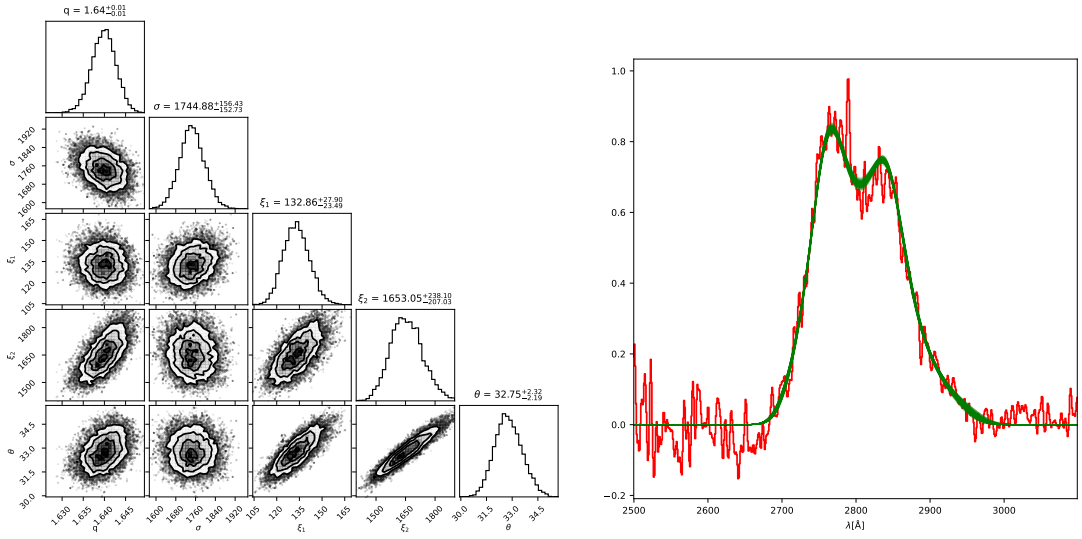

Figure 4.4: Left: Corner plot showing the posterior distributions of the five AD parameters for MgII as histograms, along with covariance maps between the parameters. Right: 250 randomly selected posterior solutions from the Bayesian fit (green) superimposed onto the observed broad profile (red) of MgII.

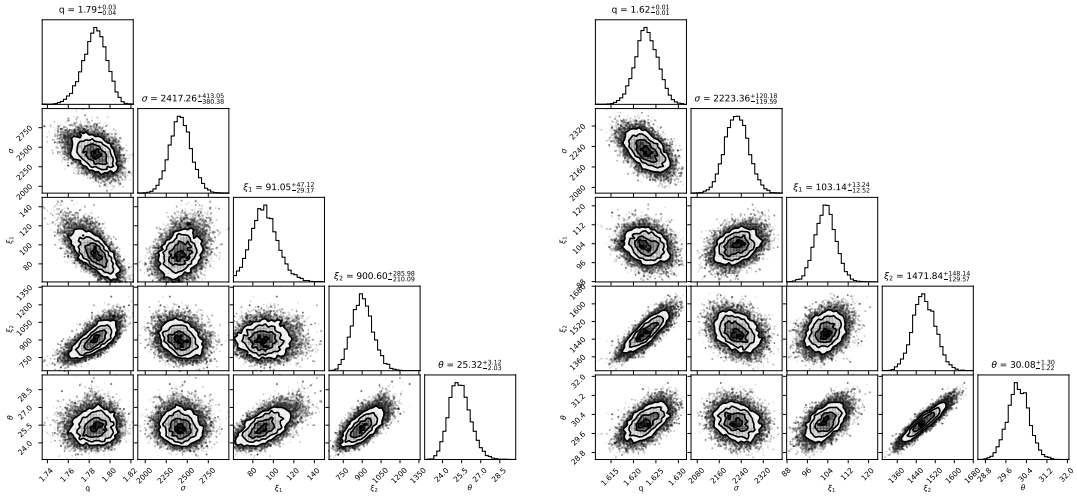

Figure 4.5: Corner plots for Hβ (left panel) and Hα (right).

4.3.3 Empirical fitting for 3C 47

4.3.3.1 MgII, Hβ and Hα

A nonlinear multicomponent fitting by using `specfit` was again implemented to obtain a global fitting, but in this case, the resulted AD model output flux was introduced to represent the two broad components and the additional VBC from the above procedure (Sect. 4.3.2.1) to represent the FP. While doing the fitting, we followed the same method as described in Sect. 4.2.2. We also included a power-law local continuum, an FeII template to model $\mathrm{FeII_{opt}}$ and $\mathrm{FeII_{UV}}$ using the templates from Marziani et al. (2009) and Bruhweiler and Verner (2008), respectively, and an additional UV Balmer continuum. In addition, to represent the non-disk emission components, we included Gaussian profiles to fit the narrow and semi-broad components (NC + SBC) from the NLR. All the narrow lines were assumed to have roughly the same width and shift values.

In the Hβ region, the overall fitting was made in the wavelength range of 4400Å – 5300Å. This includes, apart from the AD broad component, the [OIII]$\lambda\lambda$4959,5007 and HeIIλ4686 lines in addition to the Hβ NC + SBC. The near-UV MgII region was fit in the wide wavelength range from 2600Å – 3800Å, which includes the doublet NCs of MgII, and OIIIλ]3133Å, [OII]λ3727Å , and the two HILs of [NeV] at $\lambda\lambda$3346,3426ÅÅ.

The Hα region final fit was made from 6100Å – 6900Å. To obtain the best empirical fitting of the Hα + [NII] blend, we included, together with the AD model output representing the broad profile, Gaussian NC + SBC for Hα, [OI]$\lambda\lambda$6302,6365 and for the doublets of [NII]$\lambda\lambda$6549,6585 and [SII]$\lambda\lambda$6718,6732. A power-law that defines the continuum and the FeII template were also added.

To minimize the number of free parameters for the emission lines coming from the same region, the flux ratio and their respective wavelength separation of the components are also constrained by atomic parameters. The two [OI]$\lambda\lambda$6302,6365 doublet lines were assumed to have a flux ratio I([O I]λ6302)/I([OI]λ6364) of 3:1. The two [NII] lines were set to have a flux ratio I([NII]λ6549)/I([NII]λ6584) of 1:3. For the [SII]$\lambda\lambda$6718,6732 line, we kept the flux ratio between the doublets to be unity. Regarding the line width and shift, all the narrow lines were assumed to have roughly the same width and shift values.

The resulting `specfit` fits, including the AD model for the observed broad profiles as well as the non-disk emission components with a minimum χ^2 in the regions of Hβ, Hα, and MgII, are shown in Figures 4.6, 4.7, and 4.8, respectively, on a rest-frame wavelength scale.

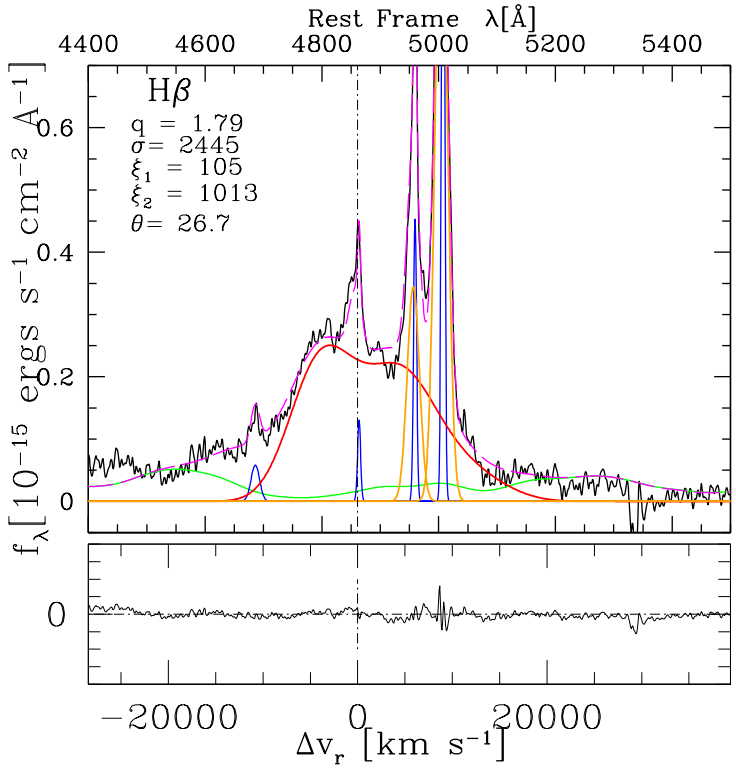

Figure 4.6: Multicomponent empirical `specfit` analysis, including the AD model fitting result in the Hβ region after subtracting the continuum from the best fit. The upper abscissa is the rest-frame wavelength in Å, and the lower abscissa is in radial velocity units. The vertical scale corresponds to the specific flux in units of 10^{-15}ergs s^{-1} cm^{-2} Å^{-1}. The emission line components used in the fit are FeII (green), the broad AD model representing the fit for the broad double-peaked profile (red line), SBC (orange), and NC (blue). The black continuous line corresponds to the rest-frame spectrum. The dashed magenta line shows the final fitting from `specfit`. The dot-dashed vertical lines trace the rest-frame wavelength of Hβ. The lower panel shows the residual of the empirical fit.

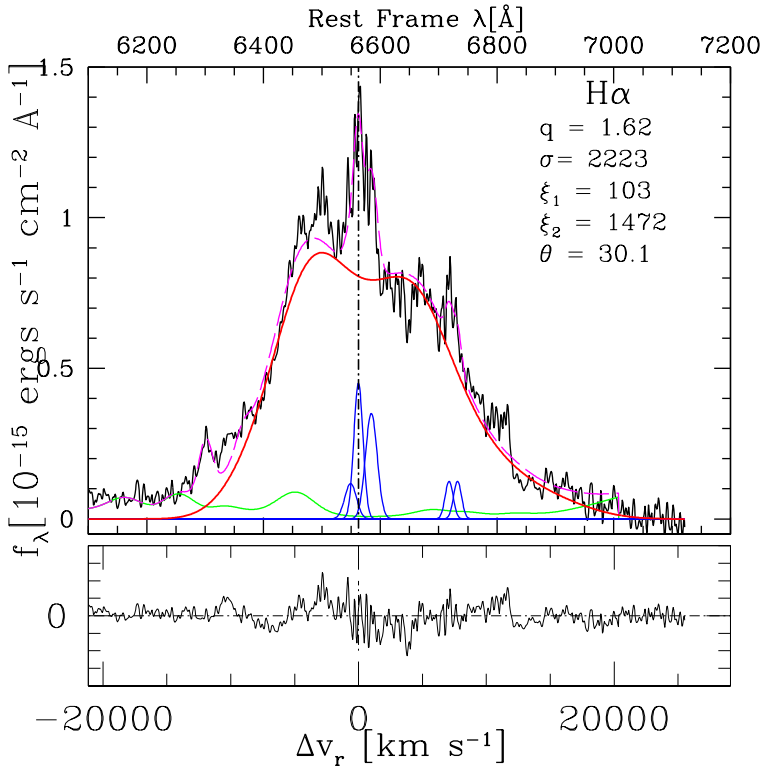

Figure 4.7: Multicomponent empirical analysis and AD model fitting results in the Hα region. The description is as in Fig. 4.6**.**

4.3.3.2 Civλ1549 and Ciii]λ1909

Theoretical predictions and studies of double-peaked profile sources indicate that the disk predominantly emits LILs (e.g., Balmer lines, MgII and FeII). High-ionization species such as CIVλ1549 may not be produced and may lack double-peaked profiles, even when the LILs do show them (e.g., Collin-Souffrin and Dumont, 1990; Eracleous and Halpern, 1994; Eracleous, 1998; Tang and Grindlay, 2009).

To perform the multicomponent non-linear Gaussian fitting with the use of `specfit` for these line profiles, we used three user-defined components that are capable of representing the double-peaked profiles: CIVλ1549, HeIIλ1640 and CIII]λ1909 regions. We created the three user-defined components by using the best-fit model output parameters of the well-studied Hβ line, detailed in Sec. 4.3.2.1. The CIVλ1549 line frequently shows blue-shifted profile, and the fitting was done in the spectral window 1420Å – 1705Å. It is modelled by the contribution of the AD, along with prominent components including a symmetric Gaussian and two blueshifted CIVλ1549 components associated with a failed-wind scenario, NIVλ1483, 5 absorption lines eating away the NLR contribution to CIVλ1549, a blueshifted SBC for HeIIλ1640, and OIIIλ1663. For the CIII]λ1909 line profile, we considered the spectral window 1850Å –1920Å,

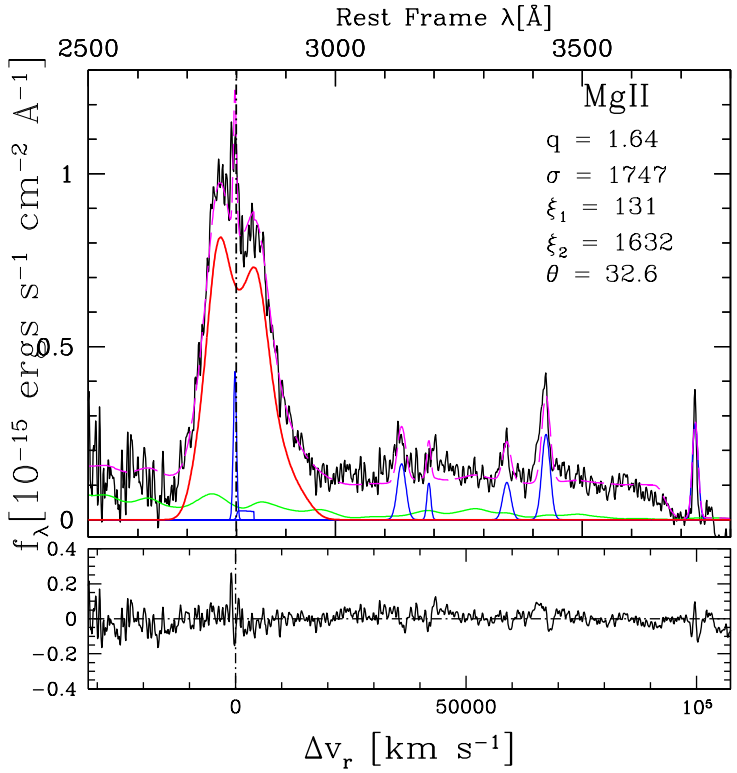

Figure 4.8: Multicomponent analysis and AD model fitting results in the MgII region. The description is as in Fig. 4.6.

which includes two AlIII$\lambda\lambda$1857,1862, SiIII]λ1892, CIII]λ1909 and two absorption lines. We also assumed an NC for CIII]λ1909. The resulting fit for the CIVλ1549 and CIII]λ1909 regions are shown in Figures 4.9 and 4.10, respectively. A discussion of the assumptions and the resulting fitting is presented in Sect. 6.4.4.

4.4 Full profile analysis

Besides the multicomponent spectral fitting to account for the individual components of the emission lines of Hβ and MgII regions, a complementary measurement that describes the full broad profile (FP) is required. The FP measures the parameters of the broad and very broad emission lines as a single measurement to get a single global representation of the quasar profile for further analysis. The parameterization of the FP has been made by its equivalent width (EW), FWHM, centroids at different fractional line intensities ($c(i/4)$ for i = 1, 2 and 3), asymmetry (A.I.) and kurtosis (K.I) indexes. The latter three quantities are used as defined according to Zamfir et al. (2010) as in Eqs. 4.1, 4.2, and 4.3. This information helps to infer the line width to indicate the velocity range of the gas emitting the line, the total amount of light emitted by the line relative

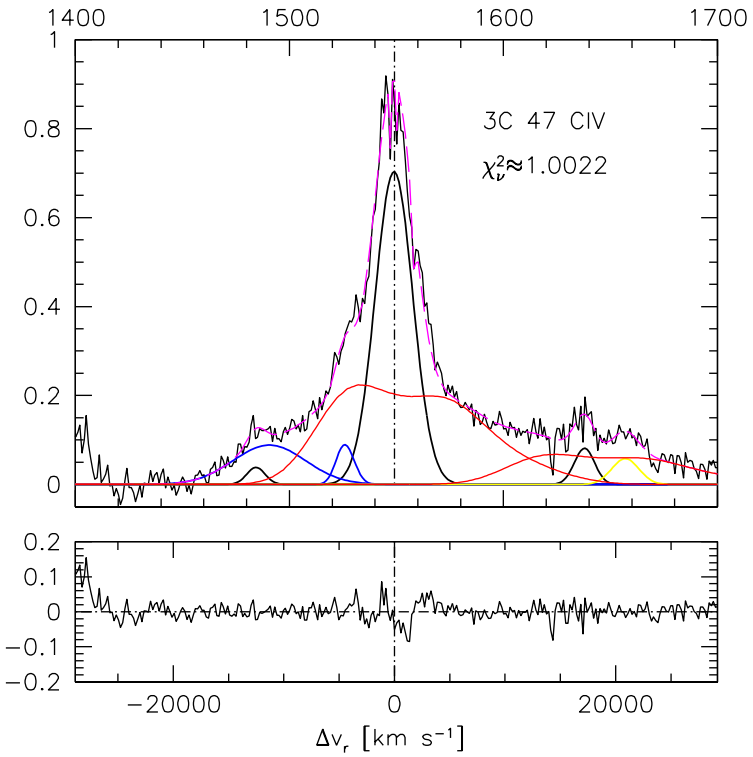

Figure 4.9: Multicomponent empirical analysis and AD model fitting results for CIVλ1549 and HeIIλ1640. The black line corresponds to the rest-frame spectrum, and the emission line components used in the empirical fit are the blueshifted components (blue) and BC (black). The red line represents the model fitting result for CIV and HeIIλ1640 by using the AD model fitting parameters of Hβ. The dashed magenta line shows the final model fitting from `specfit`. The lower panel shows the residuals.

to the continuum, and the asymmetries present in the line profile to provide clues about the geometry and dynamics of the BLR. From the nonlinear multicomponent fitting and the FP analysis measurements, clear information about the gas kinematics, physical conditions, radio loudness, and physical parameters can be estimated.

For the 11 sources observed in phase I, except 3C 47, the FP is assumed to be the sum of a BC and VBC for Hβ, and a NC and an additional SBC that accounts for the blueward asymmetry in [OIII]. In the case of the MgIIλ2800 doublet, the FP implies the doublet broad components are assumed unresolved and appear as a single line, i.e., they consist of two BC and one VBC (2BC + VBC). The FWHM of the individual components of the doublet can be estimated by subtracting 300 km s^{-1} to the FWHM measured on the full profile (Trakhtenbrot and Netzer, 2012). For the double-peaked profile (3C 47), the full broad profile is considered to be the model-fitting result that represents the broad profile of the observed spectra without including the NCs.

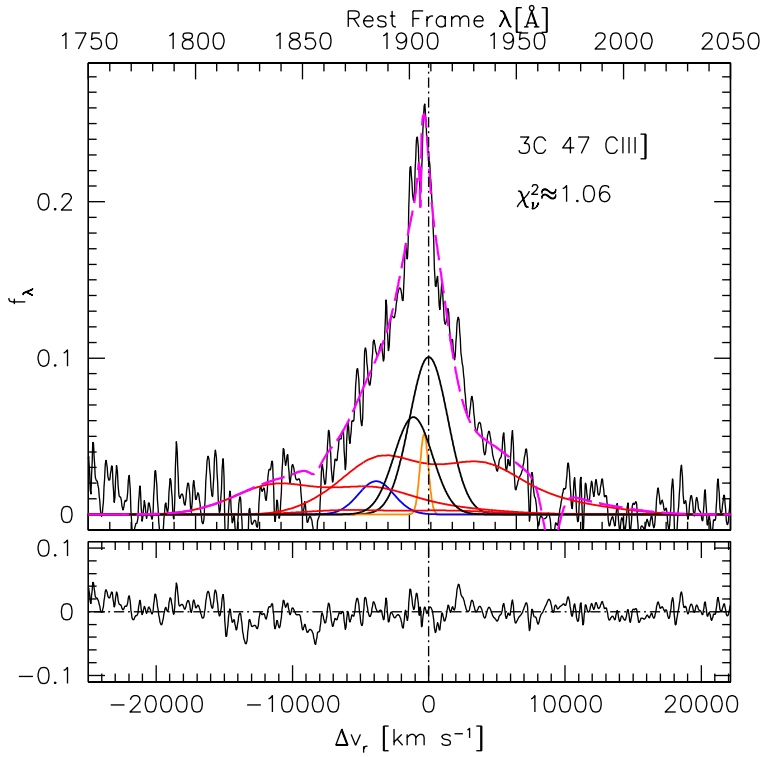

Figure 4.10: Multicomponent nonlinear empirical `specfit` and AD model fits for CIII]λ1909 blend, following the same approach as employed for CIVλ1549. The axes and the components are the same as in Fig. 4.9, except for the red line, which represents the AD model fitting result for CIII]λ1909, SiIII]λ1892, and the sum of the two AlIIIλ1857 components by using the parameters appropriate for the MgII. The resulting SiIII]λ1892 is barely visible. The black lines trace the BC components of CIII]λ1909 and SiIII]λ1892. The dot-dashed vertical line identifies the rest-frame wavelength of CIII]λ1909.

From the nonlinear multicomponent fitting and the FP analysis measurements, clear information about the gas kinematics, physical conditions in the emitting region, the 4DE1 parameters, and physical parameter estimation using the FP measures can be discussed in the upcoming chapters, Chapter 5 and 6.

4.5 Error estimation

We made a coarse estimate of the fractional errors in the fluxes and relative intensities of the lines by using the interactive IRAF task `splot`. We empirically define extreme levels for line bases or continuum placements and assign them a confidence limit of $\pm$ 2σ. The range of uncertainty and the typical errors that we derived depend on whether a feature was extended (such FeII$_{opt}$ and FeII$_{UV}$ emission) or sharp and prominent ([OIII]λλ4959,5007 narrow lines) or faint affected by a much stronger line component (i.e., HeIIλ4686Å). Con-

sidering $\mathrm{FeII_{opt}}$ emission, the uncertainty ranges between 20% and 50% at 1σ confidence level, the latter for quasars with extremely faint FeII emission like B2 0110+29 and S5 1856+73. For the weakest quasars in $\mathrm{FeII_{opt}}$, a 50% uncertainty means that the $\mathrm{FeII_{opt}}$ emission is not present.

For $\mathrm{FeII_{UV}}$, we have uncertainties between 15% and 35% the latter for relatively faint quasars. The Balmer continuum is affected by a comparable fractional uncertainty, as it is modelled over the same spectral range of $\mathrm{FeII_{UV}}$ emission. Considering the individual components of Hβ, the NC has uncertainties between 15% and 50%. The larger uncertainty applies to the case where the NC is weaker, i.e., for QSOs like 3C 179 and S5 1856+73: a small change of the BC translates into a much larger fractional change for the NC. This can also be seen from the intensity ratio between the NC and BC. For the two QSOs with larger uncertainties (3C 179 and S5 1856+73), this ratio is, $\mathrm{I_{NC}/I_{BC}} \approx 0.125$ and 0.097, respectively. The prominent BC of Hβ is affected by a small uncertainty between 10% and 20%. For the sharp, narrow, and well-defined [OIII] line, the uncertainty in flux is between 5% and 10%. For the UV lines, the MgII NC, in most cases we have uncertainties between 15% and 30%. The larger uncertainty is associated with cases in which the NC merges with the BC. For the prominent MgII BC, the uncertainty is estimated between 10% and 20%. The uncertainties for the BC can also be used for the VBC since the two components are usually of comparable strength.

Errors for the FP parameters have been estimated taking into account the effect of variation in the continuum on the profile parameters by assuming a $\pm$ 5% variation in the continuum.

The uncertainties in each measurement were derived with a quadratic error propagation formula, in which for any function $X = f(u,v,...)$, the variance of $\mathrm{x}(\sigma^2_{(x)})$ is given as:

$$\sigma^2_{(x)} = \sigma^2_u \left(\frac{\partial X}{\partial u}\right)^2 + \sigma^2_v \left(\frac{\partial X}{\partial v}\right)^2 + ... \tag{4.29}$$

The variance in the centroid velocity measures, the AI, and KI is derived using Eq. 4.29 and the required profile parameters we want to estimate the uncertainty: centroid velocity shift, AI, and KI using their expression from Eqs. 4.1, 4.2, and 4.3 as follows:

$$\sigma^2_{c(x)} = \left[\frac{c^2}{4\lambda_0^2}\right][\sigma^2_{p,r}(x) + \sigma^2_{p,b}(x)], \tag{4.30}$$

$$\sigma^2_{A.I} = \frac{4}{(\lambda_r(\frac{1}{4}) - \lambda_b(\frac{1}{4}))^2} \left[\sigma^2_{peak} + \sigma^2_{r,p}(\frac{1}{4}) \left(\frac{\lambda_b(\frac{1}{4}) - \lambda_{peak}(\frac{1}{4})}{\lambda_r(\frac{1}{4}) - \lambda_b(\frac{1}{4})} \right)^2 + \sigma^2_{b,p}(\frac{1}{4}) \left(\frac{\lambda_r(\frac{1}{4}) - \lambda_{peak}(\frac{1}{4})}{\lambda_r(\frac{1}{4}) - \lambda_b(\frac{1}{4})} \right)^2 \right], \tag{4.31}$$

$$\sigma^2_{K.I} = \frac{1}{[\lambda_r(\frac{1}{4}) - \lambda_b(\frac{1}{4})]^2} \left[\sigma^2_{r,p}(\frac{3}{4}) + \sigma^2_{b,p}(\frac{3}{4}) + \left(\frac{\lambda_r(\frac{3}{4}) - \lambda_b(\frac{3}{4})}{\lambda_r(\frac{1}{4}) - \lambda_b(\frac{1}{4})} \right)^2 (\sigma^2_{p,r}(\frac{1}{4}) + \sigma^2_{p,b}(\frac{1}{4})) \right]. \tag{4.32}$$

Using the above relations and taking into account a 5% change in the continuum level for Hβ ,[OIII]$\lambda\lambda$4959,5007ÅÅ, and MgII lines, the estimated uncertainty for the profile parameters of each line are reported in Tables 5.1, 5.2, and 5.7, respectively.

Chapter 5

Optical and near-UV spectroscopic properties of low-redshift jetted quasars in the main sequence context[1]

5.1 Introduction

Type-1 AGN exhibit distinct features that are not seen in normal galaxies (see Sect. 2.1). They also show widely different properties among themselves: different line profiles, intensity ratios, and ionization levels (e.g., Sulentic et al., 2007a; Ho, 2008; Marziani et al., 2010; Śniegowska et al., 2018). Since the discovery of quasi-stellar radio sources and quasi-stellar objects (quasars and QSOs)[2] in the early 1960s there is a general consensus about their nature (see Sect. 2.4). The last three decades have opened promising lines of investigation on the definition and contextualization of optical and UV properties (e.g., Sulentic et al., 2000b; Shen and Ho, 2014; Wolf et al., 2020b), with the exploration of a spectroscopic unification for broad-line emitting AGN, like the four-dimensional eigenvector 1 (4DE1) parameter space that organizes quasar diversity (see Sect. 2.5.1).

In this particular work, we are concerned with debated problems associated with the possibility of a real physical dichotomy between RL and RQ quasars (e.g., Xu et al., 1999; Cirasuolo et al., 2003b; Zamfir et al., 2008; Coziol et al., 2017; Panessa et al., 2019; Blandford et al., 2019): the effect of radio loud-

[1] The results presented in this chapter have been published in Mengistue et al. (2023)

[2] In the following we will use the quasar as an umbrella term that includes all type-1 AGN regardless of luminosity and radio power.

ness on the dynamics of the low-ionization broad line emitting regions. The singly-ionized iron emission is systematically fainter in RL than in RQ sources, although it is still unclear if this is an effect intrinsic to a different emitting region structure, or associated with different host galaxy properties (e.g., Marziani et al., 2021, and references therein). As suggested in Zamfir et al. (2008), the value of studying the RL phenomenon within the 4DE1 context is at least twofold: (i) the approach compares RL and RQ quasars in a parameter space defined by measures with no obvious dependence on the radio properties (Sulentic et al., 2003), and (ii) it allows predictions of the probability of radio loudness for any AGN population given a specific set of spectroscopic properties. Open questions are whether the geometry/ kinematics of RL and RQ quasars are the same or not. A related issue is also the ability to distinguish between high and low accreators from optical and UV spectroscopy, to assess any effect the black hole spin has, and to infer the structure of the accretion disc (e.g., Sikora et al., 2007; Lagos et al., 2009; Tchekhovskoy et al., 2009).

As detailed in Sect. 3.1.2, this work presents new optical and near-UV spectra and a multi-component fitting analysis of 11 jetted Pop. B (RL) quasars at low–z ($0.3 \lesssim z \lesssim 1$). This paper extends the study to near-UV with the coverage of the MgIIλ2800Å (hereafter MgII) spectral range, providing still rare simultaneous observations of Hβ and MgII. Both Hβ and MgII provide diagnostics of the low-ionization line (LIL) part of the emitting region. In addition, MgII is known to be less affected by shifts and asymmetries than Hβ and is expected to provide a reliable virial black hole mass estimation (e.g., Trakhtenbrot and Netzer, 2012). The sources we selected are among the most extreme radio emitters, those with a radio-to-optical flux density ratio (R_K) $\gtrsim 10^3$ (see Table. 3.3). For them, we want to test if the relativistic jets might have a strong effect on the emission of low-ionization UV and optical lines.

5.2 Observations and spectral analysis

In Chapter 3, we provided a comprehensive overview of the new optical and near-UV spectroscopic observations and the instruments that are relevant for the published paper (Mengistue et al., 2023) and used for this PhD thesis work. We described the construction of the sample to be studied, their properties, what data were used, what information was collected for each source, and what additional data have been used to supplement the study as archival data. Mainly, our observations were conducted using the Calar Alto 3.5-meter telescope, specifically the Cassegrain TWIN Spectrograph, due to its high resolution and wide wavelength coverage with high signal-to-noise spectra. This allowed us to capture a wider spectral range for simultaneous coverage of the optical

and near-UV lines for a more complete analysis. We targeted a sample of 11 extremely jetted RL sources with $R_K > 10^3$ in the redshift range of $0.3 < z < 1$. Based on the archival radio data, we also detailed the main radio properties of the selected sources.

Chapter 4 focused on the detailed analysis of the spectral data relevant to this thesis work. As a main spectral analysis tool, we employed the `IRAF` task `specfit` to perform non-linear multicomponent spectral fitting on the observed spectra. This fitting process involved separately modeling the Balmer line (Hβ) and the near-UV (MgIIλ2800) emission lines, as they provide a wealth of information for the study of jetted quasars. By carefully defining the model components and applying `specfit` effectively, we extract valuable information about the emission line profiles and the continuum for a given quasar spectrum. This, in turn, provides insights into the physical processes within the quasars. The fitting procedure involved comparing the observed spectral profiles of these lines with theoretical models to extract key parameters. The results of the `specfit` analysis are shown in Fig. 4.2, and the results of this analysis are presented and discussed in detail in the following sections.

5.3 Results

5.3.1 Spectral multi-component fitting results

5.3.1.1 Hβ and [Oiii]$\lambda\lambda$4959,5007Å region

Spectrophotometric measurements of the optical region as well as the parameters of the FP and the individual components of Hβ, represented in the right panels of Fig. 4.2, are presented in Table 5.1. Col. 2 contains the rest-frame specific continuum flux at 5100Å obtained from the fitted power law; Col. 3 lists the wavelength range used for the spectral fitting in the Hβ region; Cols. 4 to 12 report the FP measures H$\beta_{\rm FP}$ (BC + VBC): EW (Col. 4), total intensity (Col. 5), FWHM of H$\beta_{\rm FP}$ (Col. 6), the centroids at $\frac{1}{4}$, $\frac{1}{2}$, $\frac{3}{4}$ and $\frac{9}{10}$ fractional intensity of the peak (Cols. 7 – 10), as well as AI and KI (Cols. 11 and 12, respectively). For each line component isolated with the `specfit` analysis, we report the total flux (I), the peak shift, and the FWHM in km s^{-1}: for NC (Cols. 16 – 18), for BC (Cols. 19 – 21), and for VBC (Cols. 22 – 24). Additionally, we also provide in Table 5.1 the parameters related to FeII: the total flux of the blue blend of FeIIλ4570Å in Col. 13, and the smoothing factor applied to the FeII template to reproduce the observed FeII feature (Col. 14). In Col. 15 we report the $R_{\rm FeII,opt}$ parameter (see Sect. 2.5.1). In the two most redshifted quasars in the sample at $z > 0.9$ (3C 94 and PKS 0420), the reddest part of the spectrum has a slightly lower S/N due to the correction

of the telluric band that extends between 9250Å and 9700Å in the observed wavelength. This results in a kind of flat-topped and even multipeaked profile in Hβ (see Fig. 4.2), and slightly larger uncertainties in the determination of the higher fractional intensity centroids of Hβ, and to less extent in [OIII].

Regarding H$\beta_{\rm FP}$, in general the objects of our extreme $\log R_{\rm K} \gtrsim 3$ (hereafter eRk) sample show FWHM(Hβ) $\gtrsim$ 4000 km s^{-1}, with a median value of 5100 km s^{-1}, which is a typical value of B1 spectral type (ST) quasars at z < 1 (see Sect. 5.3.2) with similar luminosities (e.g., Sulentic et al., 2002; Zamfir et al., 2008). In two cases (3C 179 and PKS 2208-137), the FWHM is slightly less than 4000 km s^{-1}. For PKS 2208-137, the barely lower value may be caused by the uncertainty in identifying the Hβ NC, which may have been included in the BC producing a slightly narrower and sharper BC profile. In the case of 3C 179, with the lowest FWHM ($\sim$ 3600 km s^{-1}) in the eRk sample, that value may be influenced by a slightly high continuum location on the red side due to the correction of the telluric band in that region, preventing an accurate continuum determination on the redward [OIII].

The multicomponent analysis corroborates the result obtained for the FP. In all cases, a VBC needs to be included (apart from the BC) to account for the observed Hβ profile. The contribution of the VBC represents in 4/11 quasars more than 60% of the total intensity of H$\beta_{\rm FP}$ (for the whole sample the median value for VBC contribution is 57%) and that reaches FWHM(VBC) $\geq$ 10000 km s^{-1}. As a consequence of the presence of the VBC, FWHM(H$\beta_{\rm BC}$) is always smaller than the one corresponding to the FP. The ratio between both ξ = FWHM(H$\beta_{\rm BC}$)/FWHM(H$\beta_{\rm FP}$) has a mean value of 0.83 ± 0.09 for our quasars, in agreement with the values reported by Marziani et al. (2013a) for an SDSS composite spectrum of sources belonging to Pop. B, B1 ST quasars. Also, a narrow component is detected in all quasars, although in general, its intensity relative to the broad profile is small, with a median value of 6%. Considering the individual components of Hβ, both the NC and BC are almost always unshifted and centered around the rest-frame of each object. In 3C 94 and PKS 2344+09 the NC appears slightly blueshifted. Two factors may be contributing to the shift: the first one and more probable is the possible presence of an unresolved SBC included in the NC of Hβ, in correspondence with the observed SBC of [OIII] (see below), which would also explain the relatively high value obtained for the FWHM H$\beta_{\rm NC}$ $\sim$ 1600 km s^{-1} for 3C 94. A second factor to take into account in the case of 3C 94, as we mentioned previously, is that both the Hβ profile and the FeII blue blend are affected by a telluric band extending between $\approx$ 9250Å and 9700Å in observed wavelengths (that correspond to $\sim$ 4700Å - 4900Å in the rest-frame), whose correction can also introduce greater uncertainty in the determination of the position of the peak and the centroids at the highest fractional intensities.

Table 5.1: Results of the full broad profile and the `specfit` analysis for Hβ.

				Full broad profile (FP) (BC + VBC)												NC			BC			VBC		
Object	$f_{\lambda,5100}$	Fitting	range	EW	I	FWHM	C($\frac{1}{4}$)	C($\frac{1}{2}$)	C($\frac{3}{4}$)	C($\frac{9}{10}$)	AI	KI	FeIIλ4570	SF	$R_{\rm FeII,opt}$	I	Shift	FWHM	I	Shift	FWHM	I	Shift	FWHM
(1)	(2)	(3)		(4)	(5)	(6)	(7)	(8)	(9)	(10)	(11)	(12)	(13)	(14)	(15)	(16)	(17)	(18)	(19)	(20)	(21)	(22)	(23)	(24)
PHL 923	0.13	4400	- 5100	92	13.2	4420±80	2280±880	-60±140	-190±120	-230±160	0.47±0.11	0.25±0.05	8.40	2700	0.63	0.4	10	810	5.8	-330	3640	7.4	4370	11400
B2 0110+29	0.07	4400	- 5200	138	9.4	6370±740	1690±540	450±250	130±170	60±210	0.28±0.08	0.31±0.04	0.01	4000	0.001	0.6	-40	510	3.4	-1	4650	6.0	2030	12000
3C 37	0.13	4400	- 5200	126	17.7	5540±450	550±300	490±160	470±150	470±200	0.02±0.13	0.41±0.05	2.8	2800	0.16	1.2	-80	1140	10.2	-30	4770	7.5	890	11800
PKS 0230-051	0.30	4400	- 5200	126	41.5	5100±490	1370±740	190±170	70±140	40±180	0.26±0.12	0.30±0.05	7.8	3200	0.19	0.6	-30	340	15.7	-80	3880	25.8	2140	12900
3C 94[(1)]	0.82	4150	- 5100	48	44.6	5480±2906	30±350	200±150	120±150	90±200	0.14±0.08	0.40±0.05	14.7	5200	0.34	13.7	-330::	1570	28.9	-30:	4960	15.7	5 400	12500
PKS 0420-01[(1)]	0.70	4400	- 5100	42	28.9	4110±330	250±250	60±120	30:±110	10:±150	0.07±0.06	0.4±0.1	14.4	5000	0.50	1.9	80:	860	16.2	-20:	3600	12.7	2360	12200
3C 179	0.17	4400	- 5050	62	11.4	3570±350	1160±440	500±120	410±100	390±120	0.22±0.16	0.31±0.05	4.3	5000	0.37	0.5	-10	620	4.0	310	2620	7.4	1460	8300
3C 380	0.68	4400	- 5200	86	61.9	5740±750	2580±470	780±250	400±150	320±190	0.4±0.08	0.28±0.04	8.5	4800	0.14	6.7	20	1200	23.1	60	4000	38.8	3630	10600
S5 1856+73	0.72	4400	- 5500	135	102.4	5730±560	1350±540	530±190	380±150	340±200	0.2±0.12	0.33±0.05	12.3	2600	0.12	5.1	80	750	52.4	370	5300	50.0	2420	13300
PKS 2208-137	0.47	4400	- 5500	54	27.8	3850±300	360±180	230±100	190±100	180±140	0.07±0.09	0.43±0.05	12.6	4900	0.46	0.1::	70::	490::	18.1	160	3590	9.7	5380	12100
PKS 2344+09	1.34	4400	- 5500	108	151.9	4150±380	350±370	40±130	-20±110	-30±150	0.11±0.11	0.35±0.05	42.9	3500	0.28	10.6	-250:	880	70.0	-30	3640	81.9	1530	13400

Note: Col. 2 is in units of 10^{-15} ergs s^{-1} cm^{-2} Å^{-1}. Cols. 3 and 4 are in units of Å. Cols. refereed to intensities as Col. 5, 13, 16, 19, and 22 are in units of 10^{-15} ergs s^{-1} cm^{-2}. Cols. refereed to centroid velocities at different fractional intensities, FWHM, and shift as Cols. 6 - 10, 14, 17 - 18, 20 - 21, 23 - 24 are in units of km s^{-1}. [(1)] Centroid and peak shift determinations might be affected by the presence of a telluric band from 9250 to 9700 Å at observed wavelengths. Values ending with a colon (:) mean that the values are highly uncertain, and "::" that the feature is poorly defined.

Table 5.2: Results of FP and the `specfit` analysis for [OIII]λ5007Å.

Object	Full broad profile (FP)(NC + SBC)									NC			SBC		
	EW	I	FWHM	C($\frac{1}{4}$)	C($\frac{1}{2}$)	C($\frac{3}{4}$)	C($\frac{9}{10}$)	AI	KI	I	Shift	FWHM	I	Shift	FWHM
(1)	(2)	(3)	(4)	(5)	(6)	(7)	(8)	(9)	(10)	(11)	(12)	(13)	(14)	(15)	(16)
PHL 923	64	8.9	860±80	-40±50	-50±30	-50±30	-50±40	0.04±0.12	0.42±0.04	4.99	-30	806	3.86	10	1640
B2 0110+29	117	7.9	480±40	-40±20	-40±10	-40±10	-40±20	-0.04±0.09	0.42±0.05	5.24	-20	430	2.7	-60	1200
3C 37	41	5.6	580±50	-100±40	-60±20	-50±20	-40±20	-0.17±0.09	0.38±0.04	2.41	-20	440	3.23	-150	980
PKS 0230-051	37	11.4	450±40	-40±30	20±20	30±10	40±10	-0.21±0.13	0.37±0.04	4.94	40	340	6.5	-130	690
3C 94	57	49.1	620±60	-70±80	70±20	90±20	90±20	-0.29±0.20	0.32±0.05	22.0	110	490	27.1	-240	1380
PKS 0420-01	14	9.7	620±50	-140±50	-130±20	-130±20	-120±30	-0.02±0.28	0.39±0.05	4.56	-110	500	5.1	-160	1280
3C 179	27	4.8	520±40	10±30	20±10	30±10	30±20	-0.09±0.13	0.41±0.05	2.74	20	440	2.1	-80	940
3C 380	50	36.1	610±50	-30±40	-10±20	-10±20	-10±20	-0.04±0.09	0.38±0.05	14.4	10	470	21.7	-60	1070
S5 1856+73	34	25.3	410±30	10±20	1±10	1±10	10±20	0.05±0.06	0.44±0.05	18.3	30	370	7.0	120	760
PKS 2208-137	7	3.4	600±40	-70±20	-60±20	-50±20	-50±20	-0.12±0.07	0.45±0.04	2.43	20	530	1.0	-210	620
PKS 2344+09	63	85.3	660±60	-270±80	-160±20	-140±20	-130±30	-0.23±0.25	0.34±0.05	39.6	-100	520	45.7	-400	1300

Note: Col. 2 is in the unit of Å. Cols. 3, 11, and 14 are in units of 10^{-15} erg s^{-1}cm^{-2}. Cols. 4 – 8, 12 – 13, and 15 – 16 are in units of km s^{-1}.

A similar analysis was carried out for [OIII], as described in Sect. 4.2.3. The results for the FP and the individual components for $[OIII]\lambda$5007Å are reported in Table 5.2. We present the EW (Col. 2), total intensity (Col. 3), FWHM (Col. 4), centroid velocities at different fractional intensities (Cols. 5 – 10), AI (Col. 9), and KI (Col. 10). Intensity, shift, and FWHM from the `specfit` analysis are also presented for the NC (Cols. 11 – 13), and the SBC (Cols. 14 – 16) of each quasar. The resulting measurements for [OIII]λ4959, can be found by using appropriate line ratios detailed in Sect. 4.2.3.

Our sources show strong [OIII] lines separated from Hβ, presenting a spectrum characteristic of Pop. B quasars as listed in Table 5.2. The FP of [OIII] shows a slight blue asymmetry for most of the objects, with a negative AI and a median value of -0.1. This is due to the presence of a weaker SBC that is blueshifted (for 9/11 of our sources). As can be seen in Table 5.2 where the `specfit` measures are presented, while the NC is, within the uncertainties, unshifted in the rest-frame of the objects, the SBC appears blueshifted with a median shift of -130 km s^{-1}, and a slightly broader FWHM of around 1100 km s^{-1}. The presence of blue-shifts in the high ionization lines (HILs) like [OIII] is considered as one of the main detectors of outflowing gas (e.g., Zamanov et al., 2002; Komossa et al., 2008; Zhang et al., 2011; Marziani et al., 2016; Vietri et al., 2020; Deconto-Machado et al., 2022; Kovačević-Dojčinović et al., 2022). Our quasars present moderate [OIII] blueshifts, indicating perhaps the presence of outflows in the inner NLR. In no case do we have the named "blue-outlier", which is defined by a blue-shift in [OIII] larger than -250 km s^{-1} (Zamanov et al., 2002) and are preferentially observed at low-z in the Pop. A quasars of the MS.

In some objects, HeIIλ4686Å is also detected in the blue side of Hβ as a residual emission in the fit. We have fitted it with a Gaussian profile. In

Table 5.6: `Specfit` result of HeIIλ4686Å.

Object	BC			VBC		
	I	Shift	FWHM	I	Shift	FWHM
(1)	(2)	(3)	(4)	(5)	(6)	(7)
PHL 923	1.5	160	3190	–	–	–
B2 0110+29	–	–	–	1.0	2070	9630
3C 37	–	–	–	4.0	990	9600
PKS 0230-051	–	–	–	8.7	2180	10310
3C 94	–	–	–	–	–	–
PKS 0420-01	–	–	–	13.2:	2410:	9730:
3C 179	–	–	–	3.9	1510	6660:
3C 380	4.5	-420	3070	12.7	3670	8470
S5 1856+73	5.3	1200	4060	–	–	–
PKS 2208-137	–	–	–	4.6	540	7110
PKS 2344+09	8.2	-260	4760	–	–	–

Note: Cols. 2 and 5 are in units of 10^{-15} ergs $s^{-1}cm^{-2}$. Cols. 3, 4, 6, and 7 are in km s^{-1}. For (:) measurements, see the notes in Table 5.1.

most cases, it seems to correspond to a VBC, but in some cases, it is unclear whether this extra emission is actually HeIIλ4686Å or corresponds to the FeII blend. Only in the case of 3C 380 two components (BC and VBC) can be identified, and for PKS 0230-51 a NC is seen overlaid on the VBC (see Fig. 4.2). The `specfit` analysis results for HeIIλ4686Å are reported in Table 5.6. The values given in the table are only to be considered, for most objects, as an indication of the HeIIλ4686Å detection.

5.3.1.2 MgII region

The results of the spectrophotometric measurements for MgII region and measured parameters including both MgII FP and the individual components from the `specfit` analysis (plotted in left panels of Fig. 4.2), following the approach described in Sect. 4.2.4, are presented in Table 5.7. Cols. 2 and 3 contain respectively the rest-frame specific continuum flux at 3000Å, obtained from the fitted power law, and the Balmer continuum whose intensity was estimated at the Balmer edge at 3646Å. From Cols. 4 – 12 are reported the FP measurements of MgII, including 2BC and a VBC: EW (Col. 4), total intensity (Col. 5), FWHM of $MgII_{FP}$ (Col. 6), the centroids at $\frac{1}{4}$, $\frac{1}{2}$, $\frac{3}{4}$ and $\frac{9}{10}$ fractional intensity of the peak (Cols. 7 – 10), as well as the AI and KI in Cols. 11 and 12, respectively. The `specfit` fitting parameters of the individual components of the reddest line of the doublet are reported from Cols. 16 – 24. The corresponding measures of the blue component of MgII, can easily be found by taking into account the appropriate line ratio (see Sect.4.2.4). For each red line component analyzed we report the total flux (I), the peak shift, and the FWHM

of the NC (Cols. 16 – 18), BC (Cols. 19 – 21), and VBC (Cols. 22 – 24). In addition, we also provided the parameters related to $\mathrm{FeII_{UV}}$: the total flux of the blue blend (Col. 13), and the smoothing factor applied to $\mathrm{FeII_{UV}}$ template to reproduce the observed FeII feature (Col. 14). In Col. 15 we report the $R_{\mathrm{FeII,UV}}$ parameter, i.e. the ratio between the intensities of $\mathrm{FeII_{UV}}$ (in the 2200Å to 3090Å range) and MgII ($R_{\mathrm{FeII,UV}}$ = I($\mathrm{FeII_{UV}}$)/I($\mathrm{MgII_{FP}}$)).

As in the case of Hβ, the FWHM of MgII FP is higher than FWHM of MgII BC obtained from the `specfit` analysis. The median value for the ratio ξ_{Mgii} = FWHM($\mathrm{MgII_{BC}}$)/FWHM($\mathrm{MgII_{FP}}$) is 0.84±0.02 for our quasars, in good agreement with the value found by Marziani et al. (2013a) for the ST B1 by using composite spectra. This is due to the presence also of a VBC in MgII, with a FWHM $\gtrsim$ 10000 km s^{-1}, though MgII shows a weaker VBC, with a median flux representing about 42% of the total broad intensity. This manifests itself in a redward asymmetry, although showing a more symmetric profile than Hβ, with <AI> = 0.04, and a shift towards the red of the centroid velocities of MgII, more pronounced towards the base of the line, with <c($\frac{1}{4}$)> $\approx$ 300 km s^{-1}.

In addition, Table 5.8 presents the parameters obtained from the fit to a single Gaussian profile of other lines detected in the UV region, such as the OIIIλ3133Å, HIL [NeV]λ3426Å and [OII]λ3728Å doublet. For each of these lines the total flux, the peak shift, and FWHM are reported when the corresponding line is detected in the spectrum.

5.3.2 Main sequence optical plane

The optical plane of the 4DE1 parameter space is defined by the Hβ_{FP} FWHM and $R_{\mathrm{FeII,opt}}$. The quasar MS allows contextualization of the observed empirical spectroscopic properties of type-1 AGN and their connection with the physical conditions of the BLR (see e.g., Sulentic et al., 2000b; Marziani et al., 2018; Panda et al., 2019c; Wolf et al., 2020b). After performing the analysis of the Hβ region (see section 5.3.1.1), that provides us with both the FWHM(Hβ_{FP}) and R_{FeII} (Table 5.1 Cols. 6 and 15, respectively), we can locate our quasars in the MS. It is possible to subdivide the optical plane into a grid of bins (or STs) formed from FWHM(Hβ_{FP}) and $R_{\mathrm{FeII,opt}}$ that shows different spectral line profile properties (Sulentic et al., 2002): bins A1 to A4 are defined in terms of increasing $R_{\mathrm{FeII,opt}}$ with bin size $\Delta R_{\mathrm{FeII,opt}}$ = 0.5 (from A1 with $R_{\mathrm{FeII}} < 0.5$ to A4 with $1.5 < R_{\mathrm{FeII}} \leq 2$), while bins B1, B1^{+} and B1^{++} are defined in terms of increasing FWHM with ΔFWHM = 4000km s^{-1}, from B1 with $4000 <$ FWHM $\leq$ 8000 km s^{-1} to B1^{++} with FWHM > 12000 km s^{-1}.

Fig. 5.1 shows the locus of our quasars on the MS as well as the Pop. A/B

Table 5.7: Measurements of the MgII region.

			Full broad profile parameters (FP)									FeII$_{UV}$			NC(red)			BC(red)			VBC(red)		
Object	$f_{\lambda,3000}$	$f_{\lambda,3646}$	EW	I	FWHM	C($\frac{1}{4}$)	C($\frac{1}{2}$)	C($\frac{3}{4}$)	C($\frac{9}{10}$)	AI	KI	I	SF	$R_{FeII,UV}$	I	Shift	FWHM	I	Shift	FWHM	I	Shift	FWHM
(1)	(2)	(3)	(4)	(5)	(6)	(7)	(8)	(9)	(10)	(11)	(12)	(13)	(14)	(15)	(16)	(17)	(18)	(19)	(20)	(21)	(22)	(23)	(24)
PHL 923	0.43	0.02	37	17.9	4000±320	120±300	20±180	-10±180	-10±150	0.05±0.12	0.41±0.05	25.7	4660	1.44	0.2	-130	480	4.6	10	3370	7.6	1070	10610
B2 0110+29	0.13	0.02	118	16.3	5810±450	250±280	190±160	170±150	160±210	0.02±0.09	0.42±0.05	10.9	2490	0.67	0.1	150	890	4.8	180	5130	5.5	940	13010
3C 37	0.32	0.03	57	19.8	5600±440	250±280	210±160	200±150	200±210	0.02±0.09	0.42±0.05	29.1	4170	1.47	0.7	50	850	5.6	220	4910	7.2	650	13140
PKS 0230-051	0.88	0.07	42	40.5	4470±360	-40±280	-130±130	-150±120	-160±160	0.03±0.13	0.40±0.05	65.7	5720	1.62	0.6	30	890	9.8	-220	3750	18.5	750	12910
3C 94	2.22	0.19	34	79.9	5000±410	-60±320	-160±140	-180±130	-190±180	0.03±0.09	0.40±0.05	247::	3560	3.09	2.2	-30	750	18.8	-270	4230	37.4	1050	15460
PKS 0420-01	0.86	0.07	40	33.9	3600±190	330±210	260±100	240±100	240±130	0.02±0.28	0.41±0.05	85.8	5720	2.53	0.5	50	870	8.4	260	3010	15.1	1120	11140
3C 179	0.40	0.03	40	16.7	4410±360	830±280	600±130	550±120	540±160	0.10±0.13	0.40±0.05	46.9	6840	2.81	0.8	120	830	4.6	460	3630	7.6	1880	10000
3C 380	1.36	0.16	61	85.3	4610±400	320±420	140±140	120±120	110±170	0.07±0.09	0.37±0.05	59	2490	0.69	1.9	20	850	16.7	110	3680	47.8	1070	14750
S5 1856+73	1.31	0.16	39	51.2	5770±460	530±310	430±160	400±150	390±210	0.03±0.06	0.41±0.04	35.9	2490	0.70	2.8	60	900	13.1	410	4870	21.7	1100	11630
PKS 2208-137	1.32	0.07	27	39.4	4440±350	300±240	240±120	230±120	220±160	0.04±0.07	0.42±0.04	45.3	2490	1.15	0.7	20	860	10.7	270	3810	15.2	870	11100
PKS 2344+09	3.46	0.21	25	92.1	4240±340	400±240	340±120	320±110	320±160	0.04±0.25	0.41±0.05	271	3020	2.94	5.8	0	890	29.2	270	3580	39.5	910	11530

Note: Cols. 2 and 3 are in units of 10^{-15} ergs s^{-1} cm^{-2} Å^{-1}. Col. 4 is in units of Å. Cols. 5, 13, 16, 19, and 22 are in units of 10^{-15} ergs s^{-1} cm^{-2}. Cols. 6 - 10, 14, 17 - 18, 20 - 21, and 23 - 24 are in units of km s^{-1}. Cols. 16 - 24 show measurements of the red component of MgII doublet. Measurements of the blue component can be obtained by using the line ratios given in Sect. 4.2.4.

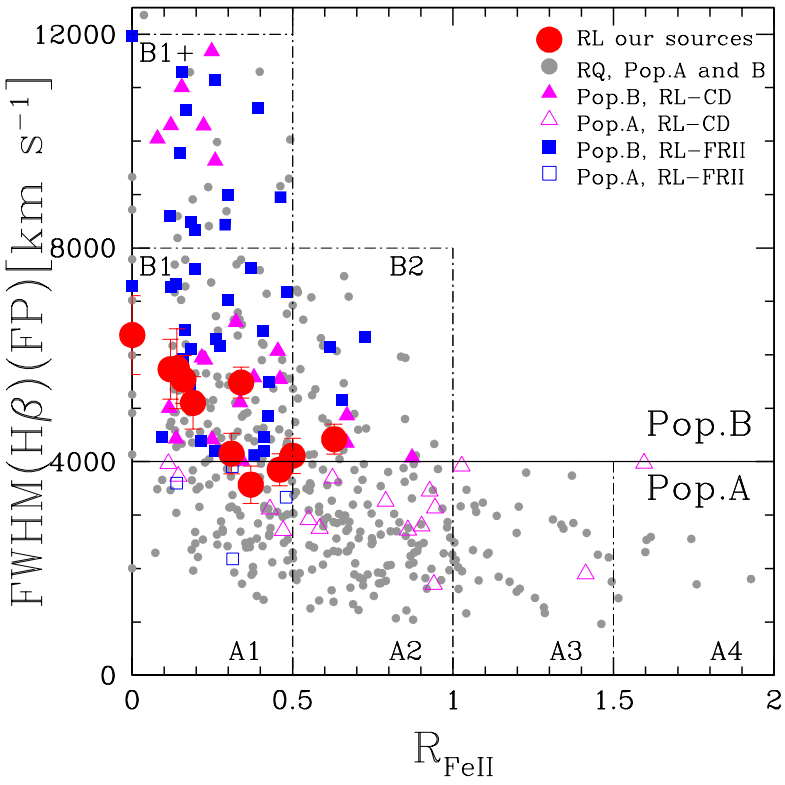

Figure 5.1: Location of our eRk quasars (large red solid circles) in the optical plane of the 4DE1 space, traced by the measures from the Zamfir et al. (2010) sample, where gray dots represent the RQ (Pop. A & B) and blue and magenta symbols corresponds to RLs. The horizontal line at 4000 km s^{-1} marks the nominal Pop. A - B boundary. For the explanation of different STs see Sect. 5.3.2. The vertical axis is truncated at, 12500 km s^{-1} for clarity.

separation and the identification of some of the most populated STs, where we have also included as a comparison the low-z SDSS sample by Zamfir et al. (2010). In Fig. 5.1, grey symbols represent the Pop. A and B RQs, meanwhile coloured symbols represent the RLs, split into core-dominated (CD; magenta triangles) and lobe-dominated (LD) FRII (blue squares). As seen in this figure, the RQ sources cover a broad domain in the MS, covering the entire range of observed values in both FWHM and $R_{\rm FeII}$, and in both A and B populations. On the converse, the RL ("jetted") sources are mainly Pop. B and populate particular bins of the optical plane, mostly in B1 and B$^+$ (Zamfir et al., 2008; Kuźmicz et al., 2021).

Our quasars are well located in the MS domain of the CD RL sources. The majority lie in the B ST (more than 80%), mostly in B1. For 3C 179 and PKS 2208, FWHM(H$\beta_{\rm FP}$) value is only marginally below 4000 km s^{-1} placing them on the upper edge of Pop. A, at the ST A1. Since in both quasars, there is no

Table 5.8: `Specfit` analysis results for the other UV lines

Object	OIIIλ3133Å			[NeV]λ3426Å			[OII]λ3728Å		
	I	Shift	FWHM	I	Shift	FWHM	I	Shift	FWHM
(1)	(2)	(3)	(4)	(5)	(6)	(7)	(8)	(9)	(10)
PHL923	–	–	–	–	–	–	1.0	170:	550:
B2 0110+29	–	–	–	–	–	–	1.8	70	1130
3C37	1.2	130:	1880:	1.0	-70	1550	0.4:	70	1090::
PKS 0230-051	4.1	-110	1940	2.1:	-260:	1170:	2.6	-40	1080
3C94	4.4	110	1950	6.1	60	1560	6.1	190	1030
PKS 0420-01	–	–	–	–	–	–	2.2:	30:	1150:
3C179	0.1::	80::	1680::	0.1:	20:	940:	0.1	-20	1030
3C380	4.1::	-310::	1910::	5.0	40	1700	3.4	60	1070
S5 1856+73	3.0::	-150::	2150::	1.8	-1	600	3.4:	-110:	1130:
PKS 2208-137	–	–	–	–	–	–	2.6	80	1090
PKS 2344+09	10.4::	-110::	2380::	5.9	-70	1420	7.0:	200:	1140:

Note: Cols. 2, 5, and 8 are in units of 10^{-15} ergs s^{-1} cm^{-2}. Other columns are in km s^{-1}. For (:) and (::) measurements see the notes in Table 5.1.

doubt about its Pop. B classification with a recognized VBC in the Hβ profile, its position may be due to an inclination effect (as we mentioned in section 5.3.1.1) since the broadening of Hβ is orientation-dependent (Wills and Browne, 1986; Sulentic et al., 2003; Zamfir et al., 2008). Our quasars also show weak FeII$_{opt}$ intensities. All except one case (PHL 923 with $R_{FeII,opt}$ = 0.63 that locates the object in B2 bin) present low $R_{FeII,opt}$ values, with a mean of 0.29 and a σ = 0.19. This is in agreement with the results obtained by Marziani et al. (2021) whom using composite spectra found that RL sources, both CD and FRII, present weaker FeII$_{opt}$ emission ($\sim$ a factor 2 lower) compared to the composite spectrum of RQ quasars sharing the same B1 ST.

5.3.3 Main sequence UV plane

In a close analogy to the optical plane, it is also possible to analyze the UV plane by using MgII, and FeII$_{UV}$ line parameters. This is possible mainly because both Hβ and MgII lines belong to LILs and are supposed to be emitted from a similar region (Collin-Souffrin et al., 1988). The UV plane is also formed by using MgII$_{FP}$ FWHM and the strength of the FeII$_{UV}$. Figure 5.2 shows the location of our eRK quasars in the UV plane where we used as a comparison sample the recently available parameters determined by the software QSFIT from Calderone et al. (2017) using SDSS-DR10 spectra, in which they incorporated spectral information in the UV, and in particular for MgII and FeII$_{UV}$ to produce a publicly available catalogue of AGN spectral properties. See also a discussion about this catalogue and the MS UV plane in Śniegowska

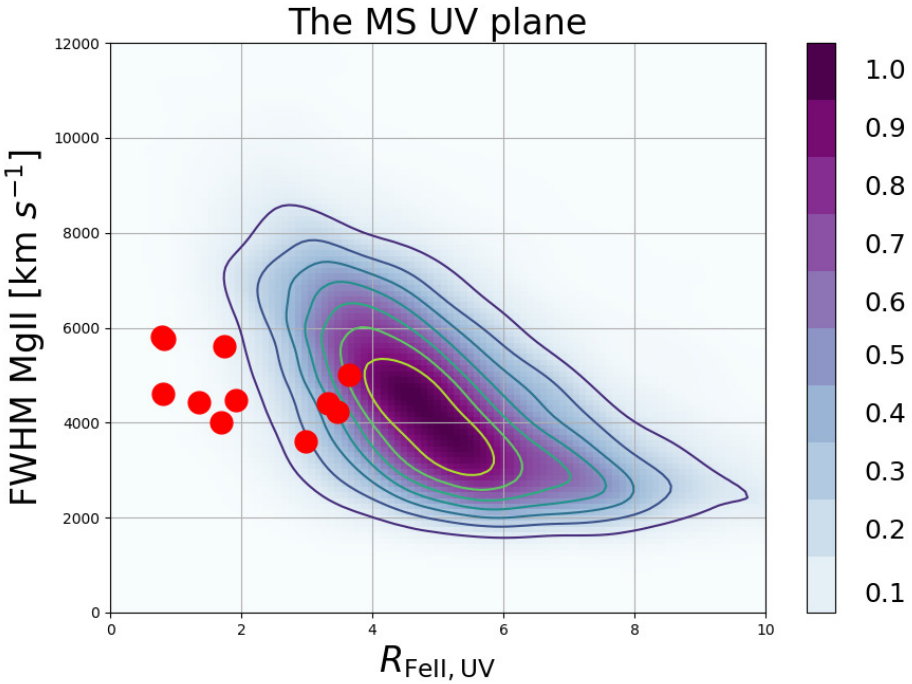

Figure 5.2: Location of our eRK quasars (red solid circles) in the UV plane defined by MgII FWHM and $R_{\mathrm{FeII,UV}}$. A comparison sample was taken from Calderone et al. (2017) catalog by considering sources that are found around our redshift range ($0.4 \lesssim z \lesssim 1$) and is shown after kernel smoothing to account for a large number of sources (10,344). The color scale is normalized to the peak density in the UV parameter plane.

et al. (2020). For the QSFIT catalogue, we selected a sample consisting of the sources in the redshift range from 0.4 to 1 and with good quality measures in MgII and FeII$_{\mathrm{UV}}$ according to this catalogue. The available comparison sample is large (10,344 spectra) and we used, therefore, a kernel smoothing for better visualization. As compared to the optical plane, the UV plane shows a larger range in $R_{\mathrm{FeII,UV}}$. This is mainly because the range of the integrated flux in FeII$_{\mathrm{UV}}$ is broader as compared to the optical, FeII$_{\mathrm{opt}}$. For the sole purpose of the representation of our sample in the UV plane together with the data obtained from the QSFIT catalogue, we have estimated a FeII$_{\mathrm{UV}}$ modified total flux for our RL sources by extrapolating the FeII$_{\mathrm{UV}}$ model fitted to our spectra to the wavelength range λ1250Å to λ3090Å used by Calderone et al. (2017). Our quasars are placed in the FWHM(MgII$_{\mathrm{FP}}$) $\gtrsim$ 4000 km s^{-1} and in the lowest FeII$_{\mathrm{UV}}$ emission, as in the case of the optical plane.

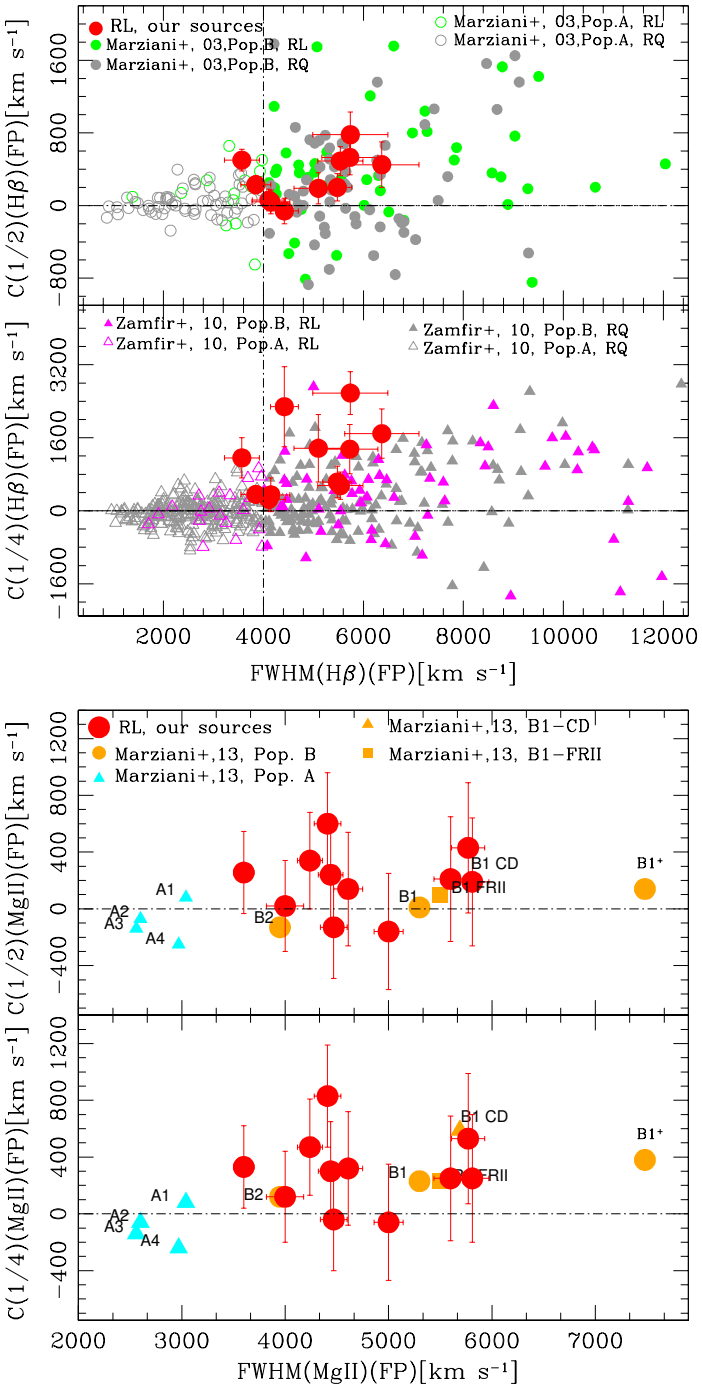

Figure 5.3: [Top panel] Centroids at $c(\frac{1}{2})$ (upper plot) and $c(\frac{1}{4})$ (bottom plot) peak intensity of H$\beta_{\rm FP}$ versus the FWHM of H$\beta_{\rm FP}$. The large red solid circles represent our RL objects. Comparison samples from Marziani et al. (2003a) and Zamfir et al. (2010) are also represented. The legends identify different populations and radio classes. The vertical dot-dashed line at 4000 km s^{-1} marks the nominal population A/B boundary. The horizontal dot-dashed line traces the symmetric line in $c(\frac{1}{2})$ and $c(\frac{1}{4})$. [Bottom panel] $c(\frac{1}{2})$ (upper) and $c(\frac{1}{4})$ (lower) versus FWHM of MgII. The additional comparison sample shown in the plot was taken from Marziani et al. (2013a). Orange symbols represent Pop. B and cyan solid triangles for Pop. A. Orange solid triangle and square represent Pop. B CD and FRII respectively.

5.3.4 Comparison between the Hβ and MgII spectral ranges

5.3.4.1 MgII and Hβ line profiles

Based on the measurements reported in Tables 5.1 and 5.7, we analyze and compare here the line profile parameters of Hβ and MgII. The upper and bottom panels of Fig. 5.3 show the location of our eRk quasars in the c($\frac{1}{2}$) and c($\frac{1}{4}$) versus FWHM(H$\beta_{\rm FP}$) plots, respectively. The comparison sample containing the c($\frac{1}{2}$) information for the RL and RQ was taken from Marziani et al. (2003a) and the c($\frac{1}{4}$) from Zamfir et al. (2010). Our eRk quasars are located in the upper right parts of both diagrams, mainly occupied by Pop. B quasars, but showing more extreme shift values in the c($\frac{1}{4}$) when compared to Zamfir et al. (2010) sample. Fig. 5.3 also shows that our quasars follow the trend observed in the other two samples in the sense that larger velocity centroids, particularly in c($\frac{1}{4}$), correspond to wider FWHM(H$\beta_{\rm FP}$). Similarly, Fig. 5.3 bottom panel shows the centroid at c($\frac{1}{2}$) (upper plot) and c($\frac{1}{4}$) (lower plot) peak intensity of the MgII profile versus the FWHM of MgII$_{\rm FP}$ for our quasars and the composite spectra by Marziani et al. (2013a) corresponding to the different STs of the MS, with cyan solid triangles denoting Pop. A and orange-filled circles for Pop. B. Also in MgII our eRk objects are located in the Pop. B region and show a larger shift towards the red of the line base, although it is less pronounced than in Hβ.

One of the first differences between the two lines is observed in the broadening estimator, FWHM of the FP, in which the FWHM(MgII$_{\rm FP}$) is narrower than FWHM(H$\beta_{\rm FP}$): the median value of MgII$_{\rm FP}$ FWHM is 4470 km s^{-1}, about 10% less than the FWHM of H$\beta_{\rm FP}$, 5100 km s^{-1}. Since for the FWHM measurements of MgII$_{\rm FP}$, a single unresolved line is assumed for the doublet, those values can be converted to the FWHM of a single component by subtracting 300 km s^{-1} (Trakhtenbrot and Netzer, 2012). Taking into account this correction, we obtained a median value for the FWHM of MgII single component of $\approx$ 4170 km s^{-1}, that corresponds to $\approx$ 0.84$\pm$0.12 the median H$\beta_{\rm FP}$ FWHM, of our eRK quasars, in agreement with previous results obtained by Wang et al. (2009), claiming that FWHM of Hβ is larger than FWHM of MgII, and later clearly identified by Marziani et al. (2013a) for the Pop. B quasars. As explained in Marziani et al. (2013a), MgII might be emitted predominantly farther out from the central continuum source than Hβ. This means only part of the gas emitting Hβ is emitting MgII. For instance, the innermost regions moving with the largest velocities close to the Hβ line base could be too highly ionized to emit MgII. This is true as much of the broad line emission's kinematics can be dominated by Keplerian motion (Peterson and Wandel, 1999, 2000).

Figure 5.4 shows the relation between FWHM of one single component of MgII and H$\beta_{\rm FP}$, along with a comparison sample built by Wang et al. (2009). This

figure shows that the correlation deviates from the one-to-one line as the profile widths are affected by the VBC present in both Hβ and MgII, significantly more pronounced in Hβ, (see Sect. 5.3.1.1 and 5.3.1.2). This deviation is larger for higher FWHM(Hβ) and in particular for FWHM$>$4000 km s^{-1} corresponding to Pop. B sources where VBC is detected.

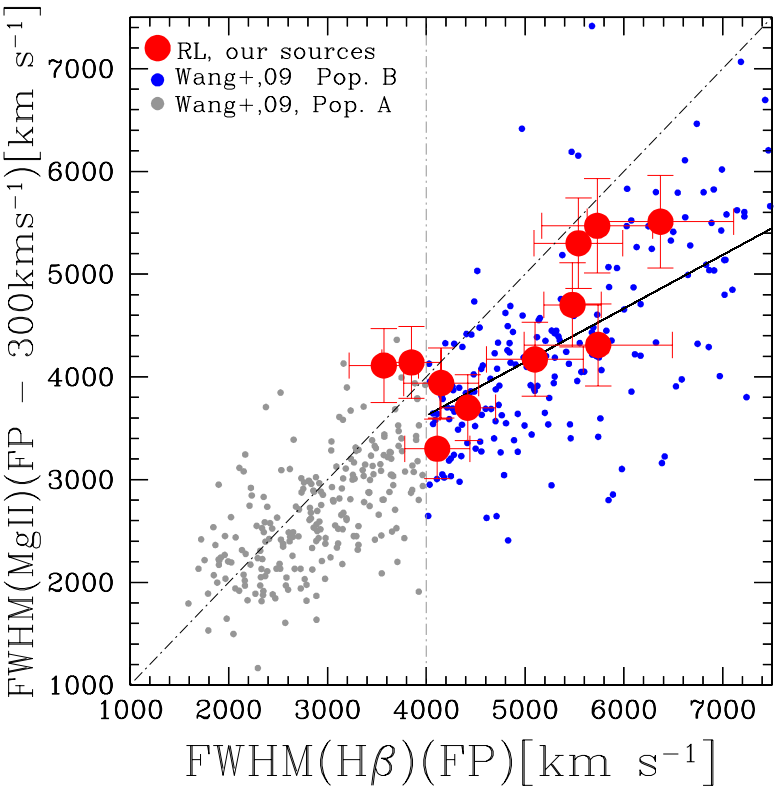

Figure 5.4: Comparison between MgII and Hβ FWHM. The ordinate is the FWHM of MgII$_{\rm FP}$ subtracted by 300 km s^{-1}. A comparison sample was taken from Wang et al. (2009), and we subdivided them into Pop. A (gray dots) and Pop. B (blue dots) by using the 4000 km s^{-1} as a separation limit. The solid line represents the correlation of both FWHM including only Pop. B sources from Wang et al. (2009) and our quasars. The two values are highly correlated, with a Pearson's correlation factor $r \approx 0.78$ and p-value ≈ 0.005.

A second difference is observed in the FP measurements deviation from the rest-frame spectra at specified fractional intensities, mainly at c($\frac{1}{2}$) and c($\frac{1}{4}$), as we mentioned above (see also Figs. 5.3 top and bottom panel.). The results of the centroid measurements on H$\beta_{\rm FP}$ and MgII$_{\rm FP}$ indicate a shift towards the red for both lines. The shift has a larger amplitude in Hβ than MgII, as shown in Fig. 5.5 (left and middle panels). This amplitude difference becomes more evident when considering the line base: the value of c($\frac{1}{4}$) is larger than the value of c($\frac{1}{2}$), suggesting that Hβ is more strongly affected than MgII by the contribution of the VBC (Sulentic et al., 2000c, 2002).

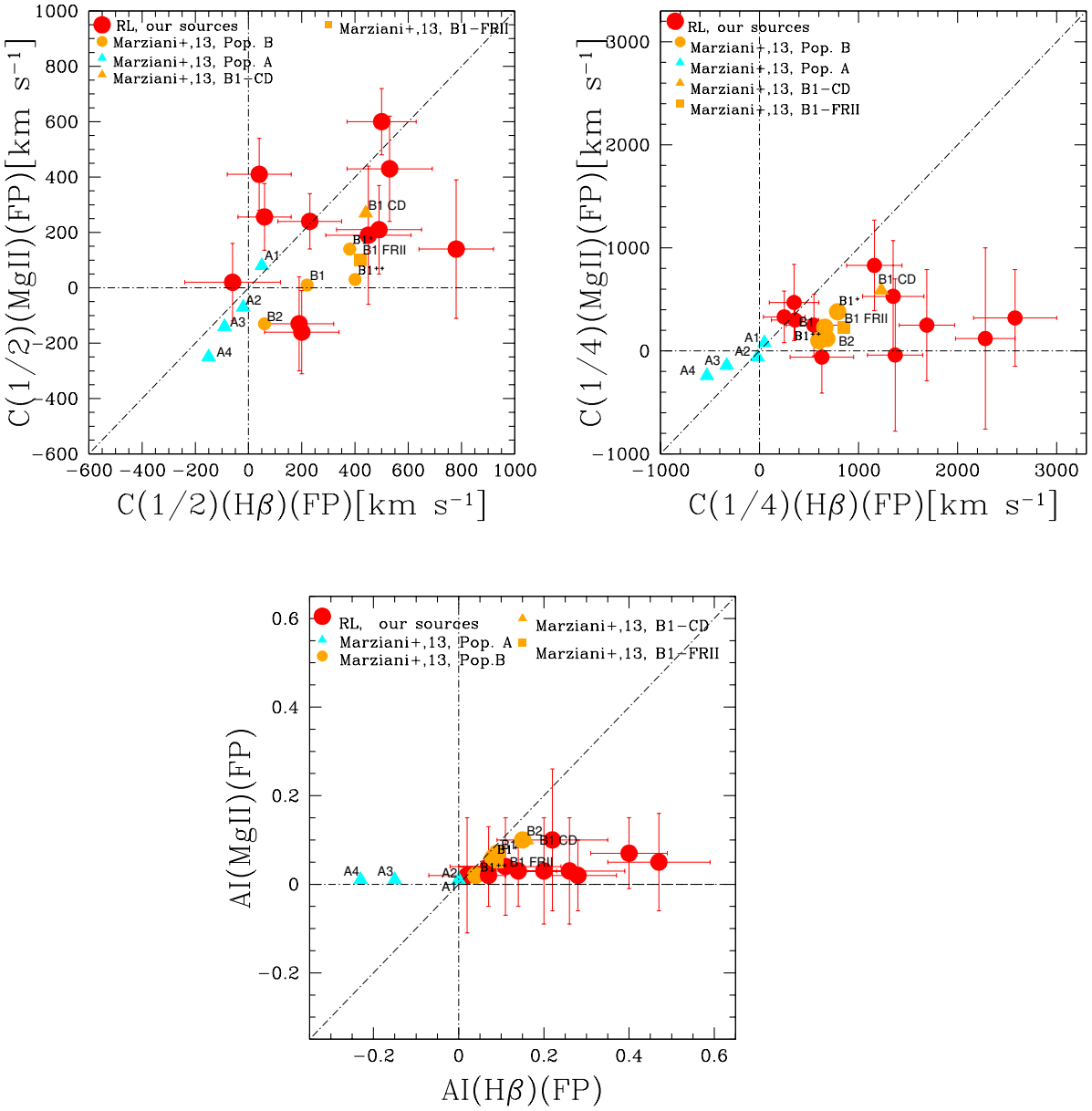

Figure 5.5: Comparison between Hβ and MgII c($\frac{1}{2}$) (left), c($\frac{1}{4}$) (middle) and asymmetry index (right) for our eRk quasars (red filled circles). An additional comparison sample was taken from composite spectra of Marziani et al. (2013a), where symbols are as in Fig. 5.3 bottom panel. The diagonal dot-dashed line in each plot represents the one-to-one line.

The same trend was shown when considering the AI (see Table 5.1 and 5.7, Col. 11, respectively). Fig. 5.5 (right) indicates that both Hβ and MgII profiles show redward asymmetry, although the AI is significantly larger for Hβ than for MgII, i.e MgII is more symmetric than Hβ. Higher KI found for MgII than Hβ are explained by the broadening of the MgII line due to its doublet

components separated by 300 km s^{-1} and by the broader Hβ profile at the line base.

The redward asymmetry in Hβ for Pop. B sources have been previously observed (e.g., Sulentic et al., 2002; Marziani et al., 2009; Wolf et al., 2020b), and can be linked to the existence of a distinct kinematic emitting region, the VBLR. The difference in the profile shape between Hβ and MgII and the `specfit` line profile analysis provides empirical evidence that the stronger Hβ VBC gives rise to a stronger redward asymmetry than in MgII.

5.3.4.2 Equivalent widths and intensities

The EW reflects the emission line strength relative to the total continuum and was obtained for each object from the best spectral fit. Fig. 5.6 (left) shows the EW of FeII$_{\rm UV}$ versus the EW of FeII$_{\rm opt}$. A correlation is not found between the two quantities. This is in agreement with the previous result by, Kovačević-Dojčinović and Popović (2015). The absence could be due to a difference in the emitting regions: the FeII$_{\rm opt}$ emission is usually thought to arise in the outer BLR before the inner radius of the torus (e.g., Popović et al., 2009; Kovačević et al., 2010; Shapovalova et al., 2012; Barth et al., 2013; Kovačević-Dojčinović and Popović, 2015). The FeII$_{\rm UV}$ might be preferentially emitted in clouds closer to the continuum source and strongly affected by the X-ray emitting corona believed to be present in most AGN (Panda et al., 2019a). Excitation mechanisms are also expected to be different: FeII$_{\rm UV}$ is produced by recombination following photoionization and enhanced by fluorescence phenomena with continuum and Lyα, while collisional excitation contributes to optical emission. A loose correlation between the intensities of the FeII$_{\rm opt}$ and FeII$_{\rm UV}$ and $R_{\rm FeII,UV}$ and $R_{\rm FeII,opt}$ might be expected in large samples of quasars because optical and UV emissions are both dependent on chemical abundances that are widely and systematically different along the quasar main sequence (e.g., Panda et al., 2019c).

The intensities of Hβ and MgII are highly correlated (Fig. 5.6, right): Pearson's $r \approx 0.77$, with a probability $P \approx 0.01$ of a stochastic correlation. The MgII/Hβ intensity ratio varies in the range 0.5–1.8, with an average of ≈ 1.2, a value consistent with the ones derived for composites RL spectra in Population B (see Table 3 of Marziani et al., 2013a).

5.4 Discussion

As pointed out in the previous sections, quasar's broad line spectra show a wide range of line profiles, line shifts, and line intensities. To explain this spectroscopic diversity, much emphasis was placed on the connection between

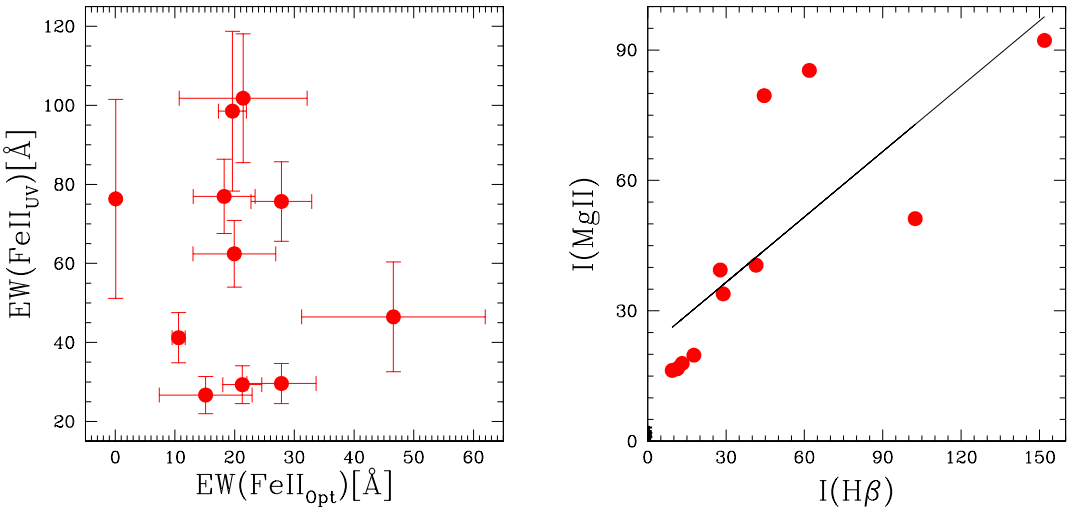

Figure 5.6: Left: relation between EW of FeII$_{opt}$ and FeII$_{UV}$. The uncertainties in the EW were taken to be proportional to the uncertainty in the flux of the FeII emissions in the two regions (see Sect. 4.5). Right: correlation between the intensities of Hβ and MgII. The intensities are highly correlated with $r \approx 0.77$ and a p-value ≈ 0.01.

profile parameters (e.g., Martínez-Aldama et al., 2015; Rakić, 2022; Kovačević-Dojčinović et al., 2022), M_{BH} (e.g., Boroson, 2002; Hernitschek et al., 2016; Bao et al., 2022), luminosity (e.g., Marziani et al., 2009; Popović and Kovačević, 2011; Rakić et al., 2017) and accretion rate (e.g., Mathur et al., 2001; Marziani et al., 2001). In this section, we present a discussion on M_{BH} and Eddington ratio (λ_E) (Sect. 5.4.1), and their effects on the line profile shapes (Sect. 5.4.2). Finally, we consider the role of radio loudness (Sect. 5.4.3).

5.4.1 Black hole mass and Eddington ratio

The estimation of M_{BH} and Eddington ratio (λ_E) is crucial for understanding the AGN phenomenon, its evolution across cosmic time, and the properties of the host galaxies (e.g., Marconi and Hunt, 2003). In addition, M_{BH} is a fundamental parameter that relates to the evolutionary stages and the accretion processes occurring within them, as the power output is directly proportional to M_{BH} (e.g., Lapi et al., 2006; Fraix-Burnet et al., 2017). The Eddington ratio ($\lambda_E = L_{bol}/L_{Edd}$) is a parameter that expresses the relative balance between gravitational and radiation forces (e.g., Marziani et al., 2010; Netzer and Marziani, 2010), a major factor influencing both the dynamics and the physical conditions of the line emitting gas (Marziani et al., 2018).

To estimate M_{BH} for type-1 AGN, we used an empirically calibrated formalism (scaling laws) that is based on single-epoch spectra (e.g., Vestergaard and Peter-

Table 5.9: Physical parameters measurement from the FP (BC + VBC) and BC of Hβ and MgII lines.

Object	Measurements from full broad profile (BC + VBC)						Measurement from broad component only (BC)			
	Accretion parameters (Hβ)			Accretion parameters (MgII)			Accretion parameters (Hβ)		Accretion parameters (MgII)	
	$\log L_{bol,5100}$	$\log M_{BH}^{a}$	$\log\lambda_E{}^{a}$	$\log L_{bol,3000}$	$\log M_{BH}^{b}$	$\log\lambda_E{}^{b}$	$\log M_{BH}^{a}$	$\log\lambda_E{}^{a}$	$\log M_{BH}^{b}$	$\log\lambda_E{}^{b}$
(1)	(2)	(3)	(4)	(5)	(6)	(7)	(8)	(9)	(10)	(11)
PHL923	45.78	8.56	-0.90	45.80	8.58	-0.89	8.39	-0.73	8.43	-0.74
B2 0110+29	45.15	8.49	-1.45	44.98	8.26	-1.40	8.21	-1.18	8.15	-1.29
3C37	45.73	8.73	-1.11	45.66	8.76	-1.21	8.60	-0.98	8.64	-1.10
PKS 0230-051	46.11	8.89	-0.90	46.10	8.90	-0.92	8.66	-0.66	8.75	-0.77
3C94	46.57	9.25	-0.74	46.53	9.33	-0.92	9.35	-0.70	9.33	-0.73
PKS 0420-01	46.49	8.94	-0.57	46.17	8.77	-0.71	8.83	-0.45	8.62	-0.56
3C179	45.95	8.49	-0.64	45.86	8.71	-0.96	8.22	-0.38	8.54	-0.79
3C380	46.33	9.13	-0.92	46.18	8.99	-0.93	8.82	-0.60	8.80	-0.73
S5 1856+73	46.11	8.99	-1.00	45.93	8.99	-1.18	8.92	-0.93	8.84	-1.03
PKS 2208-137	45.86	8.49	-0.75	45.83	8.69	-0.97	8.43	-0.69	8.56	-0.84
PKS 2344+09	46.55	8.99	-0.55	46.49	9.16	-0.78	8.87	-0.44	9.01	-0.64

$^{(a)}$Estimated from Vestergaard and Peterson (2006).$^{(b)}$Estimated from Trakhtenbrot and Netzer (2012). Cols. 2 and 5 in ergs s^{-1}. $M_{\rm BH}$ cols. in units of $M_{\odot}$.

son, 2006; Ho and Kim, 2015) and that has been applied to large and diverse samples of AGN (e.g., Marziani and Sulentic, 2012a; Shen, 2013). At low redshift ($z \lesssim 0.8$), the lines of choice for estimation can be Hβ and MgII (e.g, Kaspi et al., 2000; Vestergaard and Peterson, 2006; McLure et al., 2006). Table 5.9 reports the estimations of the accretion parameters for our eRk quasars by using both the BC and FP FWHM measurements. Cols. 2 and 5 report the Bolometric luminosity ($L_{\rm bol}$) estimated from the optical (5100Å) and UV (3000Å) continuum luminosity respectively, as λL_{λ}, by using the luminosity dependent relation from Netzer (2019) to calculate the Bolometric correction factor (K_{bol}) for the luminosity in question (L_{5100} or L_{3000}). The Bolometric luminosity of our eRk quasars estimated with $\log L_{\rm bol}$ between 45.15–46.57 and 44.98–46.53 [ergs s^{-1}] from Hβ and MgII, respectively. Cols. 3–4 and 6–7 list the $M_{\rm BH}$ and $\lambda_{\rm E}$ by using the FP FWHM measures and the relations from Vestergaard and Peterson (2006) for Hβ and Trakhtenbrot and Netzer (2012) for the MgII line, respectively. The same estimation was also done by using FWHM of the BC alone rather than the FP and reported in Cols. 8–11. $M_{\rm BH}$ values computed from the FP FWHM range from $\log M_{\rm BH}\,[M_{\odot}] \approx 8.49$ to 9.25 (Hβ) and from $\log M_{\rm BH} \approx 8.26$ to 9.33 (MgII).

In addition to the above two widely used $M_{\rm BH}$ scaling relations, different scaling relations and lines for the same source are also compared to verify the consistency of the estimation. For this, we included the prescriptions of McLure and Jarvis (2002), Vestergaard and Osmer (2009), Shen et al. (2011), Assef et al. (2011), and Shen and Liu (2012) using MgII and Hβ lines as well as using FWHM measurements of FP, BC and 0.8 x FWHM(FP) (for the case of MgII only). The resulting estimations are summarized in Table 5.10.

Fig. 5.7 indicates that the mass estimation using Hβ and Vestergaard and Pe-

Table 5.10: $M_{\rm BH}$ estimation from different scaling relations using MgII and Hβ.

Object	Log$M_{\rm BH}$ in units of $M_\odot$																	
(1)	(2)	(3)	(4)	(5)	(6)	(7)	(8)	(9)	(10)	(11)	(12)	(13)	(14)	(15)	(16)	(17)	(18)	(19)
PHL923	8.50	8.29	8.34	8.47	8.27	8.32	8.57	8.40	8.44	8.20	8.01	8.06	8.41	8.19	8.62	8.41	8.56	8.34
B2 0110+29	8.33	8.12	8.22	8.15	7.96	8.04	8.25	8.08	8.15	8.04	7.85	7.94	8.25	7.97	8.48	8.22	8.47	8.20
3C37	8.72	8.51	8.60	8.65	8.45	8.53	8.71	8.55	8.62	8.41	8.22	8.30	8.57	8.44	8.77	8.65	8.73	8.60
PKS 0230-051	8.79	8.58	8.62	8.79	8.60	8.64	8.87	8.70	8.74	8.47	8.28	8.32	8.78	8.55	8.97	8.74	8.90	8.64
3C94	9.12	8.91	8.96	9.19	9.00	9.05	9.24	9.07	9.11	8.79	8.59	8.64	9.20	9.11	9.34	9.26	9.30	9.18
PKS 0420-01	8.63	8.42	8.46	8.66	8.47	8.51	8.76	8.60	8.63	8.33	8.14	8.18	8.89	8.77	9.05	8.94	8.96	8.84
3C179	8.63	8.42	8.45	8.60	8.41	8.43	8.69	8.52	8.54	8.33	8.13	8.16	8.36	8.09	8.57	8.31	8.49	8.22
3C380	8.87	8.66	8.66	8.88	8.69	8.69	8.95	8.79	8.78	8.55	8.36	8.35	9.05	8.74	9.21	8.92	9.14	8.83
S5 1856+73	8.92	8.71	8.76	8.88	8.69	8.74	8.93	8.77	8.81	8.60	8.40	8.45	8.88	8.81	9.06	8.99	8.99	8.93
PKS 2208-137	8.61	8.41	8.47	8.58	8.39	8.45	8.67	8.50	8.55	8.31	8.12	8.18	8.35	8.29	8.56	8.51	8.49	8.43
PKS 2344+09	8.98	8.77	8.82	9.05	8.86	8.90	9.11	8.95	8.99	8.66	8.46	8.51	8.94	8.82	9.10	8.99	9.01	8.89

Note: To estimate $M_{\rm BH}$, we used FWHM(FP), 0.8 x FWHM(FP) and FWHM(BC) of MgII with Vestergaard and Osmer (2009) (Cols. 2 - 4), Shen et al. (2011) (Cols. 5 - 7), Shen and Liu (2012) (Cols. 8 - 10) and McLure and Jarvis (2002) (Cols. 11 - 13) scaling relations. Using Hβ and FWHM(FP) and FWHM(BC) estimated using McLure and Jarvis (2002) (Cols.14 - 15), Shen and Liu (2012) (Cols.16 - 17), and Assef et al. (2011) (Cols.15 - 19).

terson (2006) relation is in a very good agreement with the mass estimation from MgII, when using four different MgII scaling laws, namely the ones from Vestergaard and Osmer (2009), Shen et al. (2011), Trakhtenbrot and Netzer (2012) and Shen and Liu (2012). This result also holds if only the BC is used (see Table 5.9, Cols. 8 and 10). We also checked the mass estimation by using MgII with McLure and Jarvis (2002) relation and found a lower estimation by about 0.25 dex compared to the other scaling relations (not shown in Fig. 5.7 to avoid confusion).

The $\log(\lambda_{\rm E})$ values for our eRk quasars range from -1.45 to -0.55 and from -1.40 to -0.78 (see Table 5.9, Cols. 4 and 7) when using the Hβ and MgII lines, respectively. Previous studies suggested that around some critical value of $\lambda_{\rm E} \approx 0.2 \pm 0.1$, there could be an accretion mode change i.e., a change in the structure of the accretion disk (e.g., Abramowicz and Straub, 2014; Marziani et al., 2018; Giustini and Proga, 2019, and references therein), or at least in the BLR dynamics (Collin et al., 2006). For a given $\log M_{\rm BH} \approx 8.5$, Pop. A sources show $\log(\lambda_{\rm E}) = -0.7 - 0$, and Pop. B show $\log(\lambda_{\rm E}) = -2$ – -0.7 (Sulentic et al., 2011). All our quasars fit into the Pop. B domain of low accretion rates. The two sources (3C 179 and PKS 2208-137) with FWHM < 4000 km s^{-1} have $\log(\lambda_{\rm E}) \approx$ -0.64 and -0.75, respectively. These values are at the $\lambda_{\rm E}$ boundary between Pop. A and B, signifying a possible $M_{\rm BH}$ underestimate due to low S/N (i.e., loss of line wings in the case of 3C 179) or perhaps to a pole-on orientation of the emitting regions (e.g., Wills and Browne, 1986; Sulentic et al., 2003; Rokaki et al., 2003; Zamfir et al., 2008).

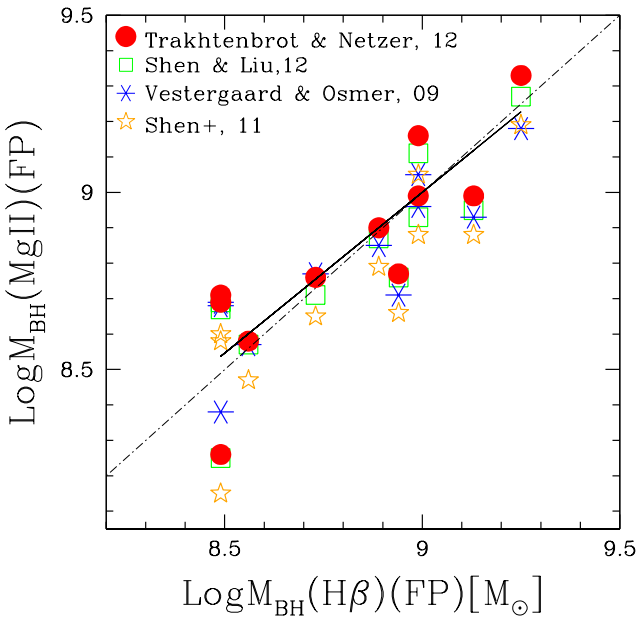

Figure 5.7: $M_{\rm BH}$ comparison for estimates from Hβ and MgII, FP FWHM measurement using different scaling laws. The abscissa is $M_{\rm BH}$ estimated using the formula from Vestergaard and Peterson (2006). In ordinate, we plot different $M_{\rm BH}$ estimates for MgII, from Vestergaard and Osmer (2009), Shen et al. (2011), Trakhtenbrot and Netzer (2012), and Shen and Liu (2012). The dot-dashed line represents the 1:1 line, and the solid one represents the correlation between the masses estimated by using Vestergaard and Peterson (2006) for Hβ and Trakhtenbrot and Netzer (2012) for MgII. The Pearson correlation coefficient between the two estimates is $r = 0.91$.

5.4.2 Correlations between profile and physical parameters

5.4.2.1 $M_{\rm BH}$ correlations

Fig. 5.8 and Fig. 5.9 show profile parameters, as AI and centroids, as a function of $M_{\rm BH}$, for Hβ and MgII respectively, including our eRk quasars and the comparison samples. The immediate result is that there is no strong, clear correlation with $M_{\rm BH}$ – although an intriguing trend appears for the joint comparison sample. This is also supported by previous statistical tests for low-z Pop. B sources (Zamfir et al., 2010).

Restricting the attention to Hβ, for the joint comparison sample and irrespective of whether the sources are Pop. A or B, below $\log M_{\rm BH} \sim 8.5 [{\rm M}_\odot]$ RL sources show a weak median redshift for $c(\frac{1}{4}) \approx 280 \pm 270$ km s^{-1}, while RQs show no significant shift nor asymmetry (median $c(\frac{1}{4}) \approx$ -20 $\pm$180 km s^{-1}, $\mu_{1/2}{\rm AI} \approx 0.01 \pm 0.08$). Above $\log M_{\rm BH} \sim 8.5\,[{\rm M}_\odot]$, there is an increase in scatter in the values of the AI and centroids, and a predominance of shifts to the

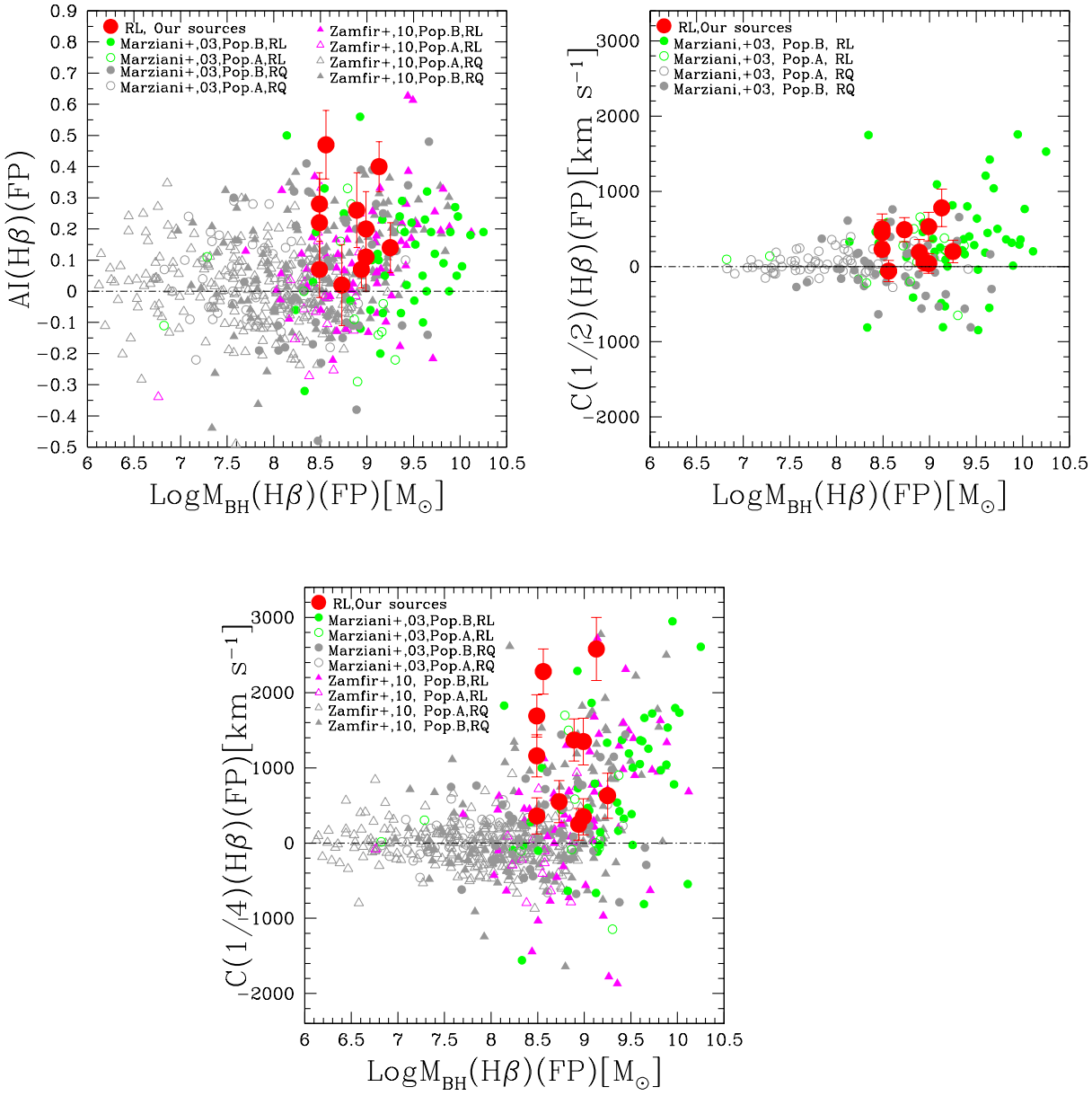

Figure 5.8: $M_{\rm BH}$ effect on the line profile parameters, AI (left), on c($\frac{1}{2}$) and c($\frac{1}{4}$) (middle and right plots, respectively). Comparison samples were taken from Marziani et al. (2003a) for c($\frac{1}{2}$) and Marziani et al. (2003a) and Zamfir et al. (2010) for AI and c($\frac{1}{4}$). The large red solid circles represent the results from our RL spectra. The horizontal dot-dashed lines trace the symmetry line for zero AI, c($\frac{1}{2}$) and c($\frac{1}{4}$).

red appears, especially for RL sources ($\mu_{1/2}$c($\frac{1}{4}$) $\approx 660 \pm 650$ km s^{-1}, $\mu_{1/2}$AI $\approx$ 0.1$\pm$0.1), while RQs remain more symmetric (median c($\frac{1}{4}$) $\approx 150 \pm 490$ km s^{-1}, AI $\approx$ 0.04$\pm$0.10), albeit with a slight net shift to the red. Restricting now the attention to only Pop. B sources, Hβ yields similar results: RL shows a

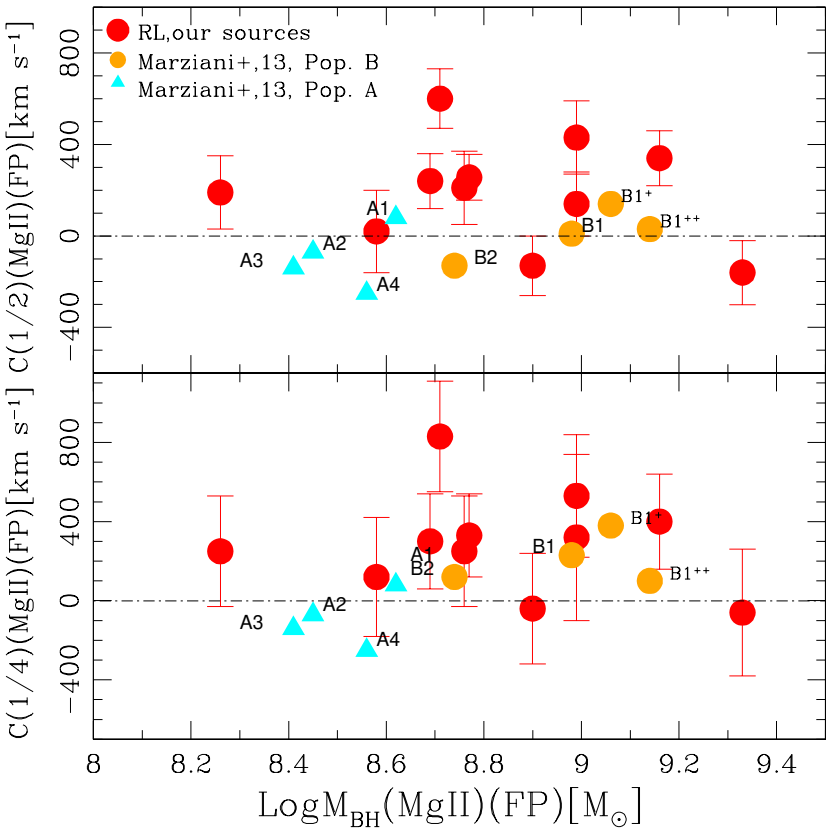

Figure 5.9: $M_{\rm BH}$ of MgII$_{\rm FP}$ and centroid shift comparison at c($\frac{1}{2}$) (upper) and at c($\frac{1}{4}$) (lower) of MgII. The large red solid circles represent the results from our RL spectra. A comparison sample was taken from the composite spectra of, Marziani et al. (2013a), and the meaning of symbols is as for Fig.5.3 bottom panel.

trend towards the red with a median c($\frac{1}{4}$) $\approx$ 300$\pm$270 km s^{-1} for $\log M_{\rm BH} \lesssim$ 8.5 [M$_\odot$], while the RQ counterpart a median centroid consistent with no shift (c($\frac{1}{4}$) $\approx$ 30$\pm$280 km s^{-1}). For the higher $M_{\rm BH}$ range, both RQ and RL Pop. B sources show a net shift to the red that reaches a median c($\frac{1}{4}$) $\approx$ 680 km s^{-1}for the RL subsample. Consistently, for the whole comparison sample, the ratio of the number of sources with negative and positive c($\frac{1}{4}$) is $\approx$1.2 for RQ for log$M_{\rm BH}$ < 8.5 and 0.61 for log$M_{\rm BH}$ > 8.5. The same ratio for RL sources is 0.45 and 0.31 for the two mass ranges, showing a net predominance of redshift. If the attention is restricted to Pop. B, we see a net predominance of redshifts for both RQ and RL in the higher mass range (ratio negative-to-positive c($\frac{1}{4}$) is 0.38 and 0.30, respectively). In the lower $M_{\rm BH}$ range, the prevalence of redshifts is higher for RL (ratio $\approx$ 0.54) than for RQ (ratio $\approx$ 0.95) for which the distribution is fairly symmetric, as expected also by the almost zero median shift amplitude of c($\frac{1}{4}$).

The intrinsic shift to red might be associated with gravitational redshift (e.g.

Bon et al., 2015; Punsly et al., 2020) or with infall plus obscuration (Wang et al., 2017). However, the origin of the redward asymmetry is still unclear and the subject of ongoing investigations (e.g., Bao et al., 2022). Infall of gas toward the centre is an alternative to gravitational redshift that may also produce significant shifts to the red expected to grow in amplitude toward the line base (Penston et al., 1990; Fromerth and Melia, 2001; Wang et al., 2017).

Related to MgII, Figure 5.9 shows the centroid shift at the two different fractional intensities of the MgII line as a function of $M_{\rm BH}$ computed from FWHM $\rm MgII_{FP}$. The values of $c(\frac{1}{2})$ and $c(\frac{1}{4})$ are comparable, with a slight systematic difference of about 100 km s^{-1}. Considering the comparison composite samples from Marziani et al. (2013a), Pop. B MgII centroid shifts close to the line base exceed the ones at the centre by a modest amount of 200 - 300 km s^{-1}, at variance with Hβ: the Hβ line base is significantly more redshifted than the centre. For instance, the eRk sample sources show an average $c(\frac{1}{4})$ - $c(\frac{1}{2}) \approx$ 800 km s^{-1}. As mentioned above, the MgII profile retains a higher degree of symmetry than Hβ because of a less prominent VBC. Whatever the cause of the reward asymmetry might be, the MgII profile is less affected than Hβ.

5.4.2.2 $\lambda_{\rm E}$ correlations

Several authors suggested that outflows are apparently more related to $\lambda_{\rm E}$ than to luminosity or $M_{\rm BH}$ (e.g., Abramowicz and Straub, 2014; Sulentic et al., 2017). How $c(\frac{1}{2})$, $c(\frac{1}{4})$, and $\lambda_{\rm E}$ are related, in our eRk quasars and the comparison samples, is shown in Fig. 5.10.

Pop. B RL and RQ quasars belonging to the comparison samples are redshifted, and they generally possess low $\lambda_{\rm E}$. If the shift to the red is gravitational in origin, the line might be emitted from a region closer to the central SMBH which results in larger shifts if the $\lambda_{\rm E}$ is lower. As there is a consensus that outflows produce blueshifts (Marziani and Sulentic, 2012b), the lower shifts at higher $\lambda_{\rm E}$ may be due to the increased relevance of radiation forces with respect to gravitation, which may push outward the emitting gas if there is a sort of radiation pressure/gravitation balance (Mathews, 1993; Marconi et al., 2009; Netzer and Marziani, 2010; Khajenabi, 2015). Therefore, a difference between RL and RQ might be due to a combination of inflows and outflows that may result in a net slightly redshifted profile for RQ where winds are stronger (e.g., Bachev et al., 2004; Sulentic et al., 2007a; Richards et al., 2011), and more redshift profiles for RLs, due to less prominent outflows.

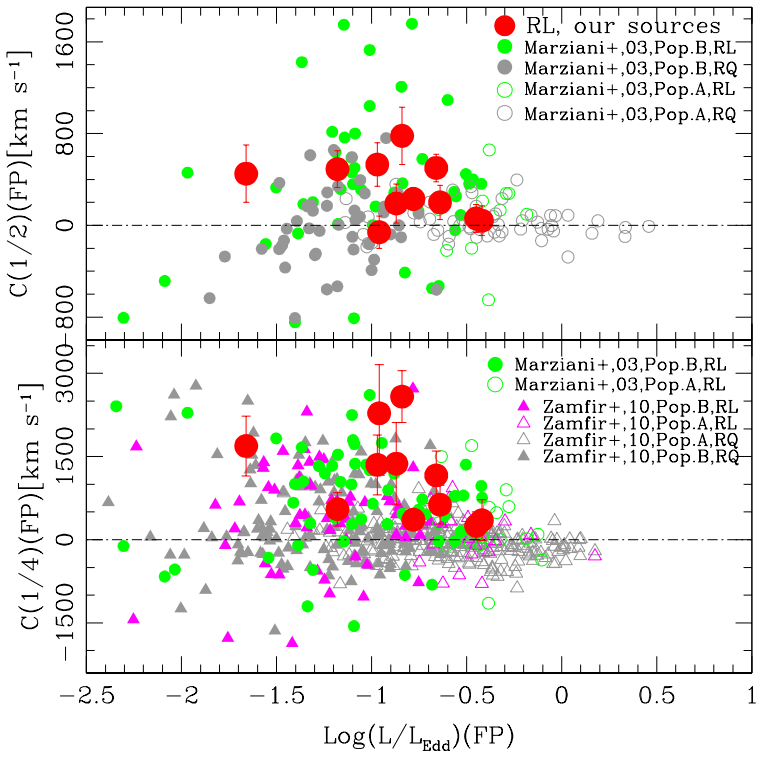

Figure 5.10: Dependence of Hβ c($\frac{1}{2}$) (upper) and c($\frac{1}{4}$) (lower) on logλ_E calculated from the FP. Comparison samples were taken from Marziani et al. (2003a) for c($\frac{1}{2}$) and Marziani et al. (2003a) and Zamfir et al. (2010) for c($\frac{1}{4}$).

5.4.3 Similarities and differences between RL and RQ quasars

For better visualization of the trends using the main comparison samples as well as the eRk sources, we analyzed the distribution of the velocity centroids at 1/4 based on their population as well as radio type. In addition, we showed the median measurements of the comparison samples in equally spaced bins by using the semi-interquartile range as an estimate of the sample dispersion. Our eRk quasars are strong radio emitters with $\log R_K > 3$ and very powerful with log $P_\nu > 33.3$ [ergs s^{-1} Hz^{-1}], and include some of the highest $\log R_K$ values ever observed. Objects with $\log R_K \geq 3$ are most likely highly beamed, but they are still expected to be very powerful radio sources as suggested previously by Cohen et al. (2007).

The first result of the inter-comparison between RL and RQ sources is their distribution in the optical plane of the MS (see Fig. 5.1). In that figure, all the eRk sources show a restricted domain occupation (mostly B1) compared to the RQ majority (taken from Zamfir et al. (2010). RQ sources are found in both Pop. A and Pop. B and are distributed along the MS in all bins. The RLs, with CD and FR II morphology, show a distribution centered in the region of low $R_{FeII,opt}$ and broader FWHM. A restricted domain space occupation of

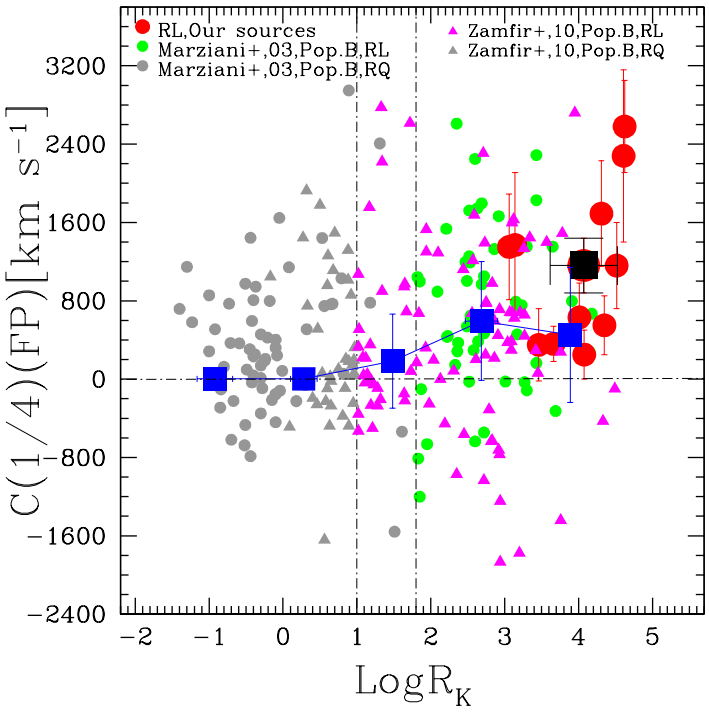

Figure 5.11: Relation between c($\frac{1}{4}$) of Hβ and radioloudness parameter. Sources from Marziani et al. (2003a) and Zamfir et al. (2010) were taken as comparison sample. The connected blue solid squares represent the median value of the comparison sample distribution in equally-spaced bins, where the vertical bars were computed by using the semi-interquartile range as an estimate of the sample dispersion. The horizontal bins denote, for each bin, the mid-point of the bin interval. The black solid square is the median value for our eRk quasars. The horizontal dot-dashed line traces the symmetric line in c($\frac{1}{4}$). The vertical lines at 1 and 1.8 mark the nominal RQ-radio intermediate and radio intermediate-RL boundaries (Zamfir et al., 2008).

Pop. B RL sources are also shown in the previous studies of Sulentic et al. (2000b, 2003). Similar considerations apply to the sources that are used to make the composite in Marziani et al. (2013a, see their Table 1 for the number of sources in different bins).

Figure 5.11 relates the velocity centroid shift, c($\frac{1}{4}$) of Hβ to the radio loudness parameter, R_K, for our eRk, and the Marziani et al. (2003a) and Zamfir et al. (2010) Pop. B subsamples, represented in equally-spaced bins of R_K. The second result is that the Pop. B RL source distribution doesn't show a clear trend with the R_K. However, there is a significant increase in the centroid shift between Pop. B RQ and Pop. B RL: the median c($\frac{1}{4}$) is $\approx$ 233 km s^{-1} and 144 km s^{-1} for Pop. B RQ, and becomes $\approx$ 720 km s^{-1} and 440 km s^{-1} for the RL sources of Marziani et al. (2003a) and Zamfir et al. (2010) samples, respectively. The centroid shift for the eRk sources even reaches 1350 km s^{-1}.

The significance of this difference needs to be further investigated in samples with matching $\lambda_{\rm E}$ and $M_{\rm BH}$ distributions, as systematic differences between RL and RQ sources are also found in terms of $M_{\rm BH}$. Considering the two comparison samples from Marziani et al. (2003a) and Zamfir et al. (2010) and our eRk, and then subdividing the Pop. B quasars only into RLs and RQs, the RQ sources have $\mu_{\frac{1}{2}}\log M_{\rm BH} \approx 8.18 \pm 0.53$ [$M_\odot$] and the RL's, $\mu_{\frac{1}{2}}\log M_{\rm BH} \approx 8.98 \pm 0.54$ [$M_\odot$], a 0.8 dex difference. In addition, considering the $\lambda_{\rm E}$, the RQs may be slightly higher accretors compared to the RLs, $\mu_{\frac{1}{2}}\log\lambda_{\rm E} \approx$ -1.081 $\pm$ 0.156 and $\mu_{\frac{1}{2}}\log\lambda_{\rm E} \approx$ -1.121 $\pm$ 0.224, respectively that become $\mu_{\frac{1}{2}}\log\lambda_{\rm E} \approx$ -0.785 $\pm$ 0.343 and $\mu_{\frac{1}{2}}\log\lambda_{\rm E} \approx$ -1.009 $\pm$ 0.348 with a difference of -0.224 dex if a constant optical Bolometric correction of 10 is applied. Systematically lower $\lambda_{\rm E}$ and larger $M_{\rm BH}$ for Pop. B RL sources have also been found in several past works (e.g., Boroson, 2002; Dunlop et al., 2003; McLure and Dunlop, 2004).

Therefore, it is not necessarily appropriate to correlate radio loudness to a single variable such as c($\frac{1}{4}$), since other parameters such as $\lambda_{\rm E}$ and $M_{\rm BH}$ are expected to play a role (Woo and Urry, 2002; Körding et al., 2006). We need to take this into account if we compare the radio parameters and centroid shifts: the distribution of shifts appears to be slightly dependent on $M_{\rm BH}$, i.e. largest c($\frac{1}{4}$) values occur for the highest $M_{\rm BH}$ (Fig. 5.8) and lowest $\lambda_{\rm E}$ (Fig. 5.10). To verify whether there is a genuine effect of radio loudness on the c($\frac{1}{4}$), we considered the samples of Zamfir et al. (2010), and of Marziani et al. (2003a), added the 11 RLs of the present work and separated RQ and RL within Pop. B only, where most RL reside. This gave us 169 RQ and 145 RL Pop. B sources, of which 53 are eRk with $\log R_{\rm K} \geq 3$. The c($\frac{1}{4}$) distributions remain different ($P \sim 3 \cdot 10^{-5}$), suggesting that the shift amplitudes are higher in RL than in RQ. However, the $M_{\rm BH}$ distributions of RQ and RL are also markedly different ($P \sim 1 \cdot 10^{-4}$ that they are drawn from the same parent populations), with medians differing by $\delta\log M_{\rm BH} \approx 0.35$, while the two $\lambda_{\rm E}$ distributions are similar (Fig. 5.12).

Bootstrap replications of the RQ Pop. B samples were computed considering only distributions of $M_{\rm BH}$ and $\lambda_{\rm E}$ that were consistent with the ones of RL Pop. B (Fig. 5.12 upper right panel). Of the 1000 bootstrap distributions for the RQ Pop. B c($\frac{1}{4}$) $\lesssim$ 85% were different from the RL one by a confidence level more than 2σ. Therefore, within the limitations of our sample, we are unable to detect a highly significant effect of radio loudness on the c($\frac{1}{4}$) shift amplitude. The majority of the RQ Pop. B bootstrapped distributions of c($\frac{1}{4}$) are largely overlapping with the RL one. The analysis thus confirms the statement of Marziani et al. (2003b) that the RQ and RL show similar velocity shift amplitudes, with the most extreme values (the ones attracting more attention) occurring for RLs.

Extreme RL sources, i.e. the 53 Pop. B sources with $\log R_K \geq 3$, have a larger c($\frac{1}{4}$) shift with respect to the full population of RL, with distributions that are different at an even higher significance ($P \sim 10^{-6}$). We repeat the bootstrap analysis matching the RQ M_{BH} and λ_E distributions to the ones of the extreme RLs, and in this case, the difference at a 2σ confidence level is highly significant: less than 1 out of 1000 RQ c($\frac{1}{4}$) resampled distributions are statistically indistinguishable from the extreme RL one. The extreme RL sources also show c($\frac{1}{4}$) in excess with respect to the RL sources with $1.8 \leq \log R_K < 3$, and the 2σ excess is still confirmed at a high confidence level. Therefore, the significance of the difference between RQ and RL sources is strongly dependent on sample biases, as it is mainly driven by the fraction of sources with a high Kellermann ratio.

Equally important is not to forget the similarity between RQ and RL Pop. B sources. The same line profile phenomenology is observed in both classes, provided that a restriction to Pop. B is done for RQ quasars: RLs appear more extreme but with a large overlap in the line profile parameter distribution with RQs. This indicates that there could be only a quantitative effect on the BLR associated with the jet, without inducing any strong structural or dynamical change. Investigations that are beyond the scope of the present paper are needed to ascertain the physical origins of the excess c($\frac{1}{4}$) shift in the most powerful RL.

5.5 Conclusions

This work presented new long-slit simultaneous near-UV and optical spectra of 11 relativistically jetted quasars selected based on their extreme radio emission ($\log R_K > 3$, the eRk sources) with redshifts $0.35 \lesssim z \lesssim 1$, and studied their spectroscopic properties by using the optical projection of the four-dimensional eigenvector 1 (4DE1) parameter space i.e., the so-called quasar main sequence (MS). Our analysis focused mainly on the spectral fitting of the strongest emission lines recorded on our spectra, MgII, and Hβ, by using `specfit` routine within the `IRAF` package. We aimed to quantify broad emission line differences between radio-loud (RL) and radio-quiet (RQ) quasars, paying special attention to the quasars with extreme radio emission.

The main findings that we draw from this study are:

- The eRk quasars presented in this paper occupy a much more restricted domain in the optical plane ($\sim$ bin B1) compared to the RQ sources of the comparison samples. This confirms the result of Zamfir et al. (2008)

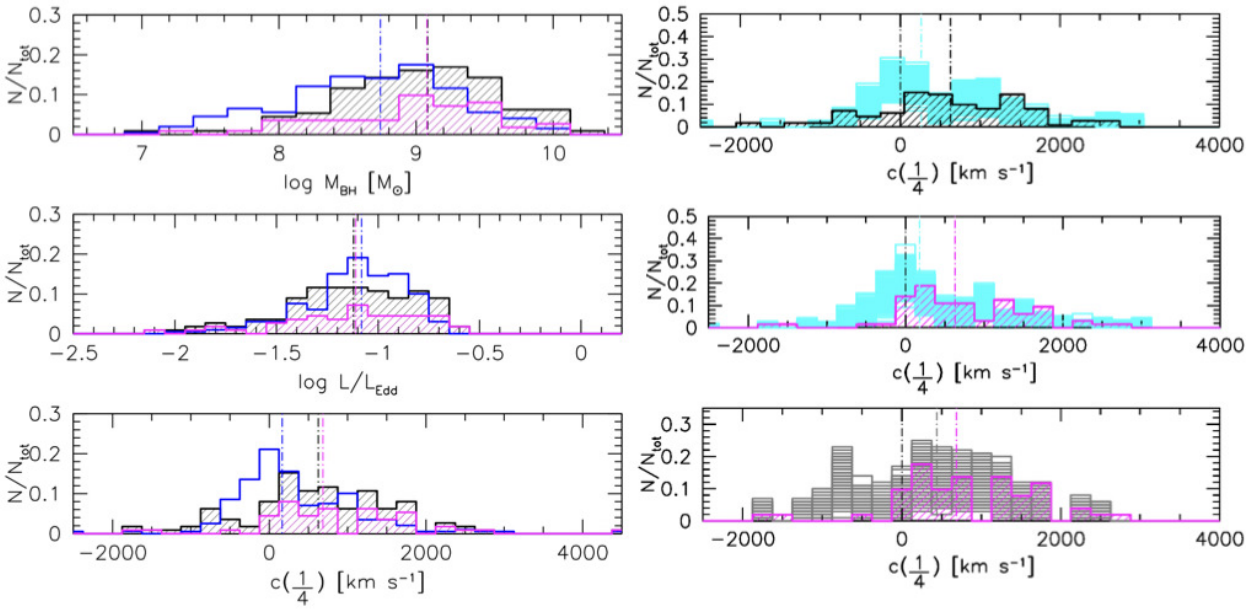

Figure 5.12: Results of the bootstrap analysis. Left panels, from top to bottom: distributions of $M_{\rm BH}$, $L_{\rm bol}/L_{\rm Edd}$, and Hβ c($\frac{1}{4}$) for the RQ (blue), RL (black shaded), and extreme RL (log $R_{\rm K} \geq 3$, magenta). Right panels: comparison between Hβ c($\frac{1}{4}$) resampled distributions matching $M_{\rm BH}$ and $\lambda_{\rm E}$ and original distributions. Top: RL vs RQ bootstrap replications; middle: extreme RL vs RQ bootstrap; bottom: extreme RL vs. rest of RL i.e., objects with $1.8 \leq \log R_{\rm K} < 3$. Vertical dot-dashed lines indicate medians.

who found that powerful jetted sources tend to occupy mainly the Pop. B region of the MS.

- The UV plane formed from FWHM of MgII and FeII$_{\rm UV}$ looks similar to the optical plane. As in the optical plane, our quasars occupy a more restricted domain than the full quasar population, with low $R_{\rm FeII,UV}$. There is no correlation between the EW of FeII$_{\rm UV}$ and FeII$_{\rm opt}$ in our eRk sample.

- The FWHM of MgII is systematically narrower than FWHM Hβ by about 10%. This holds for both the full profile (BC+VBC) and if only the broad component is considered for our eRk sample, a result consistent with previous studies.

- Both Hβ and MgII lines show profile shifts and asymmetries towards the red. The centroid shift of the line base c($\frac{1}{4}$), as well as the asymmetry index, are larger in Hβ than MgII.

- Hβ and MgII appear to provide consistent virial $M_{\rm BH}$ estimates. The eRk quasars of this paper lie within the range of $\log M_{\rm BH}$ = 8.49 – 9.25[M$_\odot$]

and 8.26 – 9.33[$M_\odot$] when using Hβ_{FP} and MgII$_{FP}$, respectively. The resulting logλ_E has a range of [-1.65, -0.42] and [-1.40,-0.71].

- Joining the sources studied in this work with comparison samples, we find that the distribution of shifts appears to be slightly dependent on M_{BH} in which larger c($\frac{1}{4}$) values occur for the highest M_{BH} and lowest λ_E values. A possible explanation is offered by a combination of outflow and infall (or gravitational redshift) contributing to blueshifted and redshifted excesses, respectively, with the outflow component being minimal in the RL Hβ and MgII profiles of our sources.
- There is a trend between the velocity shifts, stronger for c($\frac{1}{4}$), and R_K: Pop. B RL quasars tend to have larger velocity shifts to the red than RQs. The difference is found to be only marginally significant if the RQ and RL M_{BH} and λ_E distributions are matched. However, the difference becomes highly significant if the comparison is carried out between eRk and RQ Pop. B AGN.

There is apparently no evidence of outflow in the broad-line profiles of our eRk sources. The only evidence is provided by a slight asymmetry of [OIII]. Further observations of HILs such as CIVλ1549 would be needed to assess the extent of any mildly ionized outflow origination from the accretion disk.

Chapter 6

Quasar 3C 47: Extreme Population B jetted source with double-peaked profiles[1]

6.1 Introduction

An AD around the central SMBH is expected in all AGN. ADs provide an efficient mechanism for dissipating the angular momentum of the accreting matter via viscous stresses (e.g., Shakura and Sunyaev, 1973; Dai et al., 2021; Lasota, 2023). In addition, they are regarded as an essential ingredient for the production of relativistic jets, which are observed in a considerable fraction of AGN (e.g., Shende et al., 2019; Blandford et al., 2019; Chakraborty and Bhattacharjee, 2021; Mizuno, 2022). High-density material in an AD may be required for the production of the LILs (Rokaki, 1997; Zhang et al., 2019a; Hung et al., 2020). Emission from the surface of a photoionized, relativistic, Keplerian AD produces profiles of double-peaked lines with two distinctive features: (1) a stronger blueshifted peak due to Doppler boosting, and (2) a redward shift - increasing toward the line base - associated with gravitational redshift and Doppler transverse effect (Chen and Halpern, 1989).

There are pieces of evidence about a double-peaked structure that can be acquired from observations of very broad, double-peaked emission lines and identification of asymmetries and substructure in the line profiles (e.g., Popović et al., 2002; Kollatschny, 2003; Shapovalova et al., 2004). Such double-peaked emission lines are an interesting class of objects, though only a small fraction

[1]The results presented in this chapter have been published in Mengistue Terefe et al. (2024).

has been found (e.g., Eracleous and Halpern, 1994, 2003; Strateva et al., 2003; Eracleous et al., 2009; Fu et al., 2023). According to Wang et al. (2005), these double-peaked lines are among the broadest optical emission lines, with a FWHM in some cases exceeding 15000 km s^{-1}. Following the classification scheme of Sulentic et al. (2002), they are more frequently found in extreme Population B, and, more precisely, in spectral type (ST) $B1^{++}$ (see Sect.2.5.1).

A variety of mechanisms have been proposed to explain the origin of double-peaked emission line profiles and their unique kinematic signature, beyond relativistic motions in an AD (e.g., Chen and Halpern, 1989, 1990), such as two separate BLRs as a signature of binary black holes (see Sect. 2.7.1.2), a biconical outflow (see Sect. 2.7.1.3), or a highly anisotropic distribution of emission line gas (see Sect. 2.7.1.4). Careful consideration of the basic physical arguments and recent observational results, tend to confirm that the most likely origin of double-peaked emission lines is the AD, and on the converse, these double-peaked profiles provide dynamical evidence about the structure of the AD (e.g., Chen et al., 1997; Eracleous, 1998; Ho et al., 2000; Strateva et al., 2003; Eracleous and Halpern, 2003; Barrows et al., 2011; Zhang, 2011; Liu et al., 2017; Ricci and Steiner, 2019; Zhang et al., 2019b). Several additional observational tests combined with physical considerations also favored the AD origin over other possibilities (e.g., Eracleous and Halpern, 1994; Dietrich, 1998; Eracleous, 1999; Eracleous and Halpern, 2003; Strateva et al., 2003; Eracleous et al., 2009; Zhang, 2013; Wada et al., 2021; Storchi-Bergmann et al., 2017)

Nonetheless, open questions concerning the disk emission in this class of rare AGN remain. In addition, UV spectroscopy of double-peaked emitters with the HST did not provide unambiguous evidence for an AD origin (e.g., Halpern et al., 1996; Eracleous, 1998; Eracleous et al., 2004; Zhang, 2011), and HILs (e.g., Lyα and CIVλ1549) frequently lack double-peaked profiles (e.g., Halpern et al., 1996; Murray and Chiang, 1997; Eracleous et al., 2004, 2009).

To evaluate the extent to which AD is a source of the broad Balmer lines and UV HILs in RL AGN, we focused on a strong RL quasar, 3C 47 (e.g., Hocuk and Barthel, 2010). Previous studies on 3C 47 indicated that it exhibits peculiar broad emission line profiles with multiple components, making it a member of the AGN class of double-peaked emitters (Eracleous and Halpern, 2003). This work presents new simultaneous optical and near-UV spectra of the relativistically jetted double-peaked quasar, 3C 47 at redshift 0.4248 from long-slit spectroscopic observations. These new observations of 3C 47 yielded a spectrum with high S/N ratio, high resolution, and broad and strong blue and red peaks that are typical indicators of double-peaked emitters in the Balmer lines (Hβ and Hα) as well as the near-UV MgIIλ2800 (hereafter MgII) line. In addition, we also present and interpret the semi-forbidden lines of the λ1900 Å blend

dominated by CIII]λ1909 and the HIL CIVλ1549 from the HST Faint Object Spectrograph (HST-FOS) archive.

This chapter is organized as follows: the data used in this work are described in Sect. 3.1.2.2. Spectral non-linear multicomponent and model fittings, as well as full broad profile analysis, are described in Sect. 4.3. In this chapter, the results of using a model that – for the first time in this object – attributes the emission of the double-peaked lines to the surface of a photoionized, relativistic Keplerian AD plus the results of the broad profile parameters, are described in Sects. 6.3. We also discuss the resulting accretion parameters, the interpretation of the CIVλ1549 and CIII]λ1909 emission lines, the explanation of the CIVλ1549 profile due to the contribution of the AD and a failed wind, and the available alternative models in Sect. 6.4, and finally, our conclusions are given in Sect. 6.5.

6.2 Observation and double-peaked profile analysis

Building upon the groundwork laid in Chapters 3 and 4, this chapter focuses on the spectral analysis results and the corresponding discussions of the double-peaked quasar 3C 47. The data for this analysis was obtained using the 3.5m telescope at the Calar Alto observatory in Spain (see Sect. 3.1.2) and additional UV archival data was obtained using the HST-FOS telescope (see Sect. 3.4.3). To elucidate the origin of the double-peaked profile observed in this particular source, we implemented three types of fitting for each of the observed spectra regions, Hβ, MgIIλ2800, Hα and the high ionization lines, CIVλ1549 and CIII]λ1909: an empirical fitting of the observed spectra by using the IRAF task `specfit` as an empirical fitting to represent the observed broad profile of each double-peaked line of interest (i.e., for Hβ, MgII and Hα). For this, we assumed two Gaussian BCs of the same FWHM (corresponding to the blue and red components of the double-peaked profile) and an additional VBC. Secondly, using the output of the empirical fitting, a model fitting approach, using the Keplerian AD model of Chen and Halpern (1989) in combination with a Bayesian approach (see sect. 4.3.1) was performed to determine the best model parameter values that can fit the double-peaked profiles with minimum uncertainty. Lastly, we again implemented an empirical multicomponent nonlinear fitting of the continuum and the emission features by using `specfit`. In this case, while applying `specfit`, we replaced the double-peaked profiles with the model output flux obtained during the model fitting and re-run `specfit` by including the other non-disk components. The detailed fitting procedures are given in Sect. 4.3. By combining the empirical and model fitting analyses, a comprehensive understanding of the origin of the unique double-peaked emission

lines observed in the spectra of the quasar 3C 47 was obtained. The detailed results and discussions arising from these analyses are presented below.

6.3 Results

6.3.1 AD model parameters

The resulting quantitative measurements of the AD model, $\{q, \sigma, \xi_1, \xi_2, \theta\}$, determined by following the approach described in Sect. 4.3.2.1 for the MgII, Hβ, and Hα regions, are reported in Table 4.2. The line-emitting portion of the disk was found to be an annulus within $\xi_1 \approx 100 r_g$ and $\xi_2 \approx 1000 r_g$, with the highest values $\xi_1 \approx 131 r_g$ and $\xi_2 \approx 1632 r_g$ estimated for MgII. The ratio of the outer to inner radius ξ_2/ξ_1 is $\approx$ 10, 12, and 14 for Hβ, MgII and Hα, respectively. A higher value of the ξ_2/ξ_1 ratio will bring the blue and red peaks close together and will form a single peak.

We found a range of inclination angles relative to the line of sight between the two radii. The lowest inclination of $\theta \approx 26.7^\circ$ was found for the Hβ line, and the highest inclination of $\theta \approx 32.6^\circ$ was found for MgII. The average value of θ is $\approx 29.8 \pm 3.0$ or $\approx 30^\circ$.

The emissivity index ranges between 1.62 (Hα) – 1.79 (Hβ). The factor that represents the turbulent motion and is assumed to be the cause of local line broadening was represented by σ/v_0. We found the highest value of $\sigma/v_0 = 8.156 \times 10^{-3}$ for the Hβ and the lowest for MgII, of $\sigma/v_0 = 5.827 \times 10^{-3}$. This value of σ/v_0 corresponds to a velocity dispersion σ that is higher in Hβ, with a value of 2445 km s^{-1} and lower in MgII, with a value of 1747 km s^{-1}. These values are comparable to the values obtained from the AD model fitting of other double-peaked AGN (e.g., Eracleous, 1998; Strateva et al., 2003).

6.3.2 Empirical fitting results

We employed a comprehensive parameterization of the broad profiles involving the total flux, FWHM, and centroids at different fractional line intensities ($c(i/4)$ for i = 1, 2, and 3) and 9/10, $c(9/10)$ (a proxy to the line peak), as well as asymmetry (AI) and kurtosis (KI) indices (Zamfir et al., 2010). The 3C 47 parameters are reported in Table 6.1 for MgII, Hβ and Hα. The broad-line fluxes (Col. 2) and the specific fluxes of the power-law continuum (Col. 10) along with the FWHM (Col. 3) were used to compute the accretion parameters (see Sect. 6.4.1).

3C 47 shows a very large line width with FWHM of $\geq$ 15000 km s^{-1}. The

Table 6.1: Measurements of the full broad profile and the NC + SBC of the three analyzed lines.

	Full broad profile (FP)										NC + SBC		
Line	Flux	FWHM	$c(\frac{1}{4})$	$c(\frac{1}{2})$	$c(\frac{3}{4})$	$c(\frac{9}{10})$	A.I.	K.I.	f^a_λ	FeII^b	Flux	Peak	FWHM
(1)	(2)	(3)	(4)	(5)	(6)	(7)	(8)	(9)	(10)	(11)	(12)	(13)	(14)
MgII	116.7	15000±700	910±440	400±250	150±260	-3110±390	0.43±0.34	0.60±0.04	1.94	41.9	3.42^c	60	800
Hβ	68.3	16600±800	1650±460	830±290	300±340	-2360±720	0.42±0.27	0.59±0.04	0.73	9.8	3.37	30	609
Hα	313.0	15500±800	1020±460	430±270	110±300	-430±2480:	0.38±0.28	0.58±0.04	0.54	15.9	8.86	-90	840

Note: The full broad profile is considered to be the model-fitting result that represents the broad profile of the observed spectra without including the NCs. Columns 2, 11, and 12 are in units of 10^{-15}ergs s^{-1} cm^{-2}; FWHM, centroids, and peak velocities in km s^{-1}; ^{a} Column 10 corresponds to the power-law continuum flux at λ3000Å, λ5100Å, and λ6200Å for MgII, Hβ and Hα regions, respectively, in units of 10^{-15}ergs s^{-1} cm^{-2} Å^{-1}. ^{b} FeII integrated flux in the range of 2200Å – 3090Å, 4434Å – 4684Å, and 6100Å – 6400Å for MgII, Hβ and Hα respectively (in units of 10^{-15} ergs s^{-1} cm^{-2}). $^{(c)}$ The intensity of the NC is for the MgII the blue line of the doublet (a ratio of 1.5 was assumed for the NCs of the doublet λ2796.35Å and λ2803.53Å).

Hβ disk line profile is one of the broadest, with a FWHM of 16600 km s^{-1}. The centroid velocity measurements at different fractional intensities show a predominance of shifts to the red. They are more pronounced toward the line base, with c(1/4) $\approx 1650 \pm 460$ km s^{-1}. Within the uncertainty level, the redward asymmetry appears to be consistent across all three lines, with Hα showing a slightly more symmetric distribution than Hβ and MgII.

Table 6.2: Measurements of the full broad profile and the NC + SBC of the FUV lines.

	Full broad profile (FP)									NC + SBC		
Line	Flux	FWHM	$c(\frac{1}{4})$	$c(\frac{1}{2})$	$c(\frac{3}{4})$	$c(\frac{9}{10})$	A.I.	K.I.	f^a_λ	Flux	Peak	FWHM
(1)	(2)	(3)	(4)	(5)	(6)	(7)	(8)	(9)	(10)	(11)	(12)	(13)
CIV	387.0	4972	-345	-125	-100	-93	-0.06	0.33	2.37	9.45	-4500^b	1850
HeII	71.9	3758	731	-678	-525	-514	0.15	0.12	2.37	...	...	...
AlIII	92.7	14681	1000	355	113	-452	0.15	0.59	2.97	...	...	...
CIII]	373.9	5553	-817	-687	-267	-188	-0.15	0.36	2.97	4.8	-200/–500^c	910

Note: Columns 2 and 11 are in units of 10^{-15}ergs s^{-1}cm^{-2}; $^{(a)}$ Column 10 yields the continuum specific flux at 1350Å and 1750Å for the CIVλ1549 + HeIIλ1640, and the 1900Å blend regions, respectively, in units of 10^{-15}ergs s^{-1}cm^{-2}Å^{-1}. $^{(b)}$ Semi-broad blueshifted emission. $^{(c)}$ Reference wavelength 1906.7Å and 1908.7Å.

The flux of the FeII emission integrated for MgII, Hβ, and Hα regions are reported in Col. 11 of Table 6.1. With an intensity ratio of approximately 0.14 for $R_{\rm FeII,opt}$= I(FeIIλ4570)/I(Hβ), 3C 47 falls within the realm of extreme Pop-

ulation B on the optical plane of the quasar main sequence (MS), defined by the relation between Hβ FWHM and $R_{\rm FeII,opt}$ (Sulentic et al., 2002). More precisely, its Hβ FWHM of $\approx$16,000 km s^{-1} places it in the B1^{++} ST according to the classification scheme of Sulentic et al. (2002). It is noteworthy that this ST comprises a minimum fraction (lower than 1%) of optically selected quasars with weak or undetectable FeII emission (Marziani et al., 2013b). Ganci et al. (2019) revealed a higher prevalence of irregular or multiple peaked profiles in this ST and suggested a higher prevalence for binary SMBH candidates (see Sect. 6.4.5).

Cols. 1 – 9 of Table 6.2 report the full broad profile parameters for the far-UV (FUV) lines, mirroring the organization of Table 6.1 along with the specific flux (Col. 10). A key result is that the FWHM CIVλ1549 $\ll$ FWHM Hβ, which is discussed in more detail in Sect. 6.4.4. The highly blueshifted semi-broad features (blue lines in Figs. 4.9 and 4.10) visible for both CIVλ1549 and CIII]λ1909 are probably part of a continuum of outflowing gas from the outer BLR to the inner NLR. Their fluxes are much lower than those of the other components. This may indicate that outflows may have little effect over the integrated line profiles (see Sect. 6.4.4 for more detail).

In addition to the parameters of the broad profiles, we report the flux, the peak shift, and the FWHM for NCs and SBCs of identified emission lines from the `specfit` analysis (Tables 6.1 and 6.2). Individual NCs are near the rest-frame, with a broad FWHM of 840 km s^{-1} for Hα and a slightly lower value for Hβ and MgIIλ2800. The CIVλ1549 NC is absorbed by narrow lines close to the rest-frame.

Finally, Table 6.3 reports the total intensity, peak shift, and FWHM for additional narrow and semi-broad emission lines identified in the four spectral ranges (MgIIλ2800, Hβ, Hα, and CIVλ1549).

6.4 Discussion

6.4.1 Accretion parameters

Black hole masses ($M_{\rm BH}$) were computed from the virial equation applied in the form of a scaling law (SL), where $M_{\rm BH}$ was assumed to be proportional to the square of the line width (Vestergaard and Peterson, 2006), and the BLR radius was estimated from its correlation with the continuum or luminosity of different emission lines (Shen and Liu, 2012; Bentz et al., 2013). Alternatively, the line width can be increased to a power different from the second (Shen and Liu, 2012). This approach has been extensively applied in previous studies,

Table 6.3: Narrow lines and narrow-line components of 3C 47.

Spectral Range	Line	Flux	Shift	FWHM
MgII	O IIIλ3133	3.49	40	1940
	He Iλ3188	1.05	60	880
	[Ne v]λ3426	5.22	-30	1740
	[O II]λ3728	4.19	10	1140
Hβ	[OIII]λ5007]	8.86	-40	370
	[OIII]λ5007]^a	27.05	-220	1490
	HeIIλ4686	1.06	-70	1100
Hα	[O I]λ6302	0.01	380	570
	[N II]λ6585	8.79	-30	1070
	[Si II]λ6732	2,14	-10	720
	[O I]λ6302^a	5.35	-60	1310
CIVλ1549	N IV] λ1486	4.1	-420	2020
	O III] λ1663	9.2	–1100	2700

Note:$^{(a)}$represents the flux, peak shift, and FWHM of the SBC. Intensities are in units of 10^{-15} ergs s^{-1} cm^{-2}.

including large samples of quasars from the Sloan Digital Sky Survey (SDSS) (e.g., Kozłowski, 2017, and references therein).

An important input parameter does not explicitly appear in the SLs: the viewing angle (θ) between the line-of-sight and the axis of symmetry of the AGN (i.e., the AD axis or the radio axis). Double-peaked sources such as 3C 47 presumably have almost all of their low-ionization emission lines modeled by a geometrically thin, optically thick disk, and it is, therefore, easy to associate a well-defined θ with the line FWHM (for an alternative approach, see e.g., Bian et al., 2007).

When the inclination angle derived from the disk profile analysis is taken into account, the virial relation can be written as

$$M_{\rm BH} = \frac{R_{\rm BLR}\delta v_{\rm K}^2}{G} = f(\theta)\frac{R_{\rm BLR}{\rm FWHM}^2}{G}, \tag{6.1}$$

where $\delta v_{\rm K}$ is the Keplerian velocity of the line emitting gas at the radius of the BLR ($R_{\rm BLR}$). The virial factor $f(\theta)$ connects $\delta v_{\rm K}$ to the observed FWHM and can be written as (e.g., Decarli et al., 2008; Mejía-Restrepo et al., 2018; Negrete et al., 2018):

$$f(\theta) = \frac{1}{4[k^2 + \sin^2\theta]}, k = \frac{\sigma v_{\rm iso}}{\sigma v_{\rm K}} \approx 0.3, \tag{6.2}$$

where f is $f \approx 0.735$ when $\theta \approx 30$.

Table 6.4: Accretion parameters.

Line/continuum (1)	$\log L$ (2)	$\log r$ (3)	Method (4)	$M_{\rm BH}$ (5)	$L_{\rm bol}/L_{\rm Edd}$ (6)	Refs. (7)
L(Hβ)[a]	43.33	17.70	Vir	7.89E+09	0.036	1
L(5100)	45.22	17.60	Vir	6.26E+09	0.045	2
L(5100)	45.22	17.59	Vir	6.08E+09	0.047	3
L(3000)	45.42	17.63	Vir	5.42E+09	0.052	4
L(3000)	45.42	17.72	Vir	6.65E+09	0.043	5
L(3000)	45.42	18.06	Vir	1.46E+10	0.019	2
Average				6.46E+09	0.040	
St.dev.				9.14E+08	0.012	
L(Hα)	44.12	...	SL	8.04E+09	0.035	6
L(5100)	45.22	...	SL	9.14E+09	0.031	7
L(5100)	45.22	...	SL	7.96E+09	0.036	2
L(Hβ)	43.43	...	SL	5.18E+09	0.055	8
L(3000)	45.42	...	SL	9.33E+09	0.030	4
L(3000)	45.42	...	SL	8.31E+09	0.034	9
L(MgII)	43.69	...	SL	1.23E+10	0.023	7
L(3000)[b]	45.42	...	SL	5.34E+10	0.005	2
Average				8.61E+09	0.035	
St.dev.				2.12E+09	0.010	

Note: Column 2 in ergs s^{-1}, Column 3 in cm, and Column 5 in $M_\odot$. [(a)]For the same flux, the luminosity was scaled to $H_0 = 75$ km s^{-1} Mpc^{-1} as used in the Wu et al. (2004) relation. [(b)]$M_{\rm BH}$ and $L_{\rm bol}/L_{\rm Edd}$ excluded from average and standard deviation as they are outliers above a 3σ confidence level. References: (1) Wu et al. 2004; (2) Shen et al. 2023; (3) Bentz et al. 2013; (4) Trakhtenbrot and Netzer 2012; (5) Panda et al. 2019b; (6) Shen et al. 2011; (7) Vestergaard and Peterson 2006; (8) Greene and Ho 2005; and (9) Vestergaard and Osmer 2009.

Table 6.4 reports the line or continuum identifications and the corresponding luminosity values (Cols. 1 and 2, respectively), the BLR radius estimated from its correlation with luminosity (Col. 3), the method used (either using Eq. (6.1) above, or an SL that directly links the mass to the luminosity and line width, Col. 4), and the estimated $M_{\rm BH}$ (Col. 5), and the Eddington ratio ($L_{\rm bol}/L_{\rm Edd}$) (Col. 6) for several different SL (in Col. 4, with reference in Col. 7) using Hβ, MgII and Hα as virial broadening estimators.

The $L_{\rm bol}/L_{\rm Edd}$ was computed from the 3C 47 spectral energy distribution (SED) as available in the NASA/IPAC Extragalactic Database (NED). The MIR and FIR emissions were cut to avoid the inclusion of reprocessed radiation and un-

resolved emissions not associated with the AGN. The resulting bolometric correction factors are 25.59 from λf_λ 5100Å and 16.39 from λf_λ3000 Å, which is considerably higher than in the case of optically selected RQ quasars, $\approx$ 10 – 15 from λf_λ 5100Å (Richards et al., 2006; Punsly et al., 2020). For 3C 47, the bolometric correction includes the accretion luminosity (i.e., from the AD and associated coronæ), as well as the emission associated with the relativistic jet. A flat X-ray SED, expected to be due to synchrotron self-Compton (SSC; Maraschi et al. 1992) emission, produces a luminosity of $\log L_{\rm X} \approx 46.28$ [erg s^{-1}], which contributes up to $\approx$ 40 % of the bolometric luminosity $\log L \approx 46.64$ [ergs s^{-1}]. For comparison, a Pop. A AGN SED (corresponding to the Mathews and Ferland (1987) template, as implemented by the command `table AGN` in CLOUDY) with the same optical flux as 3C 47 would yield $\log L_{\rm X} \approx 45.24$ versus $\log L \approx 46.32$ [ergs s^{-1}] (e.g., Lusso et al., 2012). The $L_{\rm bol}/L_{\rm Edd}$ estimated from the average of the three $M_{\rm BH}$ determinations from Eq. (6.1) is $L_{\rm bol}/L_{\rm Edd} \approx 0.040 \pm 0.012$, including the accretion and nonthermal emission. The SSC emission may be beamed; however, beaming effects on the optical/UV synchrotron continuum are probably minor, as confirmed by the $M_{\rm BH}$ estimates based on continuum measurements, which are consistent but slightly lower than those based on emission lines for which no beaming effect is expected.

6.4.2 AD as the origin of the double-peaked profile

Two pieces of evidence support an illuminated AD as the main source of LILs (see Sects. 4.3.1 and 6.3.1, and Table 4.2):

1. The two peaks are well separated, implying a disk of modest extension with $\xi_2 \approx 10^3\,{\rm r_g}$.
2. The overall profile is asymmetric due to relativistic beaming (Doppler-boosted peak) and gravitational redshift of the entire line (redshifted line base).

The most remarkable finding is that the ξ_1 should be as low as $\approx 100\,{\rm r_g}$, implying a large shift because of gravitational and transverse redshift, $c\delta z_{\rm grav} \approx 3/2\,\xi_1 \approx 4500$ km s^{-1}. It is also remarkable that the predicted shape provides a good fit for the line red wings. 3C 47 is not an exception in this respect because blazars also show red asymmetric disk profiles characterized by large shifts at the line base, consistent with emission from the innermost disk (see e.g., Punsly et al., 2020; Marziani, 2023). In the case of blazars, the orientation angle is $\theta \lesssim 5^\circ$, however, and consequently, the profiles appear to be single peaked (Decarli et al., 2011; Marziani, 2023).

The decreasing line width in the order Hβ, Hα, and MgII is associated with a difference in the emissivity-weighted radius of the three lines. The MgII is emitted by a region of the disk that is weighted toward larger radii than Hβ and Hα (see Table 4.2, Cols. 2, 3, and 4). This effect is seen in Population B sources where emission is dominated by a virial velocity field Mengistue et al. (2023), for which the line width is inversely proportional to the square root of the distance from the central continuum source, that is, an FWHM$\propto 1/\sqrt{r}$.

In summary, the three LILs show profiles that are consistent with a relativistic flat AD, and their main features can be explained by the physical processes expected to occur for ionizing continuum radiation reprocessed by the disk. This, however, is not the case for HILs(see Sect. 6.4.4 for more details).

6.4.3 Consistency between radio and optical properties

Assuming that the relativistic jet is coaxial with the disk, that is, the jet axis and the disk plane are perpendicular, an interesting issue is whether the orientation of the jet is consistent with the inclination of the AD. The radio morphology is double-lobed, with jet, but no counterjet is easily visible at 4.9 GHz (Fernini et al., 1991). The jet-counterjet asymmetry implies the presence of a highly relativistic jet, and along with the double-lobe morphology, a significant misalignment between the jet axis and the plane of the sky as well as with the line of sight. Superluminal motion has been detected by VLBI observations of 3C 47, with an apparent superluminal speed of $\beta_{\rm app} \approx 5.3^{+1.3}_{-1.0}$ (Vermeulen et al., 1993). A high superluminal speed like this is incompatible with an angle as large as 30°, as the upper limit to $\theta_{\rm jet}$ is $\approx$ 20° with Lorentz factor $\gamma \approx 10$. However, considering that the uncertainties in the superluminal speed translate into $\theta_{\rm jet} \approx 20^{+6}_{-3}$, the difference between $\theta_{\rm jet}$ and $\theta_{\rm disk} \approx 30\pm3$ is significant at only slightly more than the $\approx 1\sigma$ confidence level. It is also important to remark that the 3C 47 $\beta_{\rm app}$ might be overestimated, as this source is an outlier in the correlation between $\beta_{\rm app}$ and deboosted core-to-lobe ratio, in the sense that the 3C 47 $\beta_{\rm app}$ is much higher than expected for its core-to-lobe ratio (Vermeulen et al., 1993).

The ratio of the jet-to-counterjet flux offers an independent test of consistency for the angle $\theta_{\rm jet}$. The counterjet is not visible, but an upper limit to the flux is $\approx$4.2 mJy (Bridle et al., 1994), yielding a lower limit to the jet-to-counterjet ratio $\approx$5.5. This in turn implies that $\gamma \gtrsim 2.5$ for $\theta \approx 29$.

Therefore, we conclude that the radio-derived angle between the line of sight and the jet and between the line of sight and the disk axis, $\theta_{\rm jet}$ and $\theta_{\rm disk}$, are not significantly discordant, leaving open the possibility of a slight bending of the parsec-sized jet over scales $\approx 10^4 r_{\rm g}$ (Yuan et al., 2018, and Section 6.4.5).

6.4.4 A failed-wind signature

The most striking result is the obvious difference between the profiles of the LILs and HILs. Unlike in the case of Population A sources, where the CIVλ1549 profile is usually broader and blueshifted in comparison to the Balmer lines, we can explain the CIVλ1549 profile for several Population B RL sources as caused by the disk profile in addition to the emission from a strong, narrower feature (FWHM $\approx$4000 km s^{-1}) that peaks at the rest-frame and has a slightly asymmetric profile. The origin of this feature is discussed below.

As mentioned above, the interpretation of the so-called double-peakers is that the LILs are produced exclusively through reprocessing of the gas of the AD (Eracleous and Halpern, 1994; Strateva et al., 2003). The contribution from the disk is expected in the general AGN population but is thought to be masked by emission due to the gas surrounding the disk itself (Popović et al., 2004; Bon et al., 2009). Therefore, double-peakers in this interpretation are low radiators and sources with little gas left and with a disk truncated at $\xi_2 \lesssim 10^3 r_g$ (Marziani et al., 2021). In addition, jetted sources are X-ray bright and may induce a high-ionization degree (an over-ionization of the gas; Murray et al. 1995; Murray and Chiang 1997). In a line-driven wind scenario, the ionic species yielding the main resonant transitions that absorb the continuum momentum are replaced by higher ionization species, and the gas can no longer be efficiently accelerated (e.g., Murray et al., 1995; Proga and Kallman, 2004; Higginbottom et al., 2024, and references therein). This scenario may apply to 3C 47. We considered the disk radii that correspond to linear distances of $\approx 10^{17}(r_g/100)$ cm, assuming $M_{BH} \approx 6.5\times10^9\,M_\odot$, and an array of photoionization simulations assuming as input (1) the SED of 3C 47 as derived from the NED data; (2) radii in the range $\log\xi_2 \approx 17-19$ [cm]; (3) a hydrogen density between $\log n \approx 10$ [cm^{-3}] and $\log n \approx 12$ [cm^{-3}], with steps of 0.5 dex; (4) a metallicity Z at 0.1 and 1 $Z_\odot$; and (5) 0 turbulence broadening.

The first basic result is that the kinetic temperature is too high for a meaningful photoionization solution for moderate densities $\log n_H \approx 9$ and ≈ 10 at $\xi \lesssim 1000 r_g$, and $\lesssim 500\ r_g$, respectively. This implies that the bulk of the HILs might come from a region beyond the outer edge of the AD. The SED of 3C 47 induces an overionization of the emitting gas, where a photoionization solution is possible. Fig. 6.1 shows that the C^{3+} ionic stage is only marginally dominant in a narrower range of depth with respect to a cloud illuminated by a typical AGN continuum for the same optical luminosity and all other conditions kept fixed. As a consequence, the force multiplier remains systematically lower for 3C 47 (right panel of Fig. 6.1), implying that a radiation-driven outflow is disfavored in this case. Another important factor hampering a radiation-driven outflow is the very low L_{bol}/L_{Edd}: radiation forces become dominant only at

low column density (Netzer and Marziani, 2010). Most of the optically thick gas will remain bound to the gravitational field of the black hole and reflect the Keplerian kinematics associated with the rotating disk. The modest blueward asymmetry of the CIVλ1549 profile is consistent with a small fraction of the line emitting gas showing a radial velocity associated with outflow motions.

We can constrain the radial extent of the BLR from the radius r_{1000} at which the AD temperature is 1000 K to the radius of dust sublimation $r_{\rm dust}$ (Czerny and Hryniewicz, 2011). The radius r_{1000} can be written as

$$r_{1000} = \left(\frac{3GM\dot{M}}{8\pi\sigma_{\rm B}T^4}\right)^{\frac{1}{3}} \approx 6.67\cdot 10^{16} T_{1000}^{-\frac{4}{3}} M_8^{\frac{2}{3}} \dot{m}_1^{\frac{1}{3}}\ {\rm cm}, \tag{6.3}$$

where $\dot{M}$ is the accretion rate, $\sigma_{\rm B}$ is the Stefan-Boltzmann constant, and $\dot{m}$ is the dimensionless accretion rate in Eddington units, that is, $\dot{m} = \dot{M}/(L/c^2)$. For the parameters of 3C 47, we obtain that $r_{1000} \approx 9.3\times 10^{17}$ cm $\approx 940 r_{\rm g}$. The ratio of $r_{\rm dust}$ and r_{1000} is (e.g., Czerny and Hryniewicz, 2011),

$$\frac{r_{\rm dust}}{r_{1000}} \approx 33 \frac{\dot{m}_1^{\frac{1}{6}} \eta_{0.1}^{\frac{1}{2}}}{M_8{}^{\frac{1}{6}}} \approx 12.98. \tag{6.4}$$

This implies that in the case of 3C 47, the BLR extension is between 1000 $r_{\rm g}$ and $\approx 12000 r_{\rm g} \approx 10^{19}$cm. At 5000 $r_{\rm g}$, the virial velocity is ≈ 4000km s^{-1}, in agreement with the expected FWHM considering $\theta \approx 30$. The FWHM of the symmetric Gaussian CIVλ1549 emission feature is therefore consistent with emission concentrated toward the outer region of the permitted space. This accounts for the separation from the disk that emits lines from within 2000 $r_{\rm g}$.

The key differences between RL and RQ AGN lie in the configuration of the magnetic field and the SMBH spin, which can significantly impact any radiation-driven wind dynamics (Blandford and Znajek, 1977; Blandford and Payne, 1982), although the exact roles remain debated. The mildly ionized wind traced by CIVλ1549 still exists in RLs, but is quantitatively affected (Marziani et al., 1996; Richards et al., 2011). The effect of the jet might ultimately be associated with a cocoon of shocked gas that develops where the pressure exerted by later expansion of the jet equals the pressure of the ambient medium. This in turn may displace the launching radius of the wind outward (Sulentic et al., 2015). Therefore, we do not expect a substantial difference between RQ and RL in the occurrence of failed winds, except for the displacement of the launching radius and a lower force multiplier implied by an SED such as that of 3C 47, which would somewhat favor wind failure in RLs.

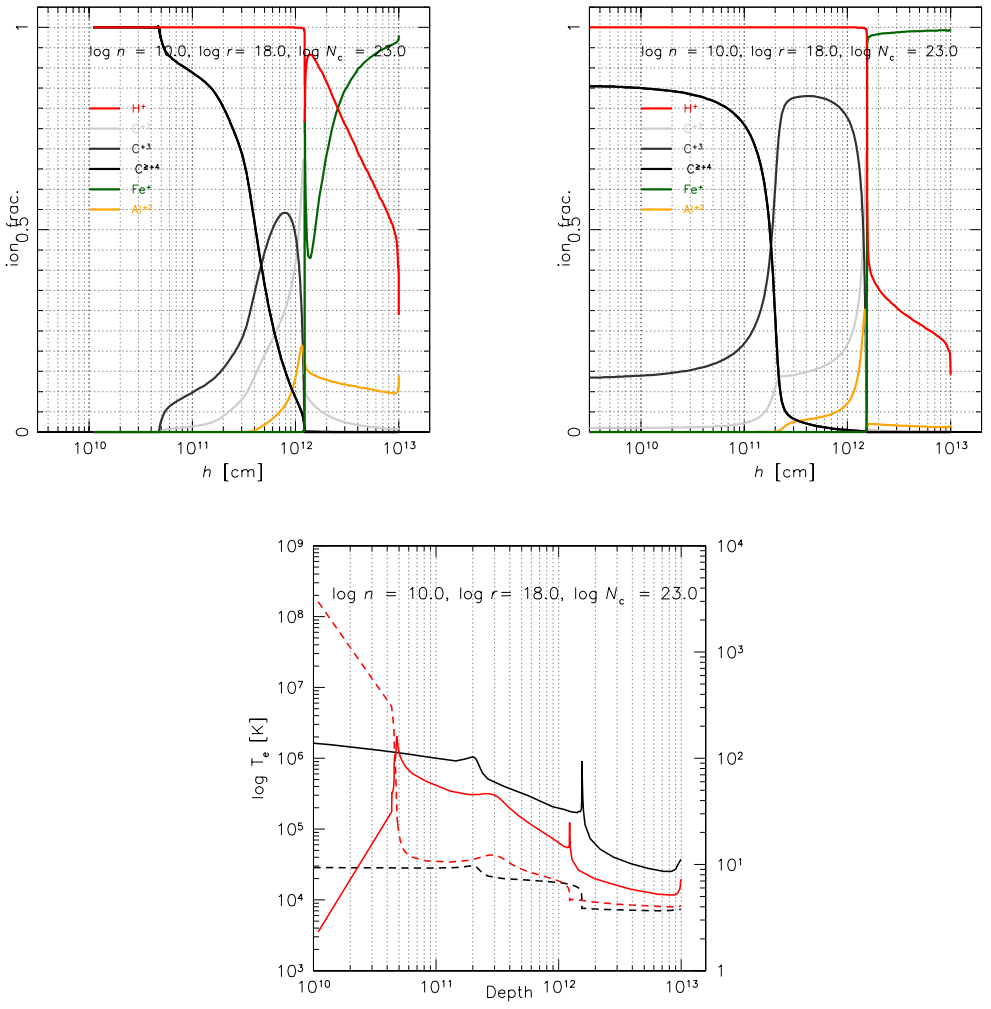

Figure 6.1: Ionization structure within a gas slab with a column density $N_c = 10^{23}$ cm^{-2}, log of the hydrogen density 10.0 [cm^{-3}], and distance from the continuum sources $\log r = 18$ [cm] corresponding to $\approx$ 1000 r_g, where the illuminated surface is at a depth $h = 0$ (left side), for the continuum of 3C 47 (left panel), and for a typical AGN continuum normalized to the same optical luminosity (middle panel). Bottom: Force multiplier (filled lines) and kinetic temperature (dashed lines) as a function of the geometrical depth of the gas slab for 3C 47 (red) and an AGN continuum (black).

6.4.5 Explanations alternative to AD: A binary broad-line region

In an alternative scenario, the observed double-peaked profiles could be attributed to emission from a twin BLR associated with a supermassive binary black hole. Under this assumption, each of the black holes has an associated BLR, and the orbital motion of the binary system produces Doppler shifts in the emission lines that result in the observed double-peaked profiles (e.g., Begelman et al., 1980; Begelman and Meier, 1982; Gaskell, 1983; Peterson et al.,

1987; Chornock et al., 2010). The hypothesis of a binary black hole appears debatable on the basis of radio data. On the one hand, there is no evidence of an obvious S-shaped configuration of the jet. The 3C 47 jet extends over ≈ 200 kpc and shows the smallest bending measures ($\lesssim 8$ degrees) of several double-lobed sources (Bridle et al., 1994). The position angle of the parsec-scale jet mapped by VLBI (Yuan et al., 2018) is consistent with the jet mapped by the VLA. This evidence favors the jet orientation's stability over the radio source's dynamical timescale, $\approx 6 \cdot 10^7$ yr (Turner et al., 2018). On the other hand, the presence of a secondary SMBH is indicated by three subtle pieces of evidence (Krause et al., 2019): (1) a jet at the edge of the lobe; (2) a ring-like feature that is well visible in the southern lobe (Fernini et al., 1991; Leahy, 1996); and (3) the S-symmetry of the hot spots with respect to the jet axis, and an estimate of the geodetic precession timescale (Barker and O'Connell, 1975),

$$P_{\rm G} \approx \frac{4\pi c^2}{G^{\frac{3}{2}}} \cdot \frac{a^{\frac{5}{2}}}{M^{\frac{3}{2}}} \cdot \frac{(1+\tilde{q})^2}{(3+4\tilde{q})} \cdot (1-e^2) \approx 10^8 r_1^{\frac{5}{2}} M_9^{-\frac{3}{2}} \mathrm{yr}, \tag{6.5}$$

where $\tilde{q} = M_1/M_2$ is the mass ratio (assumed here to be $\tilde{q} \approx 2$), and $r = a$, the semimajor axis of the orbit for an eccentricity $e = 0$, in parsecs. In the case of 3C 47, $P_{\rm G}$ is lower than (for $M_{\rm BH} \approx 6 \cdot 10^9$ $\mathrm{M}_\odot$) or comparable to the dynamic age of the radio source, and it is therefore compatible with the features seen in the radio lobes.

To examine whether this interpretation is a possible mechanism for the observed double-peaked profile in the spectra of 3C 47, we recovered two additional spectra obtained in the epoch preceding 2012 (see Sect. 3.4). The spectra were normalized to the sum of the [OIII]λ5007 NC + SBC. A previously unreported result is that the broad emission in 1996 was extremely faint and could have escaped detection if the more recent spectra had not been available for comparison: The Hβ broad profile strength in 1996 was about one-third and about half of those measured on the 2006 and 2012 spectra.

The total mass of the binary $M = M_1 + M_2$ can be estimated from the observed spectra using the third Kepler law. We used the equations from Eracleous et al. (1997) to estimate M, which corresponds to the period and orbital velocities,

$$M \approx 4.7 \times 10^8 (1+\tilde{q})^3 P_{100}\, v_{1,5000}^3\, M_\odot, \tag{6.6}$$

where v_1 is the orbital velocity of M_1 normalized to 5000 km s^{-1}, and P is the orbital period in units of 100 yr. The $v_1 \sin\theta$ corresponds to the radial velocity of the blue peak ($v_{\rm r}$ Blue) and the $v_2 \sin\theta$ to the red peak ($v_{\rm r}$ Red). We did not use v_2 because the red peak wavelength is very poorly constrained. The projected peak velocities were estimated from the empirical fittings of the lines using two Gaussian profiles as a BC to represent the two peaks. For

the Hβ line of the 2012 spectrum (presented in this paper), the corresponding blueshift and redshift velocities were found to be $\approx$ -3200 km s^{-1} and $\approx$ +5000 km s^{-1}, respectively, from the peak flux in the observed double-peaked profile fitted as shown in Fig. 6.2 for Hβ and MgII. For Hα, the blue peak is located around -2800 km s^{-1}, and the red peak is found at +5900 km s^{-1}, yielding $\tilde{q} \approx$ 1.56 and $\approx$ 2.11 for Hβ and Hα respectively. An average over Hβ, MgII and Hα at all available epochs, consistently yields $\tilde{q} \approx 1.6 \pm$ 0.5 for the putative binary. The high dispersion reflects the difficulty in carrying out precise measurements of peaks of broad features that are affected by atmospheric absorption as well as strong overlying [Oiii] emission (red peak of Hβ). The results for the measurements of Hβ and MgII are reported in Table 6.5. The 1996 spectrum yields very poor constraints on the blueshifted peak, with $v_{\rm r}$ Blue $\approx -1900^{+500}_{-1000}$ km s^{-1} at 1σ confidence level.

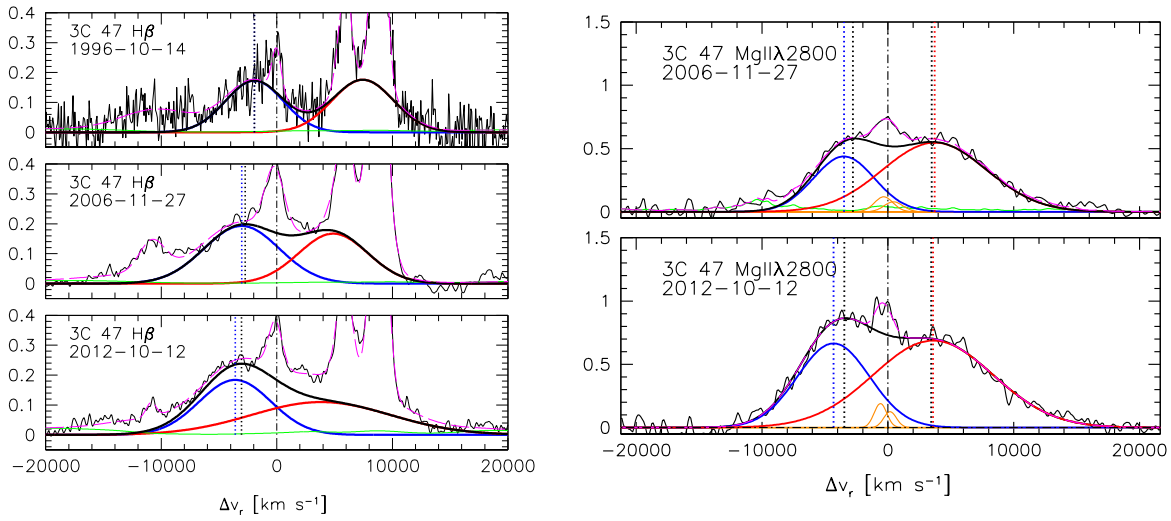

Figure 6.2: Top: Multicomponent empirical `specfit` analysis results in the Hβ line region for three epochs after subtracting the power-law and the Balmer recombination continuum (the latter for the MgII spectral range). The abscissa is in radial velocity units. The vertical scale corresponds to the specific flux in units of 10^{-15} ergs s^{-1} cm^{-2} Å^{-1}. The emission line components used in the fit are FeII (green), the blue- and red-peaked profiles (black), the VBC (red), and the full profile (sum of the two BCs and the VBC; thick black), all the NCs (blue), and [OIII]$\lambda\lambda$4959,5007 SBC (orange). The continuous black lines correspond to the rest-frame spectrum. The dashed magenta line shows the model fitting from `specfit`. The dot-dashed vertical lines trace the rest-frame wavelength of Hβ. The dotted lines identify the radial velocity of the blue- and redshifted broad Gaussian components. Bottom: Same for the MgII line after removing the FeII emission for clarity.

The only parameter that needs to be determined in Eq. 6.6 is the period from the displacement of the observed spectra. We focused on the blueshifted peak

Table 6.5: Measured shifts of broad-line profiles and lower limits on $M_{\rm BH}$.

Line	Epoch	Sum		Components	
		$v_{\rm r}$ Blue	$v_{\rm r}$ Red	$v_{\rm r}$ Blue	$v_{\rm r}$ Red
(1)	(2)	(3)	(4)	(5)	(6)
Hβ	1996-10-14	-1930[a]	7410:	-1940	8060:
Hβ	2006-11-27	-2730	4200	-3040	4890
Hβ	2012-10-12	-3050	...	-3600	3820:
MgII	2006-11-27	-2780	3490	-3495	3720
MgII	2012-10-12	-3460	3440	-4320	3600
	Δt [yr]	P [yr]	$M_{\rm BH}$ [M$_\odot$]	P [yr]	$M_{\rm BH}$[M$_\odot$]
Hβ	16.0	267	3.8E+10[b]	192	4.5E+10[b]
Hβ	5.875	259	3.7E+10[b]	166	3.9E+10[b]
MgII	5.875	119	8.1E+09[c]	102	2.0E+10[c]

Note: [(a)]Highly uncertain, an F-test yields $v_{\rm r}$ Blue $\approx -1900^{+500}_{-1000}$ km s^{-1}. [(b)]Assuming $(1+\tilde{q}) \approx 2.56$; [(c)]Assuming $(1+\tilde{q}) \approx 2.0$.

of Hβ. To estimate the period, we considered the Δv over the time span Δt, and the radial velocity span $v_2 - v_1$ (i.e., the separation of the two peaks). In the case of a circular orbit, the period should be $P \approx 2(v_2 - v_1)/\Delta v \times \Delta t$, and the values are reported for the Hβ and MgII in the cases of the full double-peaked profile and the fitting components. θ is known to be $\approx 20-30$ degrees (Sect. 6.4.3), so that all observed radial velocities are to be divided by $\sin\theta$ which we assumed here to be ≈ 30.

The second half of Table 6.5 provides the estimates of periods and total binary black hole masses from the shift variation in Hβ and MgII over the time lapses between observations. The most constraining limit in Eq. 6.6 comes from the measurement of the Hβ peak: The $\Delta v \lesssim 1100$ km s^{-1}implies a period of $P \gtrsim 200$ yr, and $M_{\rm BH} \approx 5 \cdot 10^{10}$ M$_\odot$, which is above the estimates of Sect. 6.4.1. The uncertainty of the 1996 measurement is large; the -1σ limit would imply a displacement of just 120 km s^{-1} with respect to the 2012 measurement, implying $P \approx 2800$ yr and $M_{\rm BH} \approx 4 \times 10^{11}$ M$_\odot$. In addition, the measurements between 2006 and 2012 show that there is no evidence of strong changes in the radial velocity of the blue peak. Even if there is an apparent systematic increase in the shift for both Hβ and MgIIλ2800, the change in the red peak may not be consistent with an orbital motion around a common center of mass. We can conclude that there is no evidence in favor of a binary BLR given the constraints on the mass of the putative binary black hole and the uncertainties in the data. Further spectroscopic monitoring is needed to fully dismiss this possibility.

However, assuming that a second black hole affects the shape of the line profile

in a periodic way, we write the relation between the geodetic precession and orbital period as

$$P_{\rm G} \approx \frac{4\pi c^2}{G^{\frac{3}{2}}} \cdot \frac{a^{\frac{5}{2}}}{M^{\frac{3}{2}}} \cdot \frac{(1+\tilde{q})^2}{(3+4\tilde{q})} \cdot (1-e^2) \approx 10^8 r_1^{\frac{5}{2}} M_9^{-\frac{3}{2}} \mathrm{yr}, \tag{6.7}$$

The separation of the two black holes is unconstrained, but an upper limit on $P_{\rm G}$ is given by the dynamic age of the radio source, $\approx 6 \cdot 10^7$ yr. With the black hole mass of 3C 47, the age would imply a radius of ≈ 100 pc. Smaller radii might be possible; since 1 pc ≈ 3000 $r_{\rm g}$, it is tempting to speculate that a second black hole within a few parsecs from the primary might cause the truncation of the disk at $\lesssim 2000$ $r_{\rm g}$.

6.4.6 Further alternatives

Another scenario proposed for the explanation is emission from the oppositely directed sides of a bipolar or biconical outflow. In this scenario, the double-peaked lines originate in pairs of oppositely directed cones of outflowing gas that is accelerated by the passage of the relativistic radio jets through the line-emitting region and interaction with the gas immediately around the central engine (e.g., Norman and Miley, 1984; Zheng et al., 1990; Sulentic et al., 1995). Evidence of line broadening after a flare-like event has been found (León-Tavares et al., 2013; Chavushyan et al., 2020), and can be interpreted as an unresolved bipolar outflow. These phenomena, however, are transient over timescales of years or shorter. Gas moving at ≈ 4000 km s^{-1}for slightly less than 20 years would imply a displacement of ≈ 0.1 pc. Maintenance of a stable structure within the BLR in a sort of "fountain" to replenish the outflowing gas appears to be a rather unrealistic scenario.

6.4.7 3C 47 in the context of the quasar main sequence and of the RL/RQ dichotomy

The most powerful radio sources in the local Universe belong to systems with very high $M_{\rm BH}$ and low levels of activity (e.g., Sikora et al., 2007; Chiaberge and Marconi, 2011; Fraix-Burnet et al., 2017). 3C 47 is not a peculiar object in this respect. The observational and accretion properties are consistent with extreme Population B sources with very broad double-peaked profiles and low FeII emission, which in turn imply high masses and low Eddington ratios. Even though the fraction of RL sources tends to increase with FWHM in low-z samples (Marziani et al., 2013b; Chakraborty et al., 2022), RLs remain a minority up to bin B1^{++} (12000 km s$^{-1}\leq$ FWHM $<$ 16000, $R_{\rm FeII,opt}<0.5$), to which 3C 47 belongs. In this spectral bin, the fraction of irregular and multipeaked pro-

files is highest along the MS (Ganci et al., 2019). The usefulness of 3C 47 for understanding quasar populations along the MS and the RQ/RL dichotomy resides in the fact that within the disk model, we can identify the radial distances over which the LILs are emitted, and by comparing and fitting the CIVλ1549 line, we can identify an additional emission contribution that is interpreted as due to a failed wind. This solves a question that has been open since the early 1990s, when HST/FOS became available for large samples of objects: The CIVλ1549 broad-line profile appeared to have a comparable width or appeared to be narrower than Hβ in the UV spectra of radio galaxies (Baskin and Laor, 2005; Sulentic et al., 2007a). 3C 47 has offered an interpretation based on the double-peaked profiles of LILs and the high equivalent width single-peaked CIV profile that can be accounted for by a disk profile and an almost symmetric emission with an FWHM $\approx 4000\,\mathrm{km\ s^{-1}}$. This phenomenon is thought to occur in both RQ and RL quasars and may involve additional emission of Balmer lines as well (Popović et al., 2004; Bon et al., 2009). In most cases, the disk contribution could be completely masked, and empirical parameters measured on the observed profiles would appear inconsistent with the shifts and asymmetries expected of a relativistic disk (Sulentic et al., 1990).

6.5 Conclusions

In this paper, a new long-slit near-UV and optical spectrum of the extremely jetted quasar 3C 47 with radio emission ($\log R_K > 3$) and a clearly visible double-peaked profile in low-ionization emission lines as well as UV observations from the HST-FOS were presented. The research work used an AD model, a Bayesian approach, and multicomponent nonlinear fitting to analyze the resulting spectra.

The main findings that we draw from this study are listed below.

- We applied a model based on a relativistic AD. This model successfully explained the observed double-peaked profiles of Hβ, Hα, and MgII. The agreement between the observed profile and the model is remarkable, implying that an AD is reprocessing ionizing continuum emission with 100 and 2000 gravitational radii. The main alternative, a double BLR associated with a binary black hole, is found to be less favored than the disk model for the quasar 3C 47: Although some changes in the shifts were measured, they are inconsistent with the type of systematic variations expected for a binary model. This is not to say that 3C 47 is necessarily a system with one SMBH. A second black hole might be present in the system, as suggested by the morphology of the radio lobes and by a tentative estimate of the geodetic precession timescale. However, the putative

presence of a second massive black hole only leads to speculative implications on the BLR structure.

- The profile of the high-ionization lines can also be modeled by the contribution of the AD, along with fairly symmetric additional components (a failed-wind scenario). The failed-wind scenario is supported by the lack of prominent blueshifted emission in the C IVλ1549 and in C III]λ1909 emission lines, although the asymmetry of the profiles still reveals a modest outflow component. Exploratory photoionization computations suggest that the gas at the radii at which the AD is able to reprocess the radiation is overionized for a typical BLR density $n_{\rm H} \lesssim 10^{11}$ cm^3 for the SED of 3C 47, implying a lower radiative acceleration with respect to an Mathews and Ferland (1987) SED for the same optical flux.

The study supports not only the notion that the double-peaked profiles originate from a rotating AD surrounding an SMBH, but also that the HIL profiles, which were not explained fully in previous studies, are consistent with a physical scenario involving the AD and a failed outflow associated with low $L_{\rm bol}/L_{\rm Edd}$ and an SED with a higher X-to-UV photon ratio with respect to the conventional RQ AGN. The presence of the symmetric component in addition to the disk, associated with emission at a few thousand gravitational radii, also accounts for the difficulty in interpreting the C IVλ1549 profiles, as the wind components merge smoothly with the innermost NLR profiles, which are systematically broader than the [O III]$\lambda\lambda$4959,5007 lines in most RL AGN at low-z (Sulentic and Marziani, 1999).

Chapter 7

Preliminary work done on additional radio-loud sources

To investigate the broad line properties of RL quasars, which are orientation-dependent, we need a large enough sample of RL sources to facilitate separating effects of orientation and physics by using excellent S/N spectra. In addition, some optical spectroscopic surveys cover a limited redshift range and miss powerful radio sources in this redshift range. For this purpose, we also obtained spectra of additional RL quasars other than the one observed in Phase I (see Sect. 3.1.2.2, with a concomitant coverage of both Hβ and MgIIλ2800 spectral region. Those sources were selected for observation by considering the availability of UV spectra covering the CIVλ1549 line in the HST archive. This chapter will summarize the data reduction routine carried out during this PhD thesis for sources observed in phase II (see Sect. 3.1.2.2). The phase II sources will be analysed in the near future.

7.1 Data reduction facilities

Raw astronomical data from telescopes need significant processing before they become usable for scientific analysis. The unprocessed spectra, as they are obtained from the spectrographs, are affected by several instrumental effects that must be corrected before performing any scientific analysis to get a sound result. Therefore, handling such datasets requires specialized software packages that convert the raw spectra obtained from the instruments into a useful scientific spectrum through a process called data reduction to extract a clean and meaningful spectrum from the raw data. Two general-purpose packages in com-

mon use are MIDAS (Munich Image Data Analysis System), developed by the European Southern Observatory (e.g., Banse et al., 1983; Banse, 2003), and IRAF (Image Reduction and Analysis Facility), developed by the National Optical Astronomy Observatories (NOAO) in the US (Tody, 1986).

7.1.1 Munich Image Data Analysis System, MIDAS

The first package, MIDAS is a general-purpose software package commonly used for astronomical data reduction, and it offers a broader range of functionalities extending beyond astronomical data reduction. It can be used for various scientific data analysis tasks and is potentially useful for researchers working in multiple fields. MIDAS has a more intuitive interface compared to IRAF as it uses modern graphic user interface (GUI) based software, which makes it easier to learn and apply. However, MIDAS is less specialized for astronomy; even if it handles astronomical data, it may not have the same level of dedicated tools and pre-built workflows as IRAF for specific astronomical reduction tasks. In addition, users might need to write additional scripts or utilize external tools to achieve the same level of functionality as IRAF offers for astronomy.

7.1.2 Image Reduction and Analysis Facility, IRAF

The second general-purpose package for data reduction is IRAF, a powerful, well-established, and trusted software package in the astronomical community designed to provide a large selection of programs for general image processing and graphics applications. It offers various tools for various aspects of spectral data reduction and analysis. It includes calibration and transformation from the raw data into some measure of intensity as a function of wavelength, tasks for correcting instrumental effects, subtracting unwanted background noise, and extracting the actual spectrum of the astronomical object. Furthermore, it also allows for a scripted approach that can be automated using scripts that are particularly beneficial for large datasets or repetitive tasks, ensuring consistency and efficiency. Most of the functionality in IRAF is contained in various tasks, basic commands, or programs used to perform a specific function. Those tasks doing similar and/or logically related functions are grouped to form a package for space and transparent use. Also, packages can themselves be grouped into higher-level packages to give IRAF an organized and logical structure.

For system management, the IRAF image is split into two parts: the header file with the extension ".imh", a text file with some binary data containing various descriptive details, and the pixel file with the extension ".pix", a binary file for the numerical values representing the light intensity at each pixel. Although this remains the default file format in IRAF, most astronomical images are nowadays

stored in the Flexible Image Transport System (FITS) format, which consists of a 'header' containing meta-data and a binary array containing image data.

The runtime IRAF system, a core environment within IRAF that executes user commands and facilitates data reduction tasks, consists of four basic pieces:

- **Command language (CL)** is the user's interface to IRAF. It is the core language used to interact with IRAF and control its functionalities. The basic function of the Command Language is to provide a clean, consistent interface between the user and the various packages of functions by giving the user complete control over the parameters, data, and system resources used by IRAF programs.
- **Host System Interface (HSI)** is the interface between the portable IRAF system and a particular host system. It acts as a bridge between IRAF and the underlying operating system (like Linux) and enables IRAF to access system resources like files, memory, and processes, allowing it to interact with the machine's hardware and software.
- **Application Packages** are the real data analysis algorithms, a collection of IRAF tasks that offer tools applicable to a broad range of astronomical data, not specific instruments. It essentially extends the functionalities of IRAF's core libraries for astronomical data reduction by using a particular package by offering specialized tools tailored for data from specific telescopes or instruments.
- **Virtual Operating System (VOS).** IRAF utilizes system libraries provided by the underlying OS through the I/O interfaces, which allow reading data from astronomical data files, writing processed data to new files, and interacting with other peripherals. It contains the code for the various tasks and tools available in IRAF. They provide the functionalities used for data manipulation, analysis, and visualization. The CL and all standard IRAF application programs depend upon the facilities of the IRAF VOS for their functioning.

Astronomers rely on IRAF for data reduction purposes as it offers a comprehensive suite of tasks specifically designed for astronomical data reduction, customization, flexibility, and extensive documentation in addition to being open-source (freely available), and runs on various operating systems.

7.2 Light detecting devices

Telescopes rely on light detectors to capture the faint light from distant celestial objects. These detectors can record light across a different range of the electromagnetic spectrum. However, these detectors differ greatly in their sensitivity, response to the incoming light, field of view, coverage area, and accuracy. Photographic plates, the workhorses of astronomical observations for over a century, were first used to record images of regions of the sky. However, these plates have a limited dynamic range, and their response to the brightness of the illuminating light is non-linear. This non-linearity presented challenges since darkness didn't directly correspond to light intensity and measuring the brightness of objects leads to persistent calibration problems. In the middle years of the twentieth century, photoelectric photometers, a scientific instrument that measures the brightness of celestial objects by converting light into an electrical current, were developed. The current is then measured by an electronic device to calculate the object's brightness. These devices were more sensitive and accurate, had a linear response, and had a wider dynamic range than the photographic plate. A photoelectric photometer is a point detector ideal for precise brightness measurements of a single celestial object, and it is not an imaging device as it merely produces a single output corresponding to the brightness of one point. Charge-coupled devices (CCDs) are electronic sensors that capture light as an image. Below, we describe the CCDs, the most popular and widespread imaging devices used across a wide range of wavelengths.

7.2.1 Charge Coupled Devices (CCDs)

Astronomers use spectrographs attached to telescopes to take light, separate it by wavelength, and create a spectrum that shows the relative intensity of these separate wavelengths. A spectrograph combines an entrance slit, either a prism or diffraction grating to spread the light from a source into its spectrum, a detector (usually CCD) to record the spectrum and routing optics. Fig. 7.1 shows a schematic view of a CCD spectrometer. The entrance slit allows light into the spectrometer, where a system of mirrors routes it first onto a diffraction grating. The grating splits the light into its constituent wavelength components, and the detector records the light intensity as a function of wavelength ((e.g., Neumann, 2014)). The optical detector records the intensity of the light that reaches it as a function of its wavelength.

In modern astronomy, CCDs are the detector of choice for spectrometers due to their high dynamic range and uniform pixel response. CCDs have revolutionized astronomical observation since their introduction in the 1970s and were first used in astronomy in 1976 when J. Janesick and B. Smith obtained im-

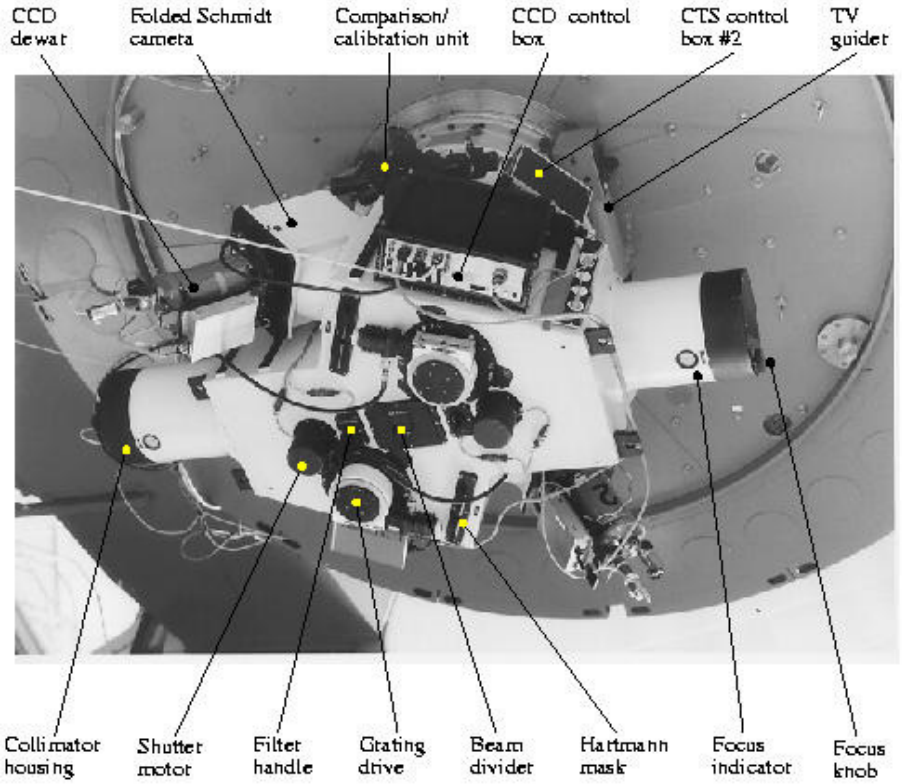

Figure 7.1: Schematic of the TWIN Spectrograph with CCD-detectors on the 3.5m telescope [Image credit: CAHA user manual].

ages of the outer planets (Jupiter, Saturn, and Uranus) using a CCD detector attached to the 61-inch telescope in Arizona and rapidly adopted in observational astronomy in the 1980's as the CCD's clear superiority over photographic plates was quickly recognized (e.g., Boyle and Smith, 1970; McLean, 2008). The CCD's clear superiority over photographic plates was quickly recognized, leading to their swift embrace by the field of astronomy. A detailed description of the equipment and working principles can be found in Martinez and Klotz (1998); Howell (2000). These small but mighty pieces of equipment are 2-D arrays, consisting of n columns and m rows of the individual light detectors, called pixels (see Fig. 7.2 left). One face is sensitive to light, and their ability to collect photons and convert them into a digital signal, are instrumental in numerous technologies. CCDs function by converting incoming photons (light particles) into electronic charges. When photons strike the light-sensitive area of a CCD, some electrons are released within it and caught in one of the potential wells within the CCD grid. Each pixel on the CCD accumulates charge, proportional to the intensity of light it receives, and changes them with some efficiency to electrons, and camera electronics transfer a certain amount to the so-called Analog to Digital Units (ADUs). The accumulated charge is then shifted pixel by pixel to an on-chip amplifier, where it is converted into a voltage and ultimately a digital signal (see Fig. 7.2 right). This digital format

allows for efficient data storage, manipulation, and analysis. By using a few clocking circuits, an amplifier, and a fast analogue-to-digital converter (ADC), it is possible to estimate the amount of light that has fallen onto each pixel by examining the amount of charge it has stored up.

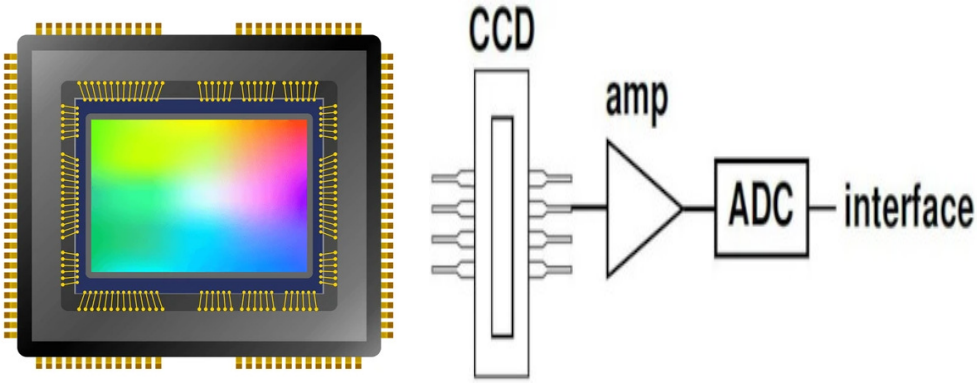

Figure 7.2: Left: Square silicon CCD mounted on a printed circuit board with gold terminals. Right: a simplified diagram of the basic internal circuit that connects the CCD line with the interface of the computer [Image credit: Smithsonian National Air and Space Museum and Nehir et al. (2019), respectively].

In many ways, CCDs combine the advantages of both photographic plates and photoelectric photometers, though their principles of operation are very different from either. They have high sensitivity due to their high quantum efficiency in converting a large fraction of incoming photons into electronic charges, they are sensitive to a broad range of wavelengths which enables observation across the electromagnetic spectrum, their response is highly linear in which the output signal is proportional to the incoming light intensity, and they provide digital data that can be easily stored, processed, and analyzed. However, CCDs also have some limitations. They suffer from readout noise, which can limit the detection of very faint objects, and they are susceptible to cosmic ray hits, which appear as random bright spots in the image.

7.2.2 Instrumental effects in CCD detectors

Raw CCD data captured from astronomical observations requires processing to remove unwanted signals and instrumental effects (intrinsic) before it becomes usable for scientific analysis. Data reduction consists of applying a set of routines to optimize the observational information. Mainly, there are two types of intrinsic effects: the additive effect which is a consequence of spurious signals added to the normal one, and the multiplicative effect due to variations in sensitivity from pixel to pixel. Such effects are usually corrected by taking various sorts of calibration frames, and non-science exposures that must be taken to reduce the data (see below) in addition to the science observations.

7.3 Data reduction using IRAF

The proliferation of linear, digital detectors on spectrographs has greatly increased the astronomer's ability to perform quantitative analysis. However, with this increased ability has come increased demands upon the tools used for reducing these data, both in the algorithms' sophistication and ease with which these tools can be used.

In addition, every raw image observed using a telescope with a CCD detector consists of many effects layered on top of the raw data due to the detector's nature and the optical imperfections in the instruments' components. Thus, removing these undesirable layers and getting relatively clean data is necessary. Data reduction consists of applying a set of standard routines to optimize the observational information by removing the instrumental signature and contaminants during the observation. Astronomers rely on IRAF, for data reduction of CCD observations, for some reason mentioned in Sect. 7.1.2. It has been designed to provide a convenient, efficient, and yet portable system for analyzing images and other classes of data. In the following, we describe the major tasks performed while doing the basic data reduction using standard IRAF procedure for the observations made using the twin spectrograph and its red and blue arms (see Sect. 3.1.1.2). While applying IRAF for the data reduction, when the `CL` starts up, it looks for a file called `login.cl` in the user's current directory. We can use the `mkiraf` command to set up the environment. This command creates the necessary file to edit (login.cl), change the defaults, and a subdirectory called `uparm`, to store the customized parameter sets.

In this work, the process of data reduction and calibration can be categorized into three major steps: i) pre-reduction, ii) wavelength calibration, and iii) flux calibration.

7.3.1 Pre-reduction

7.3.1.1 Overscan subtraction

In using CCD for astronomical observation, overscan refers to a specific region of the CCD chip that is not directly exposed to light during observation and typically there will be both overscan rows and overscan columns. Since there's no light exposure, the overscan region captures the electronic bias level and noise characteristics of the CCD itself, independent of the astronomical signal. We can estimate and remove these unwanted components from the image data by analyzing the overscan region. These regions essentially act as dark that can be illuminated directly from the image. The bias contribution can be effectively removed by subtracting the median overscan signal from the entire

science and calibration data. The specific overscan region location and size can vary depending on the CCD detector and instrument configuration.

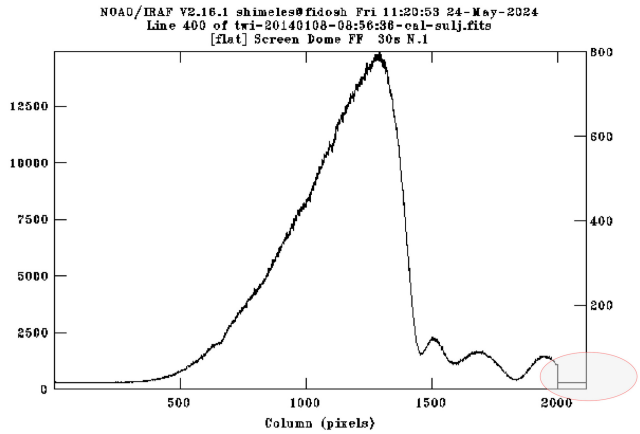

Figure 7.3: Spectra of a flat-field frame and the identification of the overscan region (bottom right).

For the overscan region identification, we used the IRAF task `implot` and image name to display it. We strike "e" key twice at the right edge at two different points to record the starting and end points of the overscan region (see Fig. 7.3). Once the overscan region is identified and recorded, the image statistics (median) value of the overscan region at these coordinates along the horizontal axis is obtained. To correct and remove the overscan region, the median value is subtracted from all, except the arc exposures as the lamps of arcs are used only for calibration in wavelength, not in flux.

7.3.1.2 Bias correction

CCD pixels have inherent electronic offsets, false signals, or biases that are imposed in addition to the real signal generated by the illuminating light and contribute a constant signal level regardless of incoming light. If left uncorrected, the bias level would add a false background to the science exposures, affecting their accuracy. To read the zero level of each pixel, bias frames are captured with the CCD shutter closed, with an exposure time of zero seconds that helps to measure the electronic offset in the absence of light. To read the zero level of each pixel, such frames can be taken before or after scientific observations. To reduce read-out noise, several frames can be taken and averaged.

To create the bias frames, multiple bias images are taken with a 0-second exposure time at the beginning of the night's observations. We used the IRAF task `imcombine` to combine the frames into a single bias frame using a median combine. The combined bias frame, typically called the "master" bias as in Fig. 7.4, is created, which is used to correct for the additive offset. The

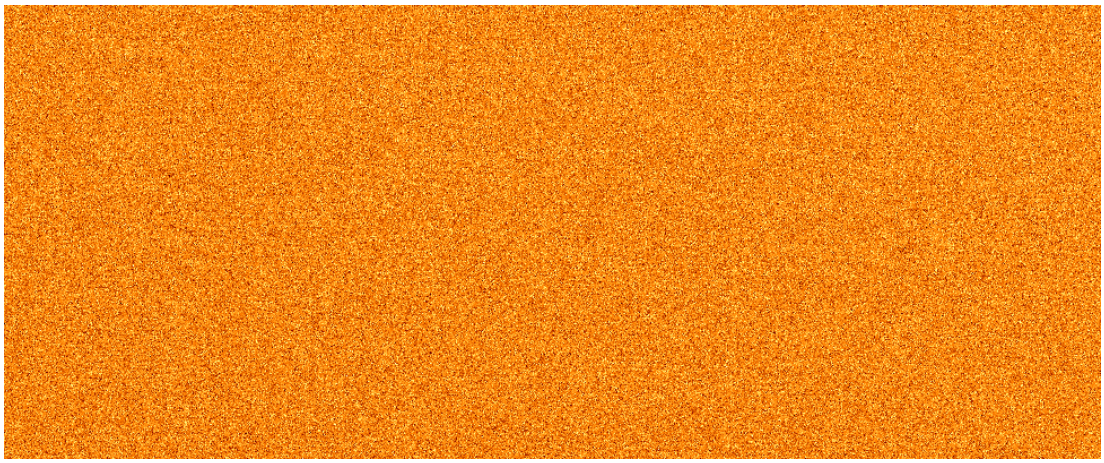

Figure 7.4: Example of the overscan subtracted, cut, and median combined bias frame in the blue part of the spectrum. Color scale is in counts/pixel.

.

resulting “master” bias frame is then subtracted using `imarith` from all the other frames acquired (to be discussed below): flat fields, standard stars, and target objects since we are using the twin spectrograph (see Sect. 3.1.2, and this resulted in an exposure from both the blue and red arms, the "master” bias is separately created for each and the subtraction is done depending on the band of the observation, i.e., the single “master” bias in blue is subtracted from all the exposures in blue and the red is subtracted from all the exposures in red.

7.3.1.3 Flat-field correction

In reality, a CCD might not be equally sensitive to photons across its entire light-collecting area, and some pixels might be more sensitive than others. Such variation might be due to variations in the quantum efficiency, dust particles on the CCD or optical surfaces in front of it, or different parts of the chip being read out through different amplifiers with slightly different gains. This variation can be accounted for by observing some spatially homogeneous light source, a uniformly illuminated surface that covers the entire light-sensitive area of the CCD, and the resulting image is called a flat-field image. Two types of flat fields are usually used: dome flats and sky flats. Dome flats are images of the inside of the telescope dome, illuminated by a bright continuum source, and are free of emission lines. They are convenient because they can be taken in unlimited numbers during the day rather than at night or during twilight, as in the case of sky flats when time is short. In the case of sky flats, it is possible to use the sky as our uniformly illuminated screen.

Once such calibration frames are known, the observed sources can be cor-

Figure 7.5: Example of the overscan subtracted, cut, bias subtracted, normalized, and median combined master flat frame in the blue part of the spectrum. Color scale is in counts/pixel.

.

rected to the values they would have had if all the pixels had been uniformly sensitive, and such correction is known as flat fielding. To create good flat fields, we take all flat frames (with equal exposure times, in the blue and red bands) and produce a median image that helps to filter out sporadic cosmic ray hits and deviating measurements, med-flat or "master" flat, with the IRAF task `imcombine`. Before that, however, to correct the sensitivity variations, the overscan-corrected and bias-subtracted flat frames are divided or normalized to the same median value of approximate unity using the IRAF task `imarith` before combining them to get the "master" flat shown in Fig. 7.5. In the case of the science exposures, once the bias level has been subtracted and overscan corrected, dividing the science exposure by the "master" flat corrects for the pixel-to-pixel variations, resulting in a flat, uniform response across the image. This ensures the measured brightness accurately reflects the actual light distribution from the observed object.

7.3.2 Wavelength calibration

The previous section listed some of the instrumental effects that must be corrected during the reduction of CCD data. However, a spectrum that has been cleaned up from instrumental effects is still meaningless, as it is now in the form of uncalibrated intensity versus pixel number. The calibration process involves a transformation of the raw data or pixel scale into some measure of intensity or flux as a function of wavelength. One of the very crucial steps to getting a meaningful spectrum is to perform a wavelength calibration so that the spectrum will now have uncalibrated intensity or flux versus a calibrated wavelength. In particular, the spectral wavelength calibration mainly consists of

establishing the dispersion relation of pixels to the wavelength profile. This is done by using calibration lamps as comparison spectra obtained by the same setup of the spectrograph as applied to the science objects (in our case, the $HeAr$ and $Fe-Ne$ arc lamps).

The main wavelength calibration steps involve the application of four IRAF tasks all located within the `twodspec.longslit` package by loading the `noao`: `identify`, `reidentify`, `fitcoor` and `transform` for each of the available arc lamps to be used. By using the already calibrated arc lamps, it is possible to calibrate in wavelength the other overscan-corrected, bias-subtracted, cut, and normalized objects, including the standard stars and science observations. Before starting the wavelength calibration process, the grating information of the lab arc spectra for the required arc lamps was obtained for both the blue and red arms of the spectrograph (T11 and T13, respectively). In our case, the lab arc spectra of $HeAr$ and Fe-Ne are extracted from the official website of CAHA (see Sect. 3.1.1) for arc lamps used[1] and kept in the current working directory. Each of the four calibration tasks and steps is described as follows:

- **Identify.** IRAF has a command that helps to identify lines within the spectrum and takes those known lines to create a relation between pixel numbers and wavelength. In the wavelength calibration process, the mapping from pixel space to wavelength can be carried out with the IRAF task `identify` that helps to identify the reference wavelength in the calibration process. While applying `identify`, we interactively identify some lines in the spectrum. This gives IRAF a first idea of the calibration function by informing it which sort of lamp produced the comparison spectrum. Then it proceeds automatically to identify based on the preliminary calibration for all the other lines.

  To run the `identify` task, we used `noao.twodspec.longslit.identify`, and the relation between the wavelength and the CCD pixel number is made using the $HeAr$ spectra as a reference spectrum with the following parameters: the line to be identified (cut, bias-subtracted, and normalized $HeAr$ arc lamp), a database to write the data, and the coordinate list, which is the path where the grating information is stored. An example command in which we applied it to identify tasks on the cut, bias-subtracted, and normalized arc lamp ($HeAr\_b4\_cut\_nobias\_noff.fits$) and the coordlist to be included in between ' ' can be,

  ```
  identify HeAr_b4_cut_nobias_noff.fits database=database
  coordlist=' ' nsum=5 maxfeatures=60 ftype=emission
  ```

  While running the `identify` task, a new window as in Fig. 7.6 (top)

[1] https://www.caha.es/pedraz/Twin/lamps.html

with the spectra of the object will be displayed and can be compared and assigned values from the lab arc lamp that has a similar spectral feature like the one in Fig. 7.6 (bottom) by comparing the appropriate regions. We identify good lines along the spectrum by positioning the cursor to the comparison line typing an "m" to mark the line, and invoking the centering algorithm to ask for the corresponding wavelength values from the user. While entering the approximate wavelength value, the task will choose the nearest entry to this value from the table of laboratory wavelengths specified with the "coordlist". By pressing "f" to fit, we obtained a fit of wavelength as a function of pixel number using the number of points we identified before. In this new interactive window, we changed the "order" of the fitting function and also checked if any discordant points might be misidentified. Once satisfied with the fitting (minimum RMS value), we then typed "q" to return to the plot of the comparison spectrum and then "l" to automatically mark and centre all the other comparison lines in the coordinate list that are not too far. Then "q" returns to the identification part of the routine. It is also possible to check and modify these additional identifications, and finally, IRAF will proceed with finding the wavelength solution using all validated comparison lines. The data describing the fit will be written to a subdirectory named "database" in the working directory and the results are written by IRAF in the spectrum header and also copied to this database as a text file like in a file called "idcompimagename" i.e., database/ide0001.0001).

- **Reidentify.** The next step involves the use of the IRAF task `reidentify` that maps the solution derived from the `identify` task for wavelength calibration, and it automatically identifies features in the spectra and handles them easily. This task will use the lab wavelengths and line centres from the entry in the working directory database for the reference spectrum obtained by the task `identify` as a starting point for the new spectrum. It will attempt to centre all the lines using the old line centres as the starting point. An example command, in which we applied the `reidentify` task on the cut, bias-subtracted, and normalized arc lamp (*HeAr_b*4*_cut_nobias_noff*, without the extension) can be:

  ```
  reidentify HeAr_b4_cut_nobias_noff HeAr_b4_cut_nobias_noff
  nsum=3 step=3 database=database coordlist=' ' overrid=yes
  trace=yes nlost=1 addfeatures=yes verbose=yes
  ```

- **Fitcoords.** The next important step in the calibration process is to find a two-dimensional fit for the arc lamps to get a full-wavelength solution. `Fitcoords` is an interactive tool that helps to refine the wavelength calibration and defines wavelength as a function of 'x' and 'y' positions. An example command in which we applied the `fitoords` task to the cut,

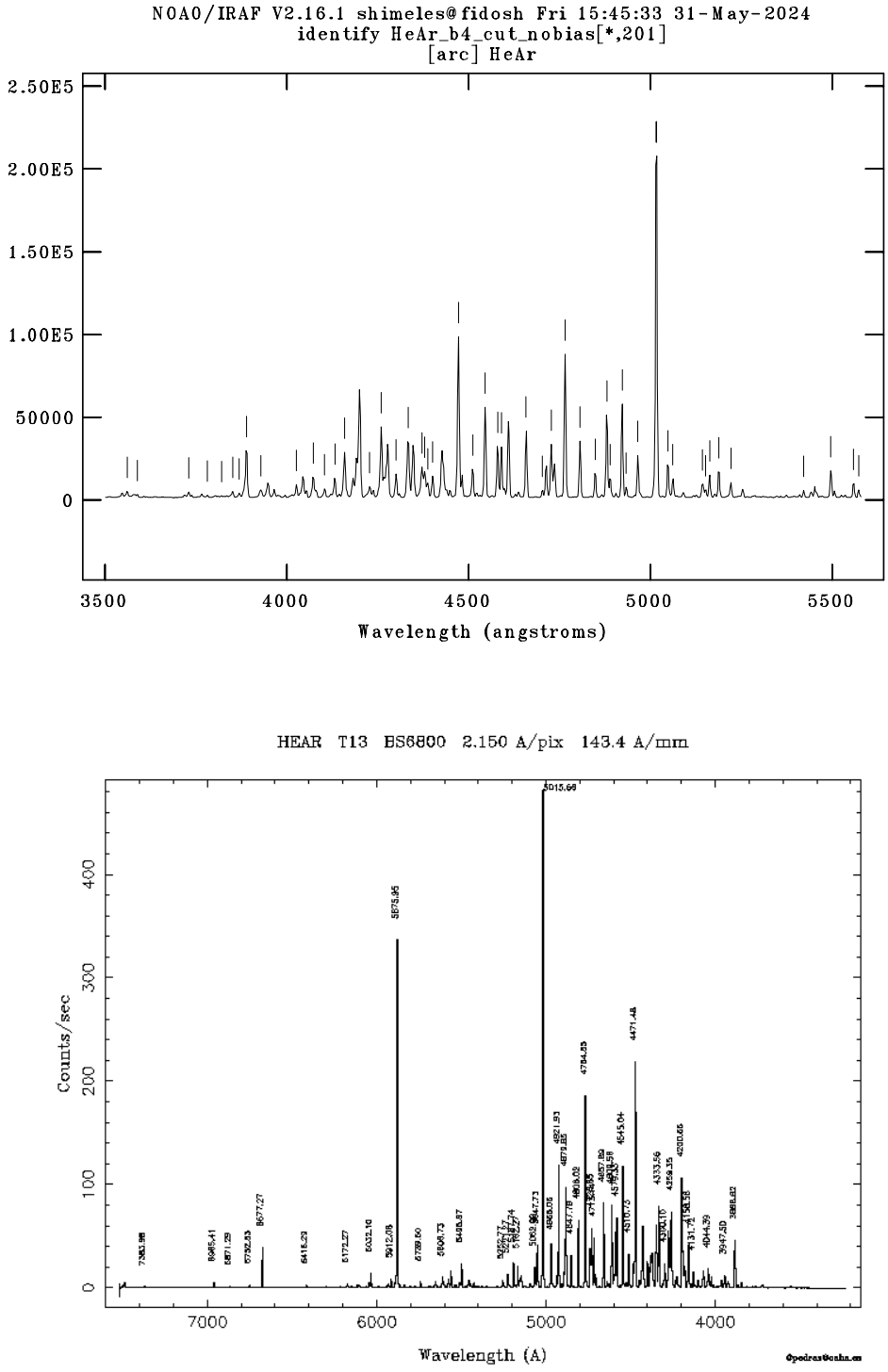

Figure 7.6: Top: The result of running the task `identify` with lines marked. Bottom: the twin calibration lab arc spectra for *HeAr* in the wide wavelength range, from 3500Å to 7400Å (increasing from left to right) used in our wavelength calibration as a reference.

bias-subtracted, and normalized arc lamp ($HeAr_b4_cut_nobias_noff$) and used the name for the coordinate fit (fitname) already identified in the database can be:

```
fitcoor HeAr_b4_cut_nobias_noff fitname=idHeAr_b4_cut
_nobias_noff
```

Allowing it to fit interactively, the `fitcoords` interactive fitting window will be displayed in the graphic terminal by displaying the residuals of the fit on the y-axis and the 'x' pixels coordinates on the x-axis as in Fig. 7.7 and can be possible to display the residuals vs. the pixels in a preferable axis. After examining the residuals as a function of 'x' in our case, and deleting any outlier points, then we get the new plot and fit the data by typing 'f'. Once satisfied with the fitting, we typed 'q' to quit the task. While quitting, we also allowed the task of writing the coordinate map to the database.

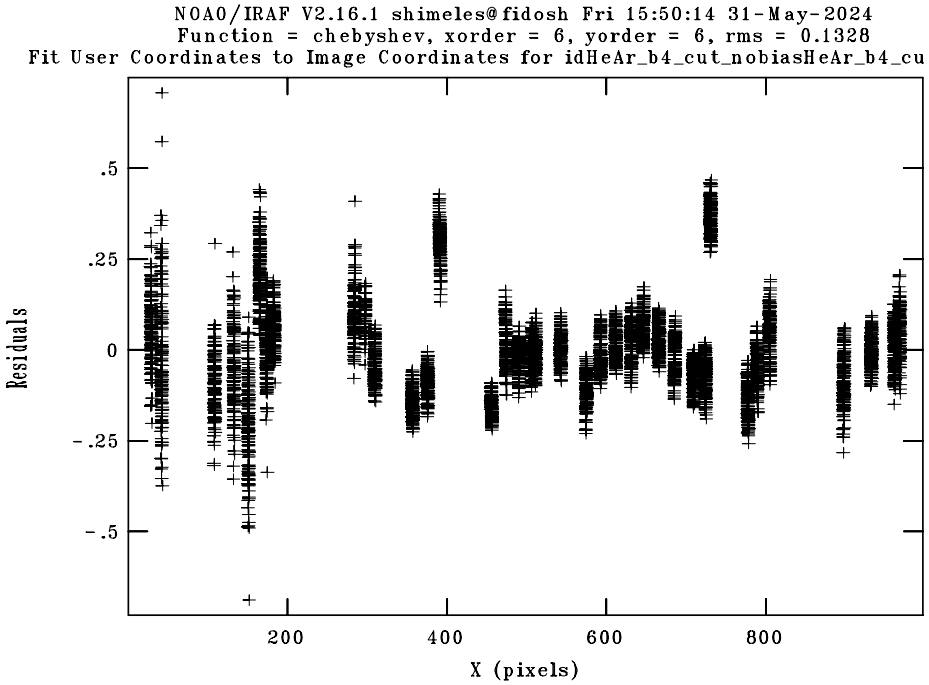

Figure 7.7: Example of the `fitcoords` interactive fitting window to examine the residuals as a function of the 'x' axis.

- **Transform.** Next, we apply the wavelength calibration and spectrum trace to the data using the task `transform` first on the standard star data. An example command in which we applied the `transform` task on the cut, bias-subtracted, and normalized arc lamp ($HeAr\_b4\_cut\_nobias\_noff$) with a new wavelength calibrated output file and the name for the coordinate transformations or calibration file (fitname) already identified in the

database (*idHeAr_b*4*_cut_nobias_noffHeAr_b*4*_cut_nobias_noff*) while applying the `fitcoords` can be:

```
transform HeAr_b4_cut_nobias_noff.fits
output=HeAr_b4_cut_nobias_noff_wavecal.fits
fitnames=idHeAr_b4_cut_nobias_noffHeAr_b4_cut_nobias_noff
```

When we apply the transform task, we will be prompted with the question of the dispersion axis, either along the lines or along columns. We chose along the line as the spectrum is aligned with the rows of the CCD and a final wavelength calibrated arc lamp can be obtained as in Fig. 7.8 by using the appropriate aperture to plot.

Using the `transform` function for each arc lamp and the appropriate coordinate transformation file (fitname), we also calibrated all the other standard stars and science exposures that are corrected for instrumental effects. Throughout the wavelength calibration process, we used properly calibrated *HeAr* lamps and their coordinate files, both in blue and red, to calibrate the other sources. A sample transformation task applied for one of the science observations (*PKS*0214+10*_b*1*_cut_nooversc_nobias_noff.fits*) and calibrated output (*PKS*0214+10*_b*1*_cut_nooversc_nobias_noff_HeAr_b*4*_wavecal.fits*) using *HeAr* and its coordinate files (*idHeAr_b*4*_cut_nobias_noffHeAr_b*4*_ cut_nobias_noff*) can be:

```
transform PKS0214+10_b1_cut_nooversc_nobias_noff.fits
output=PKS0214+10_b1_cut_nooversc_nobias_noff_HeAr_b4_
wavecal.fits fitnames=idHeAr_b4_cut_nobias_noffHeAr_b4_
cut_nobias_noff
```

7.3.3 Flux calibration

Depending on the scientific need, the next task after the wavelength calibration is flux calibration. This is a process of extracting a one-dimensional spectrum as a function of wavelength and modelling the sensitivity by comparing it with the well-known flux of the nearest standard star observed by the same spectrograph setup. The science observations are then flux calibrated using the sensitivity function obtained during the extraction process by the `calibrate` task.

In the following, we will describe the main procedures that are crucial for spectrum extraction and flux calibration:

- **Apall.** The IRAF routines for doing spectral extraction are termed as the `apextract` package, a collection of many tasks that are part of the `twodspec` in the `noao` package (`noao.twodspec.apextract`) with

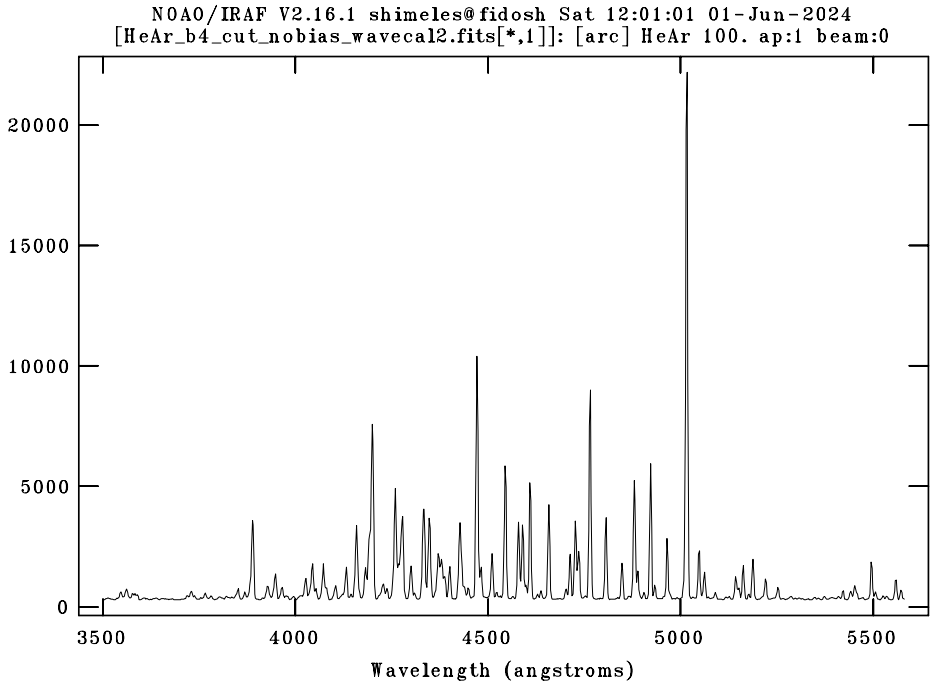

Figure 7.8: Example of wavelength calibrated arc lamp spectra of *HeAr* with the task `transform`.

the task `apall` (`noao.twodspec.apextract.apall`). In the spectral extraction process, the first step is to check if the dispersion axis of the observed standard star lies along lines or along columns.

In addition to the dispersion axis, other fundamental parameters that define the operation of spectrum extraction can be: the number of dispersion lines summed around the line used in finding a good centre for the spatial profile (`nsum`), profile width (`width`), and the lower and upper aperture limit relative to the aperture centre (`lower and upper aperture limit`). In addition, parameters that control the background window, including the location of the background regions relative to the centre of the spatial profile (`b sample`), how many adjacent points will be used (`b naver`), and the order of the function (`b order`), are crucial.

To extract the one-dimensional spectra with the `apall` task, we considered one of our overscan corrected, cut, bias subtracted, normalized, and wavelength calibrated standard stars, `Fegie34` (`Feige34_b1_cut_nooversc_nobias_noff_HeAr_b4_wavecal.fits`). By setting the fundamental parameters with an appropriate starting value and leaving the others as a default, the running command can be:

```
apall Feige34_b1_cut_nooversc_nobias_noff_HeAr_b4_
```

```
wavecal.fits lower=-10 upper=10 b_sampl='-25:-15,15:25'
format='onedspec' backgro=fit gain=1 readnoi=4.7
```

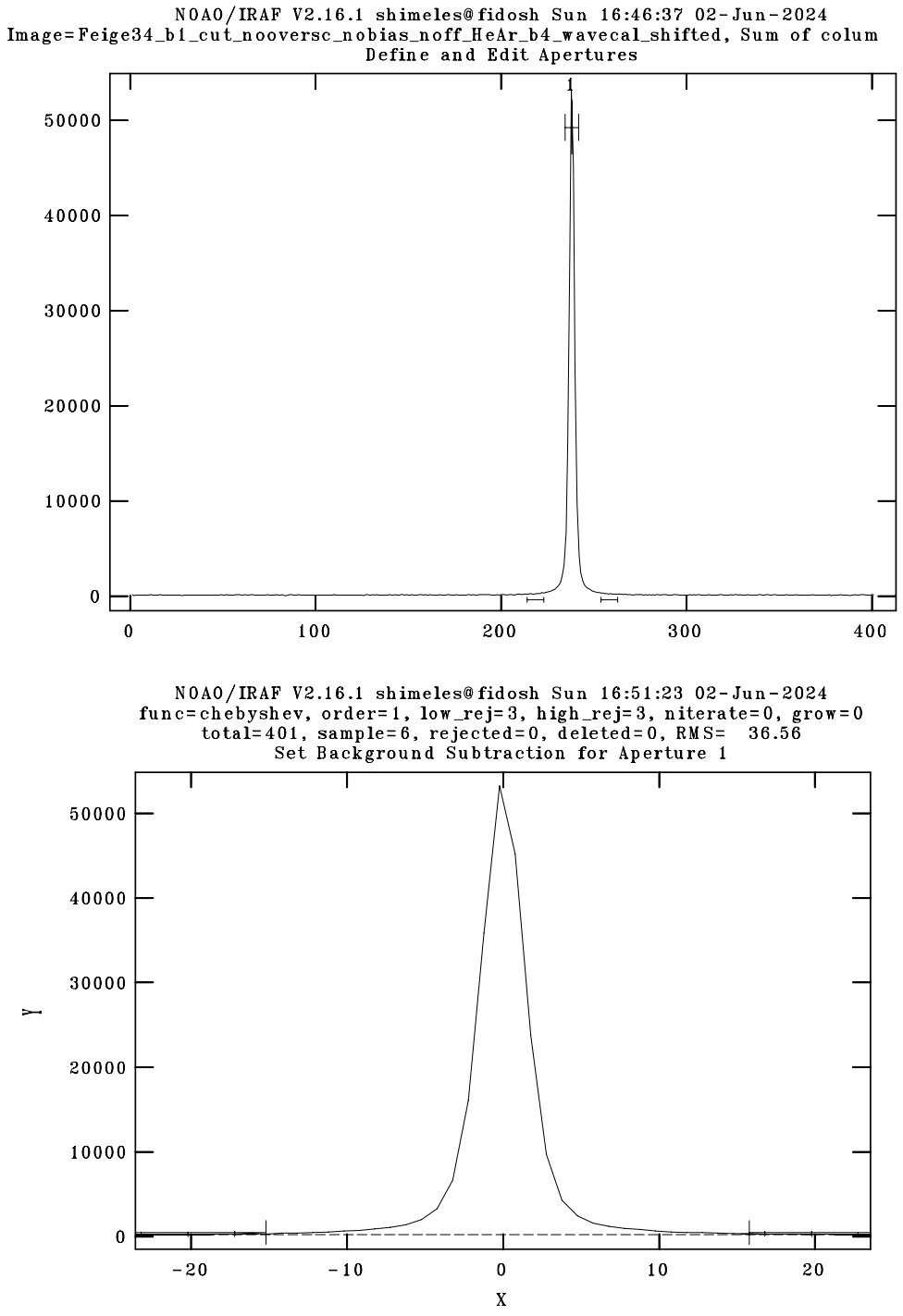

Figure 7.9: Plots showing interactive aperture (top) and background (bottom) sampling regions for the standard star `Fegie34`.

When we begin running `apall`, we first get an aperture editor to examine and modify the extraction aperture and the background fit. When we

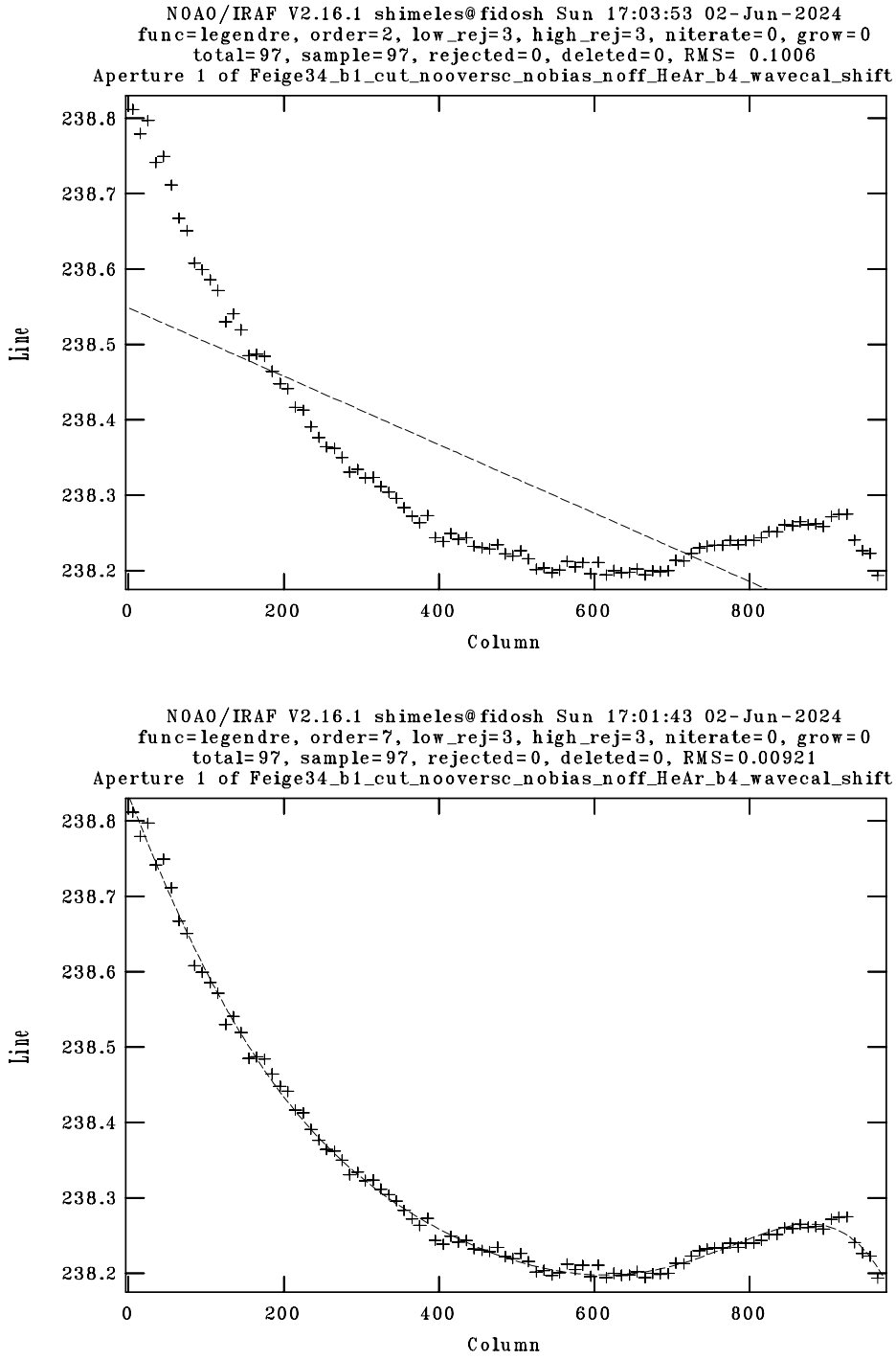

Figure 7.10: The linear fit of the spectrum with order = 2 (top) and changing to an order = 7 for a better fitting (bottom) with the same fitting function.

answer "yes" to editing the apertures, we will find a plot like that of Fig. 7.9 (top) that indicates the extraction aperture and the extracted spectrum. Once aperture extraction is completed, to check the background regions, we type a "b" and then we will get a plot that resembles that of Fig.

7.9 (bottom) that can be used to change the background region interactively. The next step is to leave the aperture editor and enter the routine that generates the trace and determines its path in the direction of dispersion. This lets us interact with the fit of the trace, and a plot is shown on the left side of Fig. 7.10 (top) with the "plus" symbols showing the measured trace, and the dashed line the best fit can be obtained. As can be seen from the header of Fig. 7.10 (top), the fit is for a 2^{nd} order Legendre polynomial, and by changing the order to a 7^{th} order polynomial, the fit improved, as in Fig. 7.10 (bottom). Finally accepting the "yes" default, our final spectrum looks like that of Fig. 7.11. Here, the overall shape of the continuum of the spectrum and some absorption lines are visible.

Once all the above steps of the extraction process are completed, an entry is made in a local subdirectory database in a file called "`apimagename`" and an image name with an extension "0.0001" that will be used for the final calibration process. Through these files and database entries, one part of the extraction process communicates with the following steps that help to complete the flux calibration process. The procedure of spectrum extraction was also done for the other standard stars and observations were obtained using the red arm of the spectrograph.

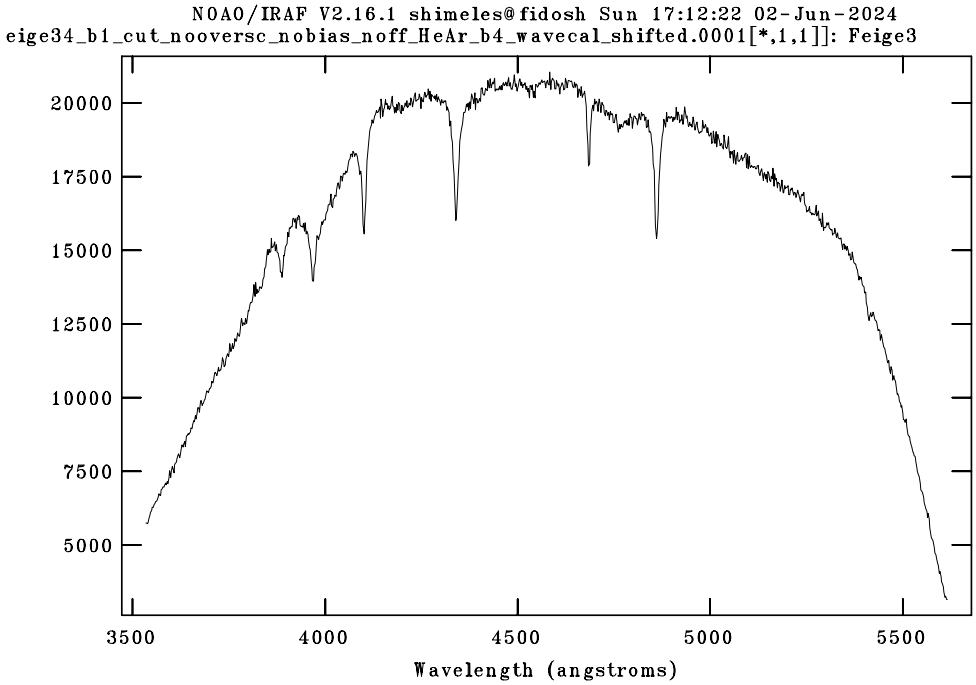

Figure 7.11: The final extracted spectrum from the standard star `Feige34`.

- **Standard.** The second IRAF routine used for flux calibration is the task

`standard`, part of the `onedspec` in the `noao` package (`noao.onedspec`) for standard star file preparation using the `noao.onedspec.standard` command that can be executed for each standard star observation. The main aim of running the task `standard` is to calibrate the instrumental response and allow for atmospheric extinction so that a spectrum as observed from outside the atmosphere with a relatively uniformly sensitive instrument can be approximated. For this purpose, we considered the energy distribution of the standard star used for extraction. We corrected the energy distribution for wavelength-dependent atmospheric extinction, compared it to the energy distribution of the observed spectrum, and finally derived the function that gives the response.

While applying the task `standard` for the same standard star considered in the extraction process using `apall`, the command can be:

```
standar Feige34_b1_cut_nooversc_nobias_noff_wavecal_
.0001.fits output=standard_Feige34_b1.dat
extinct='extincion_CAHA.dat' caldir='Standard_stars/'
observa=ca star_nam=mfeige34 answer=yes
```

This task determines calibration pass bands and writes them to a file called "std" as a default output. As IRAF needs to have some general idea of atmospheric extinction, the extinction file with the correct path and name of the extinction and flux file is used to make second-order extinction corrections across the band passes. After this run, we let the result be as it is, and we tried to remove some points outside the continuum in the next interactive window that resulted from running the task `sensfunc`.

- **Sensfunc.** The third crucial step in the flux calibration process is to put the results together and find a proper wavelength dependence of instrumental sensitivity and atmosphere transparency. For this, the `sensfunc` task in `onedspec` in the `noao` package using `noao.onedspec.sensfunc` in the IRAF terminal allows to interactively fit the sensitivity function as a function of wavelength using the output file from the `standard` task as it recorded response of each standard star.

  The command with the main parameters to be included and letting the other parameters as their default, for the task `sensfunc` can be:

  ```
  sensfunc standards=standard_Feige34_b1.dat sensitiv=
  sensfunc_standard_Feige34_b1 extinction='extincion_CAHA.dat'
  newexti='extinct.dat' observa=ca
  ```

  Once we run the above, a curve fitting phase is entered. As it is an interactive window, the familiar interactive fitting commands can be used to adjust the fitting function and order of the fit as usual. Once satisfied

with the fitting by setting the fitting function to a legendary and higher order, it is possible to quit the `sensfunc` using "q". An image with a default sensitivity name and an additional ".0001" can be created in the current working directory. Figure 7.12 shows the Feige 34 spectrum overlaid with boxes showing the fitting regions for the sensitivity function. The top plot of the pair shows the sensitivity function vs. wavelength. The bottom plot of the pair shows the residuals (magnitude) vs. wavelength.

- **Calibrate.** The sensitivity function determined by `sensfunc` is applied to our data by the `calibrate` task from `noao.onedspec.calibrate` to correct for atmospheric extinction and to transform using the sensitivity curve for each data to be calibrated. For the standard star `Fegie34` used in the previous steps, the final flux calibration command, using the extracted spectrum, and the resulting sensitivity function can be:

  ```
  calibrate Feige34_b4_cut_nooversc_nobias_noff_HeAr_b4_
  wavecal.0001.fits output=Feige34_b1_cut_nooversc_nobias_
  noff_HeAr_b4_wavecal_fluxcal.fits sensiti=sensfunc_
  standard_Feige34_b1.0001.fits extinct='extincion_CAHA.dat'
  observa=ca ignorea=yes
  ```

  Here, the resulting output is both wavelength and flux-calibrated spectra. The final, flux-calibrated spectrum is shown in Fig. 7.13.

Once all the appropriate standard stars were calibrated, the wavelength-calibrated science observations were flux calibrated using the mean sensitivity function obtained from the appropriate standard stars and the task `calibrate`.

Regarding the science observations, the exposure times were split into shorter ones for some reason, like cosmic ray (CR) hits that might affect the CCD detector. Since the CR hits are random, they will impact different pixels if another exposure is made. They can be eliminated by splitting long exposures into several shorter ones and combining them. For this purpose, we have three separate exposures for each science observation in the blue and red bands, and we combined the well-centered, wavelength, and flux-calibrated observations of the same source in each band using the `lscombine` function. Fig. 7.14 shows the final wavelength and flux calibrated image of one of our science observations, quasar PKS 0204+10 (top), and a combination of three different short exposures of the same source (bottom). As can be seen from the right image, the CR hits are removed as a result of the median combining the different short exposures.

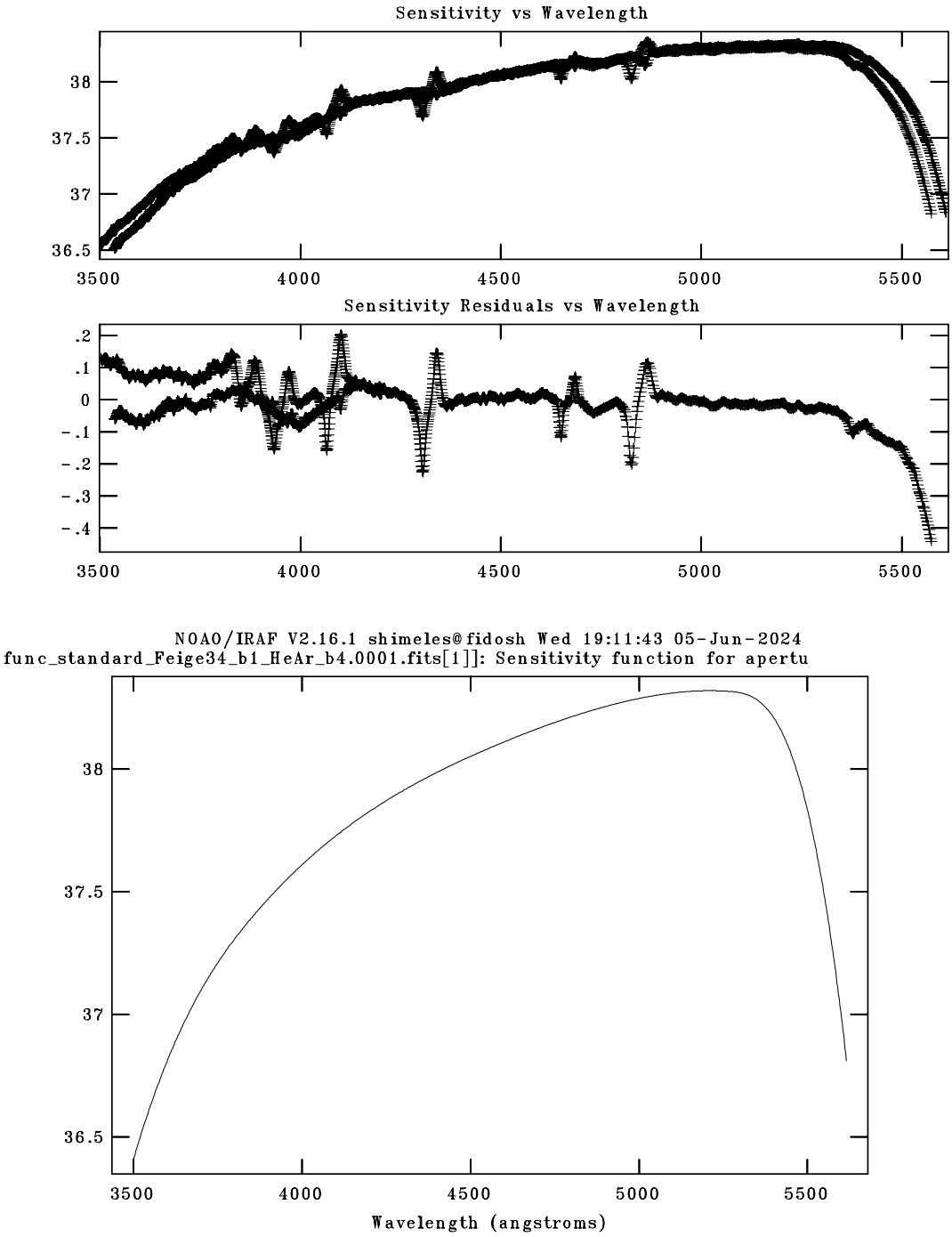

Figure 7.12: Example of the output of the `sensfunc` task for the standard star `Feige34` using order to be 7 (top) and the resulting sensitivity function (bottom).

7.3.4 Sky subtraction

The sky is not perfectly "dark," but it has some emission that can be detected by the CCD detector. To get a better science spectrum, such sky glow (which

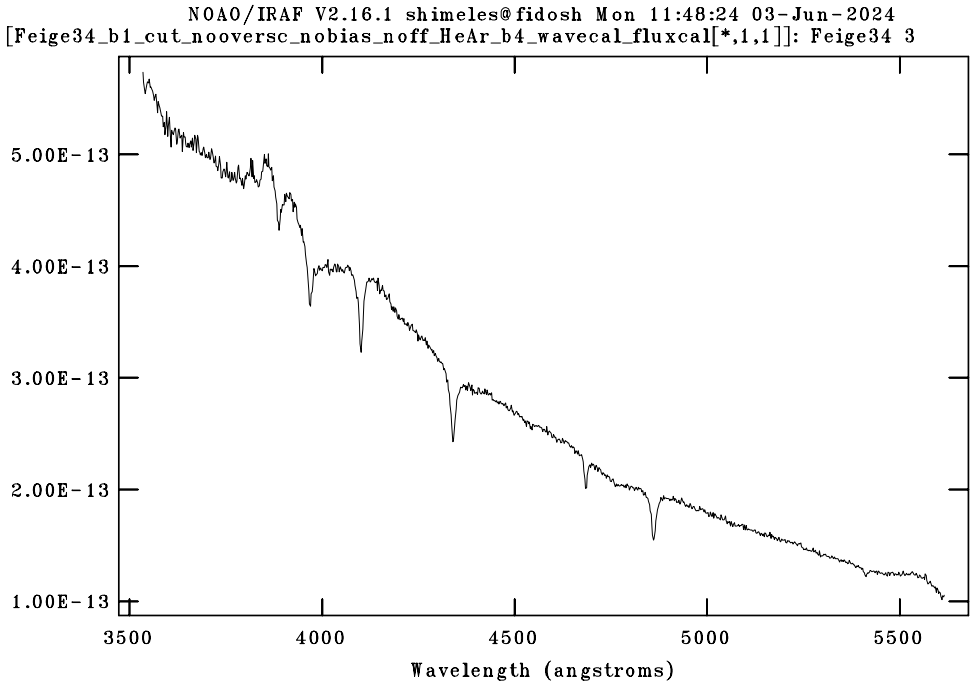

Figure 7.13: The final extracted, flux-calibrated spectrum of the standard star `fegi34`.

appeared as a faint and/or strong vertical line in Fig. 7.14) needs to be removed. Such effects can be removed by creating a sky model or spectrum by selecting two or more (of the same size in "Y" and free of bad pixels or CR hits) sky areas near the science object but not including the science object and creating new images of such regions. Using the **IRAF** task `blkavg` (`images.imgeom`), sum the images and make an average 1D sky image, and then with task `blkrep`, to replicate the images and obtain a 2D image. Finally, such 2D images are subtracted using the **IRAF** task `imarith` from the median combined flux and wavelength calibrated spectra to remove the skylines and get a final sky subtracted spectra as in Fig. 7.15.

7.3.5 Redshift correction

With the redshift values obtained from Véron-Cetty and Véron (2010), and by using the final calibrated and skyline removed spectra, we corrected for the specified Doppler shift and obtained a final rest frame spectra. The **IRAF** task `dopcor` (`noao.onedspec.dopcor`) is a powerful tool for correcting redshifted astronomical spectra and has allowed us to analyze the intrinsic properties of sources at their rest frame wavelength. Based on the provided redshift value, it calculates the corresponding shift in wavelength for each data point to account for the cosmological redshift. After applying the redshift correction,

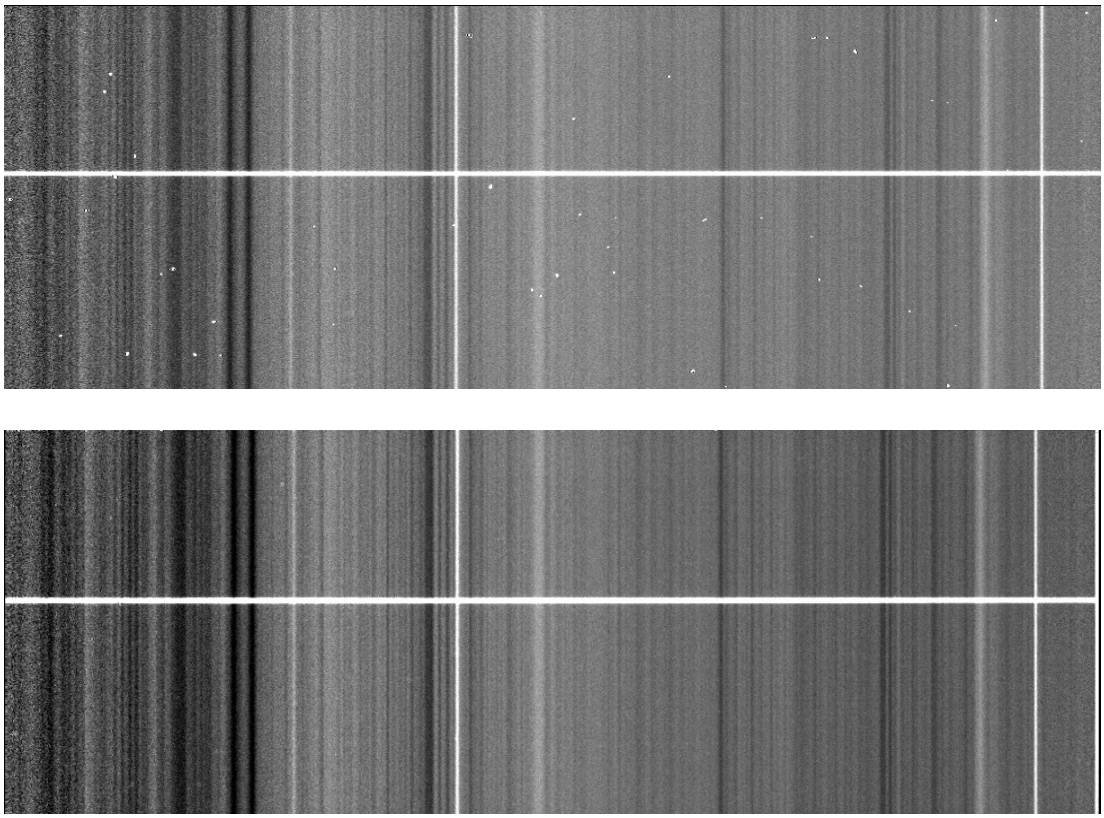

Figure 7.14: Example of the overscan corrected, cut, bias subtracted, flat-field corrected and normalized, flux and wavelength calibrated spectra of one of the science observations (PKS 0214 +10), only for a single exposure with the CR hits (top). A combination of three short-time exposures to the same source, in which the CR hits are removed in the combined spectra (bottom).

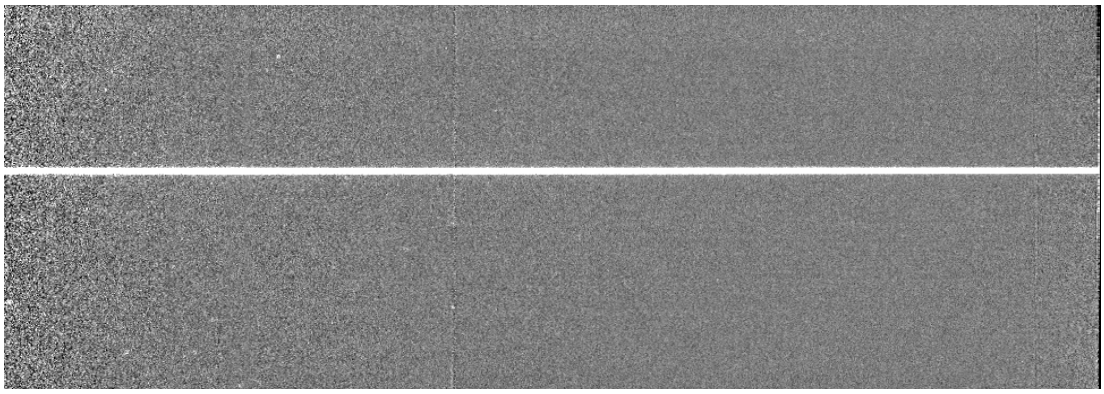

Figure 7.15: Example of the overscan corrected, cut, bias subtracted, normalized, flux, and wavelength calibrated spectra of one of the science observations (PKS 0214 +10) after eliminating the skylines.

the new spectrum contains the original intensities shifted to their corresponding rest-frame wavelengths. The final-rest frame spectra obtained as a result of the overall data reduction process for the observations made using the blue and red

arm of the spectrograph for one of our sources, 3C 95, are shown in Fig. 7.16. In both results, some more corrections still need to be included, especially for the spectra obtained by using the red arm. As part of future work, the data reduction will be revised again to get a spectrum that fulfils the nature of quasar spectra, like a clear Balmer decrement.

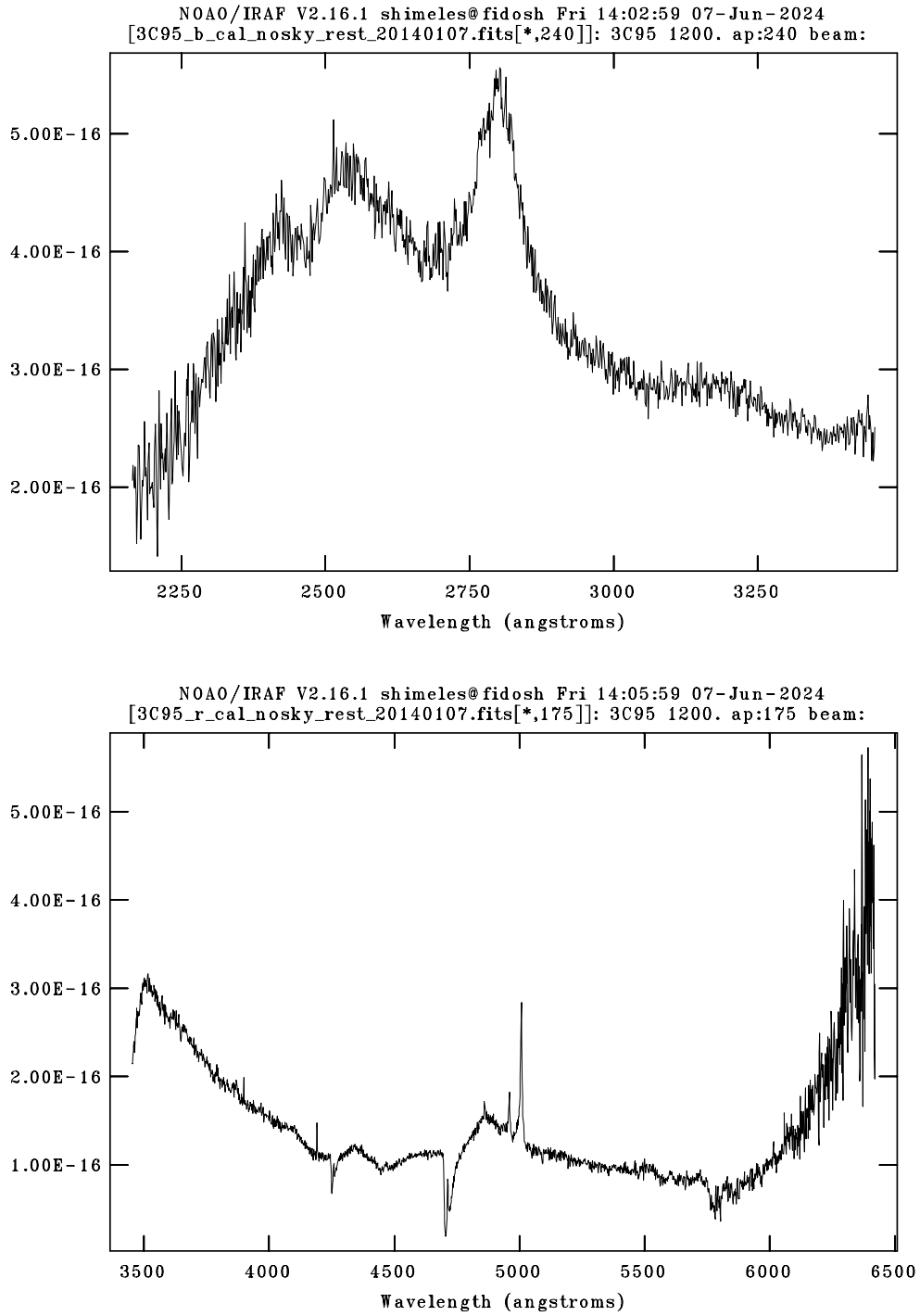

Figure 7.16: Rest-frame spectra of the quasar 3C 95 obtained by using the blue arm (top) and by the red arm (bottom). Abscissas are rest frame wavelength in Å, and ordinates are specific flux in units of ergs s^{-1} cm^{-2} $Å^{-1}$.

Chapter 8

Summary and conclusions

In this thesis, we mainly aimed at the comprehensive studies of quasars found at low redshift, z < 1. As the most distant and luminous subset of active galactic nuclei (AGN), quasars have historically been classified into two distinct classes, depending mainly on the presence or absence of strong and extended radio jets, called radio-loud (RL) and radio-quiet (RQ). Considering physical differences, they can also be classified as jetted (RL) and non-jetted (RQ). There is a long-standing open debate involving the possibility of a real physical dichotomy between RL and RQ quasars. The summary of our work in this aspect, the conclusions derived from it, and future works are presented in this chapter.

8.1 General summary

This PhD thesis, titled "Dichotomy of Radio-Loud (RL) and Radio-Quiet (RQ) Quasars in the Four-Dimensional Eigenvector 1 (4DE1) Parameter Space," explores the fascinating divide between these two quasar populations. Our primary goal is twofold.

First, we mainly aimed to ascertain the dichotomy between RL and RQ quasars by quantifying broad emission line differences. We then delve into the intriguing realm of extremely jetted quasars, examining their radio as well as optical and near-UV spectroscopic properties within the framework of the optical plane of the 4DE1 scheme, also known as the quasar's main sequence (MS). We also aimed to check the effect of powerful radio ejection on the low-ionization lines (LILs).

The second goal was to perform a detailed analysis focusing on the unique

case of the quasar 3C 47, extreme population B jetted source that exhibits a broad double-peaked profile on the Balmer and high ionization UV lines, and to address whether the accretion disk (AD) can account for the double-peaked profile observed in the spectra.

In general, the thesis was based on the analysis of radio, near-UV (MgII), and optical (Hβ) lines to achieve the first goal and radio, near-UV, optical, and UV (CIII]λ1909 and CIVλ1549) for the second one. For this, we used 12 newly observed quasars with a high signal-to-noise ratio in the redshift range, 0.35 $\lesssim$ z $\lesssim$ 1 from long-slit optical observations with the Cassegrain TWIN Spectrograph of the 3.5m telescope at the Calar Alto Observatory (Almería, Spain) and additional comparison samples from the archive. The sources we selected are among the most extreme radio emitters, those with a radio-to-optical flux density ratio $\gtrsim 10^3$ that concomitantly cover MgII and Hβ, FeII blends, and Hα in some cases. Chapter 3 of this thesis describes the new observations from the 3.5 m telescope and the archival data in detail. Hβ and MgII provide diagnostics of the LIL and CIII]λ1909 and CIVλ1549 for the high ionization line (HIL) emitting regions.

To achieve the first goal, we set different objectives and specifically focused on studying the properties of the radio emission and the relation between radio and optical parameters, analyzing the broad emission lines particularly, Hβ, FeII, and MgII, evaluating the parameters characteristics such as FWHM of the full emission line profiles, and studying the spectroscopic differences of the RL sample with RQ quasars of population B and comparison with quasars of population A, which are mostly RQ in the 4DE1 Scheme. The objectives were attained by doing two complementary approaches: a multicomponent non-linear fitting using the IRAF task `specfit` and by analyzing the full broad profile. Spectral non-linear multi-component fittings and full broad profile (FP) analysis are described in Chapter 4. The results have been presented in detail in Chapter 5, and partly published in Mengistue et al. (2023). In addition to profile parameters like FWHM, centroids at different fractional intensities, kurtosis, asymmetry index, total flux, and equivalent width, we also computed the basic accretion parameters, M_{BH} and L/L_{Edd} by using the two LILs, Hβ and MgII. We also checked the correlation and the effect of the physical parameters on the profile parameters. Some of the main results are:

- Most of our RL quasars occupy a much more restricted domain in the optical plane compared to the RQ sources of the comparison samples. They populated in the bin B1 with FWHM Hβ $>$ 4000 km s^{-1} and $R_{FeII,opt}$ $<$ 0.5. This confirms the result of Zamfir et al. (2008) who found that powerful jetted sources occupy mainly the Pop.B region of the MS as compared to RQ.

- The UV plane formed from FWHM of MgII, and $\mathrm{FeII_{UV}}$ looks similar to the optical plane, based on Hβ and the $\mathrm{FeII_{opt}}$. As in the optical plane, our quasars occupy a more restricted domain than the full quasar population, with low R_{Feii}UV.

- The singly-ionized iron emission is systematically fainter in RL than in RQ sources, although it is still unclear if this is an effect intrinsic to a different emitting region structure, or associated with different host galaxy properties

- There is no correlation between the EW $\mathrm{FeII_{UV}}$ and, $\mathrm{FeII_{opt}}$ as already mentioned in the work of Kovačević-Dojčinović and Popović (2015).

- The FWHM of MgII is systematically narrower than FWHM Hβ by about 10%. This holds for both the full broad profile and if only the broad component is considered for our AGN a result consistent with previous studies.

- Both Hβ and MgII lines showed profile shifts and asymmetries towards the red. The centroid shift of the line base c($\frac{1}{4}$), as well as the asymmetry index, are larger in Hβ than MgII and this mainly attributes to the strong effect of the very broad component (VBC), which was larger in Hβ than in MgII.

- Both Hβ and MgIIλ2800Å appear to be suitable for M_{BH} virial estimation.

- The extremely jetted quasars lie within the range of $\log M_{\mathrm{BH}}$ = 8.49 – 9.25 [$\mathrm{M_\odot}$] and 8.26 – 9.37 [$\mathrm{M_\odot}$] when using $\mathrm{H\beta_{FP}}$ and $\mathrm{MgII_{FP}}$, respectively. The resulting $L_{\mathrm{bol}}/L_{\mathrm{Edd}}$ has a range of 0.022 - 0.380 and 0.019 – 0.195. In addition, $L_{\mathrm{bol}}/L_{\mathrm{Edd}}$ is lower while using MgII than Hβ.

- We found that, compared to RQ, our extreme RL quasars show a larger median Hβ full width at half maximum (FWHM), weaker FeII emission, a larger SMBH mass (M_{BH}), lower Eddington ratio ($L_{\mathrm{bol}}/L_{\mathrm{Edd}}$), and a restricted space occupation in the optical and UV MS planes with weak $\mathrm{FeII_{UV}}$ emission and broad MgII. The differences are more elusive when the comparison is carried out by restricting the RQ population to the region of the MS occupied by RL sources.

- Joining the sources studied in this work with comparison samples, we find that the distribution of shifts appears to be slightly dependent on M_{BH} in which larger c($\frac{1}{4}$) values occur for the highest M_{BH} and lowest $L_{\mathrm{bol}}/L_{\mathrm{Edd}}$ values. A possible explanation is offered by a combination of outflow and infall (or gravitational redshift) contributing to blueshifted and redshifted

excesses, respectively, with the outflow component being minimal in the RL Hβ and MgII profiles.

- There is a trend between the velocity shifts, c($\frac{1}{2}$), c($\frac{1}{4}$) and $R_{\rm K}$: Pop. B RL quasars tend to have larger velocity shifts to the red than RQs. The trend is however found to be not significant if the RQ and RL $M_{\rm BH}$ and $L_{\rm bol}/L_{\rm Edd}$ distributions are matched.
- There is apparently no evidence of outflow in the broad line profiles of our 11 sources. The only evidence is provided by a slight asymmetry of [OIII]$\lambda\lambda$4959,5007. Further observations of HILs such as CIVλ1549 would be needed to assess the extent of any mildly ionized outflow originating from the accretion disk.

The radio data was fundamental to identify quasars according to their morphology in radio frequencies as well as to determine the power of the radio emission. A well-defined criteria in radio have been also used to isolate the RL quasars from the RQ: resulting Kellermann parameter, log$R_{\rm K}$ > 3 and radio power in excess of logP_ν = 33.3 [ergs $s^{-1}Hz^{-1}$]. These values for our quasars meet by far the requirement to classify them as extreme jetted quasars. A visual classification based on the radio images at different radio frequencies and scales allowed us to classify our sources as lobe-dominated (LD), core-dominated (C), core jet (CJ), and core lobe (CL).

On the other hand, even if the majority of AGN spectra are single-peaked, there are evidence about the double-peaked structure that can be assured from observations of very broad, double-peaked emission lines and the identification of asymmetries and substructures in the line profiles. In the second part, to evaluate the extent to which the AD is a source of the broad Balmer lines and high ionization UV lines in RL AGN, we focused on a unique case of the strong RL quasar 3C 47, an extreme population B jetted source with a clearly visible double-peaked profile. This new observation of 3C 47 yielded a spectrum with a high S/N ratio, high resolution, and broad and strong blue and red peaks that are typical indicators of double-peaked emitters in the Balmer lines (Hβ and Hα) as well as the near-UV (MgII) line. We also analyzed the UV spectra from the Hubble Space Telescope (HST) Faint Object Spectrograph (FOS), (HST-FOS) archives for the CIVλ1549 and CIII]λ1909. A variety of mechanisms have been proposed to explain the origin of double-peaked emission-line profiles and their unique kinematic signature, including relativistic motions in an AD, two separate broad line regions (BLRs) as a signature of binary black holes, originate in a biconical outflow, or are produced by a highly anisotropic distribution of emission-line gas. Careful consideration of the basic physical arguments and recent observational results tends to confirm that the most likely

origin of double-peaked emission lines is the AD, and on the converse, these double-peaked profiles provide dynamical evidence about the structure of the AD.

The main objective in this regard was to provide evidence for the presence of an AD as a possible source of the broad emission lines observed in the spectra by applying a model based on a relativistic Kepplerian AD to explain the observed double-peaked profiles, to study the geometry and kinematics of the AD and the presence of winds/outflows and jets in the sources as well as their effect in the surrounding medium. A relativistic Keplerian AD model, a Bayesian approach, and a multicomponent non-linear fitting were utilized to analyze the optical spectra and UV observations as detailed in Chapter 4. In addition, the profile of the prototypical high ionization lines is also modeled by the contribution of the AD, along with fairly symmetric additional components due to outflows and emissions from the innermost part of the narrow line region (NLR). Disk parameters, such as inner and outer radii, inclination to the line of sight, emissivity index, and local broadening parameters, are determined. In addition, physical parameters, supermassive black hole (SMBH,$M_{\rm BH}$), and Eddington ratio ($\lambda_{\rm E}$) using virial equations and scaling laws are estimated. The results have been presented in detail in Chapter 6, and partly published in Mengistue Terefe et al. (2024).

The main findings that we draw from this analysis are:

- The broad, double-peaked profile of the Hβ, Hα, and MgII lines in 3C 47 successfully fitted with a relativistic Keplerian AD model.
- The agreement between the observed profile and the model is remarkable, implying that an AD is reprocessing ionizing continuum emission with 100 and 2000 gravitational radii. The main alternative a double BLR associated with a binary black hole is found to be less appealing than the disk model for the quasar 3C 47.
- Considering the width of the broad profile, disklike emitters tend to have larger widths, especially at half-maximum and 3C 47 has an enormous width with FWHM > 15000 km s^{-1}. The Hβ disk line profile is among the broadest: its FWHM $\approx$ 16600 km s^{-1} and is wider than Hα and MgII in which FWHM(Hα) $\approx$ 0.93*FWHM(Hβ) and FWHM(MgII) $\approx$ 0.90*FWHM(Hβ).
- The profile of the HILs can also be modeled by the contribution of the AD, along with fairly symmetric additional components (a failed wind scenario) and emissions from the innermost part of the narrow line regions

(NLRs). The failed wind scenario is supported by the lack of prominent blueshifted emission in CIVλ1549 and in CIII]λ1909 emission lines.

In general, our study contributes to quantifying the broad emission line difference between RL and RQ quasars by implementing the 4DE1 parameter space that provides spectroscopic contextualization for all classes of broad-line emitting AGN. It also provides a piece of evidence to assert the potential dichotomy between them, which will solve the debated problems associated with bimodality or the possibility of a real physical dichotomy between them. The results strengthen and give additional evidence in refining quasars classification by offering a more robust method, which leads to a more nuanced understanding of quasar populations and the difference between an observational set of accretion parameters such as $M_{\rm BH}$ and $\lambda_{\rm E}$ as a physical parameter and centroid velocity shift and asymmetry measurements as a profile parameter. As far as the LILs BLR is concerned, the jet may not have a strong effect on their dynamics. More nuanced may be the effect on the HILs; however, the main parameter affecting red asymmetric and blueshifts seems to be $M_{\rm BH}$ (leading to gravitational redshift or infall) and $\lambda_{\rm E}$ (leading to failed winds, lack of blue shifts), more than radio power or radio-to-optical power ratio.

Our study also gave a piece of evidence about a double-peaked structure which is a rare case as the majority of AGN spectra are single-peaked, and the extent to which AD is a source of the broad and double-peaked profiles observed in the Balmer lines, near-UV, and the high-ionization UV lines. Such detailed analysis results are crucial in understanding the geometry and kinematics of the AD, the presence of winds/outflows, and jet activity. In addition, the findings can contribute to developing more refined quasar classification methods, give additional information for the study of quasars and their model development, and offer broader insights into the nature of AGN activity and galaxy evolution.

8.2 Conclusions

This work can be taken as a comprehensive one in studying the spectroscopic properties of quasars, their components, and their effect on the surrounding environment. Working towards achieving our objectives, we have concluded at the end of each chapter, while the main conclusions derived from this work are given as follows.

A comparative analysis between a large sample of radio-loud (RL) and radio-quiet (RQ) quasars confirms intriguing differences in emission line properties deduced from this small sample. RL quasars exhibit a larger Hβ full width

at half maximum, weaker FeII emission, and distinct characteristics in the optical and UV main sequence (MS) planes. Notably, the most powerful RL quasars exhibit strong redward asymmetries in the Hβ emission lines. Despite the presence of relativistic jets in these powerful RL quasars, they do not seem to affect the low ionization lines strongly. However, extremely powerful jetted quasars tend to possess a strong shift towards the red in the velocity centroids around the line base. The differences are more elusive when the comparison is carried out by restricting the RQ population to the region of the quasar MS occupied by RL sources (i.e., consistent domains in black hole mass and Eddington ratio), and the RL and RQ quasars spectral properties become more similar, also in terms of the strong redward asymmetries in Hβ emission lines that is a defining characteristic of low accretors (Population B quasars). Only the most powerful RL quasars display systematically stronger redward asymmetries in the Hβ emission lines with respect to the matching RQ sample. Also, large black hole mass and low radiative output more than radio power and the presence of a relativistic jet is associated with two of the most striking features revealed in the emission profiles of RL quasars, namely the redward asymmetry at the base of the line profile and the almost unshifted and symmetric CIVλ1549 profiles. The redward asymmetry might be ultimately ascribed to gravitational redshift, at least in systems with very large black hole masses ($M_{\rm BH} > 10^{8.5}$ M$_\odot$).

Furthermore, the work in this thesis provides compelling direct observational evidence supporting the presence of an accretion disk (AD) as the source of the broad emission lines observed in quasar 3C 47. The study supports not only the notion that the double-peaked profiles originate from a rotating AD surrounding a supermassive black hole but also that the high ionization line profiles that were not explained in full previously are consistent with a physical scenario involving the AD and a failed outflow associated with a low Eddington ratio and a spectral energy distribution with a higher X-to-UV photon ratio with respect to the conventional RQ quasar. The presence of the symmetric component on top of the disk, also accounts for the difficulty in the interpretation of the CIVλ1549 profiles, as the wind components merge smoothly with the innermost narrow line region profiles that are systematically broader than the [OIII]$\lambda\lambda$4959,5007 lines. The CIVλ1549 profile can be attributed to the AD plus a strong central feature. The flat spectral energy distribution of 3C 47, dominated by synchrotron and synchrotron-self-Compton emission, results in the overionization of the gas, and this overionization leads to a lower force multiplier, which may contribute to the formation of a failed wind. The study suggests that a model involving a double broad-line region associated with a binary black hole is less appealing than the AD model for explaining the characteristics observed specifically in quasar 3C 47. The model successfully explained the observed double-peaked profiles, and the agreement between the observed

profiles of the low ionization lines and the model is remarkable.

8.3 Future works

The proposed research lays a strong foundation for a comprehensive understanding of the debating problems associated with the possibility of a real physical dichotomy between RL and RQ quasars, the effect of radio loudness on the dynamics of the low-ionization broad line emitting regions, the geometry, and kinematics of the AD, the presence of winds/outflows, and jet activity.

However, in the future, we plan to carry out some additional analyses that could help in getting more solid results by utilizing existing and upcoming datasets. An immediate possible future development of this work is to analyze the ultraviolet (UV) spectra of the 11 sources obtained from the HST-FOS archive to characterize the outflow behavior of gas in these sources and gain valuable insights into the dynamics and energetics of these processes. This will be done mainly as there is apparently no evidence of outflow in the broad line profiles of the 11 sources. The only evidence provided by a slight asymmetry of [OIII]λ5007 and further observations of HILs such as CIVλ1549 would be needed to assess the extent of any mildly ionized outflow originating from the accretion disk.

In addition, the ongoing data reduction of an additional 25 extremely jetted quasars will be completed, and this will significantly enhance our sample size in terms of optical spectra and allow for a better understanding of the differences and similarities between RL and RQ quasars and the effect of the jet on the surrounding medium. As all these sources are selected based on the availability of UV data from the HST-FOS, a comparison between the CIVλ1549 and low ionization lines, like Hβ with a large sample size will allow measuring very different aspects of the broad line region as well as a very different relationship between these two components in RQ and RL quasars.

Finally, we also plan to include variability studies by monitoring the sources over time, to get information that can shed light on the timescales of physical processes occurring within the quasar, and the variability of outflows.

These future research endeavors will provide valuable insights into the complex nature of different types of quasars and contribute significantly to our overall understanding of these sources.

References

Abramowicz, M. A. (2005). Super-Eddington black hole accretion: Polish doughnuts and slim disks. In Merloni, A., Nayakshin, S., and Sunyaev, R. A., editors, *Growing Black Holes: Accretion in a Cosmological Context*, pages 257–273.

Abramowicz, M. A. et al. (1988). Slim Accretion Disks. *ApJ*, 332:646.

Abramowicz, M. A. and Fragile, P. C. (2013). Foundations of Black Hole Accretion Disk Theory. *Living Reviews in Relativity*, 16(1):1.

Abramowicz, M. A. and Straub, O. (2014). Accretion discs. *Scholarpedia*, 9:2408.

Aihara, H. et al. (2011). The Eighth Data Release of the Sloan Digital Sky Survey: First Data from SDSS-III. *ApJS*, 193(2):29.

Alloin, D. et al. (1988). Evidence for an accretion disc in AKN 120. *A&A*, 200:17–20.

Antonucci, R. (1993). Unified models for active galactic nuclei and quasars. *ARA&A*, 31:473–521.

Antonucci, R. (2012). A panchromatic review of thermal and nonthermal active galactic nuclei. *Astronomical and Astrophysical Transactions*, 27(4):557–602.

Antonucci, R. R. J. (1984). A statistical study of the properties of radio galaxies. *ApJ*, 281:112–125.

Antonucci, R. R. J. and Miller, J. S. (1985). Spectropolarimetry and the nature of NGC 1068. *ApJ*, 297:621–632.

Araudo, A. T. et al. (2010). Gamma rays from cloud penetration at the base of AGN jets. *A&A*, 522:A97.

Armitage, P. J. (2004). Theory of Disk Accretion onto Supermassive Black Holes. In Barger, A. J., editor, *Supermassive Black Holes in the Distant Universe*, volume 308 of *Astrophysics and Space Science Library*, page 89.

Arshakian, T. G. et al. (2010). Radio-optical scrutiny of compact AGN: correlations between properties of pc-scale jets and optical nuclear emission. *A&A*, 520:A62.

Assef, R. J. et al. (2011). Black Hole Mass Estimates Based on C IV are Consistent with Those Based on the Balmer Lines. *ApJ*, 742(2):93.

Azadi, M. (2017). *Multi-Wavelength Analysis of Active Galactic Nuclei and Host Galaxies Physical Properties*. PhD thesis, University of California, San Diego.

Bachev, R. et al. (2004). Average Ultraviolet Quasar Spectra in the Context of Eigenvector 1: A Baldwin Effect Governed by the Eddington Ratio? *ApJ*, 617(1):171–183.

Balbus, S. A. and Hawley, J. F. (1998). Instability, turbulence, and enhanced transport in accretion disks. *Reviews of Modern Physics*, 70(1):1–53.

Ballo, L. et al. (2012). Exploring X-ray and radio emission of type 1 AGN up to z ∼2.3. *A&A*, 545:A66.

Baloković, M. et al. (2012). Disclosing the Radio Loudness Distribution Dichotomy in Quasars: An Unbiased Monte Carlo Approach Applied to the SDSS-FIRST Quasar Sample. *ApJ*, 759(1):30.

Baloković, M. et al. (2021). Properties of the Obscuring Torus in NGC 1052 from Multiepoch Broadband X-Ray Spectroscopy. *ApJ*, 916(2):90.

Bannikova, E. Y. and Sergeyev, A. V. (2017). Dynamics and formation of obscuring tori in AGNs. *Frontiers in Astronomy and Space Sciences*, 4:60.

Banse, K. (2003). The Munich Image Data Analysis System. In Heck, A., editor, *Information Handling in Astronomy - Historical Vistas*, volume 285 of *Astrophysics and Space Science Library*, page 89.

Banse, K. et al. (1983). MIDAS - Eso's New Image Processing System. *The Messenger*, 31:26.

Bao, D.-W. et al. (2022). Monitoring AGNs with Hβ Asymmetry. III. Long-term Reverberation Mapping Results of 15 Palomar-Green Quasars. *ApJS*, 262(1):14.

Barker, B. M. and O'Connell, R. F. (1975). Relativistic effects in the binary pulsar PSR 1913+16. *ApJL*, 199:L25.

Barrado, D. et al. (2011). The Calar Alto Observatory: current status and future instrumentation. In Zapatero Osorio, M. R., Gorgas, J., Maíz Apellániz, J., Pardo, J. R., and Gil de Paz, A., editors, *Highlights of Spanish Astrophysics VI*, pages 637–646.

Barrows, R. S. et al. (2011). Unusual double-peaked emission in the SDSS quasar J093201.60 + 031858.7. *ARA&A*, 16(2):122–127.

Barth, A. J. et al. (2013). The Lick AGN Monitoring Project 2011: Fe II Reverberation from the Outer Broad-line Region. *ApJ*, 769(2):128.

Baskin, A. and Laor, A. (2005). What controls the CIV line profile in active galactic nuclei? *MNRAS*, 356(3):1029–1044.

Becker, R. H. et al. (1991). A New Catalog of 53,522 4.85 GHz Sources. *ApJS*, 75:1.

Becker, R. H. et al. (1995). The FIRST Survey: Faint Images of the Radio Sky at Twenty Centimeters. *ApJ*, 450:559.

Beckmann, V. and Shrader, C. R. (2012). *Active Galactic Nuclei*.

Begelman, M. C. et al. (1980). Massive black hole binaries in active galactic nuclei. *Nature*, 287(5780):307–309.

Begelman, M. C. et al. (1984). Theory of extragalactic radio sources. *Reviews of Modern Physics*, 56(2):255–351.

Begelman, M. C. and Meier, D. L. (1982). Thick accretion disks - Self-similar, supercritical models. *ApJ*, 253:873–896.

Bennert, N. et al. (2006). Size and properties of the narrow-line region in Seyfert-1 galaxies from spatially-resolved optical spectroscopy. *A&A*, 459(1):55–69.

Bensch, K. et al. (2015). Measures of the Soft X-ray Excess as an Eigenvector 1 Parameter for Active Galactic Nuclei. *Journal of Astrophysics and Astronomy*, 36(4):467–474.

Bentz, M. C. et al. (2013). The Low-luminosity End of the Radius-Luminosity Relationship for Active Galactic Nuclei. *ApJ*, 767(2):149.

Berton, M. et al. (2017). An orientation-based unification of young jetted active galactic nuclei: the case of 3C 286. *Frontiers in Astronomy and Space Sciences*, 4:8.

Best, P. N. and Heckman, T. M. (2012). On the fundamental dichotomy in the local radio-AGN population: accretion, evolution and host galaxy properties. *MNRAS*, 421(2):1569–1582.

Bevington, P. R. and Robinson, D. K. (2003). *Data reduction and error analysis for the physical sciences*.

Bhatta, G. et al. (2018). Signatures of the Disk-Jet Coupling in the Broad-line Radio Quasar 4C+74.26. *ApJ*, 866(2):132.

Bian, W.-H. et al. (2007). Active Galactic Nuclei with Double-Peaked Balmer Lines. I. Black Hole Masses and Eddington Ratios. *ApJ*, 668(2):721–729.

Bianchi, S. et al. (2012). AGN Obscuration and the Unified Model. *Advances in Astronomy*, 2012:782030.

Binney, J. et al. (2000). Galactic Astronomy. *American Journal of Physics*, 68(1):95–96.

Blandford, R. et al. (2019). Relativistic Jets from Active Galactic Nuclei. *ARA&A*, 57:467–509.

Blandford, R. D. and Königl, A. (1979). Relativistic jets as compact radio sources. *ApJ*, 232:34–48.

Blandford, R. D. and McKee, C. F. (1982). Reverberation mapping of the emission line regions of Seyfert galaxies and quasars. *ApJ*, 255:419–439.

Blandford, R. D. and Payne, D. G. (1982). Hydromagnetic flows from accretion disks and the production of radio jets. *MNRAS*, 199:883–903.

Blandford, R. D. and Znajek, R. L. (1977). Electromagnetic extraction of energy from Kerr black holes. *MNRAS*, 179:433–456.

Bloom, J. S. et al. (2009). Observations of the Naked-Eye GRB 080319B: Implications of Nature's Brightest Explosion. *ApJ*, 691(1):723–737.

Boccardi, B. et al. (2017). Radio observations of active galactic nuclei with mm-VLBI. *A&A*, 25(1):4.

Boccardi, B. et al. (2021). Accretion mode and jet collimation in active galactic nuclei. *Astronomische Nachrichten*, 342(1071):1071–1076.

Bon, E. et al. (2009). Contribution of a disc component to single-peaked broad lines of active galactic nuclei. *MNRAS*, 400(2):924–936.

Bon, N. et al. (2015). Gravitational redshift of emission lines in the AGN spectra. *Ap&SS*, 360:7.

Bon, N. et al. (2020). Selection of highly-accreting quasars. Spectral properties of Fe II_{opt} emitters not belonging to extreme Population A. *A&A*, 635:A151.

Bornancini, C. and García Lambas, D. (2018). Active galactic nuclei at high redshifts: properties and environment of Type 1 and 2 AGNs. *MNRAS*, 479(2):2308–2317.

Boroson, T. A. (2002). Black Hole Mass and Eddington Ratio as Drivers for the Observable Properties of Radio-loud and Radio-quiet QSOs. *ApJ*, 565(1):78–85.

Boroson, T. A. and Green, R. F. (1992a). The Emission-Line Properties of Low-Redshift Quasi-stellar Objects. *ApJS*, 80:109.

Boroson, T. A. and Green, R. F. (1992b). The emission-line properties on low-redshift QSOs: What physical parameters drive the observed properties? In Holt, S. S., Neff, S. G., and Urry, C. M., editors, *Testing the AGN paradigm*, volume 254 of *American Institute of Physics Conference Series*, pages 584–587. AIP.

Bower, G. A. et al. (1996). Double-Peaked Broad Emission Lines in the Nucleus of M81. *AJ*, 111:1901.

Boyle, W. and Smith, G. (1970). Charge Coupled Semiconductor Devices. *Bell System Technical Journal*, 49:587–593.

Bridle, A. H. et al. (1994). Deep VLA Imaging of Twelve Extended 3CR Quasars. *AJ*, 108:766.

Bruhweiler, F. and Verner, E. (2008). Modeling Fe II Emission and Revised Fe II (UV) Empirical Templates for the Seyfert 1 Galaxy I Zw 1. *ApJ*, 675(1):83–95.

Burenkov, A. N. et al. (2001). Double-peaked broad-line Hβ profiles of 3C390.3 FROM 1995-99. II. the accretion disk model. *Astronomical and Astrophysical Transactions*, 20(2):353–355.

Buttiglione, S. et al. (2010). An optical spectroscopic survey of the 3CR sample of radio galaxies with z < 0.3 . II. Spectroscopic classes and accretion modes in radio-loud AGN. *A&A*, 509:A6.

Caccianiga, A. et al. (2024). Obscuration in high-redshift jetted quasi-stellar objects. *A&A*, 684:A98.

Cackett, E. M. et al. (2021). Reverberation mapping of active galactic nuclei: from X-ray corona to dusty torus. *iScience*, 24(6):102557.

Calderone, G. et al. (2017). QSFIT: automatic analysis of optical AGN spectra. *MNRAS*, 472(4):4051–4080.

Carpenter, J. et al. (2020). The ALMA Development Program: Roadmap to 2030. *arXiv e-prints*, page arXiv:2001.11076.

Carroll, B. W. and Ostlie, D. A. (2017). *An introduction to modern astrophysics, Second Edition*.

Cattaneo, A. (2001). Quasars and galaxy formation. *MNRAS*, 324(1):128–140.

Cavagnolo, K. W. et al. (2010). A Relationship Between AGN Jet Power and Radio Power. *ApJ*, 720(2):1066–1072.

Cavanagh, M. K. et al. (2021). Morphological classification of galaxies with deep learning: comparing 3-way and 4-way CNNs. *MNRAS*, 506(1):659–676.

Chakraborty, A. and Bhattacharjee, A. (2021). Black hole mass, jet, and accretion disk connection: An analysis of radio loud and radio quiet quasars. *Astronomische Nachrichten*, 342(1-2):142–146.

Chakraborty, A. et al. (2022). Radio dichotomy in quasars with H β FWHM greater than 15 000 km s^{-1}. *MNRAS*, 516(2):2824–2832.

Chamani, W. et al. (2021). Testing the magnetic flux paradigm for AGN radio loudness with a radio-intermediate quasar. *A&A*, 652:A14.

Chambers, K. C. et al. (2016). The Pan-STARRS1 Surveys. *arXiv e-prints*, page arXiv:1612.05560.

Chavushyan, V. et al. (2020). Flare-like Variability of the Mg II λ2798 Å Emission Line and UV Fe II Band in the Blazar CTA 102. *ApJ*, 891(1):68.

Chen, K. et al. (1997). Polarization of Line Emission from an Accretion Disk and Application to Arp 102B. *ApJ*, 483(1):194–199.

Chen, K. and Halpern, J. P. (1989). Structure of Line-emitting Accretion Disks in Active Galactic Nuclei: ARP 102B. *ApJ*, 344:115.

Chen, K. and Halpern, J. P. (1990). Spectropolarimetric Test of the Relativistic Disk Model for the Broad Emission Lines of Active Galactic Nuclei. *ApJL*, 354:L1.

Chen, Y. C. (2021). Classifying Seyfert Galaxies with Deep Learning. *ApJS*, 256(2):34.

Chen, Y. C. and Hwang, C. Y. (2018). Morphology of Seyfert Galaxies. *Astronomy Reports*, 62(12):853–858.

Chevalier, R. A. (1998). Synchrotron Self-Absorption in Radio Supernovae. *ApJ*, 499(2):810–819.

Chiaberge, M. and Marconi, A. (2011). On the origin of radio loudness in active galactic nuclei and its relationship with the properties of the central supermassive black hole. *MNRAS*, 416(2):917–926.

Chornock, R. et al. (2010). The Quasar SDSS J1536+0441: An Unusual Double-peaked Emitter. *ApJL*, 709(1):L39–L43.

Cirasuolo, M. et al. (2003a). Is there a dichotomy in the radio loudness distribution of quasars? *MNRAS*, 346(2):447–455.

Cirasuolo, M. et al. (2003b). The radio-loud/radio-quiet dichotomy: news from the 2dF QSO Redshift Survey. *MNRAS*, 341(3):993–1004.

Cohen, M. H. et al. (2007). Relativistic Beaming and the Intrinsic Properties of Extragalactic Radio Jets. *ApJ*, 658(1):232–244.

Colina, L. et al. (1991). IRAS 02366-3101: an Accretion Disk Candidate among Luminous IRAS Galaxies. *ApJL*, 382:L63.

Collin, S. (2007). Uncertainties of the masses of black holes and Eddington ratios in AGN. In Karas, V. and Matt, G., editors, *Black Holes from Stars to Galaxies – Across the Range of Masses*, volume 238, pages 111–116.

Collin, S. et al. (2006). Systematic effects in measurement of black hole masses by emission-line reverberation of active galactic nuclei: Eddington ratio and inclination. *A&A*, 456(1):75–90.

Collin, S. and Zahn, J.-P. (1999). Star formation and evolution in accretion disks around massive black holes. *A&A*, 344:433–449.

Collin-Souffrin, S. and Dumont, A. M. (1990). Line and continuum emission from the outer regions of accretion discs in active galactic nuclei. II. Radial structure of the disc. *A&A*, 229:292–301.

Collin-Souffrin, S. et al. (1988). The environment of active galactic nuclei - I. A two-component broad emission line model. *MNRAS*, 232:539–550.

Condon, J. J. (1992). Radio emission from normal galaxies. *ARA&A*, 30:575–611.

Condon, J. J. et al. (1998). The NRAO VLA Sky Survey. *AJ*, 115(5):1693–1716.

Conselice, C. J. (2006). The fundamental properties of galaxies and a new galaxy classification system. *MNRAS*, 373(4):1389–1408.

Couto, G. S. and Storchi-Bergmann, T. (2023). The Interplay between Radio AGN Activity and Their Host Galaxies. *Galaxies*, 11(2):47.

Coziol, R. et al. (2017). What sparks the radio-loud phase of nearby quasars? *MNRAS*, 466(1):921–944.

Cresci, G. et al. (2015). The MAGNUM survey: positive feedback in the nuclear region of NGC 5643 suggested by MUSE. *A&A*, 582:A63.

Croom, S. M. et al. (2004). The 2dF QSO Redshift Survey - XII. The spectroscopic catalogue and luminosity function. *MNRAS*, 349(4):1397–1418.

Czerny, B. (2017). Quasars in cosmology. In *From the Dolomites to the Event Horizon: Sledging Down the Black Hole Potential*, page 13.

Czerny, B. (2019). Slim Accretion Disks: Theory and Observational Consequences. *Universe*, 5(5):131.

Czerny, B. et al. (2023a). Accretion disks, quasars and cosmology: meandering towards understanding. *Ap&SS*, 368(2):8.

Czerny, B. et al. (2023b). Dusty plasma in active galactic nuclei. *European Physical Journal D*, 77(4):56.

Czerny, B. and Hryniewicz, K. (2011). The origin of the broad line region in active galactic nuclei. *A&A*, 525:L8.

Dai, J. L. et al. (2021). The Physics of Accretion Discs, Winds and Jets in Tidal Disruption Events. *SSR*, 217(1):12.

Davies, R. I. et al. (2015). Insights on the Dusty Torus and Neutral Torus from Optical and X-Ray Obscuration in a Complete Volume Limited Hard X-Ray AGN Sample. *ApJ*, 806(1):127.

de Gouveia Dal Pino et al. (2010). On the role of magnetic reconnection in jet/accretion disk systems. *Highlights of Astronomy*, 15:247–248.

Decarli, R. et al. (2008). On the geometry of broad emission region in quasars. In Lanteri, L., Raiteri, C. M., Capetti, A., and Rossi, P., editors, *8th National Conference on AGN*, page 14.

Decarli, R. et al. (2011). Geometry and inclination of the broad-line region in blazars. *MNRAS*, 413(1):39–46.

Deconto-Machado, A. et al. (2022). Optical and UV properties of a radio-loud and a radio-quiet Population A quasar at high redshift. *Astronomische Nachrichten*, 343(1-2):e210084.

Dessauges-Zavadsky, M. et al. (2000). Spectral classification of emission-line galaxies. *A&A*, 355:89–98.

Di Matteo, T., Springel, V., and Hernquist, L. (2005). Energy input from quasars regulates the growth and activity of black holes and their host galaxies. *Nature*, 433(7026):604–607.

Dietrich, M. (1998). The Broad-Line Region Cloud Model. In *Astronomische Gesellschaft Abstract Series*, Astronomische Gesellschaft Abstract Series, page 61.

Dietrich, M. et al. (2002). Continuum and Emission-Line Strength Relations for a Large Active Galactic Nuclei Sample. *ApJ*, 581(2):912–924.

Dihingia, I. K. and Vaidya, B. (2022). Properties of the accretion disc, jet and disc-wind around Kerr black hole. *Journal of Astrophysics and Astronomy*, 43(1):23.

Dimitrijević, M. S. et al. (2007). The flux ratio of the [OIII] $\lambda\lambda$5007, 4959 lines in AGN: comparison with theoretical calculations. *MNRAS*, 374(3):1181–1184.

Dojčinović, I. et al. (2023). The flux ratio of the [N II] $\lambda\lambda$ 6548, 6583 Å lines in sample of Active Galactic Nuclei Type 2. *Advances in Space Research*, 71(2):1219–1226.

Done, C. et al. (2012). Intrinsic disc emission and the soft X-ray excess in active galactic nuclei. *MNRAS*, 420(3):1848–1860.

D'Onofrio, M. et al. (2012). *Fifty years of quasars: from early observations and ideas to future research*, volume 386. Springer Science & Business Media.

D'Onofrio, M. and Marziani, P. (2018). A multimessenger view of galaxies and quasars from now to mid-century. *Frontiers in Astronomy and Space Sciences*, 5:31.

Du, P. et al. (2018). Supermassive Black Holes with High Accretion Rates in Active Galactic Nuclei. IX. 10 New Observations of Reverberation Mapping and Shortened Hβ Lags. *ApJ*, 856(1):6.

Dultzin, D. et al. (2020). Extreme quasars as distance indicators in cosmology. *Frontiers in Astronomy and Space Sciences*, 6:80.

Dunlop, J. S. et al. (1989). The Parkes selected regions : deep optical and infrared observations of radio galaxies and quasars at high redshifts. *MNRAS*, 238:1171–1231.

Dunlop, J. S. et al. (2003). Quasars, their host galaxies and their central black holes. *MNRAS*, 340(4):1095–1135.

Ehler, H. J. S. et al. (2018). Exploring the spectral variability of the Seyfert 1.5 galaxy Markarian 530 with Suzaku. *MNRAS*, 478(3):4214–4224.

Ekers, J. A. (1969). The Parkes catalogue of radio sources, declination zone +20 to -90 . *Australian Journal of Physics Astrophysical Supplement*, 7:3–75.

Elitzur, M. (2008). The toroidal obscuration of active galactic nuclei. *NAR*, 52(6):274–288.

Elitzur, M. et al. (2004). IR emission from AGNs. In Aalto, S., Huttemeister, S., and Pedlar, A., editors, *The Neutral ISM in Starburst Galaxies*, volume 320 of *Astronomical Society of the Pacific Conference Series*, page 242.

Elitzur, M. and Shlosman, I. (2006). The AGN-obscuring Torus: The End of the "Doughnut" Paradigm? *ApJL*, 648(2):L101–L104.

Elmegreen, B. G. and Elmegreen, D. M. (2005). Stellar Populations in 10 Clump-Cluster Galaxies of the Hubble Ultra Deep Field. *ApJ*, 627(2):632–646.

Elsmore, B. and Mackay, C. D. (1969). Observations of the structure of radio sources in the 3C catalogue-III. The absolute determination of positions of 78 compact sources. *MNRAS*, 146:361.

Eracleous, M. (1998). The quest for the dynamical signature of accretion disks in active galactic nuclei. *Advances in Space Research*, 21(1-2):33–45.

Eracleous, M. (1999). Double-Peaked Emission Lines and Their Implications for the Dynamics of the Line-Emitting Gas in Radio-Loud Active Galaxies. In Gaskell, C. M., Brandt, W. N., Dietrich, M., Dultzin-Hacyan, D., and Eracleous, M., editors, *Structure and Kinematics of Quasar Broad Line Regions*, volume 175 of *Astronomical Society of the Pacific Conference Series*, page 163.

Eracleous, M. et al. (1997). Rejection of the Binary Broad-Line Region Interpretation of Double-peaked Emission Lines in Three Active Galactic Nuclei. *ApJ*, 490(1):216–226.

Eracleous, M. et al. (2004). The ultraviolet spectra of active galaxies with double-peaked emission lines. In Storchi-Bergmann, T., Ho, L. C., and Schmitt, H. R., editors, *The Interplay Among Black Holes, Stars and ISM in Galactic Nuclei*, volume 222, pages 29–32.

Eracleous, M. et al. (2009). Double-peaked emission lines as a probe of the broad-line regions of active galactic nuclei. *NAR*, 53(7-10):133–139.

Eracleous, M. and Halpern, J. P. (1994). Double-peaked Emission Lines in Active Galactic Nuclei. *ApJS*, 90:1.

Eracleous, M. and Halpern, J. P. (2003). Completion of a Survey and Detailed Study of Double-peaked Emission Lines in Radio-loud Active Galactic Nuclei. *ApJ*, 599(2):886–908.

Event Horizon Telescope Collaboration et al. (2019). First M87 Event Horizon Telescope Results. I. The Shadow of the Supermassive Black Hole. *ApJL*, 875(1):L1.

Ewart, P. (2019). *Atomic Physics*.

Falanga, M. et al. (2015). *The Physics of Accretion onto Black Holes*.

Falocco, S. et al. (2020). Accretion and jets in a low-luminosity AGN: the nucleus of NGC 1052. *A&A*, 638:A67.

Fanaroff, B. L. and Riley, J. M. (1974). The morphology of extragalactic radio sources of high and low luminosity. *MNRAS*, 167:31P–36P.

Fanidakis, N. et al. (2012). The evolution of active galactic nuclei across cosmic time: what is downsizing? *MNRAS*, 419(4):2797–2820.

Fedorova, E. et al. (2022). Non-Thermal Emission from Radio-Loud AGN Jets: Radio vs. X-rays. *Galaxies*, 10(1):6.

Feltre, A. et al. (2023). Optical and mid-infrared line emission in nearby Seyfert galaxies. *A&A*, 675:A74.

Ferland, G. J. et al. (1992). Anisotropic Line Emission and the Geometry of the Broad-Line Region in Active Galactic Nuclei. *ApJ*, 387:95.

Fernini, I. et al. (1991). Depolarization Asymmetry in the Quasar 3C 47. *ApJ*, 381:63.

Ferrarese, L. and Ford, H. (2005). Supermassive Black Holes in Galactic Nuclei: Past, Present and Future Research. *SSR*, 116(3-4):523–624.

Fischer, T. C. et al. (2023). No Small-scale Radio Jets Here: Multiepoch Observations of Radio Continuum Structures in NGC 1068 with the VLBA. *ApJ*, 953(1):87.

Foreman-Mackey, D. et al. (2013). emcee: the mcmc hammer. *Publications of the Astronomical Society of the Pacific*, 125(925):306.

Foschini, L. (2018). Jetted Active Galactic Nuclei. In *AGN13: Beauty and the Beast*, volume 13, page 11.

Foschini, L. (2020). Seyfert Galaxies Astrophysics. *Universe*, 6(8):126.

Foschini, L. (2022). The physics of relativistic jets. *Frontiers in Astronomy and Space Sciences*, 8:234.

Foschini, L. et al. (2024). The power of relativistic jets: a comparative study. *arXiv e-prints*, page arXiv:2403.17581.

Fraix-Burnet, D. et al. (2017). The phylogeny of quasars and the ontogeny of their central black holes. *Frontiers in Astronomy and Space Sciences*, 4:1.

Francis, P. J. et al. (1991). A High Signal-to-Noise Ratio Composite Quasar Spectrum. *ApJ*, 373:465.

Fritz, J., Franceschini, A., and Hatziminaoglou, E. (2006). Revisiting the infrared spectra of active galactic nuclei with a new torus emission model. *MNRAS*, 366(3):767–786.

Fromerth, M. J. and Melia, F. (2001). The Formation of Broad-Line Clouds in the Accretion Shocks of Active Galactic Nuclei. *ApJ*, 549(1):205–214.

Fu, Y. et al. (2023). A complete catalogue of broad-line AGNs and double-peaked emission lines from MaNGA integral-field spectroscopy of 10K galaxies: stellar population of AGNs, supermassive black holes, and dual AGNs. *MNRAS*, 524(4):5827–5843.

Gabuzda, D. C. (2015). Parsec-Scale Jets in Active Galactic Nuclei. In Contopoulos, I., Gabuzda, D., and Kylafis, N., editors, *The Formation and Disruption of Black Hole Jets*, volume 414 of *Astrophysics and Space Science Library*, page 117.

Ganci, V. et al. (2019). Radio loudness along the quasar main sequence. *A&A*, 630:A110.

Gao, F. et al. (2020). Mergers trigger active galactic nuclei out to z $\sim$ 0.6. *A&A*, 637:A94.

García-Bernete, I. et al. (2024). The Galaxy Activity, Torus, and Outflow Survey (GATOS). III. Revealing the inner icy structure in local active galactic nuclei. *A&A*, 681:L7.

Gardner, J. P. et al. (2023). The James Webb Space Telescope Mission. *PASP*, 135(1048):068001.

Garofalo, D. et al. (2014). Constraints on the radio-loud/radio-quiet dichotomy from the Fundamental Plane. *MNRAS*, 442(4):3097–3104.

Garrido, J. et al. (2023). Status of the SKA project and the SKA Regional Centre Network. In Manteiga, M., Bellot, L., Benavidez, P., de Lorenzo-Cáceres, A., Fuente, M. A., Martínez, M. J., Vázquez Acosta, M., and Dafonte, C., editors, *Highlights on Spanish Astrophysics XI*, page 360.

Gaskell, C. M. (1983). Quasars as supermassive binaries. In Swings, J.-P., editor, *Liege International Astrophysical Colloquia*, volume 24 of *Liege International Astrophysical Colloquia*, pages 473–477.

Gaskell, C. M. (1996). Evidence for Binary Orbital Motion of a Quasar Broad-Line Region. *ApJL*, 464:L107.

Gaskell, C. M. et al. (2022). Estimating reddening of the continuum and broad-line region of active galactic nuclei: the mean reddening of NGC 5548 and the size of the accretion disc. *arXiv e-prints*, page arXiv:2208.11437.

Gasparini, A. (2022). Hubble Find Provides Key to Early Supermassive Black Holes. *Physics Online Journal*, 15:64.

George, I. M. and Fabian, A. C. (1991). X-ray reflection from cold matter in Active Galactic Nuclei and X-ray binaries. *MNRAS*, 249:352.

Gezari, S. et al. (2007). Long-Term Profile Variability of Double-peaked Emission Lines in Active Galactic Nuclei. *ApJS*, 169(2):167–212.

Ghisellini, G. et al. (2011). The transition between BL Lac objects and flat spectrum radio quasars. *MNRAS*, 414(3):2674–2689.

Giustini, M. et al. (2011). Variable X-ray absorption in the mini-BAL QSO PG 1126-041. *A&A*, 536:A49.

Giustini, M. and Proga, D. (2019). A global view of the inner accretion and ejection flow around super massive black holes. Radiation-driven accretion disk winds in a physical context. *A&A*, 630:A94.

Goad, M. and Wanders, I. (1996). The Effect of a Variable Anisotropic Continuum Source upon the Broad Emission Line Profiles and Responses. *ApJ*, 469:113.

Goad, M. R. et al. (2012). The broad emission-line region: the confluence of the outer accretion disc with the inner edge of the dusty torus. *MNRAS*, 426(4):3086–3111.

González Delgado, R. M. et al. (2016). Star formation along the Hubble sequence. Radial structure of the star formation of CALIFA galaxies. *A&A*, 590:A44.

Goodman, J. and Weare, J. (2010). Ensemble samplers with affine invariance. *Communications in Applied Mathematics and Computational Science*, 5(1):65–80.

Grafton-Waters, S. (2020). A deeper look at the Seyfert 2 NGC 5643. XMM-Newton Proposal ID #88441.

Graham, A. W. et al. (2011). An expanded M_{bh}-σ diagram, and a new calibration of active galactic nuclei masses. *MNRAS*, 412(4):2211–2228.

Grandi, S. A. (1982). The 3000 A bump in quasars. *ApJ*, 255:25–38.

Gravity Collaboration et al. (2023). Toward measuring supermassive black hole masses with interferometric observations of the dust continuum. *A&A*, 669:A14.

Gredel, R. (2001). The Calar Alto Observatory — present and future instrumentation. *NAR*, 45(1-2):33–36.

Greene, J. E. and Ho, L. C. (2005). Estimating Black Hole Masses in Active Galaxies Using the Hα Emission Line. *ApJ*, 630(1):122–129.

Greenstein, J. L. (1978). The HR Diagram. In Philip, A. G. D. and Hayes, D. S., editors, *The HR Diagram - The 100th Anniversary of Henry Norris Russell*, volume 80, page 101.

Grier, C. et al. (2014). The Broad Line Region in AGNs: Structure, Physics, and the f Factor. In *American Astronomical Society Meeting Abstracts #223*, volume 223 of *American Astronomical Society Meeting Abstracts*, page 126.03.

Grueff, G., Vigotti, M., and Spinrad, H. (1980). Optical identifications and redshifts of faint radiogalaxies from theB2 catalogue. *A&A*, 86:50–54.

Gu, W.-M. and Lu, J.-F. (2007). A Note on the Slim Accretion Disk Model. *ApJ*, 660(1):541–545.

Gürkan, G. et al. (2015). Herschel-ATLAS: the connection between star formation and AGN activity in radio-loud and radio-quiet active galaxies. *MNRAS*, 452(4):3776–3794.

Hada, K. (2019). Relativistic Jets from AGN Viewed at Highest Angular Resolution. *Galaxies*, 8(1):1.

Halpern, J. and Filippenko, A. (1992). Double-peaked line profiles in AGNs testing for supermassive binary black holes. In Holt, S. S., Neff, S. G., and Urry, C. M., editors, *Testing the AGN paradigm*, volume 254 of *American Institute of Physics Conference Series*, pages 57–60.

Halpern, J. P. (1990). Line Emission from Another Relativistic Accretion Disk: 3C 332. *ApJL*, 365:L51.

Halpern, J. P. and Eracleous, M. (1999). The Mysterious, Dust-Free, X-Ray Absorber in ARP 102B. In *American Astronomical Society Meeting Abstracts #194*, volume 194 of *American Astronomical Society Meeting Abstracts*, page 34.03.

Halpern, J. P. et al. (1996). Hubble Space Telescope Ultraviolet Spectrum of ARP 102B, the Prototypical Double-peaked Emission-Line AGN. *ApJ*, 464:704.

Halpern, J. P. and Filippenko, A. V. (1988). A test of the massive binary black hole hypothesis: Arp 102B. *Nature*, 331(6151):46–48.

Hao, H. et al. (2014). Inter-comparison of Radio-Loudness Criteria for Type 1 AGNs in the XMM-COSMOS Survey. *arXiv e-prints*, page arXiv:1408.1090.

Harlaftis, E. T. (2001). Applications of Indirect Imaging Techniques in X-ray Binaries. In Boffin, H. M. J., Steeghs, D., and Cuypers, J., editors, *Astrotomography, Indirect Imaging Methods in Observational Astronomy*, volume 573, page 359.

Harrison, C. M. et al. (2018). AGN outflows and feedback twenty years on. *Nature Astronomy*, 2:198–205.

Hartley, P. et al. (2019). Strong lensing reveals jets in a sub-microJy radio-quiet quasar. *MNRAS*, 485(3):3009–3023.

Heckman, T. M. (1980). An Optical and Radio Survey of the Nuclei of Bright Galaxies - Activity in the Normal Galactic Nuclei. *A&A*, 87:152.

Heckman, T. M. and Best, P. N. (2014). The Coevolution of Galaxies and Supermassive Black Holes: Insights from Surveys of the Contemporary Universe. *ARA&A*, 52:589–660.

Hennawi, J. F. et al. (2006). Binary Quasars in the Sloan Digital Sky Survey: Evidence for Excess Clustering on Small Scales. *AJ*, 131(1):1–23.

Hermosa Muñoz, L. et al. (2024). A biconical ionised gas outflow and evidence for positive feedback in NGC 7172 uncovered by MIRI/JWST. *arXiv e-prints*, page arXiv:2407.15807.

Hernández-García, L. et al. (2016). Unveiling the Physics of Low-luminosity AGNs through X-Ray Variability: LINER versus Seyfert 2. *ApJ*, 824(1):7.

Hernitschek, N. et al. (2016). Finding, characterizing and classifying variable sources in multi-epoch sky surveys: QSOs and RR Lyraes in PS1 3Pi. *CoKon*, 105:85–92.

Higginbottom, N. et al. (2024). State-of-the-art simulations of line-driven accretion disc winds: realistic radiation hydrodynamics leads to weaker outflows. *MNRAS*, 527(3):9236–9249.

Hippler, S. et al. (2000). ALFA: three years of experience in adaptive optics with a laser guide star. In Wizinowich, P. L., editor, *Adaptive Optical Systems Technology*, volume 4007 of *Society of Photo-Optical Instrumentation Engineers (SPIE) Conference Series*, pages 41–49.

Ho, L. and Kormendy, J. (2000). Supermassive Black Holes in Active Galactic Nuclei. In Murdin, P., editor, *Encyclopedia of Astronomy and Astrophysics*, page 2365.

Ho, L. C. (2008). Nuclear activity in nearby galaxies. *ARA&A*, 46:475–539.

Ho, L. C. et al. (2000). Double-peaked Broad Emission Lines in NGC 4450 and Other LINERS. *ApJ*, 541(1):120–125.

Ho, L. C. and Kim, M. (2015). A Revised Calibration of the Virial Mass Estimator for Black Holes in Active Galaxies Based on Single-epoch Hβ Spectra. *ApJ*, 809(2):123.

Hocuk, S. and Barthel, P. D. (2010). The asymmetric radio structure and record jet of giant quasar 4C 34.47. *A&A*, 523:A9.

Hönig, S. F. (2019). Redefining the Torus: A Unifying View of AGNs in the Infrared and Submillimeter. *ApJ*, 884(2):171.

Hopkins, P. F. et al. (2005). Black Holes in Galaxy Mergers: Evolution of Quasars. *ApJ*, 630(2):705–715.

Hopkins, P. F. et al. (2012). The origins of active galactic nuclei obscuration: the 'torus' as a dynamical, unstable driver of accretion. *MNRAS*, 420(1):320–339.

Hopkins, P. F. and Hernquist, L. (2009). A Characteristic Division Between the Fueling of Quasars and Seyferts: Five Simple Tests. *ApJ*, 694(1):599–609.

Horne, K. (1998). Lessons from accretion disks in cataclysmic variables. In Holt, S. S. and Kallman, T. R., editors, *Accretion processes in Astrophysical Systems: Some like it hot! - eigth AstroPhysics Conference*, volume 431 of *American Institute of Physics Conference Series*, pages 426–436.

Hossain, M. S. et al. (2023). Morphological Classification of Radio Galaxies using Semi-Supervised Group Equivariant CNNs. *Procedia Computer Science*, 222:601–612.

Howell, S. B. (2000). *Handbook of CCD Astronomy*.

Hung, T. et al. (2020). Double-peaked Balmer Emission Indicating Prompt Accretion Disk Formation in an X-Ray Faint Tidal Disruption Event. *ApJ*, 903(1):31.

Ivezić, Ž. et al. (2002). Optical and Radio Properties of Extragalactic Sources Observed by the FIRST Survey and the Sloan Digital Sky Survey. *AJ*, 124(5):2364–2400.

Jackson, N. and Browne, I. W. A. (2013). Quasar emission lines, radio structures and radio unification. *MNRAS*, 429(2):1781–1790.

Jaffe, W. et al. (2004). The central dusty torus in the active nucleus of NGC 1068. *Nature*, 429(6987):47–49.

Jauncey, D. L., editor (1977). *Radio astronomy and cosmology*, volume 74 of *IAU Symposium*.

Jha, V. K. et al. (2020). Properties of Broad and Narrow Line Seyfert galaxies selected from SDSS. *Communications of the Byurakan Astrophysical Observatory*, 67:219–226.

Jha, V. K. et al. (2023). Exploring the AGN Accretion Disks using Continuum Reverberation Mapping. *arXiv e-prints*, page arXiv:2307.16568.

Jiang, J. (2020). X-ray studies of the innermost regions of black-hole accretion. *The Observatory*, 140:73–74.

Jiang, L. et al. (2007). The Radio-Loud Fraction of Quasars is a Strong Function of Redshift and Optical Luminosity. *ApJ*, 656(2):680–690.

Jiang, Y.-F. et al. (2019). Super-Eddington Accretion Disks around Supermassive Black Holes. *ApJ*, 880(2):67.

Jiménez Andrade, E. F. (2015). A study of optical and radio properties of radio-loud AGN. Master's thesis, National Institute of Astrophysics, Optics and Electronics, Mexico.

Jin, C. et al. (2017). Super-Eddington QSO RX J0439.6-5311 - I. Origin of the soft X-ray excess and structure of the inner accretion flow. *MNRAS*, 468(3):3663–3681.

Johnson, K. E. (2004). Star formation, massive stars, and super star clusters in nearby galaxies. *NAR*, 48(11-12):1337–1347.

Jolliffe, I. T. and Cadima, J. (2016). Principal component analysis: a review and recent developments. *Philosophical Transactions of the Royal Society of London Series A*, 374(2065):20150202.

Jones, M. H. et al. (2015). *An Introduction to Galaxies and Cosmology*.

Jun, H. D. et al. (2017). The Most Massive Active Galactic Nuclei at $1 \lesssim z \lesssim 2$. *ApJ*, 838(1):41.

Kakkad, D. et al. (2018). Spatially resolved electron density in the narrow line region of $z < 0.02$ radio AGNs. *A&A*, 618:A6.

Kalfountzou, E. et al. (2014). Herschel-ATLAS: far-infrared properties of radio-loud and radio-quiet quasars. *MNRAS*, 442(2):1181–1196.

Kaspi, S. et al. (2000). Reverberation Measurements for 17 Quasars and the Size-Mass-Luminosity Relations in Active Galactic Nuclei. *ApJ*, 533(2):631–649.

Kauffmann, G. et al. (2003). The host galaxies of active galactic nuclei. *MNRAS*, 346(4):1055–1077.

Kawakatu, N. et al. (2009). On the Origin of Fanaroff-Riley Classification of Radio Galaxies: Deceleration of Supersonic Radio Lobes. *ApJL*, 697(2):L173–L176.

Keller, P. M. et al. (2024). The radio-loud fraction of quasars at $z > 6$. *MNRAS*, 528(4):5692–5702.

Kellermann, K. I. (2013). The discovery of quasars. *Bulletin of the Astronomical Society of India*, 41(1):1.

Kellermann, K. I. (2014). The discovery of quasars and its aftermath. *Journal of Astronomical History and Heritage*, 17(3):267–282.

Kellermann, K. I. et al. (1989). VLA Observations of Objects in the Palomar Bright Quasar Survey. *AJ*, 98:1195.

Kellermann, K. I. et al. (2016). Radio-loud and Radio-quiet QSOs. *ApJ*, 831(2):168.

Khachikian, E. Y. and Weedman, D. W. (1974). An atlas of Seyfert galaxies. *ApJ*, 192:581–589.

Khajenabi, F. (2015). On the dynamics of clouds in the broad-line region of AGNs with an ADAF atmosphere. *MNRAS*, 446(2):1848–1854.

Kim, C. et al. (2022). Determining Star Formation Rates of Active Galactic Nucleus Host Galaxies Based on SED Fitting with Submillimeter Data. *ApJ*, 928(1):73.

Kim, Y. S. (1997). Refined SIMPLEX Method for Data Fitting. In Hunt, G. and Payne, H., editors, *Astronomical Data Analysis Software and Systems VI*, volume 125 of *Astronomical Society of the Pacific Conference Series*, page 206.

Kimura, S. S. et al. (2017). Evolution of an accretion disc in binary black hole systems. *MNRAS*, 465(4):4406–4413.

Kollatschny, W. (2003). Accretion disk wind in the AGN broad-line region: Spectroscopically resolved line profile variations in Mrk 110. *A&A*, 407:461–472.

Komossa, S. et al. (2008). On the Nature of Seyfert Galaxies with High [O III] λ5007 Blueshifts. *ApJ*, 680(2):926–938.

Komossa, S. et al. (2024). The extremes of AGN variability: outbursts, deep fades, changing looks, exceptional spectral states, and semi-periodicities. *arXiv e-prints*, page arXiv:2408.00089.

Körding, E. G. et al. (2006). Accretion states and radio loudness in active galactic nuclei: analogies with X-ray binaries. *MNRAS*, 372(3):1366–1378.

Korista, K. et al. (1997). An Atlas of Computed Equivalent Widths of Quasar Broad Emission Lines. *ApJS*, 108(2):401–415.

Korista, K. T. et al. (1995). Steps toward Determination of the Size and Structure of the Broad-Line Region in Active Galactic Nuclei. VIII. an Intensive HST, IUE, and Ground-based Study of NGC 5548. *ApJS*, 97:285.

Kormendy, J. and Ho, L. C. (2013). Coevolution (Or Not) of Supermassive Black Holes and Host Galaxies. *ARA&A*, 51(1):511–653.

Koudmani, S. et al. (2023). A unified accretion disc model for supermassive black holes in galaxy formation simulations: method and implementation. *arXiv e-prints*, page arXiv:2312.08428.

Kovačević, J. et al. (2010). Analysis of Optical Fe II Emission in a Sample of Active Galactic Nucleus Spectra. *ApJS*, 189(1):15–36.

Kovačević, J. et al. (2014). A model for the Balmer pseudocontinuum in spectra of type 1 AGNs. *Advances in Space Research*, 54(7):1347–1354.

Kovačević-Dojčinović, J. et al. (2017). Black Hole Mass Estimation in the Type 1 AGN: H beta vs. Mg II lines and the role of Balmer continuum. *Frontiers in Astronomy and Space Sciences*, 4:7.

Kovačević-Dojčinović, J. et al. (2022). Tracing the outflow kinematics in Type 2 active galactic nuclei. *A&A*, 659:A130.

Kovačević-Dojčinović, J. and Popović, L. Č. (2015). The Connections Between the UV and Optical Fe ii Emission Lines in Type 1 AGNs. *ApJS*, 221(2):35.

Kozłowski, S. (2017). Virial Black Hole Mass Estimates for 280,000 AGNs from the SDSS Broadband Photometry and Single-epoch Spectra. *ApJS*, 228(1):9.

Kozłowski, S. (2021). A Survey Length for AGN Variability Studies. *Acta Astronaut*, 71(2):103–112.

Krause, M. G. H. et al. (2019). How frequent are close supermassive binary black holes in powerful jet sources? *MNRAS*, 482(1):240–261.

Kriss, G. (1994). Fitting models to uv and optical spectral data. In *Astronomical Data Analysis Software and Systems III*, volume 61, page 437.

Król, D. Ł. et al. (2023). On the Origin of the X-ray Emission in Heavily Obscured Compact Radio Sources. *arXiv e-prints*, page arXiv:2312.13418.

Kurk, J. D. et al. (2007). Black Hole Masses and Enrichment of z ∼6 SDSS Quasars. *ApJ*, 669(1):32–44.

Kuźmicz, A. et al. (2021). Giant Radio Quasars: Composite Optical Spectra. *ApJ*, 922(1):52.

Lacerda, E. A. D. et al. (2020). Galaxies hosting an active galactic nucleus: a view from the CALIFA survey. *MNRAS*, 492(3):3073–3090.

Lagos, C. D. P. et al. (2009). Black hole spin and radio loudness in a Λ cold dark matter universe. *MNRAS*, 395(2):625–636.

Laing, R. A. et al. (2008). Multifrequency VLA observations of the FR I radio galaxy 3C 31: morphology, spectrum and magnetic field. *MNRAS*, 386(2):657–672.

Lakićević, M. et al. (2018). Narrow vs. broad-line Seyfert 1 galaxies: X-ray, optical, and mid-infrared AGN characteristics. *MNRAS*, 478(3):4068–4083.

Landt, H. et al. (2004). A physical classification scheme for blazars. *MNRAS*, 351(1):83–100.

Landt, H. et al. (2008). A Search for Synchrotron X-Ray Emission in Radio Quasars. *ApJ*, 676(1):87–100.

Laor, A. (2004). What is the Broad Line Region? In Richards, G. T. and Hall, P. B., editors, *AGN Physics with the Sloan Digital Sky Survey*, volume 311 of *Astronomical Society of the Pacific Conference Series*, page 169.

Lapi, A. et al. (2006). Quasar Luminosity Functions from Joint Evolution of Black Holes and Host Galaxies. *ApJ*, 650(1):42–56.

Lasota, J.-P. (2023). AGN Accretion Discs. *arXiv e-prints*, page arXiv:2302.07925.

Leahy, J. P. (1996). The Laing-Garrington effect: Implications for tori. *Vistas in Astronomy*, 40(1):173–177.

Lefa, E. (2012). *Non-thermal Radiation Processes in Relativistic Outflows from AGN*. PhD thesis, Ruprecht-Karls University of Heidelberg, Germany.

León-Tavares, J. et al. (2013). Flare-like Variability of the Mg II λ2800 Emission Line in the Γ-Ray Blazar 3C 454.3. *ApJL*, 763(2):L36.

Levenberg, K. (1944). A method for the solution of certain non-linear problems in least squares. *QApMa*, 2(2):164–168.

Lewis, K. T. et al. (2010). Long-term Profile Variability in Active Galactic Nucleus with Double-peaked Balmer Emission Lines. *ApJS*, 187(2):416–446.

Li, J. and Cao, X. (2019). The Large-scale Magnetic Field of a Thin Accretion Disk with Outflows. *ApJ*, 872(2):149.

Li, Z. et al. (2018). The Ensemble Photometric Variability of Over 10^5 Quasars in the Dark Energy Camera Legacy Survey and the Sloan Digital Sky Survey. *ApJ*, 861(1):6.

Lindegren, L. and Perryman, M. A. C. (1996). GAIA: Global astrometric interferometer for astrophysics. *AAPS*, 116:579–595.

Lister, M. L. et al. (2021). Monitoring Of Jets in Active Galactic Nuclei with VLBA Experiments. XVIII. Kinematics and Inner Jet Evolution of Bright Radio-loud Active Galaxies. *ApJ*, 923(1):30.

Liu, B. F. and Qiao, E. (2022). Accretion around black holes: The geometry and spectra. *iScience*, 25(1):103544.

Liu, F. K. et al. (2017). Disc origin of broad optical emission lines of the TDE candidate PTF09djl. *MNRAS*, 472(1):L99–L103.

Liu, H. et al. (2021). On the Observational Difference between the Accretion Disk-Corona Connections among Super- and Sub-Eddington Accreting Active Galactic Nuclei. *ApJ*, 910(2):103.

Lohfink, A. M. et al. (2017). The X-Ray Reflection Spectrum of the Radio-loud Quasar 4C 74.26. *ApJ*, 841(2):80.

López-Navas, E. et al. (2023). The Type 1 and Type 2 AGN dichotomy according to their ZTF optical variability. *MNRAS*, 518(1):1531–1542.

Loubser, S. I. et al. (2024). The star formation histories of galaxies in different stages of pre-processing in the Fornax A group. *MNRAS*, 527(3):7158–7172.

Lu, J.-F. et al. (2004). The Shakura-Sunyaev Disk Can Smoothly Match an Advection-dominated Accretion Flow. *ApJL*, 602(1):L37–L40.

Lu, N. et al. (2003). Infrared Emission of Normal Galaxies from 2.5 to 12 Micron: Infrared Space Observatory Spectra, Near-Infrared Continuum, and Mid-Infrared Emission Features. *ApJ*, 588(1):199–217.

Ludwig, R. R. et al. (2012). Physical Properties of the Narrow-line Region of Low-mass Active Galaxies. *ApJ*, 756(1):51.

Lupi, A. et al. (2021). Forming massive seed black holes in high-redshift quasar host progenitors. *MNRAS*, 503(4):5046–5060.

Lusso, E. et al. (2012). Bolometric luminosities and Eddington ratios of X-ray selected active galactic nuclei in the XMM-COSMOS survey. *MNRAS*, 425(1):623–640.

MacDonald, G. H. et al. (1968). Observations of the structure of radio sources in the 3C catalogue-I. *MNRAS*, 138:259.

Machalski, J. et al. (2008). J1420-0545: The Radio Galaxy Larger than 3C 236. *ApJ*, 679(1):149–155.

Machalski, J. et al. (2011). Understanding Giant Radio Galaxy J1420-0545: Large-scale Morphology, Environment, and Energetics. *ApJ*, 740(2):58.

Malizia, A. et al. (2014). The INTEGRAL High-energy Cut-off Distribution of Type 1 Active Galactic Nuclei. *ApJL*, 782(2):L25.

Malkan, M. A. et al. (2017). Emission Line Properties of Seyfert Galaxies in the 12 μm Sample. *ApJ*, 846(2):102.

Malkan, M. A. and Oke, J. B. (1983). IUE observations of Markarian 3 and 6 : reddening and the nonstellar continuum. *ApJ*, 265:92–106.

Malkan, M. A. and Sargent, W. L. W. (1982). The ultraviolet excess of Seyfert 1 galaxies and quasars. *ApJ*, 254:22–37.

Maraschi, L., Ghisellini, G., and Celotti, A. (1992). A Jet Model for the Gamma-Ray–emitting Blazar 3C 279. *ApJL*, 397:L5.

Marconi, A. et al. (2004). Local supermassive black holes, relics of active galactic nuclei and the X-ray background. *MNRAS*, 351(1):169–185.

Marconi, A. et al. (2009). On the Observed Distributions of Black Hole Masses and Eddington Ratios from Radiation Pressure Corrected Virial Indicators. *ApJL*, 698(2):L103–L107.

Marconi, A. and Hunt, L. K. (2003). The Relation between Black Hole Mass, Bulge Mass, and Near-Infrared Luminosity. *ApJL*, 589(1):L21–L24.

Martel, A. R. et al. (1999). Hubble Space Telescope Snapshot Survey of 3CR Radio Source Counterparts. III. Radio Galaxies with z<0.1. *ApJS*, 122(1):81–108.

Martinez, P. and Klotz, A. (1998). *A practical guide to CCD astronomy*.

Martínez-Aldama, M. L. et al. (2015). O I and Ca II Observations in Intermediate Redshift Quasars. *ApJS*, 217(1):3.

Marziani, P. (2023). Accretion/Ejection Phenomena and Emission-Line Profile (A)symmetries in Type-1 Active Galactic Nuclei. *Symmetry*, 15(10):1859.

Marziani, P. et al. (1992). Twin Peaks: IC 4329A and Arakelian 120. *ApJ*, 393:658.

Marziani, P. et al. (1996). Comparative Analysis of the High- and Low-Ionization Lines in the Broad-Line Region of Active Galactic Nuclei. *ApJS*, 104:37.

Marziani, P. et al. (2001). Searching for the Physical Drivers of the Eigenvector 1 Correlation Space. *ApJ*, 558(2):553–560.

Marziani, P. et al. (2003a). An Optical Spectroscopic Atlas of Low-Redshift Active Galactic Nuclei. *ApJS*, 145(2):199–211.

Marziani, P. et al. (2003b). Searching for the physical drivers of eigenvector 1: influence of black hole mass and Eddington ratio. *MNRAS*, 345(4):1133–1144.

Marziani, P. et al. (2009). VLT/ISAAC spectra of the Hβ region in intermediate-redshift quasars. III. Hβ broad-line profile analysis and inferences about BLR structure. *A&A*, 495(1):83–112.

Marziani, P. et al. (2010). Broad-line region physical conditions along the quasar eigenvector 1 sequence. *MNRAS*, 409(3):1033–1048.

Marziani, P. et al. (2013a). Is MgIIλ2800 a reliable virial broadening estimator for quasars? *A&A*, 555:A89.

Marziani, P. et al. (2013b). Low-ionization Outflows in High Eddington Ratio Quasars. *ApJ*, 764(2):150.

Marziani, P. et al. (2014). Low- and high-z highly accreting quasars in the 4D Eigenvector 1 context. *The Astronomical Review*, 9(4):6–25.

Marziani, P. et al. (2015). UV spectral diagnostics for low redshift quasars: estimating physical conditions and radius of the broad line region. *Ap&SS*, 356(2):339–346.

Marziani, P. et al. (2016). Blue outliers among intermediate redshift quasars. *Ap&SS*, 361:3.

Marziani, P. et al. (2018). A main sequence for quasars. *Frontiers in Astronomy and Space Sciences*, 5:6.

Marziani, P. et al. (2019a). Black hole mass estimates in quasars. A comparative analysis of high- and low-ionization lines. *A&A*, 627:A88.

Marziani, P. et al. (2019b). Quasars: From the Physics of Line Formation to Cosmology. *Atoms*, 7(1):18.

Marziani, P. et al. (2021). Optical Singly-Ionized Iron Emission in Radio-Quiet and Relativistically Jetted Active Galactic Nuclei. *Universe*, 7(12):484.

Marziani, P. et al. (2022). Isolating an Outflow Component in Single-Epoch Spectra of Quasars. *Galaxies*, 10(2):54.

Marziani, P. and Sulentic, J. W. (2012a). Estimating black hole masses in quasars using broad optical and UV emission lines. *NAR*, 56(2-3):49–63.

Marziani, P. and Sulentic, J. W. (2012b). Quasar Outflows in the 4D Eigenvector 1 Context. *The Astronomical Review*, 7(4):33–57.

Mason, R. E. (2015). Dust in the torus of the AGN unified model. *Planet. Space Sci.*, 116:97–101.

Mathews, W. G. (1993). Bouncing Clouds: A Model for the Quasar Broad-Line Region. *ApJL*, 412:L17.

Mathews, W. G. and Ferland, G. J. (1987). What Heats the Hot Phase in Active Nuclei? *ApJ*, 323:456.

Mathur, S. et al. (2001). Evolution of active galaxies: black-hole mass-bulge relations for narrow line objects. *ARA&A*, 6(5):321–329.

Mazzucchelli, C. et al. (2017). Physical Properties of 15 Quasars at z $\gtrsim$ 6.5. *ApJ*, 849(2):91.

McClintock, J. E. et al. (2006). The Spin of the Near-Extreme Kerr Black Hole GRS 1915+105. *ApJ*, 652(1):518–539.

McLean, I. S. (2008). Charge-coupled devices. *Electronic Imaging in Astronomy: Detectors and Instrumentation*, pages 241–275.

McLure, R. J. and Dunlop, J. S. (2004). The Cosmological Evolution of Quasar Black-Hole Masses. In Mújica, R. and Maiolino, R., editors, *Multiwavelength AGN Surveys*, pages 389–392.

McLure, R. J. et al. (2006). On the evolution of the black-hole:spheroid mass ratio. *NAR*, 50(9-10):782–785.

McLure, R. J. and Jarvis, M. J. (2002). Measuring the black hole masses of high-redshift quasars. *MNRAS*, 337(1):109–116.

Meena, B. et al. (2023). Investigating the Narrow-line Region Dynamics in Nearby Active Galaxies. *ApJ*, 943(2):98.

Mejía-Restrepo, J. E. et al. (2018). The effect of nuclear gas distribution on the mass determination of supermassive black holes. *Nature Astronomy*, 2:63–68.

Mengistue, S. T. et al. (2023). Optical and near-UV spectroscopic properties of low-redshift jetted quasars in the main sequence context. *MNRAS*, 525(3):4474–4496.

Mengistue Terefe, S. et al. (2024). Quasar 3C 47: Extreme Population B jetted source with double-peaked profiles. *A&A*, 685:A116.

Menzel, M. et al. (2023). The Design, Verification, and Performance of the James Webb Space Telescope. *PASP*, 135(1047):058002.

Mickaelian, A. M. (2015). AGN Zoo and Classifications of Active Galaxies. *Iranian Journal of Astronomy and Astrophysics*, 2(1):1–38.

Miley, G. K. and Miller, J. S. (1979). Relations between the emission spectra and radio structures of quasars. *ApJL*, 228:L55–L58.

Miller, J. M. (2007). Relativistic X-Ray Lines from the Inner Accretion Disks Around Black Holes. *ARA&A*, 45(1):441–479.

Mineshige, S. (1996). Disk Instability-Induced Hard–Soft Transition in Soft X-Ray Transients. *PASJ*, 48:93–98.

Mingo, B. et al. (2019). Revisiting the Fanaroff-Riley dichotomy and radio-galaxy morphology with the LOFAR Two-Metre Sky Survey (LoTSS). *MNRAS*, 488(2):2701–2721.

Mizuno, Y. (2022). GRMHD Simulations and Modeling for Jet Formation and Acceleration Region in AGNs. *Universe*, 8(2):85.

Mondal, T. and Mukhopadhyay, B. (2019). FSRQ/BL Lac dichotomy as the magnetized advective accretion process around black holes: a unified classification of blazars. *MNRAS*, 486(3):3465–3472.

Montgomery, C., Orchiston, W., and Whittingham, I. (2009). Michell, Laplace and the origin of the black hole concept. *Journal of Astronomical History and Heritage*, 12(2):90–96.

Morell, D. F. et al. (2020). Classification and evolution of galaxies according to the dynamical state of host clusters and galaxy luminosities. *MNRAS*, 494(3):3317–3327.

Mountrichas, G. et al. (2021). Galaxy properties of type 1 and 2 X-ray selected AGN and a comparison among different classification criteria. *A&A*, 653:A70.

Mountrichas, G. et al. (2022). Comparison of star formation histories of AGN and non-AGN galaxies. *A&A*, 667:A145.

Mullaney, J. R. and Ward, M. J. (2008). Optical emission-line properties of narrow-line Seyfert 1 galaxies and comparison active galactic nuclei. *MNRAS*, 385(1):53–74.

Müller, A. L. and Romero, G. E. (2020). Radiation from the impact of broad-line region clouds onto AGN accretion disks. *A&A*, 636:A92.

Murphy, E. J. et al. (2018). Radio Continuum Emission from Galaxies: An Accounting of Energetic Processes. In Murphy, E., editor, *Science with a Next Generation Very Large Array*, volume 517 of *Astronomical Society of the Pacific Conference Series*, page 421.

Murray, N. and Chiang, J. (1997). Disk Winds and Disk Emission Lines. *ApJ*, 474(1):91–103.

Murray, N. et al. (1995). Accretion Disk Winds from Active Galactic Nuclei. *ApJ*, 451:498.

Mushotzky, R. (2004). How are AGN Found? In Barger, A. J., editor, *Supermassive Black Holes in the Distant Universe*, volume 308 of *Astrophysics and Space Science Library*, page 53.

Nandra, K. et al. (1998). New Constraints on the Continuum Emission Mechanism of Active Galactic Nuclei: Intensive Monitoring of NGC 7469 in the X-Ray and Ultraviolet. *ApJ*, 505(2):594–606.

Nandra, K. and Pounds, K. A. (1994). GINGA observations of the X-ray spectra of Seyfert galaxies. *MNRAS*, 268:405–429.

Narayan, R. et al. (2010). Advection-dominated accretion around black holes. In *Theory of Black Hole Accretion Discs*, pages 148–182.

Narayan, R. and McClintock, J. E. (2008). Advection-dominated accretion and the black hole event horizon. *NAR*, 51(10-12):733–751.

Narayan, R. and Yi, I. (1994). Advection-dominated Accretion: A Self-similar Solution. *ApJL*, 428:L13.

Negrete, C. A. et al. (2018). Highly accreting quasars: The SDSS low-redshift catalog. *A&A*, 620:A118.

Nehir, M. et al. (2019). Improving Optical Measurements: Non-Linearity Compensation of Compact Charge-Coupled Device (CCD) Spectrometers. *Sensors*, 19(12):2833.

Nemmen, R. S. et al. (2006). Modelling the jet power in elliptical galaxies: support for rapidly spinning black holes. *arXiv e-prints*, pages astro–ph/0612392.

Nemmen, R. S. et al. (2014). Spectral models for low-luminosity active galactic nuclei in LINERs: the role of advection-dominated accretion and jets. *MNRAS*, 438(4):2804–2827.

Nenkova, M. et al. (2008a). AGN Dusty Tori. I. Handling of Clumpy Media. *ApJ*, 685(1):147–159.

Nenkova, M. et al. (2008b). AGN Dusty Tori. II. Observational Implications of Clumpiness. *ApJ*, 685(1):160–180.

Netzer, H. (1990). AGN emission lines. In Blandford, R. D., Netzer, H., Woltjer, L., Courvoisier, T. J. L., and Mayor, M., editors, *Active Galactic Nuclei*, pages 57–160.

Netzer, H. (2013). *The Physics and Evolution of Active Galactic Nuclei*.

Netzer, H. (2015). Revisiting the Unified Model of Active Galactic Nuclei. *ARA&A*, 53:365–408.

Netzer, H. (2019). Bolometric correction factors for active galactic nuclei. *MNRAS*, 488(4):5185–5191.

Netzer, H. and Marziani, P. (2010). The Effect of Radiation Pressure on Emission-line Profiles and Black Hole Mass Determination in Active Galactic Nuclei. *ApJ*, 724(1):318–328.

Neumann, W. (2014). *Fundamentals of Dispersive Optical Spectroscopy Systems*.

Norman, C. and Miley, G. (1984). Jets and emission-line regions. *A&A*, 141(1):85–90.

Novikov, I. D. and Thorne, K. S. (1973). Astrophysics of black holes. In *Black Holes (Les Astres Occlus)*, pages 343–450.

Onken, C. A. et al. (2004). Supermassive Black Holes in Active Galactic Nuclei. II. Calibration of the Black Hole Mass-Velocity Dispersion Relationship for Active Galactic Nuclei. *ApJ*, 615(2):645–651.

Onken, C. A. et al. (2022). Discovery of the most luminous quasar of the last 9 Gyr. *PASP*, 39:e037.

Osterbrock, D. E. and Ferland, G. J. (2006). *Astrophysics of gaseous nebulae and active galactic nuclei*.

Osterbrock, D. E. and Mathews, W. G. (1986). Emission-line regions of active galaxies and QSOs. *ARA&A*, 24:171–203.

Padovani, P. (1997). Unified schemes for radio-loud AGN: recent results. *Mem. Soc. Astron. Italiana*, 68:47–54.

Padovani, P. (2011). The solution to the long-standing problem of radio emission in radio-quiet AGN: star-formation. In Guainazzi, M., editor, *The Starburst-AGN Connection under the Multiwavelength Limelight*, page 32.

Padovani, P. (2016). The Faint Radio Sky: Radio Astronomy Becomes Mainstream. In *Active Galactic Nuclei 12: A Multi-Messenger Perspective (AGN12)*, page 14.

Padovani, P. (2017a). Active Galactic Nuclei at all wavelengths and from all angles. *Frontiers in Astronomy and Space Sciences*, 4:35.

Padovani, P. (2017b). On the two main classes of active galactic nuclei. *Nature Astronomy*, 1:0194.

Padovani, P. et al. (2017). Active galactic nuclei: what's in a name? *A&A*, 25(1):2.

Pan, H.-W. et al. (2015). On the Black Hole Mass—X-Ray Excess Variance Scaling Relation for Active Galactic Nuclei in the Low-mass Regime. *ApJ*, 808(2):163.

Panagiotou, C. et al. (2022). A Physical Model for the UV/Optical Power Spectra of AGN. *ApJ*, 935(2):93.

Panda, S. et al. (2017). The physical driver of the optical Eigenvector 1 in Quasar Main Sequence. *Frontiers in Astronomy and Space Sciences*, 4:33.

Panda, S. et al. (2018). Modeling of the Quasar Main Sequence in the Optical Plane. *ApJ*, 866(2):115.

Panda, S. et al. (2019a). CLOUDY View of the Warm Corona. *ApJ*, 875(2):133.

Panda, S. et al. (2019b). Current and future applications of Reverberation-mapped quasars in Cosmology. *Frontiers in Astronomy and Space Sciences*, 6:75.

Panda, S. et al. (2019c). The Quasar Main Sequence Explained by the Combination of Eddington Ratio, Metallicity, and Orientation. *ApJ*, 882(2):79.

Panessa, F. et al. (2019). The origin of radio emission from radio-quiet active galactic nuclei. *Nature Astronomy*, 3:387–396.

Pauliny-Toth, I. I. K. et al. (1978). The 5 GHz strong source surveys. IV. Survey of the area between declination 35 and 70 degrees and summary of source counts, spectra and optical identifications. *AJ*, 83:451–474.

Pe'er, A. (2015). Energetic and Broad Band Spectral Distribution of Emission from Astronomical Jets. In Falanga, M., Belloni, T., Casella, P., Gilfanov, M., Jonker, P., and King, A., editors, *The Physics of Accretion onto Black Holes*, volume 49, pages 371–403.

Penston, M. V. et al. (1990). Infall or outflow from a single AGN line profile ? *MNRAS*, 244:357–361.

Perez, E. et al. (1988). An accretion disc in the broad-line radio galaxy 3C 390.3 ? *MNRAS*, 230:353–362.

Perna, M. et al. (2020). MUSE view of Arp220: Kpc-scale multi-phase outflow and evidence for positive feedback. *A&A*, 643:A139.

Peruzzi, T. et al. (2021). Interpreting automatic AGN classifiers with saliency maps. *A&A*, 652:A19.

Peterson, B. M. (1993). Reverberation Mapping of Active Galactic Nuclei. *PASP*, 105:247.

Peterson, B. M. (1997). *An Introduction to Active Galactic Nuclei*.

Peterson, B. M. (1998). Reverberation mapping of active nuclei. *Advances in Space Research*, 21(1-2):57–66.

Peterson, B. M. et al. (1987). The Double Broad-Line Emitting Regions in NGC 5548 as Possible Evidence for a Supermassive Binary. *ApJL*, 312:L1.

Peterson, B. M. et al. (2004). Central Masses and Broad-Line Region Sizes of Active Galactic Nuclei. II. A Homogeneous Analysis of a Large Reverberation-Mapping Database. *ApJ*, 613(2):682–699.

Peterson, B. M. and Wandel, A. (1999). Keplerian Motion of Broad-Line Region Gas as Evidence for Supermassive Black Holes in Active Galactic Nuclei. *ApJL*, 521(2):L95–L98.

Peterson, B. M. and Wandel, A. (2000). Evidence for Supermassive Black Holes in Active Galactic Nuclei from Emission-Line Reverberation. *ApJL*, 540(1):L13–L16.

Pfeiffer, M. J. et al. (1998). FOCES - a fibre optics Cassegrain Echelle spectrograph. *AAPS*, 130:381–393.

Pier, E. A. and Krolik, J. H. (1992a). Infrared Spectra of Obscuring Dust Tori around Active Galactic Nuclei. I. Calculational Method and Basic Trends. *ApJ*, 401:99.

Pier, E. A. and Krolik, J. H. (1992b). Radiation-Pressure–supported Obscuring Tori around Active Galactic Nuclei. *ApJL*, 399:L23.

Podigachoski, P. et al. (2015). The Unification of Powerful Quasars and Radio Galaxies and Their Relation to Other Massive Galaxies. *ApJL*, 806(1):L11.

Podigachoski, P. et al. (2016). The unification of powerful radio-loud AGN: the multi-wavelength balance. In *Active Galactic Nuclei: What's in a Name?*, page 61.

Popović, L. C. (2002). Determination of the physical properties in active galactic nuclei using Balmer lines. *Publications de l'Observatoire Astronomique de Beograd*, 74:161–163.

Popović, L. Č. et al. (2002). Balmer lines emission region in NGC 3516: Kinematical and physical properties. *A&A*, 390:473–480.

Popović, L. Č. et al. (2004). Contribution of the disk emission to the broad emission lines in AGNs: Two-component model. *A&A*, 423:909–918.

Popovic, L. C. et al. (2008). The Broad Emission Lines in AGN: Hidden Disk Emission. In *Revista Mexicana de Astronomia y Astrofisica Conference Series*, volume 32 of *Revista Mexicana de Astronomia y Astrofisica Conference Series*, pages 99–101.

Popović, L. Č. et al. (2009). Three-Dimensional Spectroscopic Study of the Line-Emitting Regions of Mrk 493. *AJ*, 137(3):3548–3557.

Popović, L. Č. et al. (2019). The structure of the Mg II broad line emitting region in Type 1 AGNs. *MNRAS*, 484(3):3180–3197.

Popović, L. Č. and Kovačević, J. (2011). Optical Emission-line Properties of a Sample of the Broad-line Active Galactic Nuclei: The Baldwin Effect and Eigenvector 1. *ApJ*, 738(1):68.

Porth, O. et al. (2011). Synchrotron Radiation of Self-collimating Relativistic Magnetohydrodynamic Jets. *ApJ*, 737(1):42.

Prieto, M. A. and Zhao, H. (1997). The giant nebulae associated with 3C 227: emission-line profiles and kinematic modelling. *MNRAS*, 290(1):34–40.

Proga, D. and Kallman, T. R. (2004). Dynamics of Line-driven Disk Winds in Active Galactic Nuclei. II. Effects of Disk Radiation. *ApJ*, 616(2):688–695.

Pugliese, D. et al. (2013). On the Polish doughnut accretion disc via the effective potential approach. *MNRAS*, 428(2):952–982.

Punsly, B. et al. (2020). The Extreme Red Excess in Blazar Ultraviolet Broad Emission Lines. *ApJ*, 903(1):44.

Qian, L. et al. (2009). The Polish doughnuts revisited. I. The angular momentum distribution and equipressure surfaces. *A&A*, 498(2):471–477.

Rafter, S. E. et al. (2011). Radio Properties of Low-redshift Broad-line Active Galactic Nuclei Including Extended Radio Sources. *AJ*, 141(3):85.

Rakić, N. (2022). Kinematics of the H α and H β broad-line region in an SDSS sample of type-1 AGNs. *MNRAS*, 516(2):1624–1634.

Rakić, N. et al. (2017). The intrinsic Baldwin effect in broad Balmer lines of six long-term monitored AGNs. *A&A*, 603:A49.

Rakshit, S. (2020). Broad line region and black hole mass of PKS 1510-089 from spectroscopic reverberation mapping. *A&A*, 642:A59.

Rakshit, S. et al. (2020). Spectral Properties of Quasars from Sloan Digital Sky Survey Data Release 14: The Catalog. *ApJS*, 249(1):17.

Ramos Almeida, C. et al. (2011). Testing the Unification Model for Active Galactic Nuclei in the Infrared: Are the Obscuring Tori of Type 1 and 2 Seyferts Different? *ApJ*, 731(2):92.

Rani, B. et al. (2011). Optical intraday variability studies of 10 low energy peaked blazars. *MNRAS*, 413(3):2157–2172.

Rashed, Y. E. et al. (2015). Line and continuum variability in active galaxies. *MNRAS*, 454(3):2918–2945.

Rawes, J. et al. (2015). Discovery of an optical and X-ray synchrotron jet in NGC 7385. *MNRAS*, 452(3):3064–3072.

Rawlings, S. and Saunders, R. (1991). Evidence for a common central-engine mechanism in all extragalactic radio sources. *Nature*, 349(6305):138–140.

Ricci, T. V. and Steiner, J. E. (2019). Detection of a double-peaked H α component from the accretion disc of NGC 4958. *MNRAS*, 486(1):1138–1145.

Richards, G. T. et al. (2006). Spectral Energy Distributions and Multiwavelength Selection of Type 1 Quasars. *ApJS*, 166(2):470–497.

Richards, G. T. et al. (2011). Unification of Luminous Type 1 Quasars through C IV Emission. *AJ*, 141(5):167.

Rokaki, E. (1997). Accretion Disks and Line Emission in AGN. In Peterson, B. M., Cheng, F.-Z., and Wilson, A. S., editors, *IAU Colloq. 159: Emission Lines in Active Galaxies: New Methods and Techniques*, volume 113 of *Astronomical Society of the Pacific Conference Series*, page 56.

Rokaki, E. et al. (2003). Is there a disc in the superluminal quasars? *MNRAS*, 340(4):1298–1308.

Sadeghi, M. et al. (2021). Morphological-based Classifications of Radio Galaxies Using Supervised Machine-learning Methods Associated with Image Moments. *AJ*, 161(2):94.

Sahakyan, N. et al. (2017). Gamma-ray emission from non-blazar AGNs. In *6th International Symposium on High Energy Gamma-Ray Astronomy*, volume 1792 of *American Institute of Physics Conference Series*, page 050002.

Saikia, D. J. (2022). Jets in radio galaxies and quasars: an observational perspective. *Journal of Astrophysics and Astronomy*, 43(2):97.

Sameshima, H. et al. (2011). Implications from the optical to ultraviolet flux ratio of Fe II emission in quasars. *MNRAS*, 410(2):1018–1026.

Sánchez, S. F. et al. (2007). The Night Sky at the Calar Alto Observatory. *PASP*, 119(860):1186–1200.

Sánchez, S. F. et al. (2008). The Night Sky at the Calar Alto Observatory II: The Sky at the Near-infrared. *PASP*, 120(873):1244.

Sandage, A. (1965). The Existence of a Major New Constituent of the Universe: the Quasistellar Galaxies. *ApJ*, 141:1560.

Sbarrato, T. et al. (2021). Jetted radio-quiet quasars at z > 5. *A&A*, 655:A95.

Schilizzi, R. T. (1986). Very long baseline interferometry. *Radio Science*, 21:665–679.

Schmidt, M. (1963). 3C 273 : A Star-Like Object with Large Red-Shift. *Nature*, 197(4872):1040.

Schmidt, R. W. and Wambsganss, J. (2010). Quasar microlensing. *General Relativity and Gravitation*, 42(9):2127–2150.

Schneider, D. P. et al. (2002). The Sloan Digital Sky Survey Quasar Catalog. I. Early Data Release. *AJ*, 123(2):567–577.

Schneider, D. P. et al. (2007). The Sloan Digital Sky Survey Quasar Catalog. IV. Fifth Data Release. *AJ*, 134(1):102–117.

Schnülle, K. (2017). *Studying the radiative response of circumnuclear dust of AGNs*. PhD thesis, Ruprecht-Karls University of Heidelberg, Germany.

Schoeller, M. (2007). The Very Large Telescope Interferometer. In *VI Reunion Anual Sociedad Chilena de Astronomia (SOCHIAS)*, page 45.

Schulze, A. et al. (2017). Evidence for Higher Black Hole Spin in Radio-loud Quasars. *ApJ*, 849(1):4.

Schutter, A. and Shamir, L. (2015). Galaxy morphology - An unsupervised machine learning approach. *Astronomy and Computing*, 12:60–66.

Sergeev, S. G. et al. (2002). Variability of the Broad Balmer Emission Lines in 3C 390.3 from 1992 to 2000. *ApJ*, 576(2):660–672.

Seyfert, C. K. (1943). Nuclear Emission in Spiral Nebulae. *ApJ*, 97:28.

Shaban, F. et al. (2022). X-ray properties of high-redshift Radio Loud and Radio Quiet Quasars observed by Chandra. *Journal of High Energy Astrophysics*, 36:152–161.

Shakura, N. I. and Sunyaev, R. A. (1973). Black holes in binary systems. Observational appearance. *A&A*, 24:337–355.

Shapovalova, A. I. et al. (2004). Profile Variability of the Hα and Hβ Broad Emission Lines in NGC 5548. In Mújica, R. and Maiolino, R., editors, *Multiwavelength AGN Surveys*, pages 199–200.

Shapovalova, A. I. et al. (2012). Spectral Optical Monitoring of the Narrow-line Seyfert 1 Galaxy Ark 564. *ApJS*, 202(1):10.

Shatalov, N. A. et al. (2019). Influence of magnetic field and density of environment on collimation of laboratory jet. In *Journal of Physics Conference Series*, volume 1390 of *Journal of Physics Conference Series*, page 012069. IOP.

Shen, Y. (2013). The mass of quasars. *Bulletin of the Astronomical Society of India*, 41(1):61–115.

Shen, Y. et al. (2007). Clustering of High-Redshift (z >= 2.9) Quasars from the Sloan Digital Sky Survey. *AJ*, 133(5):2222–2241.

Shen, Y. et al. (2011). A Catalog of Quasar Properties from Sloan Digital Sky Survey Data Release 7. *ApJS*, 194(2):45.

Shen, Y. et al. (2019). The Sloan Digital Sky Survey Reverberation Mapping Project: Sample Characterization. *ApJS*, 241(2):34.

Shen, Y. et al. (2023). The Sloan Digital Sky Survey Reverberation Mapping Project: Key Results. *arXiv e-prints*, page arXiv:2305.01014.

Shen, Y. and Ho, L. C. (2014). The diversity of quasars unified by accretion and orientation. *Nature*, 513(7517):210–213.

Shen, Y. and Liu, X. (2012). Comparing Single-epoch Virial Black Hole Mass Estimators for Luminous Quasars. *ApJ*, 753(2):125.

Shende, M. B. et al. (2019). Episodic Jets from Black Hole Accretion Disks. *ApJ*, 877(2):130.

Shields, G. A. (1978). Thermal continuum from accretion disks in quasars. *Nature*, 272(5655):706–708.

Shields, G. A. (1999). A Brief History of Active Galactic Nuclei. *PASP*, 111(760):661–678.

Siemiginowska, A. (1998). Evolution of accretion disks in AGN. In Holt, S. S. and Kallman, T. R., editors, *Accretion processes in Astrophysical Systems: Some like it hot! - eigth AstroPhysics Conference*, volume 431 of *American Institute of Physics Conference Series*, pages 211–214. AIP.

Sikora, M. et al. (2007). Radio Loudness of Active Galactic Nuclei: Observational Facts and Theoretical Implications. *ApJ*, 658(2):815–828.

Silk, J. (2013). Unleashing Positive Feedback: Linking the Rates of Star Formation, Supermassive Black Hole Accretion, and Outflows in Distant Galaxies. *ApJ*, 772(2):112.

Silk, J. et al. (2024). Which Came First: Supermassive Black Holes or Galaxies? Insights from JWST. *ApJL*, 961(2):L39.

Silva, A. et al. (2021). Galaxy Mergers up to z < 2.5. II. AGN Incidence in Merging Galaxies at Separations of 3-15 kpc. *ApJ*, 909(2):124.

Simmons, B. D. et al. (2017). Supermassive black holes in disc-dominated galaxies outgrow their bulges and co-evolve with their host galaxies. *MNRAS*, 470(2):1559–1569.

Singh, R. et al. (2014). The nature of LINER galaxies: Ubiquitous hot old stars and rare accreting black holes. In Mickaelian, A. M. and Sanders, D. B., editors, *Multiwavelength AGN Surveys and Studies*, volume 304, pages 280–281.

Sądowski, A. et al. (2011). Relativistic slim disks with vertical structure. *A&A*, 527:A17.

Smith, A. and Bromm, V. (2019). Supermassive black holes in the early universe. *Contemporary Physics*, 60(2):111–126.

Smith, H. E. et al. (1976). The revised 3C catalog of radio sources: a review of optical identifications and spectroscopy. *PASP*, 88:621–646.

Snedden, S. A. and Gaskell, C. M. (2007). The Case for Optically Thick High-Velocity Broad-Line Region Gas in Active Galactic Nuclei. *ApJ*, 669(1):126–134.

Śniegowska, M. et al. (2018). Properties of active galaxies at the extreme of Eigenvector 1. *A&A*, 613:A38.

Śniegowska, M. et al. (2020). Quasar Main Sequence in the UV Plane. *ApJ*, 900(1):64.

Soldi, S. et al. (2014). Long-term variability of AGN at hard X-rays. *A&A*, 563:A57.

Song, H. et al. (2016). Quasars as a Tracer of Large-scale Structures in the Distant Universe. *ApJ*, 827(2):104.

Spinoglio, L. et al. (2021). AGN types and unification model. In Pović, M., Marziani, P., Masegosa, J., Netzer, H., Negu, S. H., and Tessema, S. B., editors, *Nuclear Activity in Galaxies Across Cosmic Time*, volume 356, pages 29–43.

Steiner, J. E. (1981). A spectrophotometric classification of low-redshift quasars and active galactic nuclei. *ApJ*, 250:469–477.

Stern, J. and Laor, A. (2012). Type 1 AGN at low z. I. Emission properties. In *Journal of Physics Conference Series*, volume 372 of *Journal of Physics Conference Series*, page 012010.

Stockton, A. and Farnham, T. (1991). OX 169: Evidence for a Recent Merger. *ApJ*, 371:525.

Storchi-Bergmann, T. et al. (1993). Double-peaked Broad Line Emission from the LINER Nucleus of NGC 1097. *ApJL*, 410:L11.

Storchi-Bergmann, T. et al. (2003). Evolution of the Nuclear Accretion Disk Emission in NGC 1097: Getting Closer to the Black Hole. *ApJ*, 598(2):956–968.

Storchi-Bergmann, T. et al. (2017). Double-Peaked Profiles: Ubiquitous Signatures of Disks in the Broad Emission Lines of Active Galactic Nuclei. *ApJ*, 835(2):236.

Strateva, I. V. et al. (2003). Double-peaked Low-Ionization Emission Lines in Active Galactic Nuclei. *AJ*, 126(4):1720–1749.

Strateva, I. V. et al. (2006). The X-Ray Properties of Active Galactic Nuclei with Double-peaked Balmer Lines. *ApJ*, 651(2):749–766.

Straub, O. et al. (2011). Testing slim-disk models on the thermal spectra of LMC X-3. *A&A*, 533:A67.

Suh, H. et al. (2019). Multi-wavelength Properties of Type 1 and Type 2 AGN Host Galaxies in the Chandra-COSMOS Legacy Survey. *ApJ*, 872(2):168.

Sulentic, J. (2007). Our Search for an H-R Diagram of Quasars. In *The Nuclear Region, Host galaxy and Environment of Active Galaxies*, page 13.

Sulentic, J. et al. (2011). The Case for Two Quasar Populations. *Baltic Astronomy*, 20:427–434.

Sulentic, J. and Marziani, P. (2015). Quasars in the 4D Eigenvector 1 Context: a stroll down memory lane. *Frontiers in Astronomy and Space Sciences*, 2:6.

Sulentic, J. W. et al. (1990). Implications of ARP 102B: Line Emission from an Accretion Disk? *ApJL*, 355:L15.

Sulentic, J. W. et al. (1995). Pictor A: A New Double-peaked Emission-Line Quasar. *ApJL*, 438:L1.

Sulentic, J. W. et al. (2000a). Eigenvector 1: An Optimal Correlation Space for Active Galactic Nuclei. *ApJL*, 536(1):L5–L9.

Sulentic, J. W. et al. (2000b). Phenomenology of Broad Emission Lines in Active Galactic Nuclei. *ARA&A*, 38:521–571.

Sulentic, J. W. et al. (2000c). The Demise of the Classical Broad-Line Region in the Luminous Quasar PG 1416-129. *ApJL*, 545(1):L15–L18.

Sulentic, J. W. et al. (2001). Eigenvector 1: an H-R diagram for AGN? *The Messenger*, 104:25–28.

Sulentic, J. W. et al. (2002). Average Quasar Spectra in the Context of Eigenvector 1. *ApJL*, 566(2):L71–L75.

Sulentic, J. W. et al. (2003). Radio-loud Active Galactic Nuclei in the Context of the Eigenvector 1 Parameter Space. *ApJL*, 597(1):L17–L20.

Sulentic, J. W. et al. (2006). VLT/ISAAC spectra of the Hβ region in intermediate-redshift quasars. II. Black hole mass and Eddington ratio. *A&A*, 456(3):929–939.

Sulentic, J. W. et al. (2007a). C IV λ1549 as an Eigenvector 1 Parameter for Active Galactic Nuclei. *ApJ*, 666(2):757–777.

Sulentic, J. W. et al. (2007b). Eigenvector 1: Towards AGN Spectroscopic Unification. In Kurtz, S., editor, *Revista Mexicana de Astronomia y Astrofisica Conference Series*, volume 28 of *Revista Mexicana de Astronomia y Astrofisica Conference Series*, pages 83–88.

Sulentic, J. W. et al. (2008). Our Search for an H-R Diagram of Quasars. In *Revista Mexicana de Astronomia y Astrofisica Conference Series*, volume 32 of *Revista Mexicana de Astronomia y Astrofisica Conference Series*, pages 51–58.

Sulentic, J. W. et al. (2012). Fifty Years of Quasars: Current Impressions and Future Perspectives. In D'Onofrio, M., Marziani, P., and Sulentic, J. W., editors, *Fifty Years of Quasars: From Early Observations and Ideas to Future Research*, volume 386 of *Astrophysics and Space Science Library*, page 549.

Sulentic, J. W. et al. (2014). Fifty Years of Quasars: Physical Insights and Potential for Cosmology. In *Journal of Physics Conference Series*, volume 565 of *Journal of Physics Conference Series*, page 012018.

Sulentic, J. W. et al. (2015). 3C 57 as an atypical radio-loud quasar: implications for the radio-loud/radio-quiet dichotomy. *MNRAS*, 450(2):1916–1925.

Sulentic, J. W. et al. (2016). Balmer line shifts in quasars. *Ap&SS*, 361:55.

Sulentic, J. W. et al. (2017). What does CIVλ1549 tell us about the physical driver of the Eigenvector quasar sequence? *A&A*, 608:A122.

Sulentic, J. W. and Marziani, P. (1999). The Intermediate-Line Region in Active Galactic Nuclei: A Region "Præter Necessitatem"? *ApJL*, 518(1):L9–L12.

Sun, M. et al. (2015). The Sloan Digital Sky Survey Reverberation Mapping Project: Ensemble Spectroscopic Variability of Quasar Broad Emission Lines. *ApJ*, 811(1):42.

Tadhunter, C. (2008). An introduction to active galactic nuclei: Classification and unification. *NAR*, 52(6):227–239.

Tadhunter, C. (2016). Erratum: Erratum to: Radio AGN in the local universe: unification, triggering and evolution. *A&A*, 24(1):12.

Tang, S. and Grindlay, J. (2009). The Quasar SDSS J153636.22+044127.0: A Double-Peaked Emitter in a Candidate Binary Black Hole System. *ApJ*, 704(2):1189–1194.

Tanimura, H. (2017). *Probing the large-scale structure of the Universe with the Sunyaev-Zel'dovich Effect*. PhD thesis, University of British Columbia, Canada.

Tchekhovskoy, A. et al. (2009). Efficiency of Magnetic to Kinetic Energy Conversion in a Monopole Magnetosphere. *ApJ*, 699(2):1789–1808.

Timlin, John D., I., Brandt, W. N., and Laor, A. (2021). What controls the UV-to-X-ray continuum shape in quasars? *MNRAS*, 504(4):5556–5574.

Tody, D. (1986). The IRAF Data Reduction and Analysis System. In Crawford, D. L., editor, *Instrumentation in astronomy VI*, volume 627 of *Society of Photo-Optical Instrumentation Engineers (SPIE) Conference Series*, page 733.

Trakhtenbrot, B. and Netzer, H. (2012). Black hole growth to z = 2 - I. Improved virial methods for measuring M_{BH} and L/L_{Edd}. *MNRAS*, 427(4):3081–3102.

Tristram, K. (2012). The properties of dusty tori in active galactic nuclei revealed by infrared interferometry. In *Proceedings of Nuclei of Seyfert galaxies and QSOs - Central engine & conditions of star formation (Seyfert 2012). 6-8 November*, page 33.

Tsuzuki, Y. et al. (2006). Fe II Emission in 14 Low-Redshift Quasars. I. Observations. *ApJ*, 650(1):57–79.

Turner, R. J. et al. (2018). RAiSE III: 3C radio AGN energetics and composition. *MNRAS*, 474(3):3361–3379.

Ulrich, M.-H. et al. (1997). Variability of Active Galactic Nuclei. *ARA&A*, 35:445–502.

Ulvestad, J. S. et al. (2005). VLBA Imaging of Central Engines in Radio-Quiet Quasars. *ApJ*, 621(1):123–129.

Urry, C. (2004). AGN Unification: An Update. In Richards, G. T. and Hall, P. B., editors, *AGN Physics with the Sloan Digital Sky Survey*, volume 311 of *Astronomical Society of the Pacific Conference Series*, page 49.

Urry, C. M. and Padovani, P. (1995). Unified Schemes for Radio-Loud Active Galactic Nuclei. *PASP*, 107:803.

Vaddi, S. et al. (2016). Constraints on Feedback in the Local Universe: The Relation between Star Formation and AGN Activity in Early-type Galaxies. *ApJ*, 818(2):182.

Van Langevelde, H. et al. (2018). Very Long Baseline Interferometry: the EVN, WSRT, and JIVE. In *Westerbork Telescope 50th Anniversary*, volume 361, page 8.

van Velzen, S. et al. (2012). Radio galaxies of the local universe. All-sky catalog, luminosity functions, and clustering. *A&A*, 544:A18.

van Velzen, S. and Falcke, H. (2013). The contribution of spin to jet-disk coupling in black holes. *A&A*, 557:L7.

Vanden Berk, D. E. et al. (2001). Composite Quasar Spectra from the Sloan Digital Sky Survey. *AJ*, 122(2):549–564.

Vaona, L. et al. (2012). Spectral properties of the narrow-line region in Seyfert galaxies selected from the SDSS-DR7. *MNRAS*, 427(2):1266–1283.

Vermeulen, R. C. et al. (1993). Superluminal Motion in the Large, Strongly Lobe-dominated Quasar 3C 47. *ApJ*, 417:541.

Veron, P. (1977). The Revised 3C Catalogue of Radio Sources. *The Messenger*, 10:12–13.

Véron-Cetty, M. P. et al. (2004). The unusual emission line spectrum of I Zw 1. *A&A*, 417:515–525.

Véron-Cetty, M. P. and Véron, P. (2010). A catalogue of quasars and active nuclei: 13th edition. *A&A*, 518:A10.

Vestergaard, M. (2002). Determining Central Black Hole Masses in Distant Active Galaxies. *ApJ*, 571(2):733–752.

Vestergaard, M. and Osmer, P. S. (2009). Mass Functions of the Active Black Holes in Distant Quasars from the Large Bright Quasar Survey, the Bright Quasar Survey, and the Color-selected Sample of the SDSS Fall Equatorial Stripe. *ApJ*, 699(1):800–816.

Vestergaard, M. and Peterson, B. M. (2006). Determining Central Black Hole Masses in Distant Active Galaxies and Quasars. II. Improved Optical and UV Scaling Relationships. *ApJ*, 641(2):689–709.

Vestergaard, M. and Wilkes, B. J. (2001). An Empirical Ultraviolet Template for Iron Emission in Quasars as Derived from I Zwicky 1. *ApJS*, 134(1):1–33.

Vietri, G. et al. (2020). SUPER. III. Broad line region properties of AGNs at z $\sim$ 2. *A&A*, 644:A175.

Villafaña, L. et al. (2023). What Does the Geometry of the Hβ BLR Depend On? *ApJ*, 948(2):95.

Villarroel, B. and Korn, A. J. (2014). The different neighbours around Type-1 and Type-2 active galactic nuclei. *Nature Physics*, 10(6):417–420.

Vollmer, B. et al. (2010). The SPECFIND V2.0 catalogue of radio cross-identifications and spectra. SPECFIND meets the Virtual Observatory. *A&A*, 511:A53.

Vrielmann, S. (2001). Physical Parameter Eclipse Mapping. In Boffin, H. M. J., Steeghs, D., and Cuypers, J., editors, *Astrotomography, Indirect Imaging Methods in Observational Astronomy*, volume 573, page 332.

Wada, K. et al. (2021). Discovery of new changing-look quasar 3C 332 and constraints for a double-peaked emission line scenario. *PASJ*, 73(3):596–608.

Wald, R. M. (1984). *General Relativity*.

Wald, R. M. (1997). Gravitational Collapse and Cosmic Censorship. *arXiv e-prints*, pages gr–qc/9710068.

Wanders, I. et al. (1995). The Geometry and Kinematics of the Broad-Line Region in NGC 5548 from HST and IUE Observations. *ApJL*, 453:L87.

Wang, J.-G. et al. (2009). Estimating Black Hole Masses in Active Galactic Nuclei Using the Mg II λ2800 Emission Line. *ApJ*, 707(2):1334–1346.

Wang, J.-M. et al. (2006). Evidence for Rapidly Spinning Black Holes in Quasars. *ApJL*, 642(2):L111–L114.

Wang, J.-M. et al. (2017). Tidally disrupted dusty clumps as the origin of broad emission lines in active galactic nuclei. *Nature Astronomy*, 1:775–783.

Wang, J.-M. et al. (2023). Star Formation in Self-gravitating Disks in Active Galactic Nuclei. III. Efficient Production of Iron and Infrared Spectral Energy Distributions. *ApJ*, 954(1):84.

Wang, T. G. et al. (2005). Two Extreme Double-peaked Line Emitters in the Sloan Digital Sky Survey. *ApJL*, 625(1):L35–L38.

Wehrle, A. E. et al. (2009). What is the Structure of Relativistic Jets in AGN on Scales of Light Days? In *astro2010: The Astronomy and Astrophysics Decadal Survey*, volume 2010, page 310.

Weiler, K. W., Sramek, R. A., Panagia, N., van der Hulst, J. M., and Salvati, M. (1986). Radio Supernovae. *ApJ*, 301:790.

West, A. T. and Krawczynski, H. (2023). Impact of the Accretion Disk Thickness on the Polarization of the Thermal Emission from Stellar Mass Black Holes. *ApJ*, 957(1):9.

White, R. L. et al. (2007). Signals from the Noise: Image Stacking for Quasars in the FIRST Survey. *ApJ*, 654(1):99–114.

Wielgus, M. et al. (2016). Limits on thickness and efficiency of Polish doughnuts in application to the ULX sources. *A&A*, 587:A38.

Wilhite, B. C. et al. (2008). On the variability of quasars: a link between the Eddington ratio and optical variability? *MNRAS*, 383(3):1232–1240.

Williamson, D. et al. (2019). 3D Radiation Hydrodynamics of a Dynamical Torus. *ApJ*, 876(2):137.

Wills, B. J. and Browne, I. W. A. (1986). Relativistic Beaming and Quasar Emission Lines. *ApJ*, 302:56.

Witzel, G. et al. (2021). Rapid Variability of Sgr A* across the Electromagnetic Spectrum. *ApJ*, 917(2):73.

Wolf, C. et al. (2020a). Ultra-luminous quasars at redshift z > 4.5 from SkyMapper. *MNRAS*, 491(2):1970–1979.

Wolf, J. et al. (2020b). Exploring the diversity of Type 1 active galactic nuclei identified in SDSS-IV/SPIDERS. *MNRAS*, 492(3):3580–3601.

Woo, J.-H. et al. (2010). The Lick AGN Monitoring Project: The M_{BH}-σ_* Relation for Reverberation-mapped Active Galaxies. *ApJ*, 716(1):269–280.

Woo, J.-H. and Urry, C. M. (2002). Active Galactic Nucleus Black Hole Masses and Bolometric Luminosities. *ApJ*, 579(2):530–544.

Worrall, D. M. (2009). The X-ray jets of active galaxies. *A&A*, 17:1–46.

Wright, E. L. et al. (2010). The Wide-field Infrared Survey Explorer (WISE): Mission Description and Initial On-orbit Performance. *AJ*, 140(6):1868–1881.

Wu, Q. and Shen, Y. (2022). A Catalog of Quasar Properties from Sloan Digital Sky Survey Data Release 16. *ApJS*, 263(2):42.

Wu, X. B. et al. (2004). Black hole mass estimation using a relation between the BLR size and emission line luminosity of AGN. *A&A*, 424:793–798.

Xu, C. et al. (1999). Radio-loud and Radio-quiet Active Galactic Nuclei. *AJ*, 118(3):1169–1176.

Xu, D. and Komossa, S. (2011). The narrow-line region of narrow-line Seyfert 1 galaxies. In Foschini, L., Colpi, M., Gallo, L., Grupe, D., Komossa, S., Leighly, K., and Mathur, S., editors, *Narrow-Line Seyfert 1 Galaxies and their Place in the Universe*, page 6.

Yang, J. et al. (2021). Monster in the Early Universe: Unveiling the Nature of a Dust Reddened Quasar Hosting a Ten-Billion Solar Mass Black Hole at z=7.1. JWST Proposal. Cycle 1, ID. #2249.

Yi, I. (1999). Advection-Dominated Accretion Flows. In Sellwood, J. A. and Goodman, J., editors, *Astrophysical Discs - an EC Summer School*, volume 160 of *Astronomical Society of the Pacific Conference Series*, page 279.

York, D. G. et al. (2000). The Sloan Digital Sky Survey: Technical Summary. *AJ*, 120(3):1579–1587.

Yousef, Y. and Davis, S. (2020). Testing the Standard Model of AGN Accretion Disks. In *American Astronomical Society Meeting Abstracts #235*, volume 235 of *American Astronomical Society Meeting Abstracts*, page 369.09.

Yuan, Y. et al. (2018). The pc-scale radio structure of MIR-observed radio galaxies. *Research in Astronomy and Astrophysics*, 18(9):108.

Zakir, Z. (2000). The general relativistic theory of quasars. *arXiv e-prints*, page physics/0007012.

Zamanov, R. et al. (2002). Kinematic Linkage between the Broad- and Narrow-Line-emitting Gas in Active Galactic Nuclei. *ApJL*, 576(1):L9–L13.

Zamfir, S. et al. (2008). New insights on the QSO radio-loud/radio-quiet dichotomy: SDSS spectra in the context of the 4D eigenvector1 parameter space. *MNRAS*, 387(2):856–870.

Zamfir, S. et al. (2010). Detailed characterization of Hβ emission line profile in low-z SDSS quasars. *MNRAS*, 403(4):1759–1786.

Zhang, K. et al. (2008). Difference in Narrow-Emission-Line Spectra of Seyfert 1 and 2 Galaxies. *ApJL*, 685(2):L109.

Zhang, K. et al. (2011). The Blueshifting and Baldwin Effects for the [O III] λ5007 Emission Line in Type 1 Active Galactic Nuclei. *ApJ*, 737(2):71.

Zhang, S. et al. (2019a). Profile of and variability in double-peaked Balmer emission lines in 3C 445. *MNRAS*, 490(2):1738–1742.

Zhang, S. et al. (2019b). SDSS J153636.22+044127.0 and Its Analogs: Shocked Outflows, Not Active Binary Black Holes. *ApJ*, 877(1):33.

Zhang, X.-G. (2011). 3C 390.3: more stable evidence that the double-peaked broad Balmer lines originate from an accretion disc near a central black hole. *MNRAS*, 416(4):2857–2868.

Zhang, X. G. (2013). Further evidence for the accretion disc origination of the double-peaked broad hα of 3C 390.3. *MNRAS*, 431:L112–L116.

Zheng, W. et al. (1990). A Double-Stream Model for Line Profiles. *ApJ*, 365:115.

Zheng, W. et al. (1991). 3C 390.3: Modeling Variable Profile Humps. *ApJ*, 381:418.

Zhu, S. F. et al. (2021). The X-ray spectral and variability properties of typical radio-loud quasars. *MNRAS*, 505(2):1954–1971.

Zou, F. et al. (2019). The Host-galaxy Properties of Type 1 versus Type 2 Active Galactic Nuclei. *ApJ*, 878(1):11.

Zwicky, F. (1964). The Luminosity Function of Galaxies. *ApJ*, 140:1626–1628.

Zwicky, F. and Zwicky, M. A. (1971). *Catalogue of selected compact galaxies and of post-eruptive galaxies*.

•

Appendix A

Radio information and overlay with optical Pan-STARRS images

A.1 PHL 923

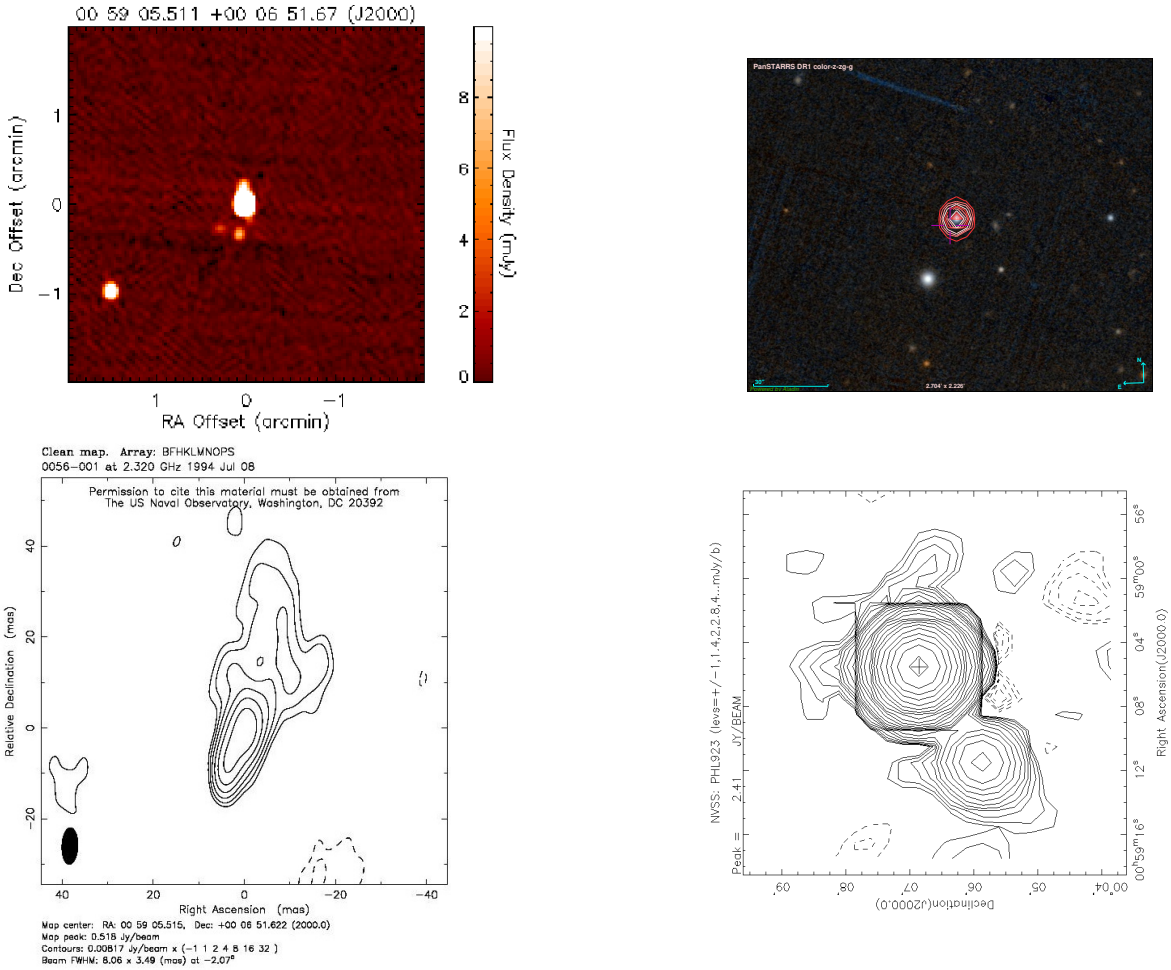

Figure A.1: FIRST cutout image in arcmin (top left) and an overlay of FIRST cutout image on the Optical Pan-STARRS image (top right), VLBA 2.3GHz (bottom left), and NVSS contour map (bottom right) of the source **PHL 923.**

A.2 B2 0110+29

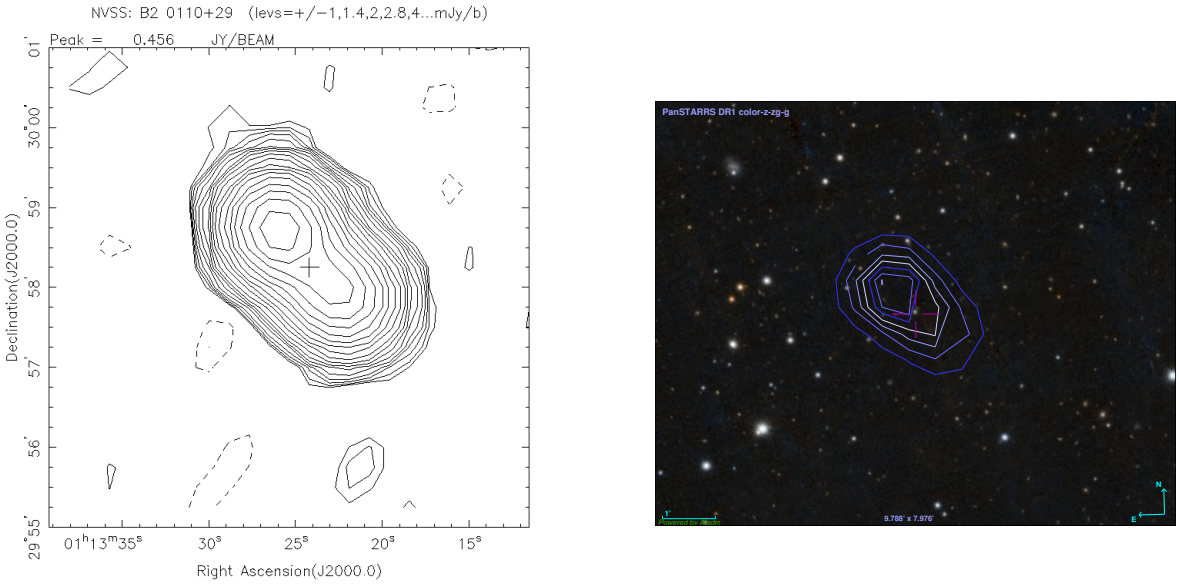

Figure A.2: NVSS contour map (left) and an overlay of NVSS contour map on the Optical Pan-STARRS image (right) of **B2 0110+29.**

A.3 3C 37

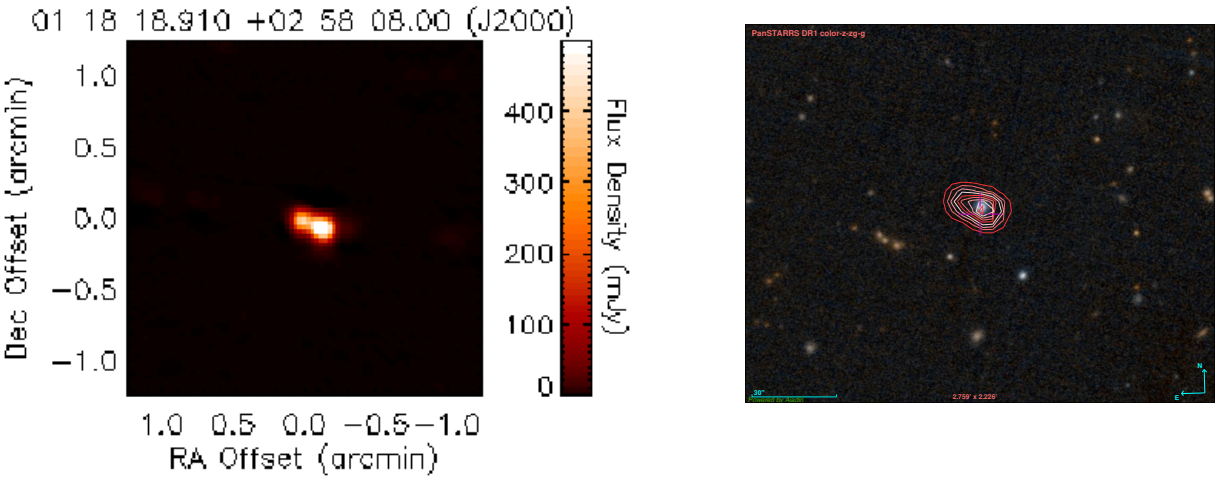

Figure A.3: FIRST cutout image obtained with maximum scaling to be 1000 mJy (left) and an overlay of FIRST cutout image on the Optical Pan-STARRS image (right) for the source **3C 37**.

A.4 3C 47

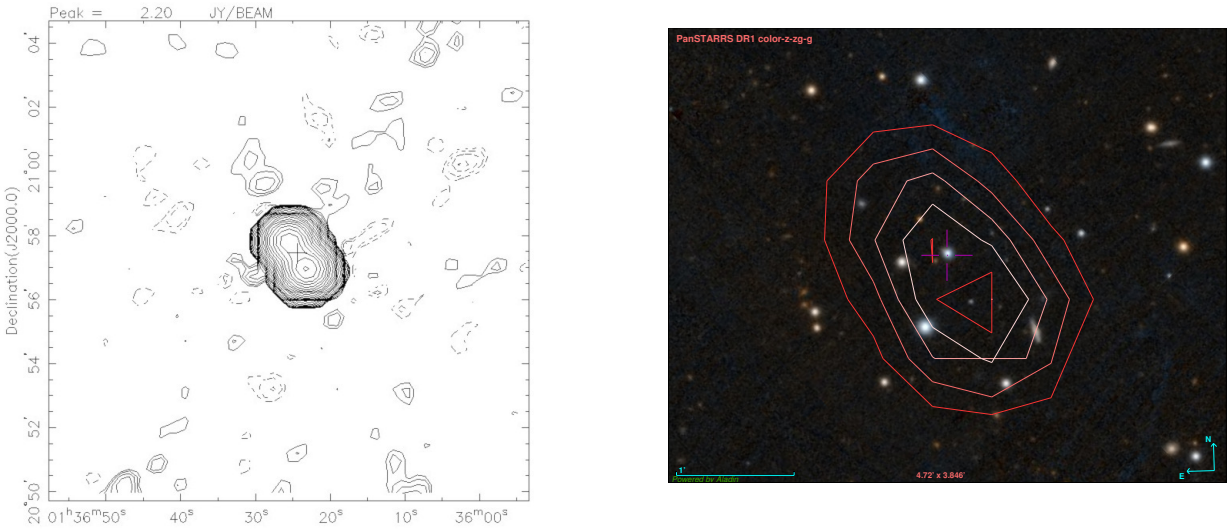

Figure A.4: NVSS contour map (left) and an overlay of NVSS contour map on the Optical Pan-STARRS image (right) of **3C 47.**

A.5 PKS 0230-051

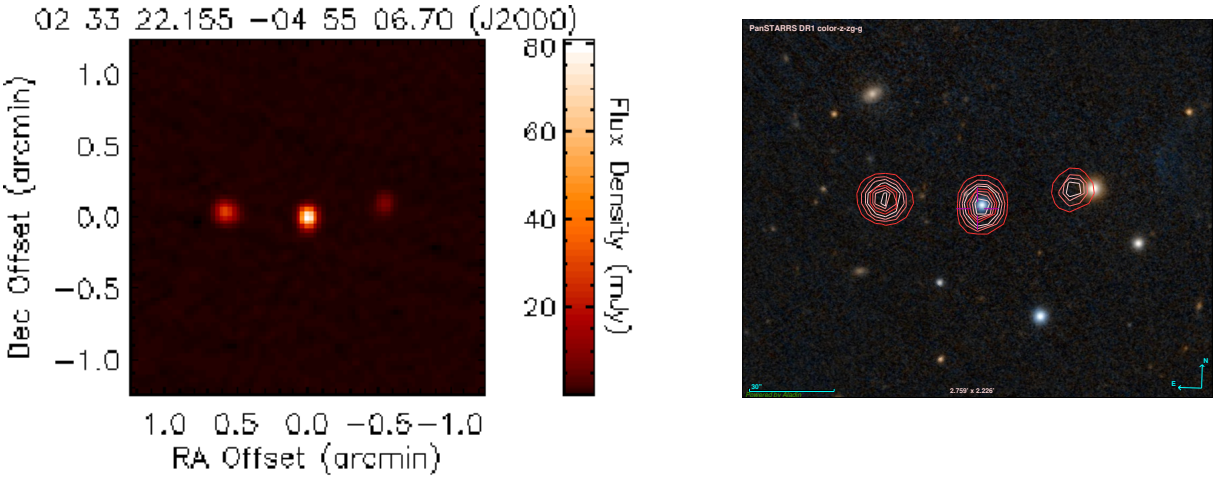

Figure A.5: FIRST cutout image obtained with maximum scaling to be 1000 mJy to show the separate components (left) and an overlay of FIRST cutout on the Optical Pan-STARRS image (right) for the source **PKS 0230-051.**

A.6 3C 94

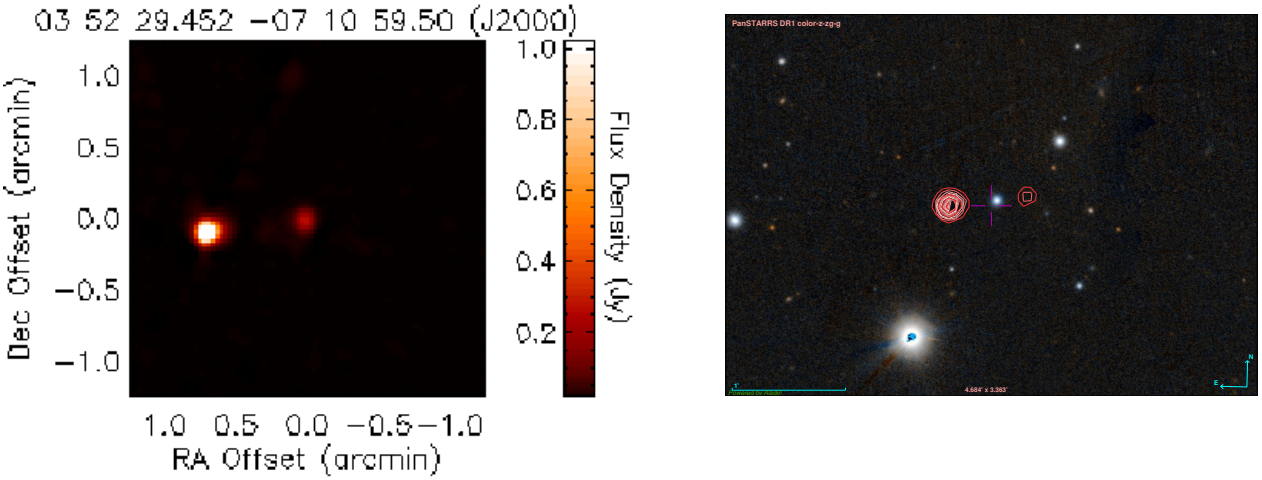

Figure A.6: FIRST cutout image obtained with maximum scaling to be 1000 mJy to show the separate components (left) and an overlay of FIRST cutout on the Optical Pan-STARRS image (right) for the source **3C 94.**

A.7 PKS 0420-01

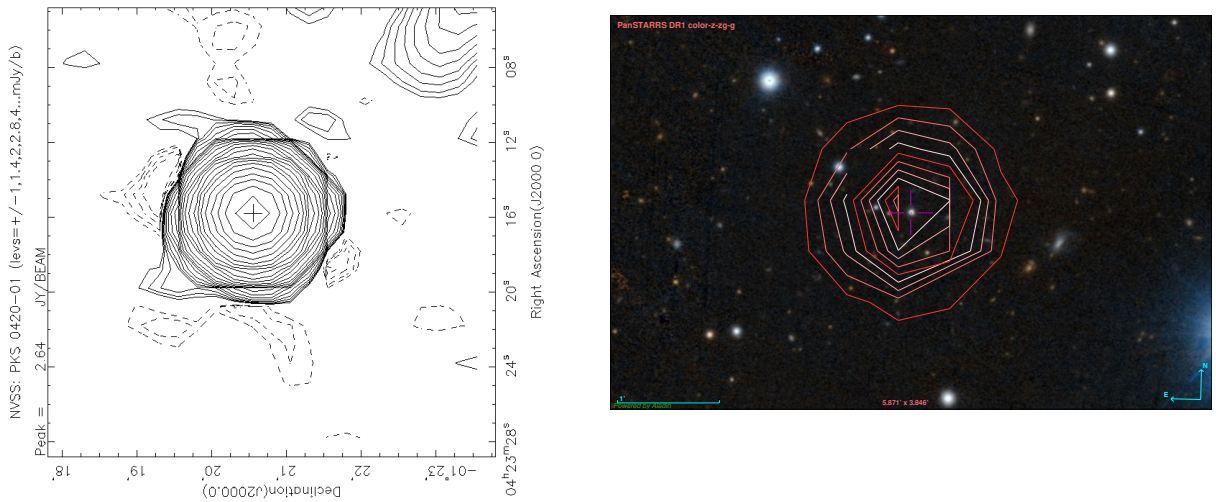

Figure A.7: NVSS contour map (left) and an overlay of NVSS contour map on the Optical Pan-STARRS image (right) for the source **PKS 0420-01.**

A.8 3C 179

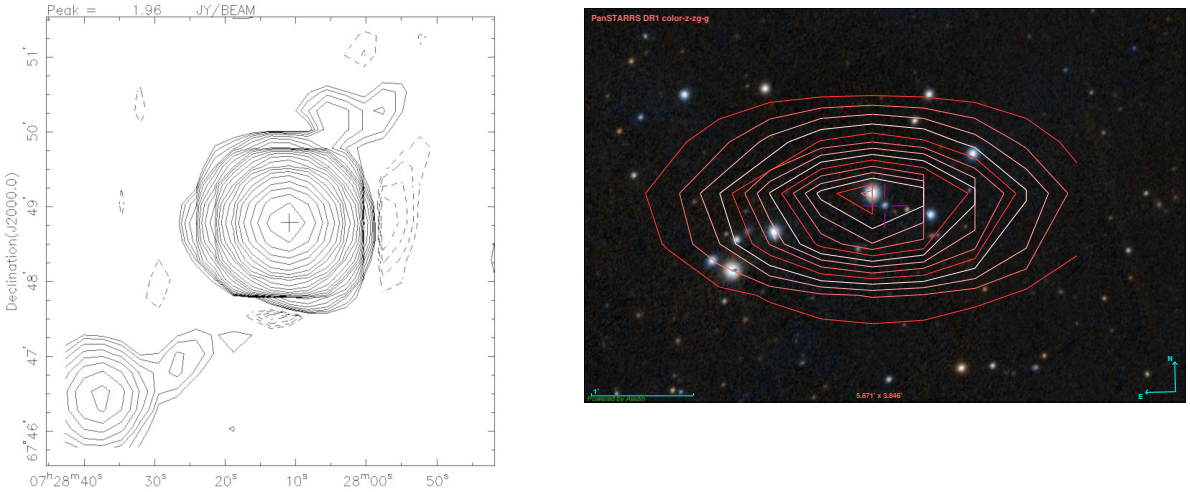

Figure A.8: NVSS contour map (left) and an overlay of NVSS contour map on the Optical Pan-STARRS image (right) for the source **3C 179.**

A.9 3C 380

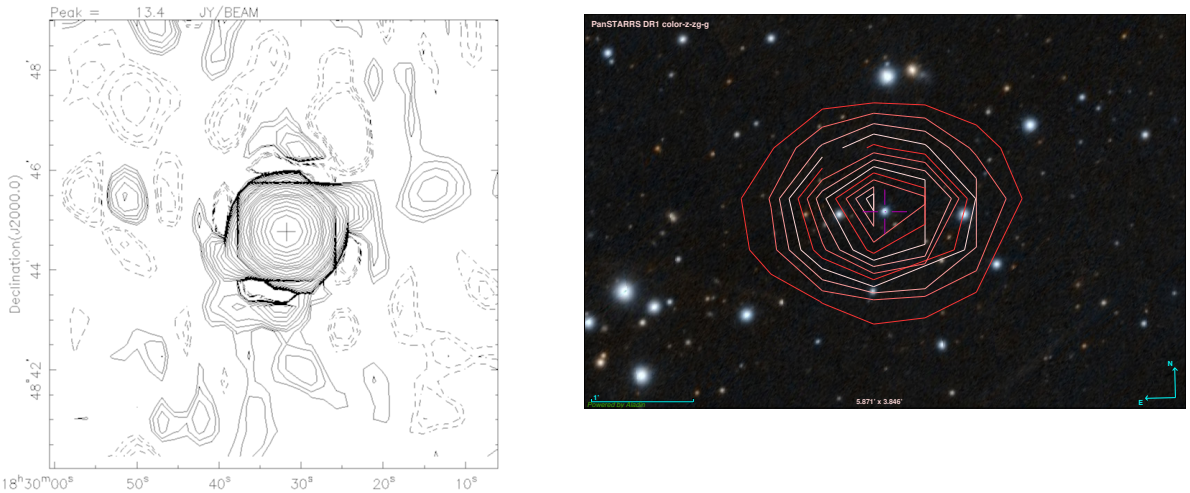

Figure A.9: NVSS contour map (left) and an overlay of NVSS contour map on the Optical Pan-STARRS image (right) for the source **3C 380.**

A.10 S5 1856+73

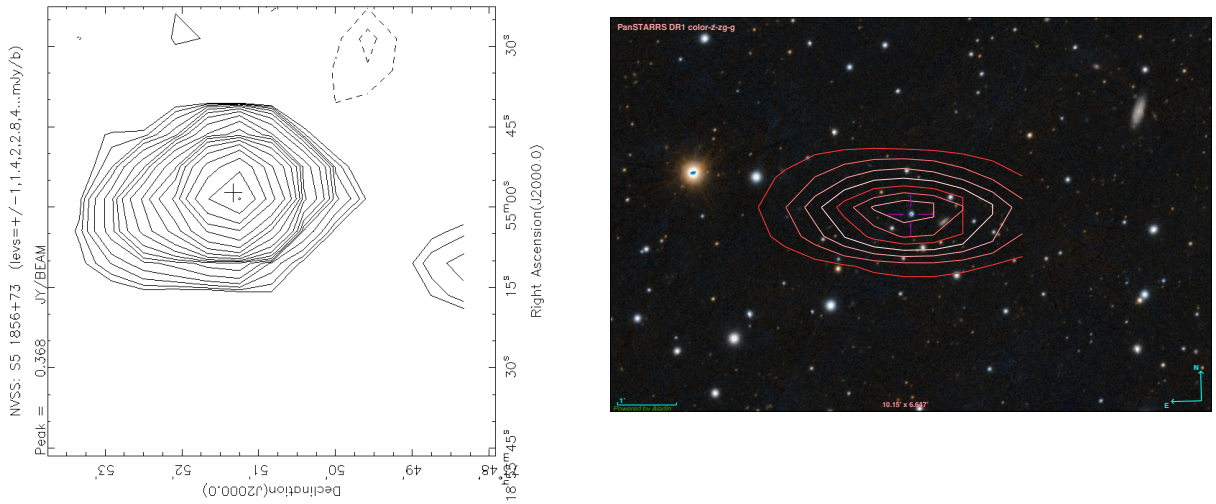

Figure A.10: NVSS contour map (left) and an overlay of NVSS contour map on the Optical Pan-STARRS image (right) for the source **S5 1856+73.**

A.11 PKS 2208-137

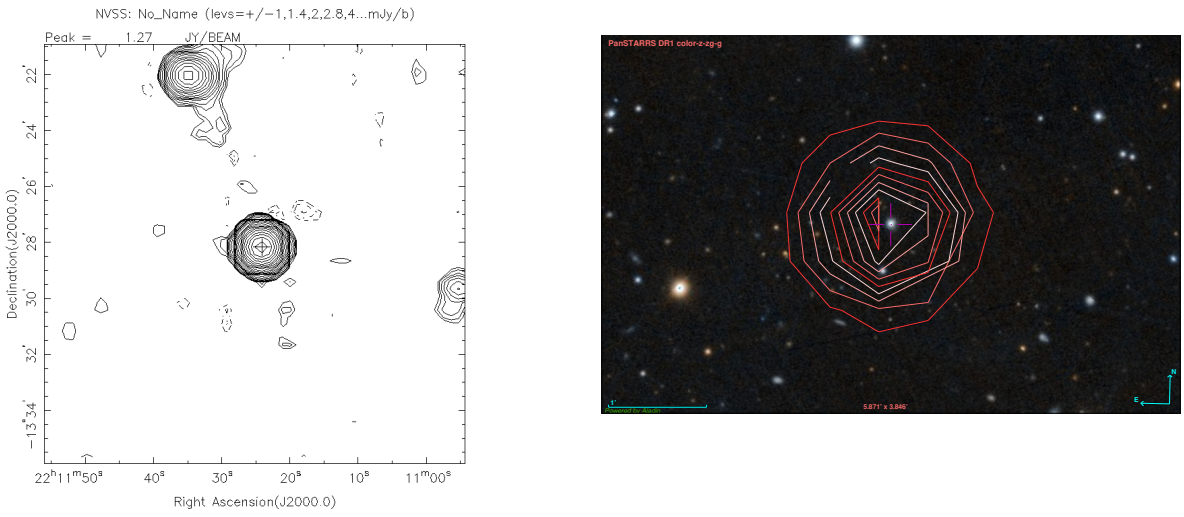

Figure A.11: NVSS contour map (**left**) and an overlay of NVSS contour map on the Optical Pan-STARRS image (**right**) of the source **PKS 2208-137.**

A.12 PKS 2344+09

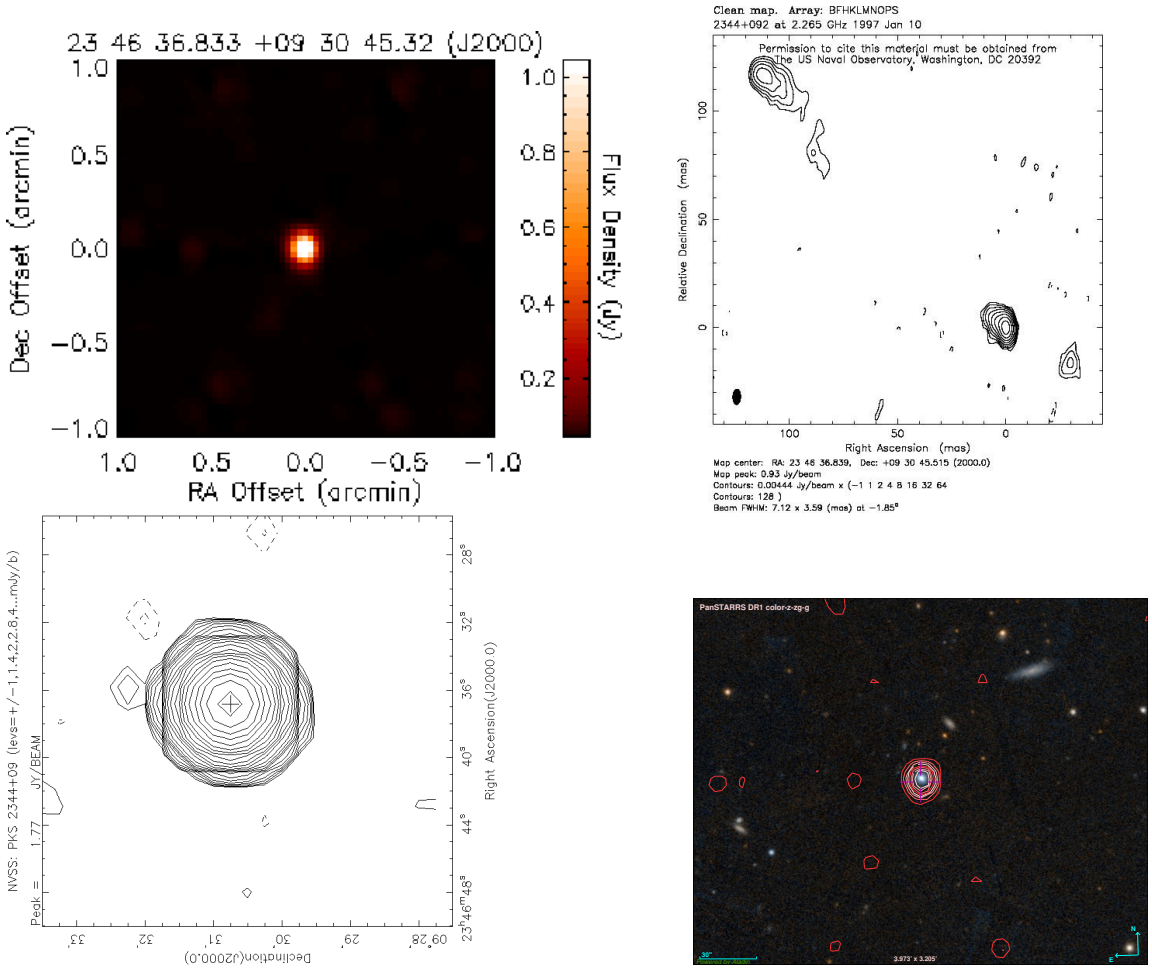

Figure A.12: FIRST cutout image obtained with maximum scaling to be 1000 mJy to show the separate components (top left), VLBA 2.3GHz, NVSS contour map and an overlay of FIRST cutout on the Optical Pan-STARRS image (**right**) for the source **PKS 2344+09.**

Appendix B

Sample `specfit` database in the Hβ and MgIIλ2800 regions for one of our sources, PHL 923.

The terms used in the sample database (Table B.1) are described below.

- ✓ The term "begin" helps to identify the name of the database used.
- ✓ The term "task" signifies the type of fitting, in this case "`specfit`.
- ✓ The term"components" signifies the number of components we will include in the fitting process, 11 in this case.
- ✓ "powerlaw", "userline" "recomb" (in the case of MgIIλ2800 for Balmer continuum), and "gaussian" represent the type of fitting we will use, and are identified by assigning a number that signifies the order.
- ✓ "powerlaw1" is for continuum fitting and "2" signifies the number of parameters used (the intensity and powerlaw index for this case.)
- ✓ **a**, **b**, **c**, **d**, **e** and **f** represents the parameter value, lower limit, upper limit, step size, tolerance and fix of the parameters, respectively.
- ✓ "userline2" is for FeII lines fitting using a template.
- ✓ "gaussian3" is for the Hβ narrow component.
- ✓ "gaussian4" is for the Hβ broad component.
- ✓ "gaussian5" is for the Hβ very broad component.
- ✓ "gaussian6" is for the [OIII]λ4959 narrow component.
- ✓ "gaussian7" is for the [OIII]λ5007 narrow component.
- ✓ "gaussian8" is for the HeIIλ4686 narrow component.
- ✓ "gaussian9" is for the HeIIλ4686 broad component.
- ✓ "gaussian10" is for the [OIII]λ4959 narrow component.
- ✓ "gaussian11" is for the [OIII]λ5007 narrow component.

Table B.1: A sample database used for fitting of the quasars PHL 923 spectral in the Hβ region using the **IRAF** task `specfit`.

```
begin       q02hbfinal
task          specfit
components      11
                    powerlaw
                    userline
                    gaussian
                    gaussian
                    gaussian
                    gaussian
                    gaussian
                    gaussian
                    gaussian
                    gaussian
                    gaussian
powerlaw1 2 # powerlaw continuum
                  31.759089[a]   0.[b]   100.[c]   0.1[d]   0.001[e]   0[f]
                    1.9716084    -5.      5.       0.04      0.001      0
 userline2    4 # # FeII emission
                    0.21617945   0.002    1.1    5.0000E-4   0.001      0
                    0.39194754   -10.     10.      0.01     1.0000E-4   -1
                      0.         0.      0.005  1.0000E-4    0.001      -1
                     20.         0.      20.      0.01       0.001      -1
 gaussian3      4 # Hβ NC
                    4.324093     0.      120.     0.1        0.001      0
                    4862.784     4852.   4900.    0.97104    0.001      7
                    806.8431     100.    2000.    1.         0.001      7
                      1.         0.1     10.      0.01       1.00E-4    -1
 gaussian4      4 # Hβ BC
                    58.66821     0.      400.     0.1        0.001      0
                    4857.339     4855.   4975.    0.1        0.001      0
                    3642.915     1000.   6000.    1.         0.001      0
                      1.         0.1     10.      0.01       1.00E-4    -1
 gaussian5      4 # Hβ VBC
                    74.03433     0.      1000.    0.1        0.001      0
                    4933.529     4872.   4950.    0.1        0.001      0
                    11384.89     4000.   18000.   1.         0.001      0
                      1.         0.1     10.      0.01       1.00E-4    -1
 gaussian6      4 # [OIII]_1 NC
                    16.64253     0.      120.     0.3331     0.001      7
                    4959.736     4955.   4965.    0.9904     0.001      7
                    806.8431     100.    2000.    1.         0.001      7
                      1.         0.1     10.      0.01       1.00E-4    -1
 gaussian7      4 # [OIII]_2 NC
                    49.96255     0.      120.     0.1        0.001      0
                    5007.811     5002.   5012.    0.1        0.001      0
                    806.8431     100.    2000.    1.         0.001      0
                      1.         0.1     10.      0.01       1.00E-4    -1
 gaussian8      4 # HeII
                    14.99179     0.      120.     0.02       0.001      0
                    4689.461     4670.   4750.    0.05       0.001      0
                    3189.626     1000.   14000.   1.         0.001      0
                      1.         0.1     10.      0.01       1.00E-4    -1
 gaussian9      4 # [OIII]_1 SBC
                    12.8978      0.      120.     0.3333     0.001      10
                    4960.297     4955.   4975.    0.99041    1.00E-4    10
                    1638.025     100.    5000.    1.         1.00E-4    10
                      1.         0.1     10.      0.01       1.00E-4    -1
gaussian10     4 # [OIII]_1 SBC
                    38.69726     0.      120.     0.1        0.001      0
                    5008.327     5005.   5015.    0.05       0.001      0
                    1638.025     100.    5000.    1.         0.001      0
                      1.         0.1     10.      0.01       1.00E-4    -1
gaussian11          4 #
                    14.99332     0.      120.     0.1        0.001      0
                    4863.286     4852.   4900.    0.97104    0.001      10
                    1638.025     100.    2000.    1.         0.001      10
                      1.         0.1     10.      0.01       1.00E-4    -1
```

Table B.2: A sample database used in the MgIIλ2800 region.

begin	q02mgiifinal						
task	specfit						
components	12						
	powerlaw						
	userline						
	recomb						
	gaussian						
	gaussian						
	gaussian						
	gaussian						
	gaussian						
	gaussian						
	gaussian						
	gaussian						
	gaussian						
	powerlaw1	2 # powerlaw continuum					
		24.26922[a]	0.[b]	100.[c]	0.001[d]	0.001[e]	0[f]
		1.568227	-1.	9.1	0.01	0.001	0
	userline2	4 # FeII emission					
		0.3574125	0	2	1.000000E-4	0.001	0
		4.200819	-10.	10.	0.01	0.001	0
		0.	0.	0.2	0.001	0.0001	-1
		20.	0.	29.	0.1	0.001	0
	recomb3	4 # Balmer continuum					
		0.2176294	0.	20.	1.000000E-4	1.00E-4	0
		3645.028	3000.	4000.	0.01	0.001	0
		19929.82	1000.	20000.	100.	0.001	0
		3965.934	100.	17500.	1.	0.001	0
	gaussian4	4 # MgII NC_1					
		1.36472	0.	120.	0.01	0.001	0
		2795.126	2793.	2799.	0.01	0.001	0
		445.5664	100.	1500.	1.	0.001	0
		1.	0.	2.	0.001	0.001	-1
	gaussian5	4 # MgII NC_2					
		5.58327	0.	20.	0.667	0.001	4
		2802.354	2797.	2810.	1.002586	0.001	4
		455.5664	100.	1500.	1.	0.001	4
		1.	0.	2.	0.001	0.001	-1
	gaussian6	4 # MgII BC_1					
		55.98567	0.	200.	0.01	0.001	0
		2798.048	2785.	2805.	0.01	0.001	0
		3500.532	500.	17500.	1.	0.001	0
		1.	0.	2.	0.001	1.00E-4	-1
	gaussian7	4 # MgII BC_2					
		41.58854	0.	200.	0.8	0.001	6
		2805.284	2797.	2810.	1.002586	0.001	6
		3000.532	500.	17500.	1.	0.001	6
		1.	0.	2.	0.001	0.001	-1
	gaussian8	4 # MgII VBC					
		75.51127	2.	200.	0.001	0.001	0
		2809.576	2800.	2830.	0.01	0.001	0
		10633.87	10000.	33000.	1.	0.001	0
		1.	0.	2.	0.001	0.001	-1
	gaussian9	4 # O III					
		8.705191	0.	120.	0.01	0.001	0
		3130.656	3125.	3140.	0.01	0.001	0
		4991.14	500.	6000.	1.	0.001	0
		1.	0.	2.	0.001	0.001	-1
	gaussian10	4 # He I					
		6.266573	0.	120.	0.01	0.001	0
		3190.171	3185.	3200.	0.01	0.001	0
		4991.718	100.	6000.	1.	0.001	0
		1.	0.	2.	0.001	0.001	-1
	gaussian11	4 # Ne V _2					
		10.04113	0.	120.	0.001	1.00E-4	0
		3426.493	3420.	3435.	0.01	1.00E-4	0
		1918.222	100.	6000.	1.	1.00E-4	0
		1.	0.	2.	0.001	1.00E-4	-1
	gaussian12	4 # [O II]					
		10.02062	0.	120.	0.001	1.00E-4	0
		3729.564	3720.	3739.	0.01	1.00E-4	0
		230.542	100.	5000.	1.	1.00E-4	0
		1.	0.	2.	0.001	1.00E-4	-1